



Habilitation Thesis

Continuum Mechanics Modeling of Materials

ausgeführt zum Zwecke der Erlangung der Lehrbefugnis im Fachgebiet

Werkstoff- und Strukturmechanik
(Mechanics of Materials and Structures)

eingereicht an der Technischen Universität Wien
Fakultät für Maschinenwesen und Betriebswissenschaften

von

Assistant Prof. Dipl.-Ing. Dr.techn. Melanie Todt

Abstract

The present thesis takes the form of a compilation of six publications in SCI-listed scientific journals, 3 proceedings papers, and one book chapter. The publications address the analytical and numerical continuum mechanics modeling of materials at different physical length scales. The main goal is the development of efficient computational models which allow characterizing the nonlinear mechanical behavior of materials but are also capable of simulating the response of large structures if appropriate material models are employed. Special focus lies on structural instabilities at the material level as well as on the modeling of damage onset and evolution. Furthermore, the limits of continuum mechanics are explored as the computational models are also applied at the atomic scale.

Specifically, the nonlinear mechanical behavior of three material systems is investigated: carbon nanostructures, thin films, and lattice materials. The developed analytical continuum mechanics models for accessing the mechanical behavior of the various material systems are based on concepts of structural mechanics such as plates, shells, and beams. The numerical methods employ the finite element method where mainly structural elements are used to guarantee a high numerical efficiency.

For all investigated material systems, the continuum mechanics models allow gaining further insight into mechanisms observed in experiments. This knowledge can be used for tailoring the material systems towards target applications. In contrast to experimental methods, the parameters characterizing the material system can be varied in an economic manner and, especially, the analytical methods allow for a computationally efficient application within optimization schemes. Furthermore, the developed computational models have the potential of reducing or even partly replacing expensive and time consuming experimental campaigns in the future.

Zusammenfassung

Die vorliegende Habilitationsschrift ist eine Zusammenfassung von sechs Publikationen in SCI-gelisteten wissenschaftlichen Journalen, drei Konferenz-Proceedings sowie eines Buchkapitels. Die Publikationen befassen sich mit der analytischen und numerischen kontinuumsmechanischen Modellierung von Materialien auf verschiedenen physikalischen Längenskalen. Ziel ist die Entwicklung von effizienten Rechenmodellen, die einerseits eine Beschreibung des nichtlinearen mechanischen Verhaltens von Materialien gestatten, andererseits aber auch die Simulation von Strukturen unter Einsatz entsprechender Materialmodelle ermöglichen. Speziell der strukturelle Stabilitätsverlust auf Materialebene sowie die Modellierung von Schädigungsbeginn und Schädigungsfortschritt sind dabei von besonderem Interesse. Zudem werden die Grenzen der Kontinuumsmechanik ausgelotet indem die Rechenmodelle bis hinunter auf die atomare Skala angewendet werden.

Konkret wird das nichtlineare mechanische Verhalten von drei Materialsystemen untersucht: Kohlenstoff-Nanostrukturen, Dünnschicht-Systemen und Gittermaterialien. Die entwickelten analytischen Modelle verwenden Konzepte der Strukturmechanik, wie die Balken- und Schalentheorie, um das mechanische Verhalten des jeweiligen Materialsystems abzubilden. Die numerischen Modelle basieren auf der Finite Elemente Methode, wobei weitestgehend Strukturelemente zum Einsatz kommen, um eine hohe numerische Effizienz zu garantieren.

Für alle untersuchten Materialsysteme ermöglichen die entwickelten kontinuumsmechanischen Modelle einen besseren Einblick in experimentell beobachtete Phänomene. Die so gewonnenen Erkenntnisse können z.B. für die Gestaltung der Materialsysteme im Hinblick auf anwendungsspezifische Eigenschaften verwendet werden. Im Gegensatz zu experimentellen Methoden lassen sich Parameter in den Modellen einfach variieren und speziell die analytischen Modelle eignen sich für einen effizienten Einsatz innerhalb von Optimierungsverfahren. Die entwickelten Rechenmodelle eröffnen zudem die Möglichkeit in Zukunft teure und zeitintensive experimentelle Kampagnen teilweise oder ganz zu ersetzen.

Contents

1	Introduction	2
1.1	Scales of Observation	2
1.2	Aspects of Continuum Mechanics Modeling	4
1.3	Continuum Mechanics Modeling at the Atomic Scale	5
1.4	Consideration of Nonlinearities	6
1.5	Relation to Experiments	7
1.6	Outline of the Thesis	8
2	Carbon Nanostructures	10
2.1	Introduction	10
2.2	Continuum Mechanics Modeling	11
2.2.1	Space Frame Models	12
2.2.2	Continuum Shell Models	13
2.3	Own Contribution to the Research Field	15
2.3.1	Elastic Constants for Continuum Shell Models	16
2.3.2	Application of Continuum Shell Models	17
2.3.3	Reviews on the Modeling of Nanostructures	19
2.3.4	Declaration of Own Contribution to the Enclosed Publications . . .	20
2.4	Bibliography	21
2.5	Publications	31
3	Thin Films	127
3.1	Introduction	127
3.1.1	Nanoscale Multilayer Coatings	127

3.1.2	Metallization Layers in Semiconductor Devices	129
3.2	Continuum Mechanics Modeling	131
3.2.1	Analytical Models	131
3.2.2	Numerical Models	134
3.3	Own Contribution to the Research Field	136
3.3.1	Material Properties of Superlattice Coatings	136
3.3.2	Fatigue Damage in Power Metallization Layers	137
3.3.3	Declaration of Own Contribution to the Enclosed Publications . . .	138
3.4	Bibliography	138
3.5	Publications	149
4	Lattice Materials	163
4.1	Introduction	163
4.2	Continuum Mechanics Modeling	164
4.2.1	Analytical Modeling	165
4.2.2	Numerical Modeling	167
4.3	Own Contribution to the Research Field	171
4.3.1	Lattice Materials with Tunable Buckling Behavior	171
4.3.2	Efficient Modeling Beyond the Elastic Response	172
4.3.3	Declaration of Own Contribution to the Enclosed Publications . . .	173
4.4	Bibliography	174
4.5	Publications	185

Chapter 1

Introduction

The applications of continuum mechanics modeling in the field of materials science are manifold. They comprise the support of experiments in materials characterization, the prediction of effective properties of a material based on its internal structure as well as the identification of physical mechanisms that determine the material's overall behavior. Ultimately, reliable continuum mechanics models have the potential to replace expensive and time consuming experiments.

Most of these points are addressed within this thesis. The main focus lies on the development of continuum mechanics models, both analytical and numerical ones, which are applicable at the atomic scale as well as on larger length scales. The developed models allow for a computationally efficient modeling of the nonlinear response of structures and materials such that they can be used in conjunction with or as a replacement of experimental campaigns. More details on these points can be found in Sections 1.3 to 1.5. As introduction to the topic some information about the scales of observation and the general aspects of continuum mechanics modeling are provided in Sections 1.1 and 1.2.

1.1 Scales of Observation

What one perceives as structure or material depends on the scale of observation. Every material shows some structural features, at least at the atomic scale. The scales of observation can be defined based on physical length scales or from a modeling perspective.

For scales of observation based on physical lengths, the actual physical size of features is considered. The lowest length scale relevant for continuum mechanics modeling is the

nm-scale where the atomic structure of a material becomes visible. The next larger scale is the μm -scale. It can be related to the size of grains in polycrystalline materials, the diameter of fibers within composite materials, or the sequence of layers in standard multi-layer coatings. Within the fields of mechanical and civil engineering both the mm- and the m-scale are linked to the size of test specimens as well as to the size of structural parts such as the wing of a plane or a framework structure.

In the context of mechanics of materials the scales of observation are rather defined from a modeling perspective than with respect to an absolute physical length. The scales of observation are denoted as micro-, meso-, and macro-scale, respectively. The micro-scale is the lowest length scale and is equal to the length scale of the individual constituents of a material, e.g., inclusions embedded in a matrix or the individual members of a lattice material. At this length scale, the mechanical behavior of the constituents is described using continuum mechanics based material models. The meso-scale is governed by the effective properties of the material. In an ideal case the material's behavior can be described in the form of a closed-form constitutive relation. The macro-scale is the largest length scale and is the scale of the structural problem. The transition from a lower to a higher length scale is called homogenization, the opposite procedure is called localization.

Using classical continuum mechanics, the micro-scale models are not linked to an absolute length scale and the information about the characteristic length of the material is lost during homogenization. This is admissible as long as the principle of separation of scales is satisfied, i.e., the material length scale is far smaller than the characteristic length of the macroscopic problem. If the principle of separation of scales is violated, enriched or generalized continuum theories may be employed which allow to account for the size of the micro-structure within the constitutive relations.

The transition between scales in terms of homogenization and localization in a strict sense does not fall within the scope of this thesis. The considerations focus either on the micro-scale (Chapter 4) or on the use of appropriate constitutive relations within macro-scale simulations (Chapter 3). In Chapter 2 continuum mechanics methods are employed at the nm-scale and a categorization within the micro-, meso-, macro-scheme becomes vague.

Within the Additional Scientific Publications the focus is on multi-scale approaches, where several length scales are contained concurrently within the models.

1.2 Aspects of Continuum Mechanics Modeling

Models attempt to describe reality by the means of mathematical equations and are based on fundamental assumptions about the underlying physics. These assumptions determine the mechanisms that can be studied with a particular model as well as the costs of the model in terms of computational requirements. The selection of a specific model depends strongly on the problem statement and the (expected) associated physical mechanisms and always involves a trade-off between accuracy and costs. For this reason, the obtained results should always be interpreted in view of the underlying model assumptions. The choice and more important also the development of appropriate continuum mechanical models pervade Chapters 2 to 4 of this thesis and is also the main focus of the publications presented in Chapter 2 of the Additional Scientific Publications. Both analytical and numerical modeling techniques are employed, always bearing in mind their inherent characteristics.

Analytical continuum mechanics models show the lowest computational costs. They are suitable for large scale parametric studies in the early design process of materials as well as for the identification of material parameters from experiments. For some simple problems even closed form solutions can be obtained. The power of analytical models is exploited in Chapters 2 and 3 (papers **CN-1**, **CN-2**, and **TF-1**, respectively) for determining material parameters from experiments as well as from atomistic simulations. The high efficiency of these models is counterbalanced by their limited complexity in terms of geometry, boundary and loading conditions, and nonlinearities that can be considered.

In contrast, numerical techniques allow to add various levels of complexity at the price of a significant increase in computational costs. In the context of continuum mechanics modeling, the finite element method is employed throughout all chapters of this thesis. For this method the computational costs strongly depend on the choice of element type and the used discretization. In this regard, structural elements such as shells or beams outperform continuum elements but their application imposes some assumptions on the kinematics as

well as on the axially of the stress state. For the thin and slender structures investigated in Chapters 2 to 4 these elements seem to be a natural choice. Nevertheless, their applicability has to be verified (see Chapter 2 for the case of carbon nanostructures) especially if material nonlinearities such as plastic yielding or damage need to be considered. This is the main focus of publication **LM-3** in Chapter 4 and is also addressed in the publications compiled in Chapter 2 of the Additional Scientific Publications.

Besides the selection of a model that is capable of capturing the essential mechanisms also an appropriate definition of the boundary and loading conditions is of key importance for the reliability of the results. This topic is especially covered in the publication **TF-2** (Chapter 3) where transient thermal loading conditions are realized for simulating thermo-mechanical fatigue in semiconductor devices.

1.3 Continuum Mechanics Modeling at the Atomic Scale

Using continuum mechanics methods at the atomic scale is far from being obvious. Atomic lattices may be viewed as discrete point-structures with their mechanical behavior being governed by the nonlinear local or non-local interactions of the individual atoms. In this respect, the application of atomistic simulation techniques seems to be more appropriate. However, these methods reach their limits in terms of computational costs once the mechanical behavior of large atomic structures such as carbon onions (see paper **CN-3** in Chapter 2) is to be investigated or material parameters need to be extracted from experiments conducted at the μm - or mm-scale (see paper **TF-1** in Chapter 3). The significantly lower computational requirements of continuum mechanics methods are the main motivation for their application at the nanoscale, but one has to be aware that this implies major simplifications.

Within this thesis, the application of continuum mechanics methods to atomic scale systems is employed in Chapters 2 and 3 and is based on two fundamental assumptions. First, the single atom or multiple atom thick layers investigated in these chapters can be represented by shells or plates in terms of structural mechanics. Second, the material behavior of the layers can be described by constitutive relations derived from classical

continuum theory. In relation to the scales of observation this is a delicate topic as for single atom thick layers the line between material and structure is blurred. For example, graphene is often viewed as material and assigned an elastic modulus, a Poisson's ratio, and a fracture strength, but still shows features of a structure in terms of a bending stiffness.

In Chapter 2 the applicability of continuum mechanics models at the atomic scale is verified against atomistic simulation techniques for the case of carbon nanostructures. Furthermore, the selected publications (**CN-1** to **CN-5**) address the question of the bending stiffness of single atom thick layers as well as the identification of appropriate material parameters from atomistic simulations. In publication **TF-1** (Chapter 3), continuum mechanics modeling is utilized to identify material parameters of nm-thick layers from experiments done at the scale of micrometers.

1.4 Consideration of Nonlinearities

In mechanical systems nonlinearities can occur in various forms viz. geometrical nonlinearities, material nonlinearities, contact and friction, and the loss of structural stability. Within this thesis the focus lies on modeling of structural instabilities, i.e., buckling of thin and slender structures, and material nonlinearities in the form of onset and evolution of damage. All other sources of nonlinearities are included in the models whenever they are considered to be essential for the mechanical behavior of the system.

Buckling can occur on several length scales and can have a critical impact on the mechanical behavior of materials at higher length scales as well as on the structural integrity at the macro-scale. The occurrence of structural instabilities may be experienced in the form of a sudden change of the effective material properties or in the form of catastrophic failure. Micro-scale buckling within lattice materials is the main topic of Chapter 4 and in Chapter 2 buckling phenomena at the atomic scale are investigated (publication **CN-3** and **CN-5**).

Damage, or more precisely the evolution of damage, leads to a degradation of effective properties of a material at its meso-scale. This degradation has its origin at lower length scales and can, e.g., be related to the growth and coalescence of micro-pores in polycrys-

talline metals or the rupture of fibers in fiber reinforced plastics. In this thesis the origins of damage are disregarded and damage is described in a phenomenological manner. Continuum damage mechanics based constitutive models in combination with suitable damage onset criteria are employed within the finite element method to account for the effects of damage in structural simulations. In Chapter 3 the evolution of fatigue cracks in semiconductor devices is modeled by this means and within the Additional Scientific Publications the impact loading of woven composite laminates is investigated.

Accounting for nonlinearities usually leads to a significant increase in computational costs. In this respect, numerically efficient models in terms of element types and discretization become of key importance, see also Section 1.2. The development of such models is mainly addressed in the Additional Scientific Publications and is also the motivation of the last publication in Chapter 4.

1.5 Relation to Experiments

In connection with experiments, continuum mechanics models mainly serve two purposes viz. are the support of experiments in the characterization of materials and the interpretation of experimental observations not directly accessible from the recorded measurement data.

The identification of material properties from experiments requires appropriate theoretical models which are readily available for standardized tests. Examples are the evaluation of the Young's modulus and yield limit of standard materials from tensile tests. For more advanced materials such as composites or thin films mainly non-standardized tests are employed requiring the development of associated analytical or numerical models for material parameter identification. Another level of complexity is added if the material of interest is not thermodynamically stable in bulk but only within a material compound. The latter point is addressed in Chapter 3 (paper **TF-1**). Therein an analytical model is developed which allows for the evaluation of material properties of metastable phases within nanolayered superlattice coatings from wafer curvature experiments.

Furthermore, theoretical models allow to gain further insight into underlying mech-

anisms of phenomena observed in experiments. This information can be utilized in the design of materials as well as structures towards specific requirements. Examples are the effect of pre-stress on the mode transition in the post-buckling regime of pre-stressed lattice materials (publications **TF-1** and **TF-2**, Chapter 4), and the contribution of ply damage and delamination to the overall energy dissipated during an impact in fiber reinforced composites (all publications within Chapter 2 of the Additional Scientific Publications). Additionally, in Chapter 2 a theory for the growth limit of carbon onions is proposed based on continuum mechanics simulations (publication **CN-3**).

Another important point are the low costs of continuum mechanics models compared to experimental studies. By employing reliable predictive tools expensive and cumbersome test campaigns can be significantly reduced or even partly replaced. Continuum mechanics models, both analytical and numerical ones, also allow for a variation of design parameters and consequently can guide the design process of both materials and structures. The development of efficient numerical models as partial replacement of experiments is addressed in Chapters 3 and 4 and within Chapter 2 of the Additional Scientific Publications.

Conversely, experimental methods are important for the validation of theoretical models. If experimental and theoretical results differ significantly, identifying the reasons is of major importance. Discrepancies may have their origin in an erroneous or incomplete set of input parameters, an incorrect definition of boundary and loading conditions, and in the worst case in wrong modeling assumptions. The verification of models against experiments is addressed in the Additional Scientific Publications. Another possibility to verify a specific model is the comparison with other modeling approaches, see Chapter 2, where continuum mechanics methods are verified against atomistic simulation techniques.

1.6 Outline of the Thesis

This cumulative thesis consists of six publications in SCI listed journals, three proceedings papers, and one book chapter within the main part. Three journal publications, two proceedings papers, and one book chapter comprise the Additional Scientific Publications.

Most of the compiled papers within the main part address more than one of the key

	CN-1	CN-2	CN-3	CN-4	CN-5	TF-1	TF-2	LM-1	LM-2	LM-3
continuum mechanics modeling at the atomic scale	●	●	●	●	●	●				
consideration of nonlinearities			●		●		●	●	●	●
relation to experiments			●			●		●	●	

Figure 1.1: Assignment of enclosed scientific publications to the key topics.

topics discussed in Sections 1.3 to 1.5. For this reason they are grouped by the material system being investigated viz. carbon nanostructures (Chapter 2, publications **CN-1** to **CN-5**), thin film substrate systems (Chapter 3, publications **TF-1** and **TF-2**), and lattice materials (Chapter 4, publications **LM-1** to **LM-3**). For reasons of clarity, the relation between the individual publications and the key topics is illustrated in Figure 1.1.

Within each chapter of the main part an introduction to the respective material system is provided and the main continuum mechanics modeling concepts for accessing its mechanical behavior are briefly discussed. The own contribution to the research field is outlined and all publications comprising the chapter are briefly introduced. Furthermore, information about the own contribution to the individual publications is provided ahead of the bibliography of each chapter.

Chapter 2

Carbon Nanostructures

2.1 Introduction

The term “carbon nanostructures” comprises all nanometer sized particles and structures that are formed by sp^2 -bonded carbon atoms in a mainly hexagonal arrangement. This includes single- and multi-layer graphene [14, 21, 22], single- and multi-layer carbon nanotubes [10, 34, 53], fullerenes [37, 39], and carbon onions [6, 33, 38, 75]. Graphene is the strongest material yet discovered [41] and possesses exceptional electrical and electronic properties [5, 15, 21, 51, 82] as well as a high thermal conductivity [40]. All other carbon nanostructures are expected to inherit or even outperform these unique properties due to their similar atomic structure. This makes carbon nanostructures promising candidates for applications in the electronics industry and for (nanoscale) mechanical devices, e.g., as fillers in nanocomposites [10, 19, 48] for electromagnetic shielding [48], as additives in lubricants [35], as nanoscopic pressure cells [6], as hydrogen storage elements [10], or as mass and strain sensors [58, 59]. More information on potential applications can be found, e.g., in [10, 11, 82].

An expedient use of carbon nanostructures within these different fields of application also calls for a deep understanding of their mechanical behavior under various loading conditions. Besides experimental methods [3, 7, 34, 39, 41, 44, 63, 64, 73], numerical simulation techniques have shown to be powerful tools for studying the mechanical properties as well as the formation of carbon nanostructures. These methods comprise *ab initio* simulations, classical atomistic simulation techniques such as molecular dynamics or Monte

Carlo simulations, and continuum mechanics methods.

Atomistic simulation techniques provide detailed information on the interactions between individual atoms and allow studying phenomena on the atomic scale such as bond breaking and bond formation. The literature on atomistic simulations of carbon nanostructures is vast. Examples related to the mechanical behavior of carbon nanostructures can be found, e.g., in [20, 24, 25, 54, 61, 76, 77]. Atomistic simulation techniques are computationally expensive and consequently the size of the nanostructures to be studied is currently limited to a few (ten-)thousand atoms for *ab initio* simulations or a few million atoms for molecular dynamics and Monte Carlo methods. Consequently, structures such as carbon onions, large multi-layer carbon nanotubes, and carbon fibers are at present outside the scope of application of these methods. An atomistic-based modeling concept that might also be feasible for larger multi-layer carbon nanostructures is presented in [29]. Therein the molecular statics method is embedded within the non-linear finite element framework allowing to use standard solution schemes and also methods for structural stability analysis employed in common finite element simulations.

For large carbon nanostructures continuum mechanics methods are more feasible due to their much lower computational requirements. Although using continuum mechanics on the atomic scale is far from being natural, these methods have been successfully employed for studying the mechanical behavior of carbon nanostructures, see, e.g., [43, 49, 53, 57, 67, 70, 84, 86]. In the following, the main continuum mechanics modeling concepts are briefly introduced. A more detailed discussion can be found in the enclosed publication CN-4 ([24]).

2.2 Continuum Mechanics Modeling

Continuum mechanics models used for investigating the mechanical behavior of carbon nanostructures can be grouped into space frame models [4, 43, 49, 83] and shell models [53, 67, 70, 86]. For all continuum mechanics based models the most important aspects are the appropriate modeling of the atomic layers and the appropriate representation of the van der Waals interactions between adjacent layers. These aspects will be discussed in

more detail in Section 2.2.1 for space frame models and in Section 2.2.2 for shell models. The discussion in these sections is an excerpt of Chapter 3 in the attached publication CN-4 ([24]). It is reduced to the key facts such that a relation to the own scientific work can be presented in a consistent manner.

2.2.1 Space Frame Models

Space frame models for nanostructures are closely related to molecular dynamics and Monte Carlo methods as each individual bond within the atomic structure is explicitly modeled. The atomic bonds are commonly represented by beams [4, 43, 56, 57] instead of the inter-atomic potentials used in the atomistic modeling techniques. Less frequently a combination of rotational and linear springs is employed for representing the atom-atom interactions [49, 52, 85]. Due to the complexity of space frame models in general the finite element method is used for solving the arising boundary value problems. It should be noted that these kinds of models are also denoted as molecular structural mechanics models, e.g., [18], or molecular-mechanics based finite element models [49]. In the following only beam models are discussed in detail.

The structural properties of the beams in terms of axial, bending, and torsional stiffness can be derived by comparing the strain energy stored within the individual beams due to a defined deformation with the associated potential energy of the atomic bonds. Under the assumption of small strains, the axial, bending, and torsional stiffnesses of the beams are equal to the bond-stretching, bond-angle-bending, and bond-torsional resistance, respectively [43]. More advanced methods for determining the beam properties can be found in [18]. Van der Waals interactions between adjacent layers can be included by linking the respective finite element nodes, representing the atoms within the layers, by nonlinear spring elements [30, 42]. The distance dependent stiffness of these “van der Waals springs” can be obtained as second derivative of the Lennard-Jones potential with respect to the distance [36].

Space frame models allow for a direct comparison with atomistic modeling techniques, as loads and displacements are applied in the same manner. Furthermore, experimentally observed point defects [26] such as Stone-Wales defects or single- and multipoint vacancies

can be directly included into the models and their impact on the mechanical behavior can be investigated in a straightforward manner [23, 65, 74]. The major drawback of these models is the complex model generation, especially when van der Waals interactions have to be included in multi-layer systems. Consequently, the models are mainly employed for single- [4, 43, 56, 57] or double-layered [30, 42] nanostructures.

2.2.2 Continuum Shell Models

For large multi-layer carbon nanostructures it is more advantageous to use continuum shell models. Within these models, the atomic layers are represented by continuum shells which possess a membrane stiffness C and bending stiffness D [53, 86]. Alternatively, the properties of the shells may equally be expressed in terms of effective material constants, i.e., the effective Young's modulus E and the effective Poisson's ratio ν in combination with the (constitutive) thickness h of the layers.

Similar to the beam properties for the space frame models, the shell properties can be derived from energy considerations [53, 86] or from computational mechanical tests using either space frame models [57] or atomistic simulations [25]. These models were first proposed by Yakobson in 1996 [86] (Yakobson-model) and were employed for studying the mechanical behavior of carbon nanotubes. The Yakobson-model assumes linear elastic material behavior which is independent of the size and chirality of the nanotubes. The assumption of isotropy results from the hexagonal arrangement of the carbon atoms and is valid as long as small strains (deformations) are considered [81]. Size and chirality effects vanish fast with increasing size of the nanostructures [16, 25] and become negligible for nanotubes with diameters of around 1 nm [16] and graphene sheets larger than 5 nm [25]. For small nanostructures for which the size effect needs to be considered, more advanced models based on nonlocal continuum theory have been developed, see, e.g., [1, 2]. Other models that allow for considering the chirality of the tubes are presented in [16, 80] where the model in [80] also allows to account for large strains. Van der Waals interactions can be included in the models by using either truss/spring elements similar to space frame models or pressure-distance relations. The latter are preferable as they reduce the modeling effort significantly. For graphene, appropriate pressure-distance relations can be found, e.g.,

in [36, 89]. For curved nanostructures such as carbon nanotubes and carbon onions the curvature effect as well as the different numbers of atoms within adjacent layers have to be considered. Appropriate pressure-distance relations are provided in [27, 47] for carbon nanotubes and in [8, 32, 68] for carbon onions.

In contrast to space frame models, it is not straightforward to consider intra-layer defects in continuum shell models. Concepts proposed in the literature introduce the defects via eigenstrains [88] or topological constraints [17]. Additionally, inter-layer defects can have an impact on the overall mechanical properties of carbon nanostructures as they influence the interlayer shear stiffness [12, 44]. A simplified model to account for such defects in continuum shell models is presented in [71]. More information on the modeling of defects in carbon nanostructures can be found in the enclosed publication **CN-4** [24].

Although continuum shell models have widely been used to study the mechanical behavior of carbon nanostructures [9, 27, 53, 55, 67, 71], their applicability is still a topic of ongoing scientific discussions. These discussions mainly focus on the question whether or not graphene possesses an intrinsic bending stiffness and on the identification of the mechanical properties of the shells. The question of the intrinsic bending stiffness is addressed, e.g., in [13, 41, 45, 46, 50, 85, 87] with an overall inconclusive outcome. In [87] it is argued that due to the non-existent change in atomic distances during bending, graphene cannot possess any bending stiffness. This is supported by nanoindentation experiments on graphene [41] but in clear contradiction to the findings in [13, 50, 45, 46, 85] where a finite bending stiffness is observed and attributed to different effects such as the misalignment of electron orbitals not directly involved in the in-plane atom-atom interactions [13, 50], multi-body atomistic interactions up to the third nearest neighbor [45, 46], and internal residual moments [85]. The question of the bending stiffness of single atom thick carbon layers is also addressed in the own scientific work, see Section 2.3.1 or enclosed publications **CN-1** and **CN-2**, respectively.

Even under the assumption that graphene possesses an intrinsic bending stiffness, the shell properties in terms of E , h , and ν are not well defined and can differ significantly, see, e.g., Table 2 in [24] and Table 3 in [78], respectively. Only for the membrane stiffness

good agreement is found between the individual studies. This phenomena is also known as Yakobson paradoxon [62]. One of the reasons for this paradoxon is the assumption that the thickness of a single graphene layer is equal to the interlayer spacing in graphite ($h = 0.34$ nm). This assumption leads to the famously known value of ≈ 1 TPa for the Young's modulus of graphene when computed from the membrane stiffness $C = Eh$. This procedure disregards the impact of h on the bending stiffness $D = \frac{Eh^3}{12(1-\nu^2)}$ and consequently leads to a significant overestimation of D . Procedures that account for both, the membrane and the bending stiffness usually lead to much higher values of E and values for h between 0.06 nm and 0.14 nm [25, 53, 60, 84, 86], see also Table 2 in [24]. Other aspects that may lead to different values for the elastic constants are the potentials used in the atomistic simulations [60], the loading conditions applied to the carbon nanostructures [25, 31], and the size of the nanostructure [25, 31]. Other discussions focus on a claimed break-down of the elastic plate/shell theory for single layer graphene, see, e.g., [87]. Nevertheless, the consistency of the Yakobson-model with atomistic modeling techniques is shown in [84] and also in [50] it is found that shell models can be used to reproduce the bending behavior of graphene at least for small strains. The evaluation of the elastic constants to be used within continuum shell models is also addressed in the own scientific work, see Section 2.3.1 or the enclosed publications **CN-1** and **CN-2**, respectively.

Overall it can be concluded that, continuum shell models provide feasible tools for studying the mechanical behavior of multi-layer carbon nanostructures. Their application to carbon nanostructures is the subject of the compiled publications **CN-2** to **CN-5**.

2.3 Own Contribution to the Research Field

The own contribution to the research field consists of five publications, viz.

- **Publication CN-1:** M.A. Hartmann, M. Todt, F.G. Rammerstorfer, F.D. Fischer, O. Paris: *Elastic Properties of Graphene Obtained by Computational Mechanical Tests*; EPL (Europhysics Letters), 103 (2013), 68004.
- **Publication CN-2:** M. Todt, F.G. Rammerstorfer, M.A. Hartmann: *Continuum Shell Models for Closed Cage Carbon Nanoparticles*; in: Shell Structures: Theory

and Applications; W. Pietraszkiewicz, J. Górski (ed.); CRC Press/Balkema, Leiden (2013), ISBN: 978-1-138-00082-7; 149 - 152.

- **Publication CN-3:** M. Todt, R.D. Bitsche, M.A. Hartmann, F.D. Fischer, F.G. Rammerstorfer: *Growth Limit of Carbon Onions - A Continuum Mechanical Study*; International Journal of Solids and Structures, 51 (2014), 3-4; 706 - 715.
- **Publication CN-4:** M.A. Hartmann, M. Todt, F.G. Rammerstorfer: *Atomistic and Continuum Modelling of Graphene and Graphene-Derived Carbon Nanostructures*; in: Structure and Multiscale Mechanics of Carbon Nanomaterials, O. Paris (ed.); Springer-Verlag, Wien, 2016, ISBN: 978-3-7091-1885-6, 135 - 179.
- **Publication CN-5:** M. Todt, F. Toth, M.A. Hartmann, D. Holec, M.J. Cordill, F.D. Fischer, F.G. Rammerstorfer: *Computational Simulation of Instability Phenomena in Nanoparticles and Nanofilms*; Computational Technology Reviews, 10 (2014), 89 - 119.

The declaration of own contribution to these publications is provided in Subsection 2.3.4.

2.3.1 Elastic Constants for Continuum Shell Models

When a commercial finite element code is used, it is preferable to describe the effective elastic properties of the shells in terms of the Young's modulus E , the Poisson's ratio ν and the (constitutive) layer thickness h . As discussed in Section 2.2, the values for E , ν , and h are topics of ongoing discussion in the scientific community. The publications **CN-1** and **CN-2** ([24, 69]) contribute to this discussion by evaluating the elastic properties of carbon layers using a combination of Monte Carlo simulations and analytical continuum mechanical models. Furthermore, the question on whether or not graphene has a bending stiffness is implicitly addressed.

In the proceedings paper **CN-2** [69] different parameter sets, obtained for nanotubes and graphene, are investigated regarding their ability to predict the effective hydrostatic stiffness and the buckling pressure of fullerenes. It is shown that parameter sets which assume the layer thickness to be equal to the interlayer spacing of graphite strongly overes-

estimate the buckling pressure although they lead to a similar membrane stiffness as all other parameter sets. This is a clear evidence that the bending stiffness plays an essential role in the mechanical behavior of carbon nanostructures. Consequently, the bending behavior has to be considered when deriving the effective elastic properties of single atomic layers, as done, e.g., in [53, 86].

The derivation of an appropriate thickness and the related elastic properties of a single atomic layer is addressed in the journal paper **CN-1** [25]. In contrast to common energy based approaches [53, 86] the layer thickness is derived from the buckling load of graphene sheets and different bending configurations comprising a three-point bending test, an anti-symmetric four-point bending test and bending under distributed loading. For all loading scenarios similar values are obtained for the layer thickness whereby a significant size effect is observed, i.e., the estimated layer thickness strongly decreases with the size of the nanostructure. This indicates that the classical continuum theory breaks down for atomic structures composed of too few atoms which is in good agreement with results in [16, 18].

The results obtained in the publications **CN-1** and **CN-2** [25, 69] clearly show that single layer carbon nanostructures possess an intrinsic bending stiffness. Consequently, bending deformations need to be considered when deriving the effective elastic properties of carbon layers. For the continuum approach to be valid the characteristic length of the carbon nanostructures should be large enough (≥ 5 nm for graphene).

2.3.2 Application of Continuum Shell Models

Continuum shell models are used for investigating the mechanical behavior of fullerenes and carbon onions in the proceedings paper **CN-2** and the journal paper **CN-3** [67, 69].

Fullerenes form the individual layers of carbon onions and contain 12 pentagonal atomic rings in an otherwise hexagonal atomic arrangement. The pentagons are responsible for the curvature of the nanostructures but also cause fullerenes to become more faceted with increasing size. The influence of the pentagons and the faceted shape on the mechanical behavior is investigated in **CN-2** [69] for the case of a C₂₄₀ fullerene. The finite element method is employed to solve the arising boundary value problem allowing for consideration of complex loading scenarios and the faceted shape of the fullerene. The results show

that the pentagonal rings lead to a local increase of the fullerenes' stiffness. For small fullerenes this also has an influence on the overall hydrostatic stiffness of the particle. This influence vanishes with increasing particle size leading concurrently to a decrease of the hydrostatic stiffness also observed in **CN-1** [25]. Furthermore, it is outlined that for a meaningful comparison between atomistic simulations and continuum shell models the loading conditions have to be equivalent, i.e., the loads applied in the continuum model have to mimic the atomistic loading scenario as closely as possible. In general, a good agreement between atomistic and continuum mechanics results is observed, confirming the applicability of continuum approaches for studying the mechanical behavior of carbon nanostructures.

In the journal paper **CN-3** [67] continuum shell models are employed for studying the growth limit of carbon onions. The onions are modeled as perfectly spherical, being in good agreement with experimental observations [6]. The layers are assumed to be fullerenes although these particles are usually faceted in shape, see, e.g. **CN-2** [69]. This is admissible if the existence of so-called Stone-Wales defects within the layers is assumed. These defects locally change the layer curvature but do not change the number of atoms within the layers [66]. The elastic constants and the thickness of the shells are chosen based on the findings in **CN-2** [69]. The van der Waals interactions between adjacent layers are included using a linear spring model as well as a more advanced pressure-distance relation, the latter being based on the non-linear Lennard-Jones potential. Additionally, the excess surface energy due to the curvature of the particles [28] is considered in the form of an inwards oriented pressure. The growth of the onions is simulated by successively adding one layer after the other in combination with the associated van der Waals interactions. It is assumed that the growth limit of a carbon onion is reached, when adding a further layer would lead to the loss of structural stability. Whether or not the stability limit of a certain onion is reached is determined by performing a buckling eigenvalue analysis. The results reveal that the instability is introduced by self-equilibrating stress states emerging due to accommodation of misfitting layers during the growth of the onion. The stresses are mainly a consequence of the van der Waals interactions between the layers and the excess

surface energy has only a minor influence. The instability mainly affects the outer layers of the onion whereas the innermost layers remain perfectly spherical. The predicted number of layers for which the growth limit is reached strongly depends on the parameters used in the van der Waals models and therefore, the results are of a rather qualitative nature. Nevertheless, the models clearly indicate a growth limit for carbon onions. This is in good agreement with experimental observations, where the size of carbon onions produced with various techniques seems to be limited as well [7, 75, 79].

2.3.3 Reviews on the Modeling of Nanostructures

Numerical simulation techniques provide useful tools for gaining insight into the mechanical behavior of nanostructures as well as nano-structured materials. For an expedient use of these tools and a critical analysis of the obtained results, knowledge about their potential fields of application, as well as their advantages and limitations are required. To provide basic information on these topics is the aim of the publications **CN-4** and **CN-5** [24, 72].

The book chapter **CN-4** [24] focuses on the modeling of carbon nanostructures. The discussion of atomistic simulation techniques concentrates on molecular dynamics and Monte Carlo methods and includes a presentation of common potentials used for carbon nanostructures. The section on continuum mechanics methods provides greater detail on the modeling concepts also discussed in Section 2.2. Especially the modeling of the van der Waals interactions, the intra- and inter-layer defects, and the excess surface energy is presented in a more detailed manner. In addition, various examples for the application of the introduced numerical methods are provided and also related experimental studies are discussed to some extent.

In the journal paper **CN-5** [72] the focus lies on instability phenomena in nanostructures and nanofilms and their investigation using numerical techniques. Different examples are provided on how stability considerations can be used to interpret experimental results and to obtain mechanical properties which are otherwise inaccessible. The presented examples involve the growth limit of carbon onions (see also Section 2.3.2 and publication **CN-3**), the shift in the neutral axis of bending within carbon fibers due to buckling of carbon crystallites (see also [71]), and a concept for determining the interface strength between

thin films and the substrate from upheaval/delamination buckling experiments.

2.3.4 Declaration of Own Contribution to the Enclosed Publications

- **Publication CN-1:** All atomistic simulations were conducted by M.A. Hartmann. My contribution involved the analytical continuum mechanics modeling of the different nanostructures and, together with M.A. Hartmann, the evaluation of the respective elastic properties of the graphene layers. I also contributed to the writing of the text where my focus was on the description of the continuum mechanics models. The main part of the text was written by M.A. Hartmann.
- **Publication CN-2:** The paper was mainly written by myself with contributions from M.A. Hartmann and F.G. Rammerstorfer. Regarding the scientific content my contribution involved the continuum mechanics modeling of the nanostructures both analytically and by means of the finite element method as well as the evaluation of the results. All atomistic simulations were carried out by M.A. Hartmann. F.G. Rammerstorfer contributed to the formulation of the analytical continuum mechanics models and to the finite element models in the form of fruitful discussions.
- **Publication CN-3:** The main research work involving the generation of the computational model, the development of the scheme for simulating the growth of carbon onions, the evaluation of the current "stability state" of the onions, as well as the postprocessing of the data was done by myself. The co-authors mainly contributed in the form of very fruitful discussions and R.D. Bitsche provided models which served as starting point for this research. The paper was mainly written by myself with contributions of the co-authors.
- **Publication CN-4:** This book chapter provides a review on different modeling strategies used for studying the mechanical behavior of carbon nanostructures. The introductory section on molecular dynamics and Monte Carlo simulations was written by M.A. Hartmann. The section on continuum mechanics modeling was mainly

written by myself with contributions of F.G. Rammerstorfer. All authors contributed equally to the applications section.

- **Publication CN-5:** This article provides a review on the simulation of instability phenomena in nano-structured systems with special focus on nanoparticles and nanofilms. The section on instabilities in carbon nanoparticles was mainly written by myself with contributions of F.G. Rammerstorfer on the continuum mechanics modeling and D. Holec and M.A. Hartmann on the atomistic modeling. I did not contribute to the section on instabilities of nanofilms. The introduction, the section on numerical tools, and the conclusion were mainly written by F. Toth and myself with contributions from all other co-authors.

2.4 Bibliography

- [1] R. Ansari and H. Rouhi. Analytical treatment of the free vibration of single-walled carbon nanotubes based on the nonlocal Flugge shell theory. *Journal of Engineering Materials and Technology*, 134:011008, 2012.
- [2] B. Arash and Q. Wang. A review on the application of nonlocal elastic models in modeling of carbon nanotubes and graphenes. *Computational Materials Science*, 51:303–313, 2012.
- [3] P. T. Araujo, M. Terrones, and M. S. Dresselhaus. Defects and impurities in graphene-like materials. *Materials Today*, 15:98–109, 2012.
- [4] S. Arghavan and A. V. Singh. Atomic lattice structure and continuum plate theories for the vibrational characteristics of graphenes. *Journal of Applied Physics*, 110:084308, 2011.
- [5] A. A. Balandin. Thermal properties of graphene and nanostructured carbon materials. *Nature Materials*, 10:569–581, 2011.
- [6] F. Banhart and P. M. Ajayan. Carbon onions as nanoscopic pressure cells for diamond formation. *Nature*, 382:433–435, 1996.

- [7] F. Banhart, T. Füller, P. Redlich, and P. M. Ajayan. The formation, annealing and self-compression of carbon onions under electron irradiation. *Chemical Physics Letters*, 269:349–355, 1997.
- [8] D. Baowan, N. Thamwattana, and J. M. Hill. Continuum modelling of spherical and spheroidal carbon onions. *European Physical Journal D*, 44:117–123, 2007.
- [9] R. C. Batra and A. Sears. Continuum models of multi-walled carbon nanotubes. *International Journal of Solids and Structures*, 44:7577–7596, 2007.
- [10] R. H. Baughman, A. A. Zakhidov, and W. A. de Heer. Carbon nanotubes – the route toward applications. *Science*, 297:787–792, 2002.
- [11] C. Berger, Z. Song, T. Li, X. Li, A. Y. Ogbazghi, R. Feng, Z. Dai, A. N. Marchenkov, E. H. Conrad, P. N. First, and W. A. de Heer. Ultrathin epitaxial graphite: 2D electron gas properties and a route toward graphene-based nanoelectronics. *The Journal of Physical Chemistry B*, 108:19912–19916, 2004.
- [12] E. M. Byrne, A. Letertre, M. A. McCarthy, W. A. Curtin, and Z. Xia. Optimizing load transfer in multiwall nanotubes through interwall coupling: Theory and simulation. *Acta Materialia*, 58:6324–6333, 2010.
- [13] E. Cadelano, S. Giordano, and L. Colombo. Interplay between bending and stretching in carbon nanoribbons. *Physical Review B*, 81:144105, 2010.
- [14] E. Cadelano, P. L. Palla, S. Giordano, and L. Colombo. Nonlinear elasticity of monolayer graphene. *Physical Review Letters*, 102:235502, 2009.
- [15] A. H. Castro Neto, F. Guinea, N. M. R. Peres, K. S. Novoselov, and A. K. Geim. The electronic properties of graphene. *Reviews of Modern Physics*, 81:109–162, 2009.
- [16] T. Chang. A molecular based anisotropic shell model for single-walled carbon nanotubes. *Journal of the Mechanics and Physics of Solids*, 58:1422–1433, 2010.
- [17] S. Chen and D. C. Chrzan. Continuum theory of dislocations and buckling in graphene. *Physical Review B*, 84:214103, 2011.

- [18] W. H. Chen, H. C. Cheng, and Y. L. Liu. Radial mechanical properties of single-walled carbon nanotubes using modified molecular structure mechanics. *Computational Materials Science*, 47:985–993, 2010.
- [19] W. Choi and J. W. Lee, editors. *Graphene Synthesis and Applications*. CRC Press, New York, 2012.
- [20] H. Dumlich and S. Reich. Nanotube bundles and tube-tube orientation: A van der Waals density functional study. *Physical Review B*, 84:064121, 2011.
- [21] A. K. Geim. Graphene: Status and prospects. *Science*, 324:1530–1534, 2009.
- [22] A. K. Geim and K. S. Novoselov. The rise of graphene. *Nature Materials*, 6:183–191, 2007.
- [23] S. K. Georgantzinos, D. E. Katsareas, and N. K. Anifantis. Limit load analysis of graphene with pinhole defects: A nonlinear structural mechanics approach. *International Journal of Mechanical Sciences*, 55:85–94, 2012.
- [24] M. A. Hartmann, M. Todt, and F. G. Rammerstorfer. Continuum modelling of graphene and graphene-derived carbon nanostructures. In *Structure and Multiscale Mechanics of Carbon Nanomaterials*, pages 135–179. Springer, Wien, 2016.
- [25] M. A. Hartmann, M. Todt, F. G. Rammerstorfer, F. D. Fischer, and O. Paris. Elastic properties of graphene obtained by computational mechanical tests. *Europhysics Letters*, 103:68004, 2013.
- [26] A. Hashimoto, K. Suenaga, A. Gloter, K. Urita, and S. Iijima. Direct evidence for atomic defects in graphene layers. *Nature*, 430:870–873, 2004.
- [27] X. Q. He, S. Kitipornchai, and K. M. Liew. Buckling analysis of multi-walled carbon nanotubes: a continuum model accounting for van der Waals interaction. *Journal of the Mechanics and Physics of Solids*, 53:303–326, 2005.

- [28] D. Holec, M. A. Hartmann, F. D. Fischer, F. G. Rammerstorfer, P. H. Mayrhofer, and O. Paris. Curvature-induced excess surface energy of fullerenes: Density functional theory and Monte Carlo simulations. *Physical Review B*, 81:235403, 2010.
- [29] S. Hollerer. Buckling analysis of carbon nanotubes – a molecular statics investigation into the influence of non-bonded interactions. *International Journal for Numerical Methods in Engineering*, 91:397–425, 2012.
- [30] S. A. Hosseini Kordkheili and M. Moshrefzadeh-Sani. Mechanical properties of double-layered graphene sheets. *Computational Material Science*, 69:335–343, 2013.
- [31] Y. Huang, J. Wu, and K. C. Hwang. Thickness of graphene and single-wall carbon nanotubes. *Physical Review B*, 74:245413, 2006.
- [32] S. Iglesias-Groth, J. Breton, and C. Girardet. An analytical approach for the interlayer interaction in spherical buckyonions. *Chemical Physics Letters*, 264:351–358, 1997.
- [33] S. Iijima. Direct observation of the tetrahedral bonding in graphitized carbon black by high resolution electron microscopy. *Journal of Crystal Growth*, 50:675–683, 1980.
- [34] S. Iijima. Helical microtubules of graphitic carbon. *Nature*, 354:56–58, 1991.
- [35] L. Joly-Pottuz, N. Matsumoto, H. Kinoshita, B. Vacher, M. Belin, G. Montagnac, J. M. Martin, and N. Ohmae. Diamond-derived carbon onions as lubricant additives. *Tribology International*, 41:69–78, 2008.
- [36] B. Kelly. *Physics of Graphite*, pages 79–80. Advanced Science Publishers, 1981.
- [37] H. W. Kroto. The stability of the fullerenes C_n , with $n = 24, 28, 32, 36, 50, 60$, and 70 . *Nature*, 329:529–531, 1987.
- [38] H. W. Kroto. Carbon onions introduce new flavour to fullerene studies. *Nature*, 359:670–671, 1992.
- [39] H. W. Kroto, J. R. Heath, S. C. O’Brien, R. F. Curl, and R. E. Smalley. C_{60} : Buckminsterfullerene. *Nature*, 318:162–163, 1985.

- [40] C. N. Lau, W. Bao, and J. Velasco Jr. Properties of suspended graphene membranes. *Materials Today*, 15:238–245, 2012.
- [41] C. Lee, X. Wei, J. W. Kysar, and J. Hone. Measurement of the elastic properties and intrinsic strength of monolayer graphene. *Science*, 321:385–388, 2008.
- [42] C. Li and T. W. Chou. Elastic moduli of multi-walled carbon nanotubes and the effect of van der Waals forces. *Composite Science and Technology*, 63:1517–1524, 2003.
- [43] C. Li and T. W. Chou. A structural mechanics approach for the analysis of carbon nanotubes. *International Journal of Solids and Structures*, 40:2487–2499, 2003.
- [44] D. Loidl, H. Peterlik, M. Müller, C. Riekkel, and O. Paris. Elastic moduli of nanocrystallites in carbon fibers measured by in-situ X-ray microbeam diffraction. *Carbon*, 41:563–570, 2003.
- [45] Q. Lu, M. Arroyo, and R. Huang. Elastic bending modulus of monolayer graphene. *Journal of Physics D*, 42:102002, 2009.
- [46] Q. Lu and R. Huang. Nonlinear mechanics of single-atomic-layer graphene sheets. *International Journal of Applied Mechanics*, 1:443–467, 2009.
- [47] W. B. Lu, B. Liu, J. Wu, J. Xiao, K. C. Hwang, S. Y. Fu, and Y. Huang. Continuum modeling of van der Waals interactions between carbon nanotube walls. *Applied Physics Letters*, 94:101917, 2009.
- [48] J. Macutkevic, D. Seliuta, G. Valusis, J. Banys, P. Kuzhir, S. Maksimenko, V. Kuznetsov, S. Moseenkov, O. Shenderova, and P. Lambin. Dielectric properties of onion-like carbon based polymer films: Experiment and modeling. *Solid State Sciences*, 11:1828–1832, 2009.
- [49] M. Meo and M. Rossi. Prediction of Young’s modulus of single wall carbon nanotubes by molecular-mechanics based finite element modelling. *Composites Science and Technology*, 66:1597–1605, 2006.

- [50] I. Nikiforov, E. Dontsova, R. D. James, and T. Dumitrică. Tight-binding theory of graphene bending. *Physical Review B*, 89:155437, 1989.
- [51] K. S. Novoselov, A. K. Geim, S. V. Morozov, D. Jiang, Y. Zhang, S. V. Dubonos, I. V. Grigorieva, and A. A. Firsov. Electric field effect in atomically thin carbon films. *Science*, 306:666–669, 2004.
- [52] G. M. Odegard, T. S. Gates, L. M. Nicholson, and K. E. Wise. Equivalent-continuum modeling of nano-structured materials. *Composites Science and Technology*, 62:1869–1880, 2002.
- [53] A. Pantano, D. M. Parks, and M. C. Boyce. Mechanics of deformation of single- and multi-wall carbon nanotubes. *Journal of the Mechanics and Physics of Solids*, 52:789–821, 2004.
- [54] H. Rafii-Tabar. *Computational physics of carbon nanotubes*. Cambridge University Press, Cambridge, 2008.
- [55] C. Q. Ru. Effect of van der Waals forces on axial buckling of a double-walled carbon nanotube. *Journal of Applied Physics*, 87:7227–7231, 2000.
- [56] A. Sakhaee-Pour. Elastic buckling of single-layered graphene sheet. *Computational Material Science*, 45:266–270, 2009.
- [57] A. Sakhaee-Pour. Elastic properties of single-layered graphene sheet. *Solid State Communications*, 149:91–95, 2009.
- [58] A. Sakhaee-Pour, M. T. Ahmadian, and A. Vafai. Applications of single-layered graphene sheets as mass sensors and atomistic dust detectors. *Solid State Communications*, 145:168–172, 2008.
- [59] A. Sakhaee-Pour, M. T. Ahmadian, and A. Vafai. Potential application of single-layered graphene sheet as strain sensor. *Solid State Communications*, 147:336–340, 2008.

- [60] A. Sears and R. C. Batra. Macroscopic properties of carbon nanotubes from molecular-mechanics simulations. *Physical Review B*, 69:235406, 2004.
- [61] S. Sharma, R. Chandra, P. Kumar, and N. Kumar. Effect of Stone-Wales and vacancy defects on elastic moduli of carbon nanotubes and their composites using molecular dynamics simulation. *Computational Materials Science*, 86:1–8, 2014.
- [62] O. A. Shenderova, V. V. Zhirnov, and D. W. Brenner. Carbon nanostructures. *Critical Reviews in Solid State and Materials Sciences*, 27:227, 2002.
- [63] Y. W. Sun, D. J. Dunstan, M. A. Hartmann, and D. Holec. Nanomechanics of carbon nanotubes. *Proceedings in Applied Mathematics and Mechanics*, 7:13, 2013.
- [64] Y. W. Sun, I. Hernández, A. J. Ghandour, C. Rice, I. F. Crowe, M. P. Halsall, A. Sapelkin, J. Gonzalez, F. Rodriguez, and D. J. Dunstan. Raman spectroscopy of carbon nanotubes: pressure effects on g-mode. *High Pressure Research*, 34:191–197, 2014.
- [65] A. Tapia, R. Peón-Escalante, C. Villanueva, and F. Avilés. Influence of vacancies on the elastic properties of a graphene sheet. *Computational Materials Science*, 55:255–262, 2012.
- [66] H. Terrones and M. Terrones. The transformation of polyhedral particles into graphitic onions. *Journal of the Physics and Chemistry of Solids*, 58:1789–1796, 1997.
- [67] M. Todt, R. D. Bitsche, M. A. Hartmann, F. D. Fischer, and F. G. Rammerstorfer. Growth limit of carbon onions - a continuum mechanical study. *International Journal of Solids and Structures*, 51:706–715, 2014.
- [68] M. Todt, F. G. Rammerstorfer, F. D. Fischer, P. H. Mayrhofer, D. Holec, and M. A. Hartmann. Continuum modeling of van der Waals interactions between carbon onion layers. *Carbon*, 49:1620–1627, 2011.
- [69] M. Todt, F. G. Rammerstorfer, and M. A. Hartmann. Continuum shell models for closed cage carbon nanoparticles. In W. Pietraszkiewicz and J. Górski, editors, *Shell*

- Structures: Theory and Applications*, pages 149 – 152. CRC Press/Balkema, Leiden, 2013.
- [70] M. Todt, F. G. Rammerstorfer, M. A. Hartmann, O. Paris, and F. D. Fischer. Shell-models for multi-layer carbon nano-particles. In H. Altenbach and V. A. Eremeyev, editors, *Advanced Structured Materials: Shell-like Structures*, pages 585–602. Springer-Verlag, Berlin, 2011.
- [71] M. Todt, F. G. Rammerstorfer, O. Paris, and F. D. Fischer. Nanomechanical studies of the compressive behavior of carbon fibers. *Journal of Material Science*, 45:6845–6848, 2010.
- [72] M. Todt, F. Toth, M. A. Hartmann, D. Holec, M. J. Cordill, F. D. Fischer, and F. G. Rammerstorfer. Computational simulation of instability phenomena in nanoparticles and nanofilms. *Computational Technology Reviews*, 10:89–119, 2014.
- [73] S. Tomita, A. Burian, J. C. Dore, D. LeBolloch, M. Fujii, and S. Hayashi. Diamond nanoparticles to carbon onions transformation: X-ray diffraction studies. *Carbon*, 40:1469–1474, 2002.
- [74] K. I. Tserpes and P. Papanikos. Finite element modeling of single-walled carbon nanotubes. *Composites: Part B*, 36:468–477, 2005.
- [75] D. Ugarte. Onion-like graphitic particles. *Carbon*, 33:989–993, 1995.
- [76] G. Van Lier, C. Van Alsenoy, V. Van Doren, and P. Geerlings. *Ab initio* study of the elastic properties of single-walled carbon nanotubes and graphene. *Chemical Physics Letters*, 326:181–185, 2000.
- [77] M. C. Wang, C. Yan, L. Ma, N. Hu, and M. W. Chen. Effect of defects on fracture strength of graphene sheets. *Mechanics of Materials*, 45:52–60, 2012.
- [78] J. M. Wernik and S. A. Meguid. Atomistic-based continuum modeling of the nonlinear behavior of carbon nanotubes. *Acta Mechanica*, 212:167–179, 2010.

- [79] P. Wesolowski, Y. Lyutovich, F. Banhart, H. D. Carstanjen, and H. Kronmüller. Formation of diamond in carbon onions under MeV ion irradiation. *Applied Physics Letters*, 71:1948–1950, 1997.
- [80] J. Wu, K. C. Hwang, and Y. Huang. An atomistic-based finite-deformation shell theory for single-wall carbon nanotubes. *Journal of the Mechanics and Physics of Solids*, 56:279–292, 2008.
- [81] J. Wu, J. Peng, K. C. Hwang, J. Song, and Y. Huang. The intrinsic stiffness of single-wall carbon nanotubes. *Mechanics Research Communications*, 35:2–9, 2008.
- [82] Y. H. Wu, T. Yu, and Z. X. Shen. Two-dimensional carbon nanostructures: Fundamental properties, synthesis, characterization, and potential applications. *Journal of Applied Physics*, 108:071301, 2010.
- [83] J. R. Xiao, B. A. Gama, and J. W. Gillespie Jr. An analytical molecular structural mechanics model for the mechanical properties of carbon nanotubes. *International Journal of Solids and Structures*, 42:3075–3092, 2005.
- [84] Z. Xin, Z. Jianjun, and Q. Y. Zhong-can. Strain energy and Young’s modulus of single-wall carbon nanotubes calculated from electronic energy-band theory. *Physical Review B*, 62:13692–13696, 2000.
- [85] R. Xu, Y. Wang, B. Liu, and D. Fang. Mechanics interpretation on the bending stiffness and wrinkled pattern of graphene. *Journal of Applied Mechanics*, 80:040910, 2013.
- [86] B. I. Yakobson, C. J. Brabec, and J. Bernholc. Nanomechanics of carbon tubes: Instabilities beyond linear response. *Physical Review Letters*, 76:2511–2514, 1996.
- [87] D. B. Zhang, E. Akatyeva, and T. Dumitrică. Bending ultrathin graphene at the margins of continuum mechanics. *Physical Review Letters*, 106:255503, 2011.
- [88] T. Zhang, X. Li, and H. Gao. Defects controlled wrinkling and topological design in graphene. *Journal of the Mechanics and Physics of Solids*, 67:2–13, 2014.

- [89] Y. X. Zhao and I. L. Spain. X-ray diffraction data for graphite to 20 GPa. *Physical Review B*, 40:993–997, 1989.

2.5 Publications

A LETTERS JOURNAL EXPLORING
THE FRONTIERS OF PHYSICS

September 2013

EPL, **103** (2013) 68004

www.epjjournal.org

doi: 10.1209/0295-5075/103/68004

Elastic properties of graphene obtained by computational mechanical tests

MARKUS A. HARTMANN¹, MELANIE TODT², FRANZ G. RAMMERSTORFER², FRANZ D. FISCHER³
and OSKAR PARIS¹¹ *Institute of Physics, Montanuniversität Leoben - Franz-Josef Strasse 18, A-8700 Leoben, Austria, EU*² *Institute of Lightweight Design and Structural Biomechanics, Vienna University of Technology
Gußhausstrasse 27-29, A-1040 Vienna, Austria, EU*³ *Institute of Mechanics, Montanuniversität Leoben - Franz-Josef Strasse 18, A-8700 Leoben, Austria, EU*

received 31 July 2013; accepted in final form 13 September 2013

published online 7 October 2013

PACS 81.05.ue – Graphene

PACS 46.70.De – Beams, plates, and shells

PACS 02.70.Uu – Applications of Monte Carlo methods

Abstract – The basic building block of many carbon nanostructures like fullerenes, carbon onions or nanotubes is the truly two-dimensional material graphene. Commercial finite element codes, widely used to predict the mechanical properties of these structures, rely on the knowledge of the mechanical properties of the basic material. In this paper using an atomistic simulation approach we determine the membrane and bending stiffness of graphene, as well as the corresponding effective parameters: the effective elastic modulus $E = 2.4$ TPa, Poisson ratio $\nu = 0.1844$ and thickness $h = 1.32$ Å. It is shown that within reasonable accuracy the obtained parameters can be applied to various loading scenarios on carbon nanostructures as long as the characteristic length of these structures is larger than ≈ 50 Å. Thus, for such large and complex structures that withstand an analytical or atomistic description, commercial finite element solvers, in combination with the found effective parameters, can be used to describe these structures.

Copyright © EPLA, 2013

Carbon and related materials like graphene-based composite materials [1] are promising candidates to revolutionize structural mechanics in the field of light and stiff materials. Graphene, *i.e.* monolayer graphite, is the strongest material ever discovered [2] and subject of intensive research [3–6]. Furthermore, graphene is the basic building block of other carbon nanostructures like single- and multi-wall carbon nanotubes [7], fullerenes [8] or carbon onions [9–11], and carbon fibers [12–16]. Understanding and predicting the mechanical properties of these nanostructures demands the description of the material on many different lengthscales, from single atomic bonds to the macroscopic behavior of carbon fibers and other large structures. This makes a multi-scale/multi-method approach necessary when dealing with such systems. The mechanical behavior of small carbon nanostructures can be studied using atomistic simulation techniques, while for larger structures these techniques become computationally expensive. For these larger nanostructures continuum mechanical (CM) methods have shown to be appropriate for investigating their mechanical behavior [17,18]. In CM

the graphene layers are modeled as thin, elastic, isotropic shells. The main stiffness parameters of these shells are the membrane stiffness $C = Eh/(1-\nu^2)$ and bending stiffness $K = Eh^3/12(1-\nu^2)$ with E and ν being the elastic modulus and the Poisson ratio of the material, respectively, and h being the shell thickness. As long as analytical continuum models work directly with C and K defining a layer thickness h explicitly can be avoided [19,20]. However, analytic models can only be defined for special, well-defined and simple systems. Whenever highly complex structures, like, *e.g.*, defective carbon fibers, are investigated, the finite element method in conjunction with a commercial solver is the adequate tool for describing this system. Standard shell elements implemented in such a commercial finite element solver usually require E , ν and h as input parameters. If the thickness and the corresponding elastic modulus are not defined properly, the deformation state and the corresponding stress state cannot be predicted correctly, as soon as bending of the carbon layers gets involved. Bending plays an essential role in many modes of deformation, as well as in rippling, wrinkling, or buckling

Markus A. Hartmann *et al.*

of graphene in nanostructures [14,21–25]. The formation of ripples in graphene is especially interesting due to the pronounced coupling of mechanical and electronic properties. Ripples were found in free-standing [26,27] and supported [28] graphene and provide an inhomogeneous strain distribution, which was shown to produce a strong effective magnetic field up to several tens of tesla [29]. Thus, by fixing the strain field of graphene, it is possible to control its electronic properties via the corresponding effective magnetic field (strain engineering) [30–32]. The first aim of this paper is to provide effective properties for the treatment of graphene using CM methods, which take in-plane as well as out-of-plane (*i.e.*, bending) deformations appropriately into account. The second aim is to critically check to which extent such methods can replace computationally expensive atomistic simulations. It should be noted that for a truly 2-dimensional material like graphene it is only possible to determine *effective* parameters E , ν and h of a “phantom” shell that shows the same mechanical behavior as graphene. While the product $Y = Eh$ and ν can directly be determined by simulations and partly also in experiments [2], the effective thickness h is more difficult to grasp. Several authors report a variety of different values for h that span a range from 0.617 Å to 6.9 Å [33]. Consequently, this variation of h corresponds to elastic moduli differing by one order of magnitude ranging from 0.764 to 5.5 TPa (“Yakobson paradox”) [34]. Different solutions are discussed in literature to resolve this paradox: Huang *et al.* [33] argue that the effective thickness of nanotubes is not constant but rather depends on the type of loading, the nanotube radius and its chirality. Zhang *et al.* state that classical plate theory breaks down for single graphene sheets, because the atoms in monolayer graphene retain their equilibrium bond length when bent [35]. Thus, the zones of compression and tension on either side of the neutral axis are missing that are crucial for plate theory to be applicable. These examples show that it is far from obvious which values of E and h provide a good representation of the mechanical properties of graphene.

In this letter computational mechanical tests on graphene are presented that allow the determination of E , ν and h for graphene. Different from previous approaches the thickness of graphene was determined from computational mechanical compression tests, rather than from the dependence of the curvature energy on the radii of carbon nanotubes [36]. The validity of the obtained values was tested by performing compression tests on fullerenes and bending tests on graphene. A further important question which is addressed in this context is, whether the effective parameters are intrinsic properties of graphene or they depend on the special loading situation, the topology of the nanostructure (graphene, nanotubes or fullerenes) or its size. In other words: can all carbon nanostructures be described as made of the same effective material or do these effective material properties depend on curvature, size or loading scenario?

Table 1: Parameters used in the classical potentials for the MC simulations. E_0 , β , and r_0 describe bond stretching, k_θ and θ_0 bond bending, and k_ϕ is the torsion force constant.

E_0	6.1322 eV
β	1.8502 Å ⁻¹
r_0	1.4322 Å
k_θ	10 eV
θ_0	120°
k_ϕ	0.35 eV

Table 2: Abbreviations used in the text.

L_x, L_y	Length in x - and y -direction
L_{x0}, L_{y0}	Initial length in x - and y -direction
ϵ_x, ϵ_y	Strain in x - and y -direction
σ_x, σ_y	Load in x - and y -direction
C, K	Membrane and bending stiffness
E	Effective elastic modulus
ν	Effective Poisson ratio
h	Effective thickness
σ_S, ϵ_S	Strength and ultimate strain

Recently we have derived classical potentials for sp^2 bonded carbon from *ab initio* calculations [37]. The reliability of these potentials was tested using MC simulations. The bonded interaction between carbon atoms is described by 2-atom bond-stretching E_S , 3-atom bond-bending E_B and 4-atom bond-torsion E_T energy contributions:

$$E_S(r_{ij}) = E_0 \{ [1 - \exp(-\beta(r_{ij} - r_0))]^2 - 1 \}, \quad (1)$$

$$E_B(\theta_{ijk}) = \frac{1}{2} k_\theta (\cos \theta_{ijk} - \cos \theta_0)^2, \quad (2)$$

$$E_T(\phi_{ijkl}) = \frac{1}{2} k_\phi (1 - \cos 2\phi_{ijkl}). \quad (3)$$

In the stretching potential E_0 denotes the binding energy of two carbon atoms, r_0 the equilibrium carbon-carbon bond length, β^{-1} the width of the potential and r_{ij} the actual distance between atoms i and j . The bending contribution is characterized by the bond angle θ_{ijk} between three carbon atoms, the equilibrium bond angle θ_0 and the bending force constant k_θ , the torsion contribution by the dihedral angle ϕ_{ijkl} between four atoms and the torsion force constant k_ϕ . The employed parameters are listed in table 1. These potentials were used in MC simulations in the (NPT) ensemble using the classical algorithm of McDonald [38] to perform computational mechanical tests on graphene: uniaxial tension tests of graphene ribbons of size (10 × 10) unit cells (corresponding to $N = 200$ carbon atoms) and uniaxial compression tests on graphene ribbons of different length (see also table 2 for used abbreviations). Being interested in the ground state only, in the simulations the temperature was set to the small value of $k_B T = 25 \mu\text{eV}$.

In the tension tests the system was loaded in x - or y -direction, the other direction being load free (being a

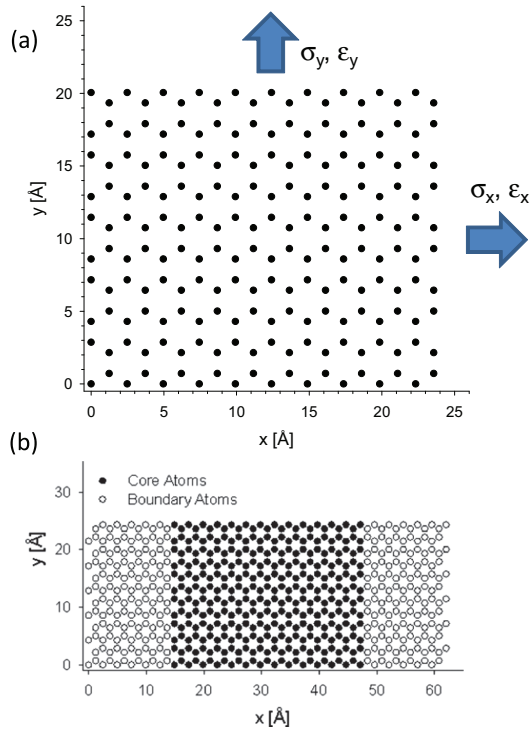


Fig. 1: (Colour on-line) The used geometry for computational mechanical tests. (a) In-plane stretching: x corresponds to the zig-zag, y to the armchair direction, periodic boundary conditions are used. (b) Compression and bending: the atoms forming the left boundary (gray) are held fixed, while the atoms on the right boundary (gray) can move collectively in x -direction allowing for a change of length of the stripe. In y -direction periodic boundary conditions are used.

membrane force the load σ_i is measured in units of force per length) (see fig. 1(a)). The corresponding (engineering) strains were recorded ($\epsilon_i = (L_i - L_{i0})/L_{i0}$ with $i = x, y$). For a load applied in x -direction Y and ν are given by $\sigma_x = Y\epsilon_x$ and $\nu = -\epsilon_y/\epsilon_x$ (and corresponding relations for loading in y -direction). In the compression tests standard periodic boundary conditions were applied in y -direction. Different boundary conditions were used in x -direction that correspond to clamped edges and prohibit rotation of the sample (see fig. 1(b)). Additional 12 rows of atoms were added on either side of the stripe. While the additional atoms on the left side of the stripe were held fixed during the simulation, the corresponding atoms on the right side were allowed to move collectively in x -direction. These boundary conditions allow for a reduction in L_x of the stripe when loaded, without the effect of dangling bonds of a stripe of finite length since the atoms of the last rows do not contribute to the total energy of the system.

Figure 2(a) shows the results from uniaxial tension tests on graphene. The upper part of the figure shows the applied load in x -direction σ_x as a function of the

corresponding strain in x -direction ϵ_x . The load was gradually increased until failure, *i.e.* until no stable elongation was found but the system steadily increased its length. The strength and ultimate strain of graphene are found to be $\sigma_S = 46 \pm 0.4$ N/m and $\epsilon_S = 0.28$. The quantity $Y = Eh = (313.2 \pm 0.17)$ N/m was obtained by a linear regression of the first, linear part of the curve ($\epsilon_x < 0.005$), and the Poisson ratio $\nu = 0.1844 \pm 0.0003$ was obtained by averaging the corresponding values of $-\epsilon_y/\epsilon_x$. A control simulation with the load applied in y -direction yielded almost the same values for Y and ν confirming the in-plane isotropy of graphene. Accordingly the membrane stiffness is given by $C = Y/(1 - \nu^2) = 324$ N/m. The values obtained are in good agreement with the measurements by Lee *et al.* [2] who report $Y = 340 \pm 50$ N/m and $\sigma_S = 42 \pm 4$ N/m and the simulation results by Kalosakas *et al.* [39] who report $Y = 320$ N/m, a slightly higher Poisson ratio of 0.22 and a strength of 39–45 N/m. A further compilation of experimental and theoretical elastic constants of graphene can be found in [19] and references therein.

The effective thickness of monolayer graphene was determined by compression tests. In these tests the load on the ribbon was gradually increased until buckling of the layer set in. For the given boundary conditions (see fig. 1(b)) the buckling load in CM is given by [40]

$$\sigma_c = 3.41Y \left(\frac{h}{L_x} \right)^2. \quad (4)$$

Thus, when σ_c is determined as a function of length L_x , the corresponding effective thickness can be calculated. The results are shown in fig. 2(b). For short ribbons (shorter than 50 Å) the thickness decreases, which can be attributed to the breakdown of the continuum approximation for structures composed of too few atoms. For increasing length the effective thickness of graphene levels off approaching approximately 1.32 Å, resulting in a bending stiffness $K = 0.47$ nN · nm = 2.94 eV in good agreement with the results from [41] obtained from molecular dynamics.

It has been argued that the effective mechanical properties are not intrinsic properties of graphene, but depend on the topology of the carbon nanostructure and on the loading situation [33,42]. Therefore, for CM calculations on nanostructures like carbon onions it is essential to know whether the different layers can be described with the effective elastic properties found for planar graphene. To answer this question additional mechanical tests were performed on fullerenes and graphene. The response of the material was then compared to the predictions of CM solutions using the effective parameters found earlier. The additional tests consisted in hydrostatic loading of fullerenes and bending of graphene. Fullerenes of different size were loaded and the change of their radius as a function of applied hydrostatic load was determined. In CM the change in radius ΔR for a sphere and the total

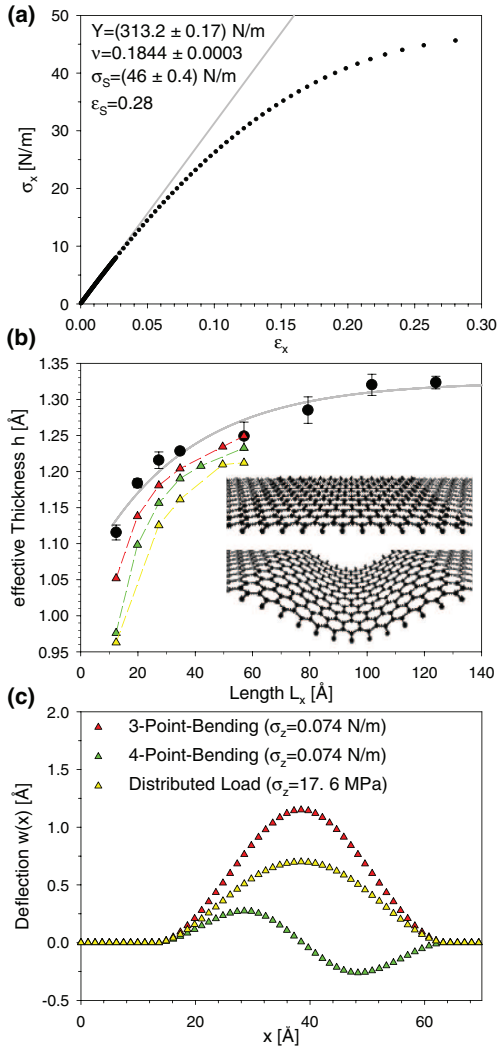
Markus A. Hartmann *et al.*


Fig. 2: (Colour on-line) (a) Uniaxial stretching of graphene in x -direction until failure. Y and ν were obtained by evaluation of the linear part of the curve ($\epsilon_x < 0.005$). For large strains the deviation from the straight line is visible. (b) The effective thickness h of monolayer graphene obtained by determining the critical buckling load as a function of length L_x (black circles). The gray line is a guide to the eye showing the leveling-off at approximately $h = 1.32 \text{ \AA}$. The inset shows the graphene ribbon exactly before and after the buckling load was reached. This interval defines the error bars given. The triangles show the results from the different bending tests: 3-point-bending (red), 4-point-bending (green) and distributed load (yellow). (c) The deformation of a graphene ribbon of size $L_x = 34 \text{ \AA}$ for three different bending tests. The effective thickness was determined by fitting these profiles to a plate model.

applied load intensity $F = \int_S p dS$ (where the integration is carried out over the surface of the sphere) are related by

$$F = \kappa \Delta R = \frac{8\pi E h}{1 - \nu} \Delta R = \frac{8\pi Y}{1 - \nu} \Delta R. \quad (5)$$

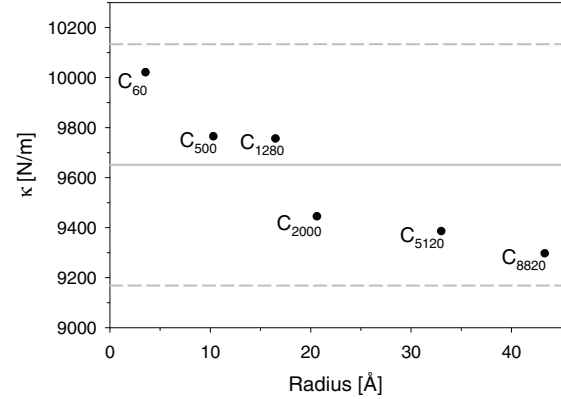


Fig. 3: The obtained values for κ (see eq. (5)) for fullerenes of different sizes. The theoretical value of κ obtained from Y and ν_{eff} of graphene is shown by the solid line, the dashed lines indicate 5% deviations.

Using the obtained values of $Y = 313.2 \text{ N/m}$ and $\nu = 0.1844$ a value of $\kappa = 9651 \text{ N/m}$ is found. Note that κ is a constant value for all spherical carbon nanostructures, especially independent of the thickness as well as of the size of the fullerenes. Equation (5) is strictly valid only for perfect spheres, while larger fullerenes are known to be strongly faceted [37]. To minimize the influence of such geometrical effects in the MC simulations an artificial constraint was implemented: the positions of the carbon atoms forming the fullerene were forced to lie on the surface of a sphere. In this type of simulation two different MC moves were used. First, displacements of single atoms on the surface and, second, a change of the radius of the surface resulting in collective changes in the coordinates of all atoms. Figure 3 compares the values of κ obtained from the simulations with the prediction of eq. (5). Although a moderate decrease in κ with fullerene size can be observed, the correspondence is good. The smallest investigated fullerene (C_{60}) shows $\kappa = 10021 \text{ N/m}$, the largest fullerene (C_{8820}) $\kappa = 9297 \text{ N/m}$, which is a decrease of $\approx 7\%$ while the radius of the fullerenes changed more than a factor of 10.

Three different out-of-plane bending tests with loading in the global z -direction were performed on the graphene system with boundary conditions as shown in fig. 1(b). First, the atoms located at $L_x/2$ were loaded with a positive force in z -direction (3-point-bending). Second, the atoms located at $L_x/3$ were loaded with a force pointing in the positive z -direction, while the atoms located at $2L_x/3$ with a force of the same magnitude but directed in the negative z -direction (4-point-bending). Third, all atoms in the ribbon were loaded with the same force in z -direction (distributed load). In the simulations the deflection $w(x)$ in z -direction of the ribbons was recorded as a function of the applied load and the thickness determined via CM models (see fig. 2(c) for typical results of

the bending tests). In the CM model the plate is assumed to have an infinite extension in y -direction and is clamped on the left and right side (one side is free to move in x -direction). According to Castigliano's principle the deflections at the loading points are calculated from the first derivative of the strain energy U^* with respect to the applied force F (as force per unit width). The strain energy per unit width of the plate is defined according to those of a beam with equivalent length and a cross-section of $1 \times h$

$$U^* = \frac{1}{2} \int_0^{L_x} \frac{M(x)^2}{K} dx \quad (6)$$

$M(x)$ is the bending moment and K the bending stiffness $K = Eh^3/12(1 - \nu^2)$. For the case of the distributed load the deflection $w(x)$ was obtained by double integrating the curvature $w'' = -M/K$. The results are shown in fig. 2(b). All tests show qualitatively the same behavior: a pronounced decrease in thickness for lengths shorter than 50 \AA and a leveling-off close to the effective thickness obtained from the compression tests for longer ribbons.

Our results show that graphene and fullerenes (and presumably also nanotubes) larger than 50 \AA can be described as thin, isotropic shells with effective parameters $E = 2.4 \text{ TPa}$, $\nu = 0.1844$ and $h = 1.32 \text{ \AA}$, independently of loading and deformation conditions. Care has to be taken for structures smaller than 50 \AA , because the continuum approximation breaks down and no consistent bending stiffness can be deduced. A similar breakdown of CM has been found for carbon nanotubes [43,44] and for nanometre wavelength ripples in graphene [45]. The results presented in this paper indicate that a fully atomistic approach is only needed when structures in graphene with a characteristic length smaller than 50 \AA are investigated. However, larger carbon structures, like carbon onions or carbon crystallites forming fibers, often exceed the minimal value of 50 \AA and allow therefore to use CM methods on reliable grounds. In particular, for structures too large and complex to be described by analytical continuum mechanical models, commercial finite element solvers may be used with E , h and ν as the effective material parameters for the implemented elements.

REFERENCES

- [1] STANKOVICH S., DIKIN D. A., DOMMETT G. H. B., KOHLHAAS K. M., ZIMNEY E. J., STACH E. A., PINER R. D., NGUYEN S. T. and RUOFF R. S., *Nature*, **442** (2006) 282.
- [2] LEE C., WEI X., KYSAR J. W. and HONE J., *Science*, **321** (2008) 385.
- [3] NOVOSELOV K. S., GEIM A. K., MOROZOV S. V., JIANG D., ZHANG Y., DUBONOS S. V., GRIGORIEVA I. V. and FIRSOV A. A., *Science*, **306** (2004) 666.
- [4] NOVOSELOV K. S., JIANG D., SCHEDIN F., BOOTH T. J., KHOTKEVICH V. V., MOROZOV S. V. and GEIM A. K., *Proc. Natl. Acad. Sci. U.S.A.*, **102** (2005) 10451.
- [5] GEIM A. K., *Science*, **324** (2009) 1530.
- [6] GIRIT Ç. Ö., MEYER J. C., ERNI R., ROSSELL M. D., KISIELOWSKI C., YANG L., PARK C.-H., CROMMIE M. F., COHEN M. L., LOUIE S. G. and ZETTL A., *Science*, **323** (2009) 1705.
- [7] BAUGHMAN R. H., ZHAKHIDOV A. A. and DE HEER W. A., *Science*, **297** (2002) 787.
- [8] KROTO H. W., HEATH J. R., O'BRIEN S. C., CURL R. F. and SMALLEY R. E., *Nature*, **318** (1985) 162.
- [9] KROTO H. W., *Nature*, **359** (1992) 670.
- [10] BANHART F., FÜLLER T., REDLICH P. and AJAYAN P. M., *Chem. Phys. Lett.*, **269** (1997) 349.
- [11] TODT M., RAMMERSTORFER F. G., FISCHER F. D., MAYRHOFER P. H., HOLEC D. and HARTMANN M. A., *Carbon*, **49** (2011) 1620.
- [12] ENDO M. and KROTO H. W., *J. Phys. Chem.*, **96** (1992) 6941.
- [13] ENDO M., KIM Y. A., HAYASHI T., NISHIMURA K., MATSUTA T., MIYASHITA K. and DRESSELHAUS M. S., *Carbon*, **39** (2001) 1287.
- [14] LOIDL D., PETERLIK H., MÜLLER M., RIEKEL C. and PARIS O., *Carbon*, **41** (2003) 563.
- [15] LOIDL D., PARIS O., BURGHAMMER M., RIEKEL C. and PETERLIK H., *Phys. Rev. Lett.*, **95** (2005) 225501.
- [16] LOIDL D., PARIS O., RENNHOFFER H., MÜLLER M. and PETERLIK H., *Carbon*, **45** (2007) 2801.
- [17] YAKOBSON B. I., BRABEC C. J. and BERNHOLC J., *Phys. Rev. Lett.*, **76** (1996) 2511.
- [18] XIN Z., JIANJUN Z. and ZHONG-CAN Q., *Phys. Rev. B*, **62** (2000) 13692.
- [19] CADELANO E., PALLA P. L., GIORDANO S. and COLOMBO L., *Phys. Rev. Lett.*, **102** (2009) 235502.
- [20] CADELANO E., GIORDANO S. and COLOMBO L., *Phys. Rev. B*, **81** (2010) 144105.
- [21] ARROYO M. and BELYTSCHKO T., *Phys. Rev. Lett.*, **91** (2003) 215505.
- [22] HAO X., QIANG H. and XIAOHU Y., *Compos. Sci. Technol.*, **68** (2008) 1809.
- [23] YAO X., HAN Q. and XIN H., *Comput. Mater. Sci.*, **43** (2008) 579.
- [24] TODT M., RAMMERSTORFER F. G., PARIS O. and FISCHER F. D., *J. Mater. Sci.*, **45** (2010) 6845.
- [25] TODT M., RAMMERSTORFER F. G., HARTMANN M. A., PARIS O. and FISCHER F. D., *Shell-Models for Multi-Layer Carbon Nano-Particles*, in *Shell-Like Structures*, edited by ALTENBACH H. and EREMEYEV V. A. (Springer) 2011, p. 585.
- [26] FASOLINO A., LOS J. H. and KATSNELSON M. I., *Nat. Mater.*, **6** (2007) 858.
- [27] HUANG B., LIU M., SU N., WU J., DUAN W., GU B. and LIU F., *Phys. Rev. Lett.*, **102** (2009) 166404.
- [28] YAMAMOTO M., PIERRE-LOUIS O., HUANG J., FUHRER M. S., EINSTEIN T. L. and CULLEN W. G., *Phys. Rev. X*, **2** (2012) 041018.
- [29] VOZMEDIANO M. A. H., KATSNELSON M. and GUINEA F., *Phys. Rep.*, **496** (2010) 109.
- [30] GUINEA F., KATSNELSON M. I. and GEIM A. K., *Nat. Phys.*, **6** (2010) 30.
- [31] DE JUAN F., CORTIJO A., VOZMEDIANO M. A. H. and CANO A., *Nat. Phys.*, **7** (2011) 810.
- [32] SLOAN J. V., SANJUAN A. A. P., WANG Z., HORVATH C. and BARRAZA-LOPEZ S., *Phys. Rev. B*, **87** (2013) 155436.

Markus A. Hartmann *et al.*

- [33] HUANG Y., WU J. and HWANG K. C., *Phys. Rev. B*, **74** (2006) 245413.
- [34] SHENDEROVA O. A., ZHIRNOV V. V. and BRENNER D. W., *Crit. Rev. Solid State Mater. Sci.*, **27** (2002) 227.
- [35] ZHANG D.-B., AKATYEVA E. and DUMITRICA T., *Phys. Rev. Lett.*, **106** (2011) 255503.
- [36] KUDIN K. N., SCUSERIA G. E. and YAKOBSON B. I., *Phys. Rev. B*, **64** (2001) 235406.
- [37] HOLEC D., HARTMANN M. A., FISCHER F. D., RAMMERSTORFER F. G., MAYRHOFER P. H. and PARIS O., *Phys. Rev. B*, **81** (2010) 235403.
- [38] McDONALD I. R., *Mol. Phys.*, **23** (1972) 41.
- [39] KALOSAKAS G., LATHIOTAKIS N. N., GALIOTIS C. and PAPAGELIS K., *J. Appl. Phys.*, **113** (2013) 134307.
- [40] WIEDEMANN J., *Leichtbau - Elemente und Konstruktion* (Springer) 2007.
- [41] KANG J. W. and LEE S., *Comput. Mater. Sci.*, **74** (2013) 107.
- [42] KYSAR J. W., *Sci. Model. Simul.*, **15** (2008) 143.
- [43] CHEN W.-H., CHENG H.-C. and LIU Y.-L., *Comp. Mater. Sci.*, **47** (2010) 985.
- [44] CHANG T., *J. Mech. Phys. Solids*, **58** (2010) 1422.
- [45] TAPASZTÓ L., DUMITRICA T., KIM S. J., NEMES-INCZE P., HWANG C. and BIRÓ L. P., *Nat. Phys.*, **8** (2012) 739.

Continuum shell models for closed cage carbon nanoparticles

M. Todt & F.G. Rammerstorfer

Vienna University of Technology, Vienna, Austria.

M.A. Hartmann

Montanuniversität Leoben, Leoben, Austria.

ABSTRACT: Fullerenes are closed cage carbon nanostructures and form the layers of carbon onions which have potential application in electronics industries. In this paper the mechanical properties of such fullerenes are investigated using continuum shell models and Monte Carlo (MC) simulations. It is shown that elastic shell parameters originally derived for graphene or carbon nanotubes are also appropriate to model the shell properties of fullerene layers. A good representation of the MC results is obtained for effective elastic moduli of $E \sim 5000$ GPa in combination with an effective layer thickness of $h \sim 0.07$ nm. The most frequently proposed parameter set for carbon nanotubes with $h \sim 0.34$ nm and $E \sim 1$ TPa completely fails to predict the mechanical behavior of fullerenes. Further it is shown that the pentagonal atomic rings, required to form a closed cage structure, locally increase the hydrostatic stiffness of the faceted fullerenes, but also significantly reduce the stiffness of the surrounding hexagonal atomic rings. As the number of pentagons in a fullerene is restricted to 12 the proportion of the surface area covered by hexagons increases for larger fullerenes leading to a decrease in hydrostatic stiffness with fullerene size.

1 INTRODUCTION

Carbon onions are multi-layered, almost spherical carbon nanostructures consisting of a number of concentric carbon layers. They have first been observed by Iijima 1980 and, e.g., form from soot when subjected to intense electron irradiation (Ugarte 1992). Carbon onions are promising candidates as fillers in composites used for electromagnetic shielding (Matcukovic et al. 2009), as additives in lubricants (Joly-Pottuz et al. 2008), as solid lubricants (Hirata et al. 2004), or as nanoscopic pressure cells for nanodiamond production (Banhart and Ajayan 1996). However, for an expedient use of these particles their mechanical properties and, hence, the properties of their individual layers have to be well understood.

The layers of carbon onions can be considered to be so called icosahedral fullerenes (Kroto 1992). Icosahedral fullerenes (Klein et al. 1986) are closed cage sp^2 bonded carbon structures, see Figure 1. In contrast to graphene and carbon nanotubes, which have a pure hexagonal atomic structure, each fullerene contains exactly 12 pentagonal rings. Pentagonal rings introduce curvature into a hexagonal atomic structure (Cataldo 2002), and thus, are necessary to form closed cage structures. The exactly 12 pentagons are an implication of Euler's theorem and cause the fullerenes

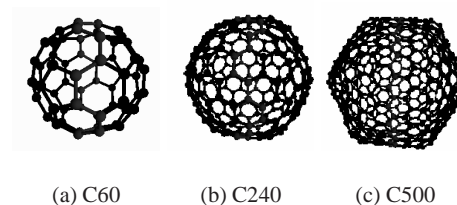


Figure 1: Icosahedral fullerenes of various sizes. Figure taken from Todt 2013.

to become more faceted with increasing size.

In this paper the mechanical properties of fullerenes and, hence, single onion layers are investigated in two steps. First, a simple continuum shell model is used in conjunction with Monte Carlo (MC) simulations to investigate which of the different shell parameter sets found in literature for graphene and carbon nanotubes gives a good representation of the mechanical behavior of the fullerenes. Second, the best fitting parameter set is used to study the influence of the pentagonal rings on the mechanical properties of a C240 fullerene. For the latter investigations the finite element method is employed as also the faceted shape of the C240 and more complex loading conditions are considered. Both steps are discussed in detail in the following sections.

2 ANALYTICAL CONSIDERATIONS

2.1 Methodology

For the analytical considerations the fullerenes are assumed to be perfectly spherical, and the atomic layers are represented by thin elastic shells according to the model of Yakobson et al. 1996. The properties of the shells can then be described by three independent effective shell parameters: elastic modulus E , layer thickness h , and Poisson's ratio ν . Instead of E and h

$$C = \frac{Eh}{1-\nu^2} \quad \text{and} \quad D = \frac{Eh^3}{12(1-\nu^2)} \quad (1)$$

can be used, representing the membrane and bendings stiffness of the shells, respectively. For graphene and carbon nanotubes different values for E , h , and ν can be found in literature, see Table 1. For a more detailed list see, e.g., Todt 2013. None of the parameter sets is derived for fullerenes and the values of E and h differ significantly. Thus, all sets are tested regarding their ability to predict the mechanical behavior of fullerenes. For this purpose fullerenes of different size are subjected to hydrostatic pressure and a radial load applied as line load along the equator of the fullerenes, respectively. The results of the continuum mechanical models are compared to those of MC simulations.

Table 1: Values found in literature for E , h , and ν .

Reference	E in GPa	h in nm	ν	Set
(Yakobson et al. 1996)	5500	0.066	0.19	S1
(Pantano et al. 2004)	4840	0.075	0.19	S2
(Sears and Batra 2004)	3100	0.098	0.26	S3
(Liu et al. 2007)	1050	0.334	0.186	S4

The MC simulations are performed according to the procedure described in Holec et al. 2010 using the parameter set given therein. The hydrostatic pressure is realized by subjecting each atom i of the fullerene to an external force $\vec{F}_H^{(\text{ext})}$ pointing towards the fullerene's center of mass. The hydrostatic stiffness is calculated as

$$K_H^{(\text{MC})} = \frac{\sum_n |\vec{F}_H^{(\text{ext})}|}{\Delta R}, \quad (2)$$

where n is the number of atoms making up the fullerene and ΔR is the change of the fullerene's mean radius. In an additional analysis the atoms of the fullerenes are enforced to be located on perfect spheres during hydrostatic deformation, where the undeformed radii of the spheres are equal to the mean radii of the undeformed fullerenes. The corresponding hydrostatic stiffness is denoted as $K_H^{(\text{MCS})}$. Further, the critical hydrostatic pressure $p_H^{(\text{MC})*}$, indicated by the collapse of the fullerene, is estimated and reads

$$p_H^{(\text{MC})*} = \frac{n |\vec{F}_H^{(\text{ext})*}|}{A_0}, \quad (3)$$

Table 2: Mean radii of different carbon fullerenes obtained from MC simulations.

fullerene	C60	C240	C500	C1280
$R^{(0)}$ in nm	0.355	0.711	1.023	1.631

where $\vec{F}_H^{(\text{ext})*}$ and A_0 denote the force per atom at the onset of collapse (buckling), and the surface area of a sphere with the same mean radius $R^{(0)}$ as the undeformed fullerene, respectively. To realize the equatorial load, a number of atoms n_E , being located within a narrow area along the equator of the fullerene, are subjected to a force $\vec{F}^{(\text{ext})}$. The "narrow area" indicates that the atoms in the equator regions are not all directly located at the equator. The corresponding equatorial stiffness reads

$$K_R^{(\text{MC})} = \frac{\sum_{n_E} |\vec{F}^{(\text{ext})}|}{\Delta R_E}. \quad (4)$$

with ΔR_E being the change of the mean radius of the area close to the equator.

In the continuum models the fullerenes are represented as spherical shells with their radii being equal to the mean radii $R^{(0)}$ of the fullerenes. The values are given in Table 2. The hydrostatic stiffness of the continuum model is obtained as

$$K_H = \frac{p_H A_0}{\Delta R} = \frac{8\pi E h}{1-\nu}, \quad (5)$$

where p_H is the applied hydrostatic pressure and ΔR and A_0 denote the change in the radius and the initial surface area of the spherical shell, respectively. The critical hydrostatic pressure for bifurcation buckling of a thin spherical shell reads (Pflüger 1975)

$$p_H^* = \frac{2Eh^2}{\sqrt{3(1-\nu^2)}(R^{(0)})^2}. \quad (6)$$

This equation holds only for perfect spheres. Thus, the considerations regarding p_H^* are restricted to C60 and C240. The equatorial stiffness of a spherical shell with radius $R^{(0)}$ can be expressed as

$$K_R = \frac{2\pi R^{(0)} f^E}{\Delta R_E} = \frac{4\pi E h}{[\frac{3(1-\nu^2)(R^{(0)})^2}{h^2}]^{1/4}}. \quad (7)$$

with ΔR_E and f^E being the change of the radius at the equator and the force per unit length applied at the equator, respectively.

2.2 Results and Discussion

The results of the analytical considerations are given in Tables 3 to 5. The hydrostatic stiffness of the faceted carbon fullerenes $K_H^{(\text{MC})}$ decreases with increasing fullerene size, but seems to approach an asymptotic value, see Table 3. This decrease in stiffness is much less observed if the fullerenes are enforced to be perfect spheres and cannot be captured by

Table 3: Hydrostatic stiffness of different fullerenes obtained from MC simulations and analytical considerations. Parameter sets S1 to S4 are defined in Table 1.

	C60	C240	C500	C1280
$K_H^{(MC)}$ in N/m	9859	9061	8499	8259
$K_H^{(MCS)}$ in N/m	10021	9750	9764	9756
K_H S1 in N/m	11263	=	=	=
K_H S2 in N/m	11263	=	=	=
K_H S3 in N/m	10318	=	=	=
K_H S4 in N/m	10828	=	=	=

the continuum model as K_H is independent of the radius, see Eq. 5. Thus, it can be concluded that the hydrostatic stiffness of a fullerene is mainly influenced by its faceted shape, which will be further investigated in Section 3. All shell parameter sets give comparable results for K_H which are in good agreement with $K_H^{(MC)}$ and $K_H^{(MCS)}$. This is because hydrostatic pressure leads to a pure membrane loading state and the product Eh is nearly the same for all parameter sets.

Table 4: Critical hydrostatic pressure of C60 and C240 obtained from MC simulations and analytical considerations. Parameter sets S1 to S4 are defined in Table 1.

Fullerene	$p_H^{(MC)*}$ in GPa		p_H^* in GPa			
	S1	S2	S3	S4	S5	S6
C60	276	224	254	282	1092	
C240	63	56	63	70	272	

As shown in Table 4, the critical pressures p_H^* calculated with parameter sets S2 and S3 are in good agreement with the MC simulations. Parameter set S4, which is often proposed for carbon nanotubes, see, e.g., Liu et al. 2007, Zhang et al. 2002 overestimates the critical pressure of the fullerenes to a large amount. As p_H^* depends on the bending stiffness in addition to the membrane stiffness, it can be concluded that a parameter set which only represents membrane stiffness, but is not able to represent the bending stiffness, is useless, if bending is involved. Thus, the value $h \sim 0.34$ nm is far to high and, hence, the corresponding elastic modulus is not appropriate, too.

Table 5: Equatorial stiffness of different fullerenes obtained from MC simulations and analytical considerations. Parameter sets S1 to S4 are defined in Table 1.

Fullerene	$K_R^{(MC)}$ in N/m		K_R in N/m			
	S1	S2	S3	S4	S5	S6
C60	2042	1508	1607	1551	3277	
C240	1394	1065	1136	1095	2315	
C500	1103	889	947	914	1930	
C1280	831	703	750	723	1529	

On first sight non of the parameter sets gives a good representation of the equatorial stiffness of C60 and C240, see Table 5. However, the load in the MC simulations is rather an area load than a line load as assumed in the continuum model. A line load is more localized, leading to larger displacements and, hence, to lower stiffness values. Set S4 completely fails to predict the ring load stiffness. As K_R is also closely

related to the bending stiffness the conclusions drawn for p_H^* in conjunction with S4 apply here, too.

Overall sets S2 and S3 give the best representation of the mechanical properties of the investigated fullerenes, where set S2 is used in Section 3.

3 FINITE ELEMENT MODEL

3.1 Methodology

The influence of the faceted shape on the mechanical properties of fullerenes is investigated using finite element shell models of a faceted C240 and a model of a C240 with all atoms mapped to a sphere, see Figure 2. This two configurations are referred to as “faceted” and “mapped”, respectively. The initial radius of the mapped configuration is equal to the initial mean radius of the faceted C240. For discretization three-noded shell elements with reduced integration are used which have a characteristic length of about $\frac{1}{10}$ of a carbon-carbon bond length. The faceted and mapped configurations are subjected to hydrostatic pressure, whereas the radial ring load along the equator is only applied to the faceted C240. All loads are applied corresponding to (i) a continuum mechanical loading and (ii) the MC loading conditions.

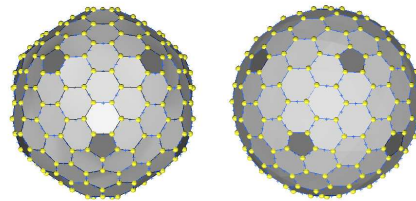


Figure 2: Shell models of the faceted (left) and mapped (right) configurations of a C240 fullerene. The finite element mesh is not shown for the sake of clarity.

3.1.1 Results and Discussion

The values obtained for the hydrostatic stiffness of the continuous loading and the MC loading conditions read 11047 N/m (faceted), 11627 N/m (mapped) and 10401 N/m (faceted), 10947 N/m (mapped), respectively. The evaluated higher stiffnesses of the mapped configurations are in analogy to the higher stiffnesses observed in the MC simulations for the enforced spherical fullerenes, and are in good agreement with the values given in Table 3. For the continuum loading the mapped C240 deforms almost uniformly with negligible influence of the pentagonal rings, see Figure 3 (right). For the faceted configuration the pentagonal rings lead to a local stiffening of the fullerene, as shown in Figure 3 (left). However, the hexagons between the pentagonal rings show significantly higher deformations than in the mapped configuration. This weakening of the hexagonal areas outweighs the stiffening due to the pentagons as the total surface area

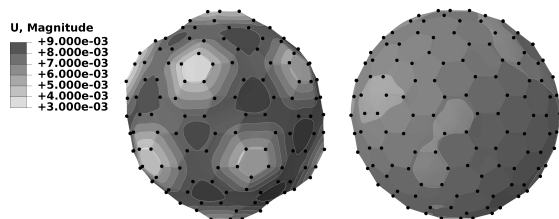


Figure 3: Displacement results of the continuum hydrostatic loading for the faceted (left) and mapped (right) configurations of a C240 fullerene. Both configurations are subjected to a hydrostatic pressure of 72 GPa.

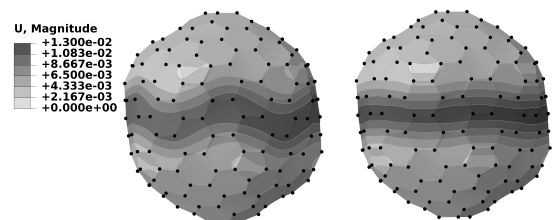


Figure 4: Displacement results for the radial equatorial load for a C240 subjected to MC loading conditions (left) and the corresponding continuum mechanical loading (right). For both loading conditions a total radial ring load of 14 nN is applied.

of the hexagons is larger than those of the pentagons. The larger the fullerene, the larger is the fraction of surface area covered by hexagons and, hence, the hydrostatic stiffness of the fullerenes must decrease with their size.

The results for the radial ring load applied along the equator are depicted in Figure 4. As stated in Section 2.2 the deformations for the continuum loading conditions are more localized than for the MC loading conditions. The equatorial stiffness obtained for the MC loading conditions is 1406 N/m, which is almost equal to the equatorial stiffness of the fullerene calculated by MC simulations, see Table 5. For the continuous loading a stiffness of 1188 N/m is evaluated. This value is close to the equatorial stiffness obtained by the simple analytical model for parameter set S2, which is also used in the present analysis. These results confirm the statements made in Section 2.2 regarding the equatorial stiffness and also show that an elastic modulus $E \sim 5000$ GPa in combination with a layer thickness of $h \sim 0.07$ nm is appropriate for modeling the mechanical properties of carbon fullerenes.

4 CONCLUSIONS

It is shown that continuum shell models can be used to predict the mechanical behavior of carbon fullerenes. The best agreement with MC simulations is obtained when an elastic modulus of $E \sim 5000$ GPa in combination with a layer thickness of $h \sim 0.07$ nm is used to describe the layer properties. The decrease in hydrostatic stiffness observed for larger faceted fullerenes is found to be due to the local stiffness re-

duction introduced in the hexagonal atomic rings, although the pentagonal rings lead to a local increase in stiffness. Further, it is shown that the loading conditions of the continuum and atomic structure have to be equivalent to lead to comparable results. Overall it can be said that continuum shell models of carbon nanostructures are computationally efficient tools for modeling the mechanical behavior of such structures.

REFERENCES

- Banhart, F. & P. Ajayan (1996). Carbon onions as nanoscopic pressure cells for diamond formation. *Nature* 382, 433–435.
- Cataldo, F. (2002). The impact of a fullerene-like concept in carbon black science. *Carbon* 40, 157–162.
- Hirata, A., M. Igarashi, & T. Kaito (2004). Study on solid lubricant properties of carbon onions produced by heat treatment of diamond clusters or particles. *Tribol. Int.* 37, 899–905.
- Holec, D., M. Hartmann, F. Fischer, F. Rammerstorfer, P. Mayrhofer, & O. Paris (2010). Curvature-induced excess surface energy of fullerenes: Density functional theory and Monte Carlo simulations. *Phys. Rev. B* 81, 235403.
- Iijima, S. (1980). Direct observation of the tetrahedral bonding in graphitized carbon black by high resolution electron microscopy. *J. Cryst. Growth* 50, 675–683.
- Joly-Pottuz, L., N. Matsumoto, H. Kinoshita, B. Vacher, M. Belin, & G. M. et al (2008). Diamond-derived carbon onions as lubricant additives. *Tribol. Int.* 41, 69–78.
- Klein, D., W. Seitz, & T. Schmalz (1986). Icosahedral symmetry carbon cage molecules. *Nature* 323, 703–706.
- Kroto, H. (1992). Carbon onions introduce new flavour to fullerene studies. *Nature* 359, 670–671.
- Liu, F., P. Ming, & J. Li (2007). *Ab initio* calculation of ideal strength and phonon instability of graphene under tension. *Phys. Rev. B* 76, 064120.
- Macutkevic, J., D. Seliuta, G. Valusis, J. Banys, P. Kuzhir, & S. M. et al (2009). Dielectric properties of onion-like carbon based polymer films: Experiment and modeling. *Solid State Sci.* 11, 1828–1832.
- Pantano, A., D. Parks, & M. Boyce (2004). Mechanics of deformation of single- and multi-wall carbon nanotubes. *J. Mech. Phys. Solids* 52, 789–821.
- Pflüger, A. (1975). *Stabilitätsprobleme der Elastostatik*. Berlin: Springer-Verlag.
- Sears, A. & R. Batra (2004). Macroscopic properties of carbon nanotubes from molecular-mechanics simulations. *Phys. Rev. B* 69, 235406.
- Todt, M. (2013). *Continuum Shell Models for Multi-Layer Carbon Nanostructures*. Ph. D. thesis, Vienna University of Technology.
- Ugarte, D. (1992). Curling and closure of graphitic networks under electron-beam irradiation. *Nature* 359, 707–709.
- Yakobson, B., C. Brabec, & J. Bernholc (1996). Nanomechanics of carbon tubes: Instabilities beyond linear response. *Phys. Rev. Lett.* 76, 2511–2514.
- Zhang, P., Y. Huang, P. Geubelle, P. Klein, & K. Hwang (2002). The elastic modulus of single-wall carbon nanotubes: a continuum analysis incorporating interatomic potentials. *Int. J. Solids Struct.* 39, 3893–3906.



ELSEVIER

Contents lists available at ScienceDirect

International Journal of Solids and Structures

journal homepage: www.elsevier.com/locate/ijsolstr

Growth limit of carbon onions – A continuum mechanical study

Melanie Todt^{a,*}, Robert D. Bitsche^{a,1}, Markus A. Hartmann^c, Franz D. Fischer^b, Franz G. Rammerstorfer^a^aInstitute of Lightweight Design and Structural Biomechanics, Vienna University of Technology, Gusshausstraße 27-29, A-1040 Vienna, Austria^bInstitute of Mechanics, Montanuniversität Leoben, Franz-Josef-Straße 18, A-8700 Leoben, Austria^cInstitute of Physics, Montanuniversität Leoben, Franz-Josef-Straße 18, A-8700 Leoben, Austria

ARTICLE INFO

Article history:

Received 6 August 2013

Received in revised form 14 October 2013

Available online 9 November 2013

Keywords:

Carbon nanostructures

Finite element modeling

Shell buckling

van der Waals interactions

ABSTRACT

The growth of carbon onions is simulated using continuum mechanical shell models. With this models it is shown that, if a carbon onion has grown to a critical size, the formation of an additional layer leads to the occurrence of a structural instability. This instability inhibits further growth of carbon onions and, thus, can be a reason for the limited size of such particles. The loss of stability is mainly evoked by van der Waals interactions between misfitting neighboring layers leading to self-equilibrating stress states in the layers due to mutual accommodation. The influence of the curvature induced surface energy and its consequential stress state is investigated and found to be rather negligible. Furthermore, it is shown that the nonlinear character of the van der Waals interactions has to be considered to obtain maximum layer numbers comparable to experimental observations. The proposed model gives insight into mechanisms which are assumed to limit the size of carbon onions and can serve as basis for further investigations, e.g., of the formation of nanodiamonds in the center of carbon onions.

© 2013 Elsevier Ltd. All rights reserved.

1. Introduction

Carbon based nanostructures like graphene (Cadelano et al., 2009; Geim and Novoselov, 2007; Geim, 2009; Novoselov et al., 2004; Zhang et al., 2011), carbon nanotubes (Baughman et al., 2002; Iijima, 1991; Pantano et al., 2004; Yakobson et al., 1996), fullerenes (Kroto et al., 1985; Tang and Huang, 1995a), and carbon onions (Banhart and Ajayan, 1996; Kroto, 1992; Ugarte, 1992, 1995) have been intensively studied within the last decades. Graphene is the main building material of all of these carbon nanostructures (Geim and Novoselov, 2007) and is stated to be the strongest and thinnest material ever discovered (Geim, 2009). Nanotubes, fullerenes, and carbon onions should inherit the exceptional mechanical, electrical and electronic properties of graphene, due to their similar structure.

Fullerenes and carbon onions take an exceptional position among the carbon nanostructures. Graphene and carbon nanotubes have an hexagonal atomic arrangement, whereas fullerenes and carbon onions also contain pentagonal atomic rings to form closed cell structures. Fullerenes must contain 12 pentagons to be stable (Tang and Huang, 1995a); therefore, these particles are of polyhedral shape. Polyhedral closed cell particles also occur in multi-layered arrangements (Blank et al., 2007; Fu et al., 2007;

Kroto et al., 1985; Zhao et al., 2007), which can be transformed to perfectly spherical carbon onions by intense electron irradiation (Banhart and Ajayan, 1996; Ugarte, 1992). Currently, several techniques are available to produce multi-layered closed cell arrangements and carbon onions like electron irradiation of graphite at elevated temperatures (≥ 300 °C) (Banhart and Ajayan, 1996; Bhanhart et al., 1997b), annealing of diamond nanoparticles (Joly-Pottuz et al., 2008; Tomita et al., 2002), high pressure transformation of single-crystal graphite (Blank et al., 2007), using a radio frequency plasma process (Fu et al., 2007), or synthesis by decomposition of phenolic resin (Zhao et al., 2007). The different production techniques lead to different growing scenarios of such multi-layered particles. Onions produced by high-pressure transformation of single-crystal graphite or from coal in a radio frequency plasma reactor are assumed to grow from the inside to the outside (Blank et al., 2007; Du et al., 2007). Carbon onions produced by high-temperature annealing of nanodiamonds start their formation at the boundaries of the nanodiamond (Kuznetsov et al., 1994; Tomita et al., 2002) and have a diameter being almost equal to that of the initial nanodiamond (Los et al., 2009). This growing scenario is also proposed in Ugarte (1995).

The multi-layered particles have a high local electronic density and consequently a high ability to absorb electromagnetic radiation. Thus, they can be used as fillers in composites for electromagnetic shielding (Macutkevic et al., 2009). Furthermore, carbon onions have a potential application as additives in lubricants (Joly-Pottuz et al., 2008), as solid lubricants (Hirata et al., 2004), or as nanoscopic pressure cells to produce nanodiamonds (Banhart

* Corresponding author. Tel.: +43 1 58801 317 10; fax: +43 1 58801 317 99.

E-mail address: mt@ilsb.tuwien.ac.at (M. Todt).¹ Present address: Technical University of Denmark, Department of Wind Energy, VEA-118, Frederiksborgvej 399, DK-4000 Roskilde, Denmark.

and Ajayan, 1996; Banhart et al., 1997a; Redlich et al., 1998). In all applications the size of the multi-layered particles is of substantial interest.

Carbon onions observed in experiments can consist only of a few layers (Joly-Pottuz et al., 2008; Ugarte, 1995), be of intermediate size (Banhart et al., 1997a; Blank et al., 2007), or consist of many layers (Wesolowski et al., 1997; Zwanger et al., 1996) with diameters up to 50 nm. The different sizes are probably a result of the different production techniques and, hence, of the different growing mechanisms. In Zwanger et al. (1996) it is shown that the precursor material and the irradiation dose influence the size of the particles. But, what limits the size of the particles? Is there something like a growth limit, and if yes, what triggers this limit? To the best of the authors' knowledge these questions are not clarified so far in the literature.

Theoretical predictions about the maximum number of layers to which carbon onions can grow can be found in Tang and Huang (1995b), where it is shown that this number can reach a big value. However, in this study the deformations of the layers due to the van der Waals (vdW) interactions are not considered and the layers are assumed to remain spherical during the growth. Thus, a possible occurrence of structural instabilities, e.g., buckling of layers, is not incorporated in the theoretical models by Tang and Huang (1995b).

In the current paper, we propose that exactly such an occurrence of a structural instability limits the size to which carbon onions can grow. The instability is assumed to be evoked by the formation of an additional layer onto an onion which has grown to its maximum layer number. Due to the expected large number of layers the application of atomistic simulation techniques would lead to enormous computational efforts. Hence, continuum mechanical shell models of carbon onions of various sizes are used to investigate whether or not these assumptions for a growth limit are reasonable.

Continuum mechanical shell models have shown to give reliable results for buckling of carbon nanostructures, such as single and multi-walled carbon nanotubes (Pantano et al., 2004; Yakobson et al., 1996), single layer graphene (Hartmann et al., 2013), or carbon crystallites (Todt et al., 2010). Continuum mechanical shell models are also applicable to investigate the mechanical properties of carbon fullerenes as shown in Todt et al. (2013) by comparison with Monte Carlo simulations. However, using continuum mechanical models of carbon onions involves some basic assumptions about the structure of the individual layers, the vdW interactions, and the growth of carbon onions, which are addressed in the following sections.

2. Methodology

For studying the growth and, hence, a possible growth limit of carbon onions using continuum mechanics the finite element method is employed. The onion layers are assumed to be deformable and the vdW interactions between the layers are taken into account. Buckling eigenvalue prediction is used to check if the occurrence of a structural instability can be the reason for the limited size of carbon onions. The finite element analyses are performed with the commercial finite element program ABAQUS.² The general concept proposed for studying the growth limit of carbon onions was already briefly discussed by the authors in Todt et al. (2011b), where also preliminary results were presented.

2.1. Axisymmetric shell model

In many cases the observed carbon onions are almost perfectly spherical in shape (Banhart and Ajayan, 1996; Kroto, 1992; Ugarte,

1992, 1995). Thus, the assumption of perfectly spherical onions seems to be admissible in the finite element model. Consequently, axisymmetric models are used in the computational analysis reducing the computational requirements significantly (see Fig. 1). In any case, the assumption of axisymmetry is justified as long as stable, i.e., pre-buckling states are considered. The axisymmetric model is used for stability considerations, too. This is because for a single thin-walled spherical shell under a constant external pressure the lowest and, therefore, relevant buckling eigenvalue appears with an extremely high multiplicity, see (Drmota et al., 1987). This high multiplicity of the eigenvalue leads to a high number of eigenfunctions being orthogonal to each other. Among these eigenfunctions several axisymmetric ones can be found, which have the same physical relevance as non-axisymmetric eigenfunctions. Regardless, whether an axisymmetric or non-axisymmetric buckling mode is considered, an imperfect shell most likely forms a single dimple in the post-buckling regime (Drmota et al., 1987), which represents an axisymmetric deformation, too. Thus, axisymmetry is also a reasonable assumption for the buckled configuration of a single spherical shell. Complete spherical shells filled with elastic media also show axisymmetric buckling modes if subjected to external pressure (Sato et al., 2012). A carbon onion can be considered as the outermost shell filled with an elastic medium formed by the layers below and the vdW interactions between these layers.

Each layer of the onion is denoted an index $i \in [1, N]$, with N being the total number of layers forming the onion, see Fig. 1. The layers are modeled as thin elastic shells with a membrane stiffness $C = Eh$ and bending stiffness $D = \frac{Eh^3}{12(1-\nu^2)}$, where E , ν , and h are the elastic modulus, the Poisson's ratio, and the layer thickness, respectively. For sake of simplicity, standard shell elements are used in the analyses requiring the direct input of parameter set E , ν , and h . However, the values found in literature for these parameter set differ strongly, e.g., $E = 1050$ GPa, $\nu = 0.186$, $h = 0.334$ nm (Liu et al., 2007) or $E = 4840$ GPa, $\nu = 0.19$, $h = 0.075$ nm (Pantano et al., 2004). A more detailed list of parameter sets can be found, e.g., in Huang et al. (2006). Although the different parameter sets give almost the same values for C , the obtained values for D are significantly different having a remarkable influence on the stability behavior of onion layers. For a single, perfectly spherical onion layer (i.e., without the supporting layers underneath) the critical pressure can be estimated as (Pflüger, 1975)

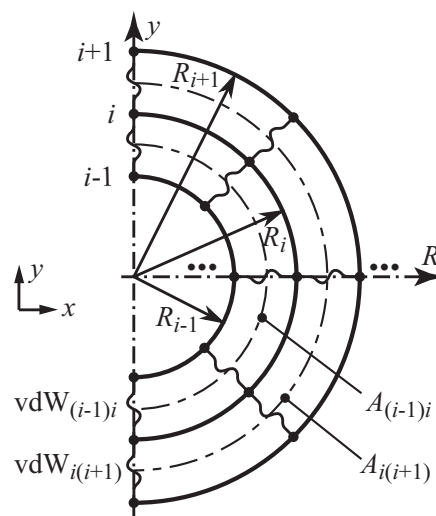


Fig. 1. Axisymmetric model of a carbon onion consisting of N layers. From Todt et al. (2011b), with permission.

² <http://www.3ds.com/products/simulia/portfolio/abaqus/overview/>.

$$p_i^* = \frac{2Eh^2}{\sqrt{3(1-\nu^2)}(R_i^{(0)})^2}, \quad (1)$$

where $R_i^{(0)}$ is the radius of layer i . As can be seen from Eq. (1) the pressure p_i^* is quite sensitive to E and h . Consequently, also the occurrence of a structural instability in a carbon onion is likely to be sensitive to these parameter sets. Thus, a different choice of E , h , and ν will lead to different proposals on the critical size of the onions. Parameter sets with $E \approx 1000$ GPa and $h \approx 0.34$ nm strongly overestimate the bending stiffness and, hence, the critical pressure of fullerenes, i.e., single onion layers as shown in [Todt et al. \(2013\)](#). Thus, also the critical size of the onions might be strongly overestimated by such parameter sets. A good representation of the stiffness properties of fullerenes and their critical pressure can be obtained with $E \approx 5000$ GPa and $h \approx 0.07$ nm ([Todt et al., 2013](#)). On account of this the parameter set proposed in [Pantano et al. \(2004\)](#) ($E = 4840$ GPa, $\nu = 0.19$, $h = 0.075$ nm) is used to describe the layer properties.

Although the layers are modeled as spherical shells it is assumed that their number of atoms is equal to those of icosahedral fullerenes with the same mean radii. According to [Tang and Huang \(1995a\)](#) the number of atoms, n , forming fullerenes with icosahedral symmetry can be calculated using $n = 60k^2$ or $n = 20m^2$, with $k, m \in \mathbb{N}$. The radius $R_i^{(0)}$ of an undeformed, i.e. stress free layer i can then be evaluated as ([Voytekhovskiy, 2003](#))

$$R_i^{(0)} = a^{(0)} \sqrt{0.103374 n_i - 0.424548}, \quad (2)$$

where $a^{(0)} = 0.142$ nm is used as carbon–carbon bond length in the undeformed configuration and n_i is the number of atoms forming this layer.

2.2. Excess surface energy

In [Holec et al. \(2010\)](#) it is shown that a curvature-dependent excess surface energy is active in curved carbon nanostructures. As a consequence of the excess surface energy the layers are subjected to surface stresses leading to a non-zero membrane stress state in the layers.

The dependency of the excess surface energy $E_i^{(S)}$ on the layer radius R_i can be described using a power law $E_i^{(S)} \propto R_i^\beta$ ([Holec et al., 2010](#)). For $E_i^{(S)}$ being expressed in J/(nm)² an average value of $\beta = -1.83$ is evaluated for the whole fullerene model; for more details see ([Holec et al., 2010](#)). Consequently a surface stress $\bar{\sigma}_i^{(S)}$ (being a membrane force per unit length) develops in the onion layers according to the Shuttelworth equation ([Fischer et al., 2008](#)),

$$\bar{\sigma}_i^{(S)} = E_i^{(S)} + \frac{dE_i^{(S)}}{d\bar{\epsilon}_i^{(S)}}. \quad (3)$$

The parameter $\bar{\epsilon}_i^{(S)}$ is the in-plane strain in a small strain setting ([Fischer et al., 2008](#)). For a first estimate usually the second term of the right hand side of Eq. (3) can be neglected, and the relation

$$\bar{\sigma}_i^{(S)} = E_i^{(S)} \quad (4)$$

can be used. Note that in Eqs. (3) and (4) the quantities $E_i^{(S)}$ and $\bar{\sigma}_i^{(S)}$ are physically different but have the same unit, namely force per unit length.

In the finite element model the surface stress $\bar{\sigma}_i^{(S)}$ is taken into account by applying a corresponding inwards oriented pressure $p_i^S = 2\bar{\sigma}_i^{(S)}/R_i$ ([Fischer et al., 2008](#)) onto layer i , resulting with Eq. (4) in

$$p_i^S = 2A R_i^{-2.83}. \quad (5)$$

The factor $A \approx 0.36$ nN nm/(nm)^{0.17} is estimated from Fig. 7 in [Holec et al. \(2010\)](#). As can be seen from Eq. (5), the pressure p_i^S

decreases fast with increasing layer radius R_i and, thus, is only of relevance for the innermost layers of a carbon onion.

2.3. Van der Waals model

For carbon onions the vdW interactions between neighboring layers must be considered as well. From an atomistic point of view the vdW interactions between two neighboring layers result from vdW interactions between the atoms forming these layers. This atom–atom interactions, however, are not applicable in continuum mechanical models, for which a pressure–distance relation is required. Appropriate continuum vdW models for different carbon nanostructures can be found in literature, see, e.g., ([He et al., 2005](#); [Kelly, 1981](#); [Lu et al., 2009](#); [Todt et al., 2011a](#)). In [Lu et al. \(2009\)](#) and [Todt et al. \(2011a\)](#) the curvature of the carbon nanostructures is taken into account in the formulation of the vdW interactions. In the present study this curvature influence on the vdW interactions is neglected for the sake of simplicity, and pressure–distance relations derived for planar graphene are used ([Kelly, 1981](#); [Todt et al., 2011a](#)). With increasing layer radii the curvature effect in the vdW interactions vanishes and, thus, for the outer layers this simplification is admissible. Onion layers with small radii, i.e., the innermost layers, are much stiffer and have a much higher resistance against buckling than the outermost layers, see Eq. (1). Therefore, it seems unlikely that buckling starts at the center of the onion. Consequently, the simplified representation of the vdW interactions in the inner region is assumed to be of minor influence.

The pressure–distance relations used for describing the vdW interactions read according to [Kelly \(1981\)](#)

$$p(\alpha) = \frac{C_{33}}{6} \left[\left(\frac{\sigma}{\alpha} \right)^{10} - \left(\frac{\sigma}{\alpha} \right)^4 \right], \quad (6)$$

or ([Todt et al., 2011a](#))

$$p(\alpha) = C_0 \left[\left(\frac{\sigma}{\alpha} \right)^{11} - \left(\frac{\sigma}{\alpha} \right)^5 \right], \quad (7)$$

respectively, where α is the current interlayer distance and σ is a Lennard–Jones Parameter. The parameters C_{33} and C_0 are compressive constants. In [Kelly \(1981\)](#) and [Zhao and Spain \(1989\)](#) a value of 36.5 GPa is reported for C_{33} , whereas C_0 is obtained as $C_0 = 8 \epsilon \sigma \pi (\rho_\infty)^2$ ([Todt et al., 2011a](#)) and, thus, depends on the atom density per unit area, $\rho_\infty = 38.18$ atoms/nm², and another Lennard–Jones parameter ϵ . In the literature different values can be found for σ and ϵ , see, e.g., $\sigma = 0.3415$ nm, $\epsilon = 0.00239$ eV in [Lu et al. \(2009\)](#) and $\sigma = 0.3345$ nm, $\epsilon = 0.00319$ eV in [Zhang et al. \(2007\)](#). Thus, it is unlikely that $C_{33}/6$ and C_0 have the same value. VdW models described by Eqs. (6) and (7) not only differ in their compressive constants but also in their exponents. This differences may lead to different results for the growth limit of carbon onions as considered in the following. It should be noted that both models give the same interlayer distance $\alpha_{eq} = \sigma$ for which $p(\alpha) = 0$. The distance α_{eq} is referred to as equilibrium vdW distance.

2.3.1. Linear van der Waals model

Taking the nonlinear behavior of the vdW interactions into account is a computationally intensive task. Thus, the vdW interactions are linearized around the vdW equilibrium distance α_{eq} for performing principle model analyses in a first attempt. This linearization is admissible if the distances α between neighboring layers are close to α_{eq} and the deviations $\Delta\alpha$ in the interlayer distances are small. The linearized vdW interactions can be interpreted as some sort of elastic bedding, and linear spring elements are used to model this bedding. The modeling procedure of the linear

vdW bedding is described for Eq. (6) only, but can be easily transferred to Eq. (7), too.

Under the above assumptions the linearized pressure–distance relation corresponding to Eq. (6) reads

$$p_{\text{lin}} = \hat{k}\Delta\alpha, \tag{8}$$

with $\hat{k} = \frac{dp}{d\alpha} \Big|_{\alpha=\alpha_{\text{eq}}} = \frac{C_{33}}{\alpha_{\text{eq}}}$ being the linearized stiffness of the vdW bedding. With Eq. (8) the vdW force F_{kl} acting on a single finite element node of the layers can be obtained as

$$-F_{kl} = p_{\text{lin}}A_{kl} = \hat{k}A_{kl}(\alpha_{kl} - \alpha_{\text{eq}}), \tag{9}$$

where α_{kl} and $A_{kl} = \frac{A_k + A_l}{2}$ are the current distance between and the area associated to nodes k and l , respectively linked by the spring element, see Fig. 2. The area A_{kl} accounts for the curvature dependent difference between areas A_k and A_l related to nodes k and l , respectively. The negative sign in Eq. (9) means that forces in the springs are positive for attraction and negative for repulsion. From Eq. (9) it follows that the stiffness, k_{kl} , of the spring element linking nodes k and l reads

$$k_{kl} = -\hat{k}A_{kl}. \tag{10}$$

In contrast to more advanced models (Todt et al., 2011a), this vdW model leads to equal forces on opposite faces of neighboring layers $p_i A_i = p_j A_j = p_{\text{lin}} \frac{A_i + A_j}{2}$, where p_i and p_j are the vdW pressures acting on the layers with areas A_i and A_j , respectively.

2.3.2. Nonlinear van der Waals model

In more advanced simulations the nonlinear behavior of the vdW interactions is taken into account. For this purpose the vdW interactions are modeled in ABAQUS as user defined contact interface UINTER (Pantano et al., 2004; Yao et al., 2008) for which the “contact” stresses in normal and tangential direction have to be defined. Although, the vdW interactions are treated as contact, the layers i and j are still separated by the interlayer distance α . The stresses in normal direction, i.e., the “contact” pressures on neighboring layers, can be directly defined by using either Eq. (6) or Eq. (7). The shear stiffness of the vdW interface is small compared to the normal stiffness and is neglected in the vdW model (Pantano et al., 2004). Therefore, the tangential stresses in the interface are set to zero corresponding to a frictionless “contact” between the layers. To ensure proper convergence characteristics, also the incremental, i.e., tangent interface stiffness matrix $\mathbf{K}^{(l)}$ has to be implemented by the user. The matrix element $K_{ij}^{(l)}$ defines the change in the i -th stress component due to an infinitesimally small perturbation of the j -th component of the array of relative displacements between adjacent layers. Thus, the current component $K_{11}^{(l)}$ is equal to the current stiffness of the vdW bedding in normal direction in terms of a pressure–distance relation

$$K_{11}^{(l)} = \frac{\partial p(\alpha + \Delta\alpha)}{\partial \Delta\alpha}. \tag{11}$$

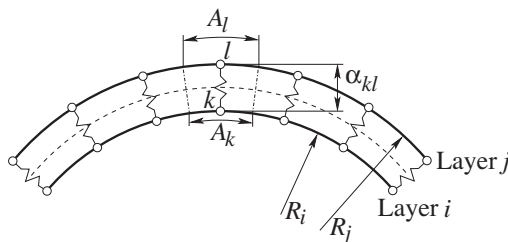


Fig. 2. Areas associated to nodes k and l in curved structures.

All other components of the interface stiffness matrix are set to zero, as the vdW interface is assumed to have zero shear stiffness. Like for the linear vdW model the vdW forces on opposite faces of neighboring layers are equal.

2.4. Simulating the growth of carbon onions

Starting with the outermost layer in the growth simulations seems to be problematic as the size of the carbon onion at its growth limit is a priori not known. Thus, it is assumed that in the model the carbon onion grows layer-by-layer starting with the innermost one.

For the first, i.e., the innermost layer the C60 fullerene is used. This layer is assigned the layer index $i = 1$. Further layers are deposited one after the other. Each new layer $i = N$ with radius $R_N^{(0)}$ in the stress free configuration is concentrically located outside onto the surface of the current onion consisting of $N - 1$ layers. The pressure p_N^s due to the surface stress is applied and kept constant during the whole growth simulation. Usually, the interlayer distance $\alpha_{(N-1),N}^{(0)} = R_N^{(0)} - R_{N-1}$ between layers N and $N - 1$ is not equal to the vdW equilibrium distance α_{eq} . Thus, the new layer N does not exactly fit the onion. Due to this misfit the vdW interactions lead, in combination with the surface stress, to either tensile or compressive stresses in this new layer. Additionally, the stresses in the layers underneath are changed, too. The new equilibrium configuration of the N -layered onion is calculated in a geometrically nonlinear analysis step and evaluated regarding its stability by performing a buckling eigenvalue analysis. The formulation of the eigenvalue problem depends on the type of model used for describing the vdW interactions between adjacent layers.

2.4.1. Simulations with the linear van der Waals model

In the linear vdW model the spring elements between the layers are introduced with a stress free length of $\alpha_{(N-1),N}^{(0)}$. The vdW interactions due to $\alpha_{(N-1),N}^{(0)} \neq \alpha_{\text{eq}}$ are calculated using Eq. (9) and are, like the surface stress being active in layer N , considered as perturbation loads in the buckling eigenvalue prediction. The corresponding eigenvalue problem reads

$$\left(\mathbf{K}_{N-1} + \tilde{\lambda}_N^j \Delta \tilde{\mathbf{K}}_N \right) \tilde{\Phi}_N^j = \mathbf{0}. \tag{12}$$

In Eq. (12) \mathbf{K}_{N-1} is the tangent stiffness matrix of the system with N layers including the effects of the surface stress and the vdW forces acting in the configuration of the carbon onion with $N - 1$ layers. The matrix $\Delta \tilde{\mathbf{K}}_N$ represents the contribution of the vdW interactions between layer $N - 1$ and N and the surface stress in layer N . The parameters $\tilde{\lambda}_N^j$ are the eigenvalues and $\tilde{\Phi}_N^j$ are the corresponding eigenfunctions. The smallest eigenvalue $\tilde{\lambda}_N^1$ is the factor by which the contribution of the N -th layer has to be multiplied in order to bring the onion consisting of N layers to an unstable state. Thus, layer N cannot be added without surpassing the stability limit if $\tilde{\lambda}_N^1 < 1.0$. The corresponding eigenvector $\tilde{\Phi}_N^1$ characterizes the buckling mode of the N -layered carbon onion.

2.4.2. Simulations with the nonlinear van der Waals model

In the nonlinear vdW model the vdW interactions due to the difference $\alpha_{(N-1),N}^{(0)} \neq \alpha_{\text{eq}}$ become active directly after the new layer is added. They are, thus, not available as perturbation loads in the eigenvalue buckling prediction. To overcome this problem an external pressure $p_N^{(\text{ext})}$ is applied to the outermost layer N in the stability analysis. The pressure $p_N^{(\text{ext})}$ is defined to be equal to the critical pressure p_i^* of this layer without its supporting layers underneath and is calculated with Eq. (1). The choice of $p_N^{(\text{ext})} = p_i^*$ is not based on any necessity but provides information about the effect of bedding due to the inner layers.

The corresponding eigenvalue problem is then defined as

$$\left(\mathbf{K}_N + \bar{\lambda}_N^j \Delta \bar{\mathbf{K}}_N \right) \bar{\Phi}_N^j = \mathbf{0} \quad (13)$$

with \mathbf{K}_N being the tangent stiffness matrix of the N -layered onion in its equilibrium state including the vdW interactions between all N layers. The matrix $\Delta \bar{\mathbf{K}}_N$ represents the change in the stiffness of the onion due to the external pressure $p_N^{(\text{ext})}$. The variables $\bar{\lambda}_N^j$ and $\bar{\Phi}_N^j$ again are the eigenvalues and the corresponding eigenvectors, respectively. For this model the smallest eigenvalue $\bar{\lambda}_N^1$ is the factor by which the pressure $p_N^{(\text{ext})}$ on the outermost layer has to be multiplied to bring the N -layered onion to a critical state. In contrast to the linearized model, $\bar{\lambda}_N^1 = 0$ indicates that the carbon onion has grown to its critical size, whereas $\bar{\lambda}_N^1 < 1$ means that the critical pressure of the onion is equal to or smaller than the buckling pressure of the outermost layer. For the linearized vdW model the eigenvalue analysis is used to check if another layer can be added without provoking a structural instability. For the nonlinear model it is checked if an existing onion is still stable when its outermost layer is subjected to an external pressure $p_N^{(\text{ext})}$. Thus, if $\bar{\lambda}_N^1 = 0$ no external pressure is required to provoke a structural instability. This means that the section forces, i.e., the membrane forces per unit length of section line, introduced due to the mutual accommodation of the layers are then sufficient to evoke buckling and, hence, the onion has grown to its critical size.

3. Results and discussion

3.1. Simulations with the linear van der Waals model

For the linear vdW model adding a further layer to the onion requires only a single linear solution step, leading to low computational requirements. This model is used to check if the surface stress has an influence on a possible growth limit of carbon onions. Furthermore, the number of atoms n_i forming the new layer to be added is calculated in two different ways. (i) It is assumed that every new layer is an icosahedral fullerene where $n_i = 60 i^2$, with i being the layer index. (ii) The new layer belongs either to the group of $n_i = 60 m^2$ or $n_i = 20 k^2$ fullerenes ($k, m \in \mathbb{N}$), where the fullerene with the smallest accommodation effort is chosen. In the following (i) and (ii) are referred to as “pure” and “mixed” configuration, respectively. The linear vdW model used is based on Eq. (6) with $\sigma = 0.3415 \text{ nm}$ (Lu et al., 2009).

The obtained eigenvalues related to buckling are depicted in Fig. 3. An eigenvalue $\bar{\lambda}_N^1 > 1.0$ means that the onion is in a stable equilibrium configuration. On one hand, the surface stress only has an influence on $\bar{\lambda}_N^1$ if the onions consists of less than six layers and, on the other hand, it “stabilizes” the model by preventing the solution from running into the negative peak which represents an artifact. For $N \geq 6$ the influence of the surface stress becomes negligible. The lowest eigenvalue $\bar{\lambda}_N^1$ approaches 1.0, if the onion has

grown to a size of $N = N_{\text{crit}} = 23$ layers, for both configurations independent of the surface stress. As can be seen from Fig. 4 only a few outer layers buckle in an interactive way, whereas the inner layers remain unaffected. The observed buckling mode is comparable to buckling modes observed for complete spheres filled with elastic media (Sato et al., 2012). This confirms the applicability of the axisymmetric model as discussed in Section 2.1.

The difference between pure and mixed configurations becomes obvious if the section forces f_i in the layers (Fig. 5) and the resulting interlayer distances α_{ij} (Fig. 6) are considered. Instead of stresses σ_i stress resultants in terms of section forces $f_i = \sigma_i h$ are used since the layer thickness h is just an effective value, see Section 2.1.

Fig. 5 shows the evolution of the section forces f_i in the individual layers during the growth of the onion. In case of the pure configuration each newly added layer k is first subjected to compressive section forces f_k whether or not the surface stress is considered. During further growth of the onion the compressive section forces are reduced and, if sufficient layers are added, tensile section forces develop in layer k . Thus, only the outer layers of the onion are under compression. The influence of the formation of a new layer on the section forces of the layers underneath vanishes towards the center. At the growth limit $N = N_{\text{crit}}$ only the four outer layers are under compression.

Taking the surface stress into account leads to a relatively large compressive section force in the innermost layer, which is reduced after the second layer is added but does not become a tensile section force during the growth of the onion. In this case also the second layer remains under compression during the growing process. The influence of the surface stress on the section forces f_i vanishes fast with increasing size of the layers, and for layers with $i > 8$ the section forces are unaffected by the surface stress. Although the surface stress introduces substantial compressive section forces in the two innermost layers, it has no influence on the growth limit of the onion. The pressure p^* required to introduce buckling in a layer with radius R scales with $\frac{1}{R^2}$, see Eq. (1). Thus, layers in the outer region of the onion are much more sensitive to buckling than those in the inner region. The radius of the outermost layer R_{23} is about 23 times the radius of the innermost layer $R_1 \approx 0.341 \text{ nm}$ and, therefore, the critical pressure of the innermost layer is about 530 times higher than that of layer $i = 23$. Thus, the influence of the compressive section forces in the inner layers and, hence, the surface stress is negligible, and buckling is introduced in the outer region of the onion.

For the mixed configuration (Fig. 5, right) a newly added layer is not a priori under compression. At the stability limit 11 layers are under compression, not all of them being located in the outer region of the onion. The absolute values of the compressive and tensile section forces are generally higher than those observed for the pure configuration.

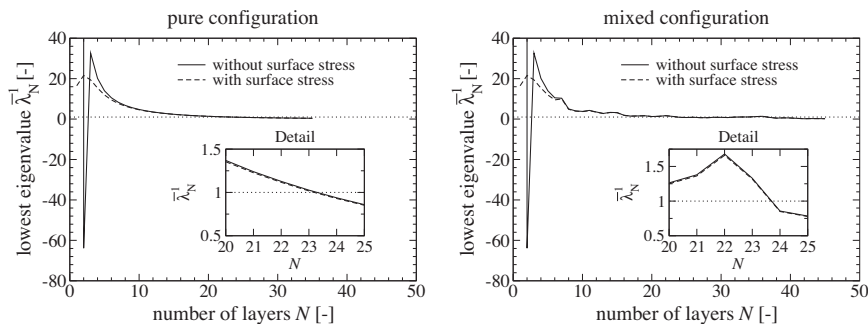


Fig. 3. Lowest eigenvalue $\bar{\lambda}_N^1$ depending on the number of layers N forming a carbon onion for the pure (left) and mixed (right) configuration. Insets show a magnification, when the eigenvalue drops below one, i.e., the onion approaches its stability limit. Left Figure from Todt et al. (2011b), with permission.

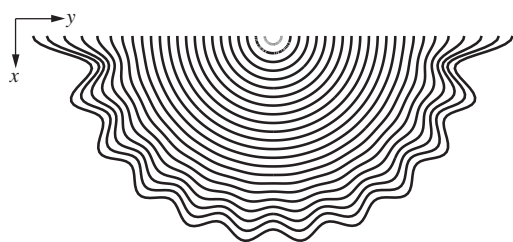


Fig. 4. Buckling mode of a carbon onion of pure configuration corresponding to the lowest eigenvalue $\lambda_N^1 = 1.0$ at the growth limit $N_{crit} = 23$ achieved by using a linear vdW model. From Todt et al. (2011b), with permission.

Fig. 6 shows the current interlayer distances α_{ij} after layer N has been added and the N -layered onion has reached its new equilibrium configuration.

For the pure configuration the interlayer distance $\alpha_{ij}^{(0)} = R_j^{(0)} - R_i$ ($i = j - 1$) between the newly formed layer $j = N$ and the onion consisting of $N - 1$ layers is always larger than the equilibrium distance of the vdW interactions, $\alpha_{eq} = 0.3415$ nm. This leads to attractive vdW forces between the $(N - 1)$ -layered onion and the new layer, introducing compressive section forces in the new layer and tensile section forces in the $N - 1$ layers forming the onion. As a consequence also the interlayer distances in the outer region of the $(N - 1)$ -layered onion increase, whereas the interlayer distances in the inner region remain almost unaffected. All interlayer distances α_{ij} of an N -layered onion in its equilibrium state are larger than α_{eq} , see Fig. 6 (left). The interlayer distances decrease from the inner region of the onion to the outer region, which is in contrast to experimental observations, see e.g. Banhart (1997). However, also in Baowan et al. (2007) a decrease in layer spacing from the inner region to the outer region of a carbon onion is

calculated using analytical continuum mechanical models. The surface stress has an influence on the interlayer distances $\alpha_{1,2}$ and $\alpha_{2,3}$ only. The interlayer distances in the outer region of an N -layered onion are completely unaffected by the surface stress.

For onions of the mixed configuration (Fig. 6, right) the interlayer distances α_{ij} do not decrease continuously from the inner region to the outer region. Generally, the formation of layers j from the series $n_j = 20 \text{ k}^2$ leads to a smaller interlayer distances α_{ij} than the formation of layers belonging to the $n_j = 60 \text{ m}^2$ series and, consequently, to a mixture of interlayer distances being smaller and larger than α_{eq} . The waviness of the interlayer distance curves and the section force curves is a consequence of this.

Although, the interlayer distances and section forces obtained for the pure and mixed configurations are different, both configurations give quite the same growth limit $N_{crit} = 23$ layers. This growth limit is significantly lower than the number of layers found in reality Banhart (1997), Banhart et al. (1997a), Blank et al. (2007), Wesolowski et al. (1997), Zwanger et al. (1996). The reason for the difference between experimentally observed and simulated values of N_{crit} is the simplification of the vdW interactions. The linear vdW model is only valid for interlayer distances α_{ij} close to α_{eq} , but the obtained interlayer distances differ considerably from α_{eq} , see Fig. 6. If α_{ij} is larger than α_{eq} the linear vdW model overestimates the stiffness of the vdW bedding and, as a consequence, the vdW interaction forces between the layers. Thus, the vdW induced section forces in the layers are too high. Since the compressive section forces in the outer layers are responsible for the occurrence of the instability, overestimating these forces introduces the instability too early. This leads to a value N_{crit} which is much lower than the experimentally observed maximum number of layers.

Nevertheless, the linear model shows that the occurrence of a structural instability most likely limits the size of carbon onions.

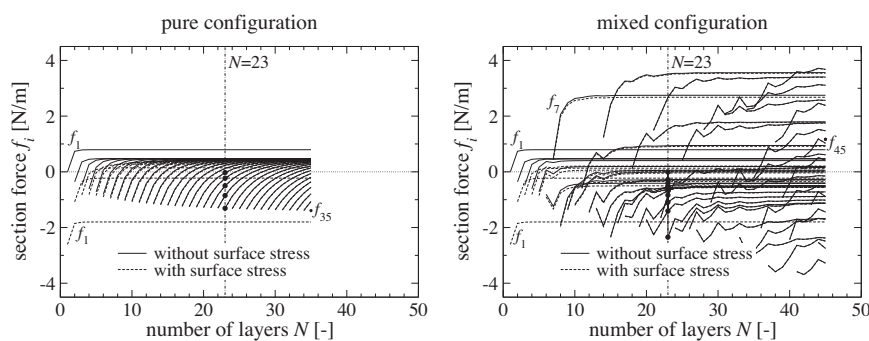


Fig. 5. Section forces f_i in the i layer of an N -layered onion for the pure (left) and mixed (right) configuration. Negative values of f_i denote compression. For $N = 23$, compressive section forces in the layers are marked with • for the case where no surface stress is considered.

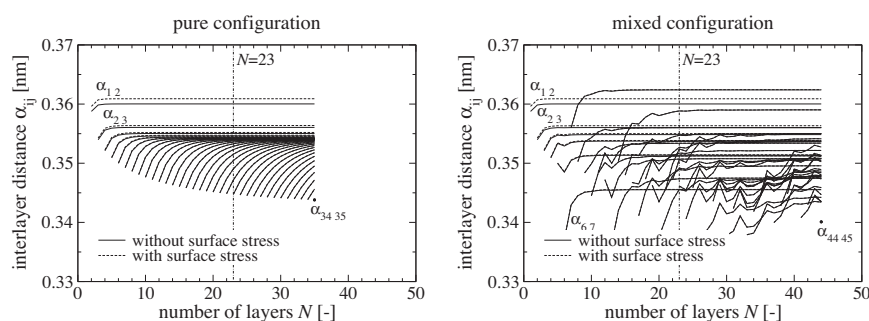


Fig. 6. Interlayer distances α_{ij} between layers i and $j = i + 1$ depending on the number of layers N for the pure (left) and mixed (right) configuration.

The vdW interactions, leading to self-equilibrating stress states in the layers due to mutual accommodation, have shown to be responsible for the loss of stability, whereas the curvature induced surface stress plays only a minor role. Using a nonlinear vdW model should lead to more realistic values of N_{crit} .

3.2. Simulations with the nonlinear van der Waals model

As the vdW interactions are the driving forces behind the growth limit of carbon onions their influence is investigated in more detail. Due to the minor influence of the surface stress on the growth limit it is neglected in the following. Furthermore, it seems to be of no importance if the carbon onion belongs to the pure or mixed configuration. Thus, only onions of pure configuration are considered.

The two different vdW models, given by Eqs. (6) and (7) are used to describe the vdW interactions and are referred to as M1 and M2, respectively. For the required Lennard–Jones parameters σ and ϵ two different sets, S1 ($\sigma = 0.3415$ nm and $\epsilon = 0.00239$ eV (Lu et al., 2009)) and S2 ($\sigma = 0.3345$ nm and $\epsilon = 0.00319$ eV (Zhang et al., 2007)) are taken from literature. The two vdW models M1 and M2 in combination with the parameter sets S1 and S2 lead to four different vdW interfaces which are defined according to Section 2.3.2. The parameters and compressive constants used in the interface definitions are summarized in Table 1.

Fig. 7 shows the results of the computational stability analysis based on Eq. (13) for the different vdW interfaces. A value $\bar{\lambda}_N^1 \geq 1$ indicates that the critical pressure of the onion is larger than the buckling pressure of the outermost layer, i.e., the outermost layer is sufficiently supported by the inner layers to prevent buckling. For a low number of layers the supporting effect becomes larger with increasing layer numbers. After reaching a certain number of layers, the inner layers are still supporting the outermost one, but the effect is reduced by every layer added. The numerical analysis terminates close before $\bar{\lambda}_N^1 = 0$ is reached due to ill-condition of the algebraic system (the matrix \mathbf{K}_N approaches a singularity) describing the boundary value problem which arises when the next layer is added. The abort of the analysis implies that the onion is very close to its stability limit. Thus, the critical size of the onion can be extracted by extrapolation of the eigenvalue curves.

The vdW interface M1S1 is the nonlinear counterpart to the linear vdW interactions used in Section 3.1. For M1S1 a growth limit of $N_{crit} \approx 64$ is estimated which is much larger than the value $N_{crit} = 23$ calculated with the linear model. N_{crit} extracted with the improved interface M1S1 is comparable to numbers of layers of large onions found in experiments (Banhart et al., 1997b). The highest critical number of layers, $N_{crit} \approx 72$, is estimated with the interface M2S1. The vdW interfaces M1S2 and M2S2 show similar eigenvalue curves, and both interfaces lead to $N_{crit} \approx 43$, although the exponents of the vdW models M1 and M2 are different. The corresponding buckling mode of M1S2 at the growth limit is depicted in Fig. 8. The same buckling patterns can be observed for all vdW interfaces. The outermost layers buckle in an interactive way, whereas the inner layers remain almost unaffected. This

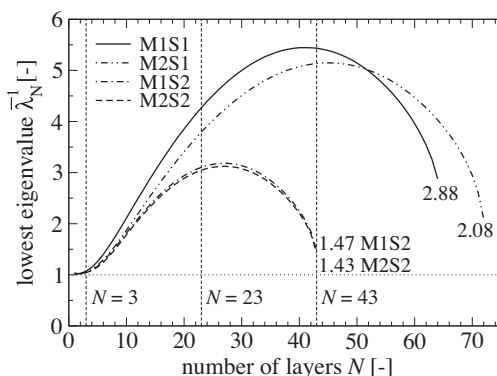


Fig. 7. Lowest eigenvalue $\bar{\lambda}_N^1$ versus the current number of layers N forming the carbon onion. The different curves correspond to the different vdW interface models.

corresponds to the buckling behavior observed already in Section 3.1.

Fig. 9 shows that, a newly added layer $i = N$ is always under compression. Adding further layers reduces the compressive section force in layer N , and if sufficient layers are added a tensile section force develops. If the onion has become large enough, adding of further layers does not lead to a further change in the section force of layer N , anymore, and also its distance to the layer underneath remains unaffected. The number of layers to be added until a tensile section force develops or until the layer remains unaffected by a new layer depends on the position of the layer in the onion. Only layers in the outer region are subjected to compressive section forces and their number increases with the size of the onion. This fact is illustrated in Fig. 10 for M1S1.

Although the qualitative behavior of all models with different nonlinear vdW interfaces is the same, their quantitative behavior is different. A higher value of the compressive constants C_{33} and C_0 leads to higher vdW pressures and, therefore, to higher compressive section forces in the layers, see Fig. 9. Higher vdW pressures are also observed if a smaller vdW equilibrium distance $\alpha_{eq} = \sigma$ is used, as the initial interlayer distance α_{ij} between a newly added layer and the layers underneath is always larger than α_{eq} ; compare M1S1 and M1S2 in Fig. 11. Higher values of the vdW pressures imply that higher compressive section forces are introduced in the outer layers and, hence, evoke the occurrence of a structural instability at lower layer numbers. If the vdW interfaces have (almost) the same compressive constant and vdW equilibrium interlayer distance (e.g., M1S2 and M2S2) the results of the eigenvalue problem, the interlayer distances, and the section forces are almost equal, too. This leads to the conclusion, that the different exponents of the vdW models M1 and M2 have only a minor influence.

The obtained maximum number of layers forming the onions is highly sensitive to the vdW parameters used. Thus, the calculated

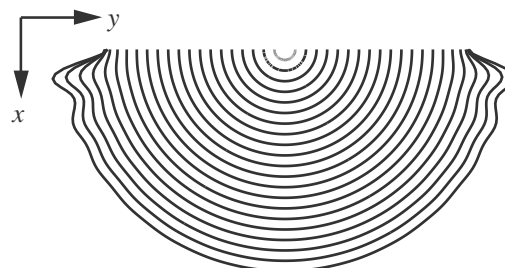


Fig. 8. Buckling mode of a carbon onion modeled with interface M1S2. Only each second layer is displayed.

Table 1 Nonlinear vdW interfaces used in the stability analysis of carbon onions.

Interface	Equation	σ in nm	ϵ in eV	$C_{33}/6$ in GPa	C_0 in GPa
M1S1	(6)	0.3415	0.00239	6.083	–
M2S1	(7)	0.3415	0.00239	–	4.79
M1S2	(6)	0.3345	0.00319	6.083	–
M2S2	(7)	0.3345	0.00319	–	6.26

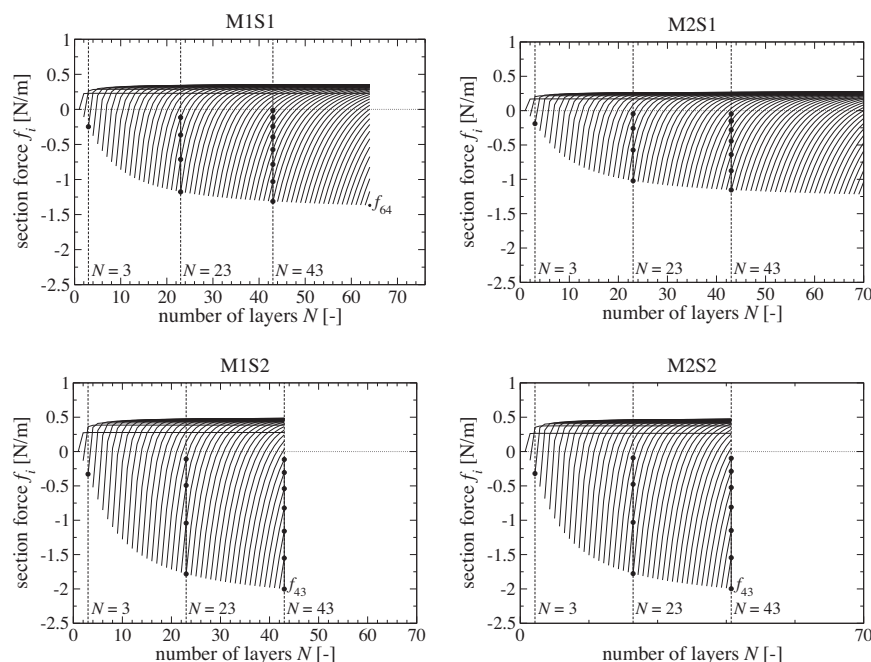


Fig. 9. Section forces f_i in the i layer of an N -layered onion for all vdW interfaces. Negative values of f_i denote compression. Layers under compression are marked with • for $N = 3, 23$ and 43 .

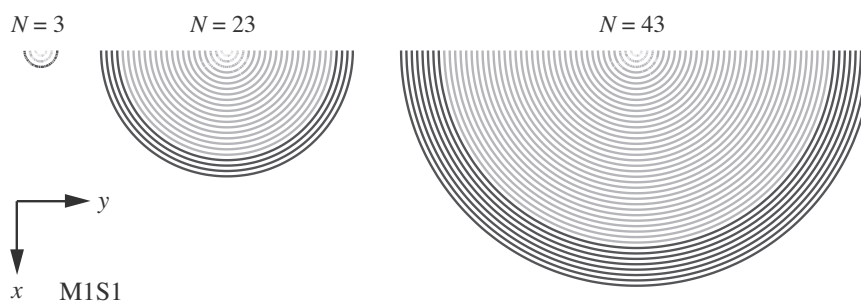


Fig. 10. Number of layers under compression (black) and tension (gray) for onions of different sizes.

growth limits have rather a qualitative than a quantitative character. Nevertheless, the results indicate that the occurrence of a structural instability is a possible explanation for the limited size of carbon onions. The obtained results for N_{crit} are in the range of the sizes of carbon onions observed in experiments (Banhart et al., 1997b), although much larger onions, e.g., consisting of 115 layers (Zwanger et al., 1996), have been observed. Possibly this high layer numbers can be achieved by allowing layers which are not a spherical representation of icosahedral fullerenes. These single layers need not to be thermodynamically stable if isolated, but may lead to a better accommodation of the different layers. This possibility is neglected in the presented model.

4. Conclusion

By using an axisymmetric continuum shell model it is shown that the occurrence of a structural instability is a possible explanation for the limited size of carbon onions. The instability is introduced by self-equilibrating stress states emerging due to accommodation of misfitting carbon layers during the growing process. The stresses are mainly introduced by van der Waals

interactions between adjacent layers, whereas the influence of the curvature induced surface stress has shown to be negligible. Under the assumption that carbon onions grow from the inside to the outside, loss of stability is introduced in the outer layers whereas the innermost layers remain unaffected. Other growing scenarios might lead to different buckling patterns and should be considered in further studies. To obtain reasonable results for the growth limit the nonlinear character of the van der Waals interactions has to be taken into account. The so obtained critical sizes of the onions are highly sensitive to the interlayer distances and compressive constants used in the van der Waals models and, thus, rather have a qualitative than a quantitative character. To obtain a better representation of reality also the assumption of the layers being icosahedral fullerenes should be abandoned in further studies. Nevertheless, the used models clearly indicate a growth limit of carbon onions and can serve as basis for further investigations concerning the growth of such particles.

Acknowledgments

The first author, Melanie Todt, is grateful for funding by the fFORTE WIT – Women in Technology Program of the Vienna

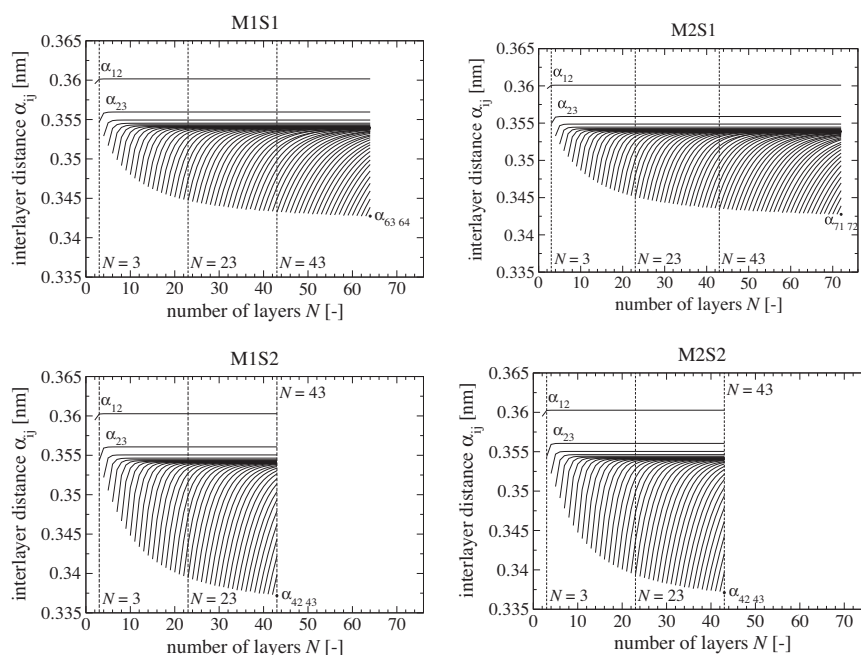


Fig. 11. Interlayer distances α_{ij} between layers i and $j = i + 1$ depending on the number of layers N for all vdW interfaces.

University of Technology and the Austrian Federal Ministry of Science and Research.

Appendix A. Supplementary data

Supplementary data associated with this article can be found, in the online version, at <http://dx.doi.org/10.1016/j.ijsostr.2013.10.038>.

References

- Banhart, F., 1997. The transformation of graphitic onions to diamond under electron irradiation. *J. Appl. Phys.* 81, 3440–3445.
- Banhart, F., Ajayan, P.M., 1996. Carbon onions as nanoscopic pressure cells for diamond formation. *Nature* 382, 433–435.
- Banhart, F., Füller, T., Redlich, P., Ajayan, P., 1997a. The formation, annealing and self-compression of carbon onions under electron irradiation. *Chem. Phys. Lett.* 269, 349–355.
- Banhart, F., Füller, T., Redlich, P., Ajayan, P.M., 1997b. The formation, annealing and self-compression of carbon onions under electron irradiation. *Chem. Phys. Lett.* 269, 349–355.
- Baowan, D., Thamwattana, N., Hill, J., 2007. Continuum modelling of spherical and spheroidal carbon onions. *Eur. Phys. J. D* 44, 117–123.
- Baughman, R., Zakhidov, A., de Heer, W., 2002. Carbon nanotubes – the route toward applications. *Science* 297, 787–792.
- Blank, V.D., Denisov, V.N., Kirichenko, A.N., Kulnitskiy, B.A., Yu Martushov, S., Mavrin, B.N., Perezhogin, I.A., 2007. High pressure transformation of single-crystal graphite to form molecular carbon-onions. *Nanotechnology* 18, 345601.
- Cadelano, E., Palla, P., Giordano, S., Colombo, L., 2009. Nonlinear elasticity of monolayer graphene. *Phys. Rev. Lett.* 102, 235502.
- Drmot, M., Scheidl, R., Troger, H., Weinmüller, E., 1987. On the imperfection sensitivity of complete spherical shells. *Comput. Mech.* 2, 63–74.
- Du, A.B., Liu, X.G., Fu, D.J., Han, P.D., Xu, B.S., 2007. Onion-like fullerenes synthesis from coal. *Fuel* 86, 294–298.
- Fischer, F.D., Waitz, T., Vollath, D., Simha, N.K., 2008. On the role of surface energy and surface stress in phase-transforming nanoparticles. *Prog. Mater. Sci.* 53, 481–527.
- Fu, D., Liu, X., Lin, X., Li, T., Jia, H., Xu, B., 2007. Synthesis of encapsulating and hollow onion-like fullerenes from coal. *J. Mater. Sci.* 42, 3805–3809.
- Geim, A.K., 2009. Graphene: status and prospects. *Science* 324, 1530–1534.
- Geim, A.K., Novoselov, K.S., 2007. The rise of graphene. *Nat. Mater.* 6, 183–191.
- Hartmann, M., Todt, M., Rammerstorfer, F., Fischer, F., Paris, O., 2013. Elastic properties of graphene obtained by computational mechanical tests. *Europhys. Lett.* 103, 68004.
- He, X.Q., Kitipornchai, S., Liew, K.M., 2005. Buckling analysis of multi-walled carbon nanotubes: a continuum model accounting for van der Waals interaction. *J. Mech. Phys. Solids* 53, 303–326.
- Hirata, A., Igarashi, M., Kaito, T., 2004. Study on solid lubricant properties of carbon onions produced by heat treatment of diamond clusters or particles. *Tribol. Int.* 37, 899–905.
- Holec, D., Hartmann, M.A., Fischer, F.D., Rammerstorfer, F.G., Mayrhofer, P.H., Paris, O., 2010. Curvature-induced excess surface energy of fullerenes: density functional theory and Monte Carlo simulations. *Phys. Rev. B* 81, 235403.
- Huang, Y., Wu, J., Hwang, K., 2006. Thickness of graphene and single-wall carbon nanotubes. *Phys. Rev. B* 74, 245413.
- Iijima, S., 1991. Helical microtubules of graphitic carbon. *Nature* 354, 56–58.
- Joly-Pottuz, L., Matsumoto, N., Kinoshita, H., Vacher, B., Belin, M., Montagnac, G., Martin, J.M., Ohmae, N., 2008. Diamond-derived carbon onions as lubricant additives. *Tribol. Int.* 41, 69–78.
- Kelly, B., 1981. *Physics of Graphite*. Advanced Science Publishers, pp.79–80.
- Kroto, H.W., 1992. Carbon onions introduce new flavour to fullerene studies. *Nature* 359, 670–671.
- Kroto, H.W., Heath, J.R., O'Brien, S.C., Curl, R.F., Smalley, R.E., 1985. C60: Buckminsterfullerene. *Nature* 318, 162–163.
- Kuznetsov, V.L., Chuvilin, A.L., Butenko, Y.V., Malkov, I.Y., Titov, V.M., 1994. Onion-like carbon from ultra-disperse diamond. *Chem. Phys. Lett.* 222, 343–348.
- Liu, F., Ming, P., Li, J., 2007. Ab initio calculation of ideal strength and phonon instability of graphene under tension. *Phys. Rev. B* 76, 064120.
- Los, J.H., Pineau, N., Chevrot, G., Vignoles, G., Leyssale, J.M., 2009. Formation of multiwall fullerenes from nanodiamonds studied by atomistic simulations. *Phys. Rev. B* 80, 155420.
- Lu, W.B., Liu, B., Wu, J., Xiao, J., Hwang, K.C., Fu, S.Y., Huang, Y., 2009. Continuum modeling of van der Waals interactions between carbon nanotube walls. *Appl. Phys. Lett.* 94, 101917.
- Macutkevic, J., Seliuta, D., Valusis, G., Banys, J., Kuzhir, P., Maksimenko, S., Kuznetsov, V., Moseenkov, S., Shenderova, O., Lambin, Ph., 2009. Dielectric properties of onion-like carbon based polymer films: experiment and modeling. *Solid State Sci.* 11, 1828–1832.
- Novoselov, K.S., Geim, A.K., Morozov, S.V., Jiang, D., Zhang, Y., Dubonos, S.V., Grigorieva, I.V., Firsov, A.A., 2004. Electric field effect in atomically thin carbon films. *Science* 306, 666–669.
- Pantano, A., Parks, D.M., Boyce, M.C., 2004. Mechanics of deformation of single- and multi-wall carbon nanotubes. *J. Mech. Phys. Solids* 52, 789–821.
- Pflüger, A., 1975. *Stabilitätsprobleme der Elastostatik*. Springer-Verlag, Berlin.
- Redlich, P., Banhart, F., Lyutovich, Y., Ajayan, P.M., 1998. EELS study of the irradiation-induced compression of carbon onions and their transformation to diamond. *Carbon* 36, 561–563.
- Sato, M., Wade, M.A., Iiboshi, K., Sekizawa, T., Shima, H., 2012. Buckling patterns of complete spherical shells filled with an elastic medium under external pressure. *Int. J. Mech. Sci.* 59, 22–30.
- Tang, A.C., Huang, F.Q., 1995a. Stability rules of icosahedral (Ih or I) fullerenes. *Chem. Phys. Lett.* 247, 494–501.
- Tang, A.C., Huang, F.Q., 1995b. Theoretical study of multishell fullerenes. *Phys. Rev. B* 52, 17435–17438.

- Todt, M., Hartmann, M.A., Rammerstorfer, F.G., 2013. Continuum shell models for closed cage carbon nanoparticles. In: Pietraszkiewicz, W., Górski, J. (Eds.), *Shell Structures: Theory and Applications*, vol. 3. CRC-Press, London, pp. 149–152.
- Todt, M., Rammerstorfer, F., Paris, O., Fischer, F., 2010. Nanomechanical studies of the compressive behavior of carbon fibers. *J. Mater. Sci.* 45, 6845–6848.
- Todt, M., Rammerstorfer, F.G., Fischer, F.D., Mayrhofer, P.H., Holec, D., Hartmann, M.A., 2011a. Continuum modeling of van der Waals interactions between carbon onion layers. *Carbon* 49, 1620–1627.
- Todt, M., Rammerstorfer, F.G., Hartmann, M.A., Paris, O., Fischer, F.D., 2011b. Shell-models for multi-layer carbon nano-particles. In: Altenbach, H., Eremeyev, V. (Eds.), *Advanced Structured Materials: Shell-like Structures*. Springer-Verlag, Berlin, pp. 585–602.
- Tomita, S., Burian, A., Dore, J.C., LeBolloch, D., Fujii, M., Hayashi, S., 2002. Diamond nanoparticles to carbon onions transformation: X-ray diffraction studies. *Carbon* 40, 1469–1474.
- Ugarte, D., 1992. Curling and closure of graphitic networks under electron-beam irradiation. *Nature* 359, 707–709.
- Ugarte, D., 1995. Onion-like graphitic particles. *Carbon* 33, 989–993.
- Voytekhovskiy, Y.L., 2003. A formula to estimate the size of a fullerene. *Acta Crystallogr. A* 59, 193–194.
- Wesolowski, P., Lyutovich, Y., Banhart, F., Carstanjen, H., Kronmüller, H., 1997. Formation of diamond in carbon onions under MeV ion irradiation. *Appl. Phys. Lett.* 71, 1948–1950.
- Yakobson, B.I., Brabec, C.J., Bernholc, J., 1996. Nanomechanics of carbon tubes: Instabilities beyond linear response. *Phys. Rev. Lett.* 76, 2511–2514.
- Yao, X., Han, Q., Xin, H., 2008. Bending buckling behaviors of single- and multi-walled carbon nanotubes. *Comput. Mater. Sci.* 43, 579–590.
- Zhang, D., Akatyeva, E., Dumitrică, T., 2011. Bending ultrathin graphene at the margins of continuum mechanics. *Phys. Rev. Lett.* 106, 255503.
- Zhang, H., Wang, L., Wang, J., 2007. Computer simulation of buckling behavior of double-walled carbon nanotubes with abnormal interlayer distances. *Comput. Mater. Sci.* 39, 664–672.
- Zhao, M., Song, H., Chen, X., Lian, W., 2007. Large-scale synthesis of onion-like carbon nanoparticles by carbonization of phenolic resin. *Acta Mater.* 55, 6144–6150.
- Zhao, Y., Spain, I., 1989. X-ray diffraction data for graphite to 20 GPa. *Phys. Rev. B* 40, 993–997.
- Zwanger, M.S., Banhart, F., Seeger, A., 1996. Formation and decay of spherical concentric-shell carbon clusters. *J. Cryst. Growth* 163, 445–454.

Atomistic and continuum modelling of graphene and graphene-derived carbon nanostructures

Markus A. Hartmann ^{*} and Melanie Todt [†] and F.G. Rammerstorfer [†]

^{*} Institute of Physics, Montanuniversität Leoben, Franz-Josef Strasse 18, 8700 Leoben, Austria

[†] Institute of Lightweight Design and Structural Biomechanics, Vienna University of Technology, Getreidemarkt 9, 1060 Vienna, Austria

1 Introduction

Nanometer sized particles formed by carbon atoms mainly arranged in a hexagonal atomic structure are called carbon nanostructures (CNS). In this chapter we focus exclusively on *sp*²-bonded CNS that include graphene (Geim, 2009; Geim and Novoselov, 2007), single- and multi-walled carbon nanotubes (Iijima, 1991; Pantano et al., 2004), fullerenes (Kroto et al., 1985), and carbon onions (Banhart and Ajayan, 1996; Kroto, 1992; Ugarte, 1992, 1995). Especially graphene has drawn a lot of attention within the last years, because it possesses exceptional mechanical and electrical properties (Geim, 2009; Novoselov et al., 2004) and a high thermal conductivity (Lau et al., 2012). It is the main building block of all other CNS based on *sp*²-bonded carbon, which therefore should inherit its exceptional properties making them promising candidates for applications in the field of structural mechanics and the electronics industry, as fillers in nanocomposites (Choi and Lee, 2012; Baughman et al., 2002; Stankovich et al., 2006) and as solid lubricants (Hirata et al., 2004). This chapter will focus on the amazing mechanical properties of CNS only. Information regarding the extraordinary electronic and thermal properties can be found elsewhere (Novoselov et al., 2004; Castro Neto et al., 2009; Balandin, 2011).

For an expedient and reliable application of CNS their (mechanical) properties have to be well understood. Besides experimental characterization (Banhart and Ajayan, 1996; Iijima, 1991; Kroto et al., 1985) different computational simulation techniques have shown to be powerful tools for investigating the formation and properties of CNS (Chuvilin et al., 2010;

Pantano et al., 2004; Yakobson et al., 1996). The different simulation techniques that can be used range from *ab initio* (first principle) studies to continuum mechanical methods. The choice of the appropriate method mainly depends on the size, i.e., the number of atoms forming the CNS and the property to be investigated.

Ab initio simulations require the solution of the many-body Schrödinger equation, which is a computational expensive task. Therefore, the applicability of this technique is limited to small CNS consisting of a few hundred to thousand atoms. The biggest advantage of this method is that only the atomic number (i.e., the number of electrons) of the involved atoms is required as input. *Ab initio* methods are used, e.g., in (Lier et al., 2000) and (Dumlich and Reich, 2011) to investigate the mechanical properties of CNS and the binding energy and intertube distance of bundles of carbon nanotubes, respectively. In (Dumlich and Reich, 2011) van der Waals (vdW) interactions are considered in the model, which is not a straight forward task in *ab initio* simulations. Workarounds are presented, e.g., in (Dion et al., 2004; Grimme, 2004). *Ab initio* techniques are not further discussed in this chapter, but more details can be found, e.g., in (Dreizler and Gross, 1990; Ruffi-Tabar, 2008).

Classical atomistic simulation methods like Monte Carlo or molecular dynamics give the possibility of investigating larger systems than can be done using *ab initio* techniques. But the quality of the results of these classical methods crucially depends on the quality of the used potentials or force fields. These methods will be discussed in detail in section 2.

Compared to the previously described atomistic simulation techniques the computational requirements of continuum mechanical methods are rather low. This allows the investigation of single and multi-layered CNS consisting of many million atoms. CM methods have shown – within some limits – to be appropriate to investigate the mechanical properties of CNS, see e.g., (Li and Chou, 2003a; Yakobson et al., 1996; Xin et al., 2000) and allow the treatment of vdW interactions in multi-layered CNS (Kelly, 1981; Lu et al., 2009b; Todt et al., 2011). The required input parameters are derived from atomistic simulations (Li and Chou, 2003a; Yakobson et al., 1996; Pantano et al., 2004) and are the subject of intense discussion in the scientific community, see e.g., (Hartmann et al., 2013; Lu et al., 2009a; Pantano et al., 2004; Wu et al., 2008a; Yakobson et al., 1996). Continuum modeling techniques and the determination of appropriate input parameters are discussed in more detail in Section 3.

For the sake of completeness also multi-scale methods are mentioned but not discussed in detail. An exhaustive review of these methods can be found, e.g., in (Liew and Sun, 2010; Liu et al., 2004). Multi-scale methods take

advantage of both, atomistic and continuum mechanical approaches. Thus, they can be used to investigate the mechanical behavior of large CNS, where at specific positions the local atomic configurations are of importance. The main issue of multi-scale approaches lies on the smooth bridging between the atomistic and continuum length scale. A multi-scale approach is, e.g., used in (Xu et al., 2012b) to investigate the crack propagation in a graphene sheet.

2 Monte Carlo Simulations and Molecular Dynamics

In classical physics the state of a many-body system is described by specification of the momenta and positions of all N particles in the system. This information is summarized in a vector r which is an element of the $6N$ -dimensional phase space Γ

$$\Gamma \ni r(t) = \begin{pmatrix} x_1 \\ y_1 \\ z_1 \\ \vdots \\ p_N^x \\ p_N^y \\ p_N^z \end{pmatrix}. \quad (1)$$

Here $x_1, y_1, z_1 \dots x_N, y_N, z_N$ and $p_1^x, p_1^y, p_1^z \dots p_N^x, p_N^y, p_N^z$ describe the three components of the position and the momentum vectors of particles 1 to N and the time dependency of the vector r is explicitly indicated. $r(t)$ describes a one-dimensional curve in phase space. This curve is given by Hamilton's equations of motion (that are equivalent to Newton's equations of motion)

$$\begin{aligned} \frac{dp_k}{dt} &= -\frac{\partial H}{\partial x_k} \\ \frac{dx_k}{dt} &= \frac{\partial H}{\partial p_k}, \end{aligned} \quad (2)$$

with the Hamilton function

$$H(p, x) = \sum_{k=1}^{3N} \frac{p_k^2}{2m} + \sum_{i=1}^N U_i(x_j). \quad (3)$$

The Hamilton function gives nothing else than the total energy of the system. The first sum gives the kinetic energy of the system, while the second

sum corresponds to the potential energy. While the kinetic energy depends solely on the momenta (velocities) of the particles, the potential energy depends on the positions of the particles in the system. This is why this part is also called the configurational part of the energy. It is the quality of the potential used that largely determines the reliability of the results obtained from a molecular dynamics or Monte Carlo simulation. The different types of potentials used for the simulation of CNS will be discussed in Chapter 2.3

In principle, when the interactions between the particles are defined, then Equations (2) to (3) suffice to calculate the time evolution of the system and, thus, to know the system in every detail, i.e. to calculate the positions and the momenta of the particles at all times starting from an initial configuration. This route taken is what classical molecular dynamics is doing: macroscopic variables like energy, pressure or density are obtained by performing a time average over the microscopic trajectories. In contrast, Monte Carlo simulations produce a sequence of states of the system, where in equilibrium each state occurs with its proper Boltzmann weight. Macroscopic parameters are then determined by an ensemble average. It should be noted that while molecular dynamics also gives the time evolution of a system (in particular, the route the system takes to equilibrium), the results of Monte Carlo simulations are strictly valid only when the system has reached equilibrium.

This chapter can only very briefly introduce the two methods. For more detailed information the interested reader is referred to textbooks on this topic, e.g., the excellent treatise (Landau and Binder, 2009) or (Frenkel and Smit, 2002).

2.1 Molecular dynamics simulations

Molecular dynamics starts from Equations 2. The equations of motion are then numerically integrated. This means that the result of a MD simulation is the vector $r(t)$ as given in Equation (1). When this trajectory is known, then any desired quantity can be obtained by performing an average over the obtained configurations. This kind of average corresponds to a time average. Many different algorithms exist that allow an efficient integration of the equations. The most famous is probably the Verlet Algorithm (Verlet, 1967). Here the positions a time step Δt ahead can be calculated via

$$x_i(t + \Delta t) = 2x_i(t) - x_i(t - \Delta t) + \frac{F_i(t)}{m_i} \Delta t^2 + O(\Delta t^4), \quad (4)$$

with $F_i(t)$ the total force exerted on particle i from all other particles and external forces. The forces can be calculated from the potential by building the negative gradient

$$F_i(t) = -\nabla V(x_1, \dots, x_{3N}). \quad (5)$$

Note, that to calculate the new positions the positions of the particles at time step t and $t - \Delta t$ are needed.

One of the most common variants of the MD method is to change from the microcanonical ensemble of constant energy as described above to the canonical ensemble of constant temperature. Here the Andersen or the Nosé-Hoover thermostat are two of the most common methods to switch between the ensembles (Frenkel and Smit, 2002).

2.2 Monte Carlo simulations

Another approach taken is the Monte Carlo method. Here one considers a system in contact with a heat bath at temperature T . The probability of finding the system with an energy U is given by

$$p(U) = \frac{1}{Z} \exp\left(-\frac{U}{k_B T}\right), \quad (6)$$

with the normalization

$$Z = \sum_r \exp\left(-\frac{U_r}{k_B T}\right), \quad (7)$$

where the sum runs over all possible configurations of the system. $Z(V, T, N)$ is called the *canonical partition sum* of the system and contains all thermodynamic information of the system. In particular Z is connected to the free energy $F(V, T, N)$ of the system via

$$F(T, V, N) = -k_B T \ln Z(V, T, N). \quad (8)$$

Only for very simple systems it is possible to calculate the partition sum analytically. These special cases include non-interacting particles like the ideal gas or non-interacting spins in an external field.

Direct estimation of the partition sum via numerical integration in a computer simulation is often not possible. The problem is twofold. First, already for a small number of particles the number of grid points, where the function has to be evaluated, becomes astronomically large. A regular grid of P points per phase space dimension results in P^{3N} grid points. Thus, for $N = 100$ particles and only 10 points per dimension the sum in

Equation (7) has to be evaluated at 10^{300} points. Second, the partition function is sharply peaked and non-zero only in a limited region in phase space. This is a direct consequence of the central limit theorem and the law of large numbers. Consequently, the mesh has to be very fine to resolve these details of the partition sum.

Monte Carlo simulations give a possibility to circumvent these problems. The idea is not to sample all regions of phase space with equal probability, but to sample regions of phase space in which the partition sum is not negligible small with higher weight. This concept is called Importance Sampling. Of course there is also a drawback. It is not possible to calculate the partition sum itself, but observables of the kind

$$\langle A \rangle = \frac{\sum_r A_r \exp\left(-\frac{U_r}{k_B T}\right)}{\sum_r \exp\left(-\frac{U_r}{k_B T}\right)}. \quad (9)$$

The idea is to generate a so-called Markov chain. This is a successive chain of states of the system in which the single states occur with their proper Boltzmann weight. Thus, the averaging procedure simplifies to a standard mean

$$\langle A \rangle = \frac{1}{n} \sum_{i=1}^n A_i, \quad (10)$$

with A_i the value of the observable in the i -th configuration of the system.

Generating a Markov chain with these properties can be done in several ways. Most importantly the algorithm has to fulfill detailed balance. This means that the algorithm must not destroy equilibrium once it is reached. This is achieved when on average all jumps out of a special configuration are exactly canceled by the jumps in this configuration from all other configurations. Detailed balance now poses an even stronger condition that is more easily implemented in a computer code. The jumps out of a configuration o into a new configuration n have to be exactly canceled by the jumps from n to o . One of the most prominent algorithms fulfilling detailed balance is the Metropolis Algorithm (Metropolis and Ulam, 1949; Metropolis et al., 1953). Here one chooses a new configuration, mostly by a small perturbation of the current configuration. Then the energy of the current and the new configuration is evaluated. The new configuration is accepted with probability

$$p = \min \left\{ 1, \exp \left(-\frac{\Delta U}{k_B T} \right) \right\}. \quad (11)$$

2.3 Potentials for carbon

As stated before the quality of the results of atomistic simulations crucially depends on the quality of the potentials/force fields used in the simulations to describe the interactions of the particles. In the following some of the most prominent examples of potentials used for the description of CNS will be introduced. These potentials can be roughly classified in two groups: non-reactive force fields that do not allow for changes in bond coordination and reactive force fields that do so. The free parameters of these force fields can be obtained by *ab initio* calculations or semi-empirically by fitting the potential functions to known experimental data like elastic constants or phonon frequencies.

Non-reactive force fields One way to derive a classical potential for carbon (and other covalently bonded structures) is to start from a Taylor expansion of the full potential

$$\begin{aligned}
 U &= \sum_i U_1(x_i) + \sum_{j<i} U_2(x_i, x_j) + \sum_{k<j<i} U_3(x_i, x_j, x_k) + \\
 &+ \sum_{l<k<j<i} U_4(x_i, x_j, x_k, x_l) + \dots \quad (12)
 \end{aligned}$$

Here the first, i.e. single-body term U_1 corresponds to an external potential. The second, i.e. two-body term U_2 is corresponding to a pair potential describing bond stretching. The three coordinates involved in the three-body term U_3 define an angle and, thus, correspond to changes in energy due to changes of the bond angle. The four-body term U_4 corresponds to the torsion angle that is defined as the angle between the planes containing atoms (x_i, x_j, x_k) and atoms (x_j, x_k, x_l) . The functional form of these potentials are normally given by a Morse potential for the stretching term, a harmonic bending term and a dihedral torsion term

$$U_2(r) = E_0 \left[\left(1 - e^{-\beta(r-r_0)} \right)^2 - 1 \right] \quad (13)$$

$$U_3(\theta_{ijk}) = \frac{1}{2} k_\theta (\cos \theta_{ijk} - \cos \theta_0)^2 \quad (14)$$

$$U_4(\phi_{ijkl}) = \frac{1}{2} k_\phi (1 - \cos 2\phi_{ijkl}), \quad (15)$$

here E_0 is the binding energy of the structure, r and r_0 are the actual and the equilibrium bond distance, respectively, and β is a measure for the width of the stretching potential. k_θ is the bending constant and θ_{ijk} and

θ_0 the actual and equilibrium bond angle, respectively. k_ϕ and ϕ_{ijkl} are the torsion constant and the torsion angle, respectively.

The parameters needed in this potential can be obtained by performing *ab initio* calculations on the structures and fits to these results. An example for this strategy can be found in (Maple et al., 1994; Holec et al., 2010). Another possibility is to fit these expressions to experimental data like lattice constants, elastic constants and phonon frequencies, respectively. Famous examples include the DREIDING (Mayo et al., 1990; Guo et al., 1991), CHARMM (Brooks et al., 1983) and AMBER (Weiner et al., 1984; Cornell et al., 1995) force fields. The major advantage of such potentials is that they are easy to implement and relatively low in computational cost. One disadvantage is that they do not allow for changes in bond coordination of the atoms involved. One possibility to circumvent this problem is discussed in the next section.

Reactive Empirical Bond Order (REBO) Potentials These potentials were developed starting from the 80ies to take also into account changes in the bond coordination. Pure pair potentials always lead to closed packed structures. It was Abell who made the observation that the strength of individual bonds decreases when the coordination of an atom increases (Abell, 1985). Thus, there is a trade-off of having either few strong or many weak bonds. If there is a weak dependence of bond strength on coordination then closed packed structures, i.e. structures with a maximum number of neighbors, are favored, while a strong dependence of bond strength on coordination favors dimers, i.e. having only one neighbor. This is the principal idea of the family of so called reactive empirical bond order (REBO) potentials that were first introduced by Tersoff (Tersoff, 1988b,a).

The proposed form of the potential is given by

$$U_{REBO} = \sum_{\langle ij \rangle} f_c [f_R(r_{ij}) + b_{ij} f_A(r_{ij})], \quad (16)$$

where the sum runs over all pairs of atoms i and j that have a distance of r_{ij} . f_c is a smooth cutoff function taking into account the short range character of covalent bonds. In molecular dynamics, where the derivative of the potential functions (the force) enters in the main equations (see Equations (4) and (5)) it is beneficial to use a smooth (differentiable) cutoff instead of a simple step function to keep the forces finite. Tersoff proposes the

following form of the cutoff (Tersoff, 1988b)

$$f_c(r_{ij}) = \begin{cases} 1 & r_{ij} < R \\ \frac{1}{2} \left(1 + \cos \left[\pi \frac{r_{ij}-R}{S-R} \right] \right) & R < r_{ij} < S, \\ 0 & r_{ij} > S \end{cases}, \quad (17)$$

with R and S being two constants (see Table 1). This cutoff ensures that two atoms that are closer than R together interact completely, while particles a distance larger than S apart do not have any interaction. f_c is interpolating smoothly between these two regimes.

The two functions f_R and f_A correspond to the repulsive and attractive part of the potential, respectively. Motivated by the general exponential distance dependence of atomic orbitals they are chosen as Morse like functions

$$f_R(r_{ij}) = A \exp(-\lambda r_{ij}) \quad (18)$$

$$f_A(r_{ij}) = -B \exp(-\mu r_{ij}), \quad (19)$$

with A , B , λ and μ being constants (see Table 1).

Finally, b_{ij} is the term that takes into account bond order. b_{ij} is chosen such that it effectively reduces the attractive part of the potential when the number of neighbors of a given atom increases

$$b_{ij} = (1 + \beta^n \zeta_{ij}^n)^{-1/2n} \quad (20)$$

$$\zeta_{ij} = \sum_{k \neq i, j} f_c(r_{ik}) g(\theta_{ijk}) \quad (21)$$

$$g(\theta_{ijk}) = 1 + \frac{c^2}{d^2} - \frac{c^2}{d^2 + (h - \cos \theta_{ijk})^2}. \quad (22)$$

Here β , n , c , d and h are constants (see Table 1). For any pair of atom $\langle ij \rangle$ the sum runs over all atoms k (excluding the atoms i and j) inside the cutoff region of atom i and θ_{ijk} is the angle defined by the three atoms.

One of the advantages of the REBO potential is that the bond order may change in the course of the simulation. This means also that bonds may open and reform and that the covalent network may evolve.

More recent refinements of the original potential given by Tersoff is the Tersoff-Brenner potential that corrects for overbinding of radicals (Brenner, 1990), the 2nd Generation REBO, where improved analytical functions are used (Brenner et al., 2002) and the AIREBO (Adaptive Intermolecular REBO) potential that includes also non-bonded and dihedral interactions (Stuart et al., 2000).

Table 1. Parameters of the Tersoff potential for carbon.

A	1393.6 eV
B	346.74 eV
λ	3.4879 Å
μ	2.2119 Å
β	1.572×10^{-7}
n	0.72751
c	38049
d	4.3484
h	-0.57058
R	1.8 Å
S	2.1 Å

3 Continuum Mechanics

If continuum mechanics is used for modeling CNS, the atomic layers are represented using continuum structures. These continuum structures can be either beams and/or trusses (Meo and Rossi, 2006; Li and Chou, 2003a; Sakhaee-Pour, 2009) representing the interatomic bonds or continuum shells (Pantano et al., 2004; Yakobson et al., 1996) describing the overall layer behavior. Both concepts are briefly described in the following sections, where the focus of this review is on continuum shell models of CNS.

In general the resulting boundary value problem is solved using the finite element (FE) method. For continuum shell models an analytical treatment of the mechanical behavior of single and multi-layer CNS is possible within certain limits regarding geometry and nonlinearities see, e.g., (Hartmann et al., 2013; Baowan et al., 2007; He et al., 2005). These analytical relations can become rather complex for multi-layer CNS, such that a closed-form analytical solution is not possible. In this case the set of equations has to be solved numerically (Baowan et al., 2007; He et al., 2005).

3.1 Space Frame Models

Space frame models are closely related to MD simulations. Instead of interatomic potentials structural elements like beams, trusses and/or springs are used to describe the interatomic bonds. Truss/spring models are not further considered within this section but are discussed in more detail, e.g., in (Meo and Rossi, 2006; Xu et al., 2013).

In the following, a short overview about beam models is given. Further details can be found, e.g., in (Li and Chou, 2003a). In literature the

continuum beam modeling of atomistic structures is often denoted as lattice structure method (Arghavan and Singh, 2011) or molecular structural mechanics approach (Sakhaee-Pour, 2009). Within this approach each interatomic bond is modeled using a single beam element which usually is assumed to have a circular cross section (Li and Chou, 2003a; Sakhaee-Pour, 2009). The structural properties of the beams are derived from corresponding interatomic potentials used in MC or MD simulations. According to Equation (12) the total potential energy of an atomic system can be split into a bond-stretching, bond bending, and a dihedral torsion term, which are explicitly stated in, e.g., Equations (13) to (15). If small strains are assumed the potentials can be described by simple harmonic forms (Li and Chou, 2003a) reading

$$U_2 = \frac{1}{2}\tilde{k}_S(\Delta r)^2, \quad U_3 = \frac{1}{2}\tilde{k}_\theta(\Delta\theta)^2, \quad U_4 = \frac{1}{2}\tilde{k}_\phi(\Delta\phi)^2. \quad (23)$$

The parameters \tilde{k}_S , \tilde{k}_θ , and \tilde{k}_ϕ denote the bond stretching, bond angle bending, and bond torsional resistance, respectively. The changes in bond length, bond angle and the twisting increment are described by Δr , $\Delta\theta$, and $\Delta\phi$, respectively. Note that \tilde{k}_θ and \tilde{k}_ϕ are the limiting values for small deformations of k_ϕ and k_θ used in Equations (14) and (15), respectively.

Under the assumption of small strains the strain energy contributions of a beam subjected to pure tension, pure bending, and pure torsion take a similar form given as

$$U^S = \frac{1}{2}k^S(\Delta L)^2, \quad U^B = \frac{1}{2}k^B(2\Delta\alpha)^2, \quad U^T = \frac{1}{2}k^T(\Delta\beta)^2, \quad (24)$$

where k_S , k_B , and k_T are the axial, bending, and torsional stiffness of the beam elements, respectively. The quantities ΔL , $\Delta\alpha$, and $\Delta\beta$ denote the change in beam length, the beam bending angle, and the torsional angle of the beam, respectively. More details on the definition of ΔL , $\Delta\alpha$, and $\Delta\beta$ can be found in (Li and Chou, 2003a). Under the assumption of analogous beam and bond deformations, i.e., $\Delta L = \Delta r$, $2\Delta\alpha = \Delta\theta$, and $\Delta\beta = \Delta\phi$, the stiffness properties of the beam are directly obtained by comparing Equations (23) with (24) reading

$$k^S = \tilde{k}_S, \quad k^B = \tilde{k}_\theta, \quad k^T = \tilde{k}_\phi. \quad (25)$$

In contrast to using the stiffness parameters k , as proposed in (Li and Chou, 2003a), a corresponding parameter set consisting of diameter d , Youngs modulus E , and shear modulus G can be obtained leading to (Tserpes and Papanikos, 2005)

$$d = 4\sqrt{\frac{k^B}{k^S}}, \quad E = \frac{(k^S)^2 l}{4\pi k^B}, \quad G = \frac{(k^S)^2 k^T l}{8\pi (k^B)^2}, \quad (26)$$

where l is the length of the beam and therefore, equal to the carbon-carbon bond length. This parameter set has the advantage of a straight forward use in standard FE programs. The force field parameters $k_S = 6.52 \cdot 10^{-7}$ N/nm, $k_B = 8.76 \cdot 10^{-10}$ N nm rad⁻², and $k_T = 2.78 \cdot 10^{-10}$ N nm rad⁻² used in most of the space frame models are usually those used in (Li and Chou, 2003a) and stem originally from (Cornell et al., 1995) and (Jorgensen and Severance, 1990) and were derived for benzene molecules. In (Li and Chou, 2003a) the influence of the choice of k_S and k_B is investigated showing that small deviations of these values are only of minor influence on the overall elastic properties. Furthermore, it is found that k_T has almost no influence on the obtained overall Young's moduli of carbon nanotubes.

The model proposed by Li and Chou (2003a) and the forcefield parameters therein have widely been applied to investigate the mechanical behavior of graphene (Arghavan and Singh, 2011; Li and Chou, 2003a; Sakhae-Pour, 2009; Kordkheili and Moshrefzadeh-Sani, 2013) or carbon nanotubes (Arghavan and Singh, 2011; Li and Chou, 2003a,b; Domínguez-Rodríguez et al., 2014) and to derive the homogenized elastic properties of the atomic layers see, e.g., (Sakhae-Pour, 2009; Kordkheili and Moshrefzadeh-Sani, 2013). The overall elastic parameters derived with the space frame models can be used as input for continuum shell models.

3.2 Shell Models

Continuum shell models for investigating the mechanical behavior of CNS have first been proposed by (Yakobson et al., 1996). The shell properties are expressed in terms of the membrane stiffness C , the bending stiffness D , and the Poisson's ratio ν and have been derived from MD simulations. The considerations made in (Yakobson et al., 1996) are briefly reviewed in the following.

The parameters C and D are derived from energy considerations in which the total energy obtained by MD simulations is assumed to be equal to the strain energy introduced into a continuum model of a carbon nanotube for the same deformation state. For a carbon nanotube subjected to axial compression the induced energy change per atom ΔU_A in a MD simulation can be expressed as

$$\Delta U_A = \frac{1}{2}(\Delta U_A)'' \epsilon_x^2. \quad (27)$$

The quantity $(\Delta U_A)''$ denotes the second derivative of ΔU_A with respect to the axial strain ϵ_x where a value of 59 eV/atom is found for $\Delta U_A''$ in (Yakobson et al., 1996). For the whole nanotube the change in total energy

is obtained as

$$\Delta U = \int_S \rho \Delta U_A dS = \int_S \rho \frac{1}{2} (\Delta U_A)'' \epsilon_x^2 dS, \quad (28)$$

with ρ and S being the atom density per unit area and the surface area of the nanotube, respectively.

For the same loading case the strain energy V_A reads

$$V = \frac{1}{2} \int_S \frac{C}{1 - \nu^2} [(\epsilon_x + \epsilon_y)^2 - 2(1 - \nu)(\epsilon_x \epsilon_y)] dS, \quad (29)$$

where it is assumed that the nanotube is a thin-walled cylindrical shell. In this case V depends only on the axial strain ϵ_x and the circumferential strain ϵ_y . If further the strains are assumed to be small, ϵ_y can be expressed as

$$\epsilon_y = -\nu \epsilon_x, \quad (30)$$

and Equation (29) simplifies to

$$V = \frac{1}{2} \int_S C \epsilon_x^2 dS. \quad (31)$$

A comparison between Equations (28) and (31) leads to (Yakobson et al., 1996)

$$C = \rho (\Delta U_A)'' = 360 \text{ N/m}. \quad (32)$$

The bending stiffness D is estimated under the assumption that a carbon nanotube with radius R is a rolled graphene sheet. The change in total energy $|U_{\text{NT}} - U_{\text{G}}|$, i.e. the difference between the total energy of a carbon nanotube U_{NT} and a planar graphene sheet U_{G} is then equal to the strain energy U_{R} introduced by rolling a graphene sheet. If thin shells are assumed U_{R} can be expressed as

$$U_{\text{R}} = \frac{1}{2} \frac{D}{R^2}, \quad (33)$$

leading finally to a bending stiffness $D = 0.16 \text{ nN nm}$ (Yakobson et al., 1996). The Poisson's ratio $\nu = 0.19$ is evaluated from the change in tube diameter due to axial deformation (Yakobson et al., 1996).

Using the relations

$$C = Eh, \quad D = \frac{Eh^3}{12(1 - \nu^2)}, \quad (34)$$

one obtains a Young's modulus $E = 5500 \text{ N/mm}^2$ and a thickness $h = 0.066 \text{ nm}$. Note that E and h should not be interpreted as quantities with

a real physical meaning but as effective parameters describing the overall mechanical properties of a single carbon layer. In (Xin et al., 2000) it is confirmed that modeling the atomic layer with continuum shells is consistent with atomistic modeling techniques and that the values derived in (Yakobson et al., 1996) are in the correct order of magnitude. In the following the model is denoted as Yakobson-model.

For the Yakobson-model the layers are assumed to possess isotropic linear elastic material behavior, i.e. the model does not account for the chirality of carbon nanotubes. Further, the type of loading seems to have an influence on the elastic parameters (Huang et al., 2006) being also not considered within the Yakobson-model. A more advanced continuum shell model accounting also for the anisotropy and chirality of the nanotubes is proposed, e.g., in (Wu et al., 2008a; Chang, 2010). Inelastic effects are considered in the nonlocal shell model derived in (Ansari and Rouhi, 2012). This analytical model gives a very good representation of the fundamental frequencies of nanotubes if appropriate nonlocal parameters are used (Ansari and Rouhi, 2012). An exhaustive review on nonlocal shell models of carbon nanotubes is given, e.g., in (Arash and Wang, 2012). Such advanced models allow to capture effects not considered in the Yakobson-model, but are in general more complex. For example, the nonlocal shell parameter used in (Arash and Wang, 2012) depends on the size of the nanotube, the boundary conditions, and on the number of layers in a multi-walled carbon nanotube. Therefore, this parameter has to be derived from atomistic models for each tube configuration leading to high computational costs. Further, in (Chang, 2010) it is shown that the influence of chirality on the elastic properties vanishes fast with increasing tube radius. For nanotubes with their diameter being larger than 1 nm this effect is already negligible. Additionally, the assumption of isotropic layers used in the Yakobson-model is admissible as long as small strains (deformations) are considered (Wu et al., 2008b).

Overall, the Yakobson-model seems to give a good representation of the mechanical behavior of CNS as long as the CNS are large enough and if small strains are considered. Continuum shell models have widely been used to investigate the mechanical behavior of CNS like carbon nanotubes (Yakobson et al., 1996; Pantano et al., 2004), graphene (Hartmann et al., 2013), carbon crystallites (Todt et al., 2010), and carbon onions (Todt et al., 2014a).

The elastic parameters of the shells in terms of E , ν , and h derived by various authors differ significantly, see Table 2. This phenomenon is also known as the Yakobson paradox (Shenderova et al., 2002). Good agreement can only be found for the membrane stiffness C , whereas the bending stiffness also seems to be a topic of ongoing discussion. To resolve this paradox,

different solutions were discussed: in (Huang et al., 2006) it was argued that the effective thickness of nanotubes is not constant but depends on the size of the nanotube, its chirality and the loading type. In (Zhang et al., 2011) it was suggested that the Yakobson paradox can be understood by the breakdown of plate theory for a single layer of graphene. It should be noted that the Young's modulus of graphene or carbon nanotubes is often calculated from the membrane stiffness C under the assumption that the thickness of a carbon layer is equal to the interlayer spacing in graphite and, therefore, reads $h = 0.34$ nm (Arghavan and Singh, 2011; Lier et al., 2000; Xu et al., 2012a). This layer thickness leads in combination with the corresponding values of E and ν to a strong overestimation of the bending stiffness obtained, e.g., in (Lu et al., 2009a; Lu and Huang, 2009). However, in (Xu et al., 2012a) it was possible to reproduce nanoindentation experiments conducted in (Lee et al., 2008) with an assumed layer thickness of $h = 0.34$ nm. In the nanoindentation experiments the contribution of the bending deformation to the total strain energy is found to be three orders of magnitude smaller than the contribution due to membrane strains. From this outcome it is concluded that graphene has no intrinsic bending stiffness (Lee et al., 2008). Zero bending stiffness of graphene is also proposed in (Zhang et al., 2011), as bending of a single layer graphene sheet does not lead to a change in the atom-atom distances. However, zero bending stiffness of graphene is in clear contradiction with results obtained in (Cadelano et al., 2010; Lu et al., 2009a; Lu and Huang, 2009). In (Lu et al., 2009a) it is shown that further effects like three-atom bending or four-atom out-of-plane torsion contribute to the total potential energy of the system. In (Nikiforov et al., 2014) the π -orbital axis vector scheme is used to show that graphene has a non-vanishing bending stiffness resulting from the torsional misalignment of the π hybrid orbitals. This contribution can be considered using an additional dihedral-angle term in the 2nd-generation Brenner potential as is done, e.g., in (Lu et al., 2009a). However, this term has to be parameterized appropriately (Nikiforov et al., 2014). Further, in (Nikiforov et al., 2014) it is shown that although continuum plate/shell theory does not correspond to the physical molecular orbital description, it can be used to reproduce the bending behavior of graphene, at least for small strains. In (Xu et al., 2013) the non-zero bending stiffness of graphene is attributed to residual internal moments and not to changes in bond-lengths and used to investigate self-buckling of free standing graphene sheets. This discussion shows that whether or not continuum shell models can be used to describe the mechanical behavior of CNS is far from being clarified. Especially the question which combination of E , h , and ν gives the best description of CNS needs further investigation. Examples for the application of contin-

uum models for investigating the mechanical behavior of CNS and further concepts for obtaining the elastic shell parameters are given in Section 4.

Table 2. Values for C , D , E , h and ν taken from literature.

Method/Structure/Ref.	C [J/m ²]	D [mNm]	E [GPa]	h [nm]	ν [-]
(Arghavan and Singh, 2011) molecular structural mechanics					
graphene, in-plane	-	-	~ 1000	0.34^1	0.16^1
graphene, out-of-plane	-	-	~ 110	0.34^1	0.16^1
(Lee et al., 2008) nanoindentation experiments					
graphene	342 ± 30	0	-	-	-
(Lier et al., 2000) <i>ab initio</i>					
graphene	-	-	1110	0.34^1	-
nanotube $r = 0.344$ nm	-	-	1060	0.34^1	0.125
nanotube $r = 0.369$ nm	-	-	940	0.34^1	0.047
(Lu et al., 2009a) analytically, graphene					
1st gen. Brenner pot.	-	0.133	-	-	-
2nd gen. Brenner pot	-	0.110	-	-	-
incl. dihedral angle effect	-	0.225	-	-	-
(Lu and Huang, 2009) analytically, graphene	340 ± 50	0.255	-	-	0.398
(Pantano et al., 2004) finite element method, nanotubes	363	0.176	4840	0.075	0.19^1
(Sears and Batra, 2004) molecular mechanics, nanotubes					
MM3 ((Allinger et al., 1989))	-	-	2520	0.134	0.21
Tersoff-Brenner	-	-	3100	0.098	0.26
(Wu et al., 2008b) atomistic-based shell theory					
graphene ²	~ 470	~ 0.22	-	-	-
nanotubes ²	~ 480	~ 0.225	-	-	-
(Xin et al., 2000) electronic band theory, nanotubes	377.4 (357.7)	0.183 (0.176)	5100	0.074	0.24
(Xu et al., 2012a) <i>ab initio</i> , graphene	-	-	1030	0.34^1	0.22
(Yakobson et al., 1996) molecular dynamics, nanotubes	363	0.137	5500	0.066	0.19
(Zhang et al., 2011) molecular dynamics, graphite	-	0	1240	0.34^1	0.24
(Hartmann et al., 2013)	324	0.476	2400	0.132	0.1844

¹ Values are assumed in the cited papers.² Values obtained for the unstrained CNS.

3.3 Further aspects

Besides the layer properties, further aspects have to be considered in continuum mechanical modeling of CNS. In multi-layered CNS vdW interactions play an important role, and in curved CNS like carbon nanotubes and carbon onions the curvature induced surface stress has to be considered. Furthermore, the carbon layers are not perfect but contain defects like vacancies or interstitial atoms. In multi-layer CNS these defects may also lead to covalent interlayer bonds which cross-link adjacent layers. All of these aspects are briefly discussed in the following.

Van der Waals interactions In multi-layer CNS the van der Waals (vdW) interactions between adjacent layers result from the vdW interactions between individual atoms making up the layers. vdW interactions are relatively weak compared to the covalent interlayer bonds and result from induced dipole interactions between uncharged atoms. vdW interactions between individual atoms can be described as a function of the atom-atom distance r using a pair potential, e.g., the Lennard-Jones potential (Kelly, 1981)

$$U_{12} = 4\epsilon \left[\left(\frac{\sigma}{r} \right)^{12} - \left(\frac{\sigma}{r} \right)^6 \right], \quad (35)$$

where ϵ and σ are Lennard-Jones parameters describing the depth of the potential well and the atom-atom distance at $U_{12} = 0$, respectively. The first derivative of Equation (35) with respect to r describes the force $F_{12} = -\frac{dU_{12}}{dr}$ between the interacting atoms. If $F_{12} = 0$, i.e., the potential U_{12} possesses a minimum and the two atoms have reached their equilibrium distance $r_0 = 2^{1/6} \sigma$.

In continuum mechanical modeling of CNS, vdW interactions can be either considered using linear or nonlinear springs or trusses or using a nonlinear pressure-distance relation. Truss/spring elements are applicable for space frame models and continuum shell models, whereas pressure-distance relations are only applicable in continuum shell models.

The first attempt is used, e.g., in (Li and Chou, 2003b) and (Kordkheili and Moshrefzadeh-Sani, 2013) where two interacting atoms represented by finite element nodes are connected with a truss/spring element. The stiffness of these elements is derived as the second derivative of the Lennard-Jones potential given by Equation (35) with respect to r . Theoretically, one atom of a layer interacts with all atoms of the adjacent layers meaning that each atom has to be connected with all other atoms by truss or spring elements. As the vdW interactions vanish fast with increasing atom-atom distance usually only interactions between nearest neighboring layers are considered.

Further, only atoms with a maximum distance of approximately 4 to 8 times the equilibrium distance r_0 are taken into account.

For deriving a pressure distance relation the vdW interactions between atoms of adjacent layers can be summed up and related to the surface area of the layers leading, e.g., to

$$p(\alpha) = \frac{C_{33}}{6} \left[\left(\frac{\sigma}{\alpha} \right)^{10} - \left(\frac{\sigma}{\alpha} \right)^4 \right], \quad (36)$$

for graphite, where $C_{33} = 36.5$ GPa is the compressive constant (Kelly, 1981; Zhao and Spain, 1989) and α is the current interlayer distance. If the condition $p(\alpha = \alpha_{\text{eq}}) = 0$ is satisfied two adjacent layers have reached their equilibrium distance. This leads to

$$\alpha_{\text{eq}} = \sigma, \quad (37)$$

being by factor of $2^{1/6}$ smaller than the atom-atom equilibrium distance r_0 . Another possible way of obtaining a pressure-distance relation for planar CNS is to replace the discrete sum by a surface integral and use the atom density per unit area, ρ_∞ , to describe the number of atoms in an infinitesimally small area of the layers, see e.g. (Hamaker, 1937; Lu et al., 2009b; Todt et al., 2011). This approach leads to a different result for graphite as obtained in Equation (36) reading

$$p(\alpha) = C_0 \left[\left(\frac{\sigma}{\alpha} \right)^{11} - \left(\frac{\sigma}{\alpha} \right)^5 \right], \quad (38)$$

with

$$C_0 = 8 \epsilon (\rho_\infty)^2 \sigma \pi. \quad (39)$$

In this approach the compressive constant C_0 depends on the Lennard-Jones parameters and the exponents are different than those in Equation (36). The influence of the differences between Equations (36) and (38) are investigated in more detail in Section 4.3. It should be noted that Equations (38) and (36) lead to the same α_{eq} . The pressure distance relations given by Equations (38) and (36) are both derived for graphite under the assumption that neighboring layers consist of the same number of atoms. In carbon nanotubes or carbon onions the number of atoms is different in adjacent layers. This difference has to be considered in the pressure distance relations. In (He et al., 2005; Ru, 2000; Wang et al., 2003) the curvature effect in carbon nanotubes is considered by assuming that the vdW pressure on opposing faces of adjacent layers is inversely proportional to their radii, leading to $p_{\text{in}} R_{\text{in}} = p_{\text{out}} R_{\text{out}}$. In more advanced approaches like in (Lu

et al., 2009b) for carbon nanotubes or in (Hamaker, 1937; Iglesias-Groth et al., 1997; Todt et al., 2011) for spherical CNS the curvature effect is already considered in the derivation of the pressure-distance relations. In (Lu et al., 2009b) it is shown that the critical pressure of carbon nanotubes is overestimated by 25% or 75% if $p_{\text{in}}R_{\text{in}} = p_{\text{out}}R_{\text{out}}$ or $p_{\text{in}} = p_{\text{out}}$ (graphite relation) are used, respectively, instead of the relation directly considering the different number of atoms in the layers. In (Todt et al., 2011) the influence of the vdW formulation on the equilibrium interlayer distances and on the layer deformation in two-layered carbon onions is investigated. It is shown that although the simplified models lead to the same equilibrium interlayer distance as the model considering the curvature effect, substantial differences could be observed for the layer deformations. In the advanced model the outer layer undergoes larger deformations than the inner layer especially for large fullerenes. This leads also to larger membrane forces in the outer layer, which become of major interest if the structural stability of carbon onions is considered. Concluding it can be said that accounting for the different number of atoms in adjacent layers in the formulation of the vdW model is of great importance, especially if the stability of multi-layer CNS is investigated.

Comparing the nonlinear truss/spring approach with the pressure-distance approach one can say that the truss/spring models are cumbersome from a modeling point of view if large CNS are considered. Nevertheless, truss/spring models offer some advantages. If an atom of one layer is connected by springs/trusses to all other atoms of the adjacent layers the curvature effect is naturally taken into account. Furthermore, the interlayer shear stiffness of the vdW interactions is considered, which is usually neglected when pressure distance relations are used, see e.g., (Pantano et al., 2004; Yao et al., 2008; Todt et al., 2014a). The interlayer shear modulus is in the range of 4 – 5 GPa (Kelly, 1981). Compared to the inplane stiffness of the carbon layers and the vdW stiffness perpendicular to the layers the interlayer shear stiffness is small and becomes only of importance if sliding between adjacent layers occurs, e.g., in (Byrne et al., 2010).

Intra- and interlayer defects CNS are not defect-free. Defects can occur within a single layer or lead to covalent cross linking between the layers. Defects within a single layer can occur as point defects and one dimensional line defects. Point defects are Stone-Wales (SW) defects, single and multiple vacancies, carbon or foreign add atoms, and substitutional impurities. Some of these defects are experimentally observed, e.g., in (Hashimoto et al., 2004; Meyer et al., 2008). The one dimensional line defects comprise dislocation like defects separating two graphene domains with different lattice orien-

tations, see e.g., (Huang et al., 2011; Kim et al., 2011) and defects at the edges of graphene layers involving dangling bonds and the saturation of free atoms with, e.g., hydrogen atoms. Detailed reviews on the different defect types, their structure, their formation, and their influence on the chemical, magnetic, electronic, and mechanical properties can be found, e.g., in (Banhart et al., 2011; Terrones et al., 2012). Methods for the experimental characterization of defects in graphene and graphene based materials are reviewed in (Araujo et al., 2012).

To study the influence of defects on the mechanical properties mainly MD simulations, e.g., (Ansari et al., 2011; Wang et al., 2012; Sharma et al., 2014) or space frame continuum models (Tapia et al., 2012; Tserpes, 2012; Georgantzinos et al., 2012) are used. In (Tapia et al., 2012) a structural mechanics approach is used to show that already a single vacancy defect significantly reduces the fracture strength of graphene but has only minor influence on the Young's modulus. This is in good agreement with the results obtained in (Ansari et al., 2011) using MD simulations and results of (Georgantzinos et al., 2012; Tserpes, 2012) using space frame models. The influence of SW defects on the fracture strength seems to be only of minor importance due to the fact that SW defects annihilate by inverse bond rotation under mechanical loading (Sun et al., 2012). The findings of (Sun et al., 2012) are in contradiction to the results obtained in (Wang et al., 2012) where a significant reduction of the fracture strength due to SW defects is observed. With increasing number of defects also the Young's modulus decreases as shown in (Sharma et al., 2014) for carbon nanotubes. Similar results have been obtained in (Tapia et al., 2012; Tserpes, 2012). Vacancy and SW defects also reduce the axial buckling load of carbon nanotubes, but seem to have only minor influence on the compressive modulus (Eftekhari et al., 2013). In general, SW defects show a stronger influence on the buckling load and the elastic properties than vacancies (Eftekhari et al., 2013). SW defects locally reduce the load carrying capacity of CNTs and lead to a stress and strain concentration around the defect (Chandra et al., 2004). To investigate the local influence of SW defects, atomic scale stress and strain measures are employed in (Chandra et al., 2004), where the strains are formulated in a - from a continuum mechanics point of view - unusual form. It is shown that the stress concentration decreases for higher overall strains, whereas the strain concentration increases. Structures containing defects show a lower overall energy than defect free structures when subjected to mechanical loading (Chandra et al., 2004), which may explain spontaneous defect formation at higher strains. The formation of defects in pristine graphene under mechanical loading is investigated, e.g., in (Wang et al., 2012), revealing that vacancy defects are easier generated than SW

defects. Dewapriya et al. (2014) studied the fracture behavior of graphene in more detail and also investigated the capability of different continuum mechanics based fracture criteria to predict the fracture strength. It turned out that the quantized fracture mechanics approach (Pugno and Ruoff, 2004) captures the fracture strength of graphene quite well (Dewapriya et al., 2014).

In contrast to MD simulations or space frame approaches continuum shell models are less frequently used to investigate the influence of defects in CNS. This is because considering the structure and local influences of the defects is not as straight forward in continuum shell models as in space frame models. In (Zhang et al., 2014) a generalized von Karman equation for flexible solid membranes is utilized to account for topological defects, like heptagonal-pentagonal pairs, via corresponding eigenstrains. The arising set of differential equations is solved using FEM and allows to predict the stress field and the out-of-plane deformations in a graphene sheet under uniaxial and biaxial strains, respectively. (Chen and Chrzan, 2011) use a similar approach where the arising set of differential equations is solved in the Fourier Space. The defects are modeled via topological constraints. The received in-plane strains and out-of-plane deformations due to the defects are in good agreement with results of atomistic simulations. Pentagonal rings increase the local curvature of carbon structures (Cataldo, 2002) and are required to form closed caged structures like fullerenes or carbon onions. SW defects – as combination of two pentagonal and two heptagonal atomic rings – can also increase the sphericity of fullerenes (Terrones and Terrones, 1997). Further, a combination of pentagonal-heptagonal rings might be utilized to design curved graphene structures, such as graphene funnels (Zhang et al., 2014). In (Todt et al., 2014b) a continuum shell model of a C_{240} fullerene is used to investigate the influence of the required 12 pentagonal atomic rings on the membrane stiffness of fullerenes. It is shown that the pentagonal rings lead to a local stiffening of the fullerene structure, which is also observed in MD simulations (Todt et al., 2014b).

Intra-layer defects, such as vacancies or interstitial atoms and dangling bonds at the edges of the graphene layers, can be the source for a formation of covalent interlayer bonds (Telling et al., 2003; Vollath, 2008). Further, nanoindentation of multi-walled nanotubes and multi-layer graphene can give rise to the formation of such bonds (Guo et al., 2004). Interlayer bonds influence the mechanical properties of CNS, like multi-walled carbon nanotubes (Byrne et al., 2010; Huang et al., 2010; Peng et al., 2012) and carbon nanotube bundles (Kis et al., 2004). Cross links constrain sliding between nanotube walls (Byrne et al., 2010) and adjacent nanotubes (Kis et al., 2004), the load transfer between the tubes being best if the bonds

are uniformly distributed (Byrne et al., 2010). However, for covalent bonds formed by Frenkel pair defects (Telling et al., 2003) a decrease in the axial buckling load of double-walled nanotubes is observed, as the Frenkel pair defect weakens the layers and stresses are concentrated around these defects (Peng et al., 2012). Furthermore, the increased interlayer shear stiffness of carbon crystallites forming carbon fibers (Loidl et al., 2003; Sauder and Lamon, 2005) is attributed to the formation of covalent interlayer bonds (Loidl et al., 2003). Interlayer bonds may also play a role in the formation of nanodiamonds due to the irradiation induced self-compression of carbon onions (Banhart et al., 1997).

The examples above show that interlayer defects should be considered in a continuum mechanical analysis of CNS. As a first attempt a continuum truss model is used in (Todt et al., 2010) to represent such covalent interlayer bonds in carbon crystallites. Therein, the defects are assumed to correspond to a fourfold coordinated interstitial atom (Telling et al., 2003) locally reducing the interlayer distance from 0.34 nm to approximately 0.258 nm. Each defect is represented by a single truss element (Todt et al., 2010), and hence, the actual structure of the defects is ignored. The axial stiffness of the trusses is assumed to be high enough, so that the conflating effect of the interlayer bonds is not significantly influenced by the membrane stiffness of the layers. With this model it is shown that the amount and the distribution of interlayer defects has an influence on the occurrence of buckling in carbon crystallites, see Section 4.4.

Curvature induced excess surface energy In curved CNS a curvature induced excess surface energy is present (Holec et al., 2010) being defined as the curvature induced increase in total energy with respect to planar graphene. Due to the excess surface energy a surface stress develops in curved carbon layers leading to a non-zero membrane stress state in the absence of external loading (Fischer et al., 2008). In a continuum mechanical model this surface stress can be taken into account by applying a corresponding inwards oriented mechanical pressure, see e.g., (Todt et al., 2014a). The excess surface energy being present in carbon fullerenes is discussed in more detail in Section 4.3 and (Holec et al., 2010).

4 Applications

In the following sections we discuss some examples on how the concepts introduced in the preceding chapters can be used to study the mechanical behavior of CNS. Starting from planar graphene it is explained how atomistic simulations were used to extract effective mechanical properties for this

fascinating material. Then nanotubes are discussed. These cylindrically shaped objects are obtained when graphene is rolled up in one direction. Nanotubes are typically characterized by a very large aspect ratio, i.e., the ratio of length to diameter is very large. Typical questions concern the stability of nanotubes during uniaxial compression, bending or hydrostatic loading, thermal buckling and the influence of defects. When graphene is not only curved in one but in two dimensions then spherical fullerenes are obtained. In contrast to plane graphene and nanotubes, fullerenes intrinsically contain structural defects, because it is not possible to close a structure consisting of three fold coordinated particles and hexagons only. At least 12 pentagons have to be included. When many of such fullerenes of different size are “stacked” into each other then so called carbon onions form. In these multilayered structures the non-covalent vdW interactions are of utmost importance. Special care has to be taken in the description of vdW interactions in the framework of continuum mechanics when these forces act between curved surfaces. In carbon onions it is most likely that vdW forces define the maximum number of layers that an onion can consist of. Finally, the mechanics of carbon fibers is discussed. It is shown that the mechanical properties of these fibers strongly depend on the concentration and distribution of defects in the carbon nano-crystallites the fibers are consisting of.

4.1 Graphene

Graphene is a single layer of graphite, i.e., a truly 2-dimensional material. Graphene consists of sp^2 bonded carbon, i.e., each atom has exactly 3 neighbors. Note, that graphene is not a bravais lattice. The smallest unit cell of graphene consists of 2 atoms. Although graphene seems to be a simple structure, some tricky questions may arise. One of these is: What is the thickness of a two-dimensional material? Even if on first sight this question may seem academical it has important implications. Graphene is the elementary building block of all other CNS, like nanotubes, fullerenes, carbon onions, and carbon crystallites in carbon fibers. Thus, a thorough understanding of graphene is essential to understand also the larger structures. Because of the small size of graphene experiments on these structures are scarce. One of the few examples is presented in (Lee et al., 2008). Consequently, computer simulations are of utmost importance to gain additional insight into these structures. Nevertheless, studying the mechanical properties of these structures using a full atomistic description is often not feasible due to the large number of atoms in graphene layers being sufficiently large. A possible solution is to use methods from continuum mechanics to inves-

tigate such structures. A natural way describing these structures is as thin elastic shells. This demands the input of three macroscopic parameters: the Young's modulus E , the Poisson's ratio ν and the thickness h of the shell. In other words, the goal is to find *effective* elastic parameters of a hypothetical shell that shall show the same elastic behavior as a sheet of graphene. While the determination of a membrane stiffness $Y = Eh$ can easily be done in a simulation and partly also in experiments, the bending stiffness and, thus, the effective thickness explicitly is harder to grasp as already discussed in Section 3.2. Using potentials obtained in (Holec et al., 2010) in (Hartmann et al., 2013) computational loading tests were performed on graphene using the Monte Carlo method. The membrane stiffness, Poisson's ratio and the strength of graphene were obtained by computational tension tests, while the bending stiffness (and, thus, the effective thickness) were derived by compression tests, in which buckling was enforced. It was shown that the continuum approximation breaks down for systems composed of too few atoms, but that a constant effective thickness of $h = 1.32 \text{ \AA}$ is reached for graphene longer than 50 \AA (see also Figure 1).

4.2 Nanotubes

An infinite sheet of planar graphene is the lowest energy conformation of sp^2 bonded carbon. The edges of any finite sheet of graphene increase the energy of this structure. Thus bending and closure of the sheet may become energetically favorable, and structures like nanotubes (Baughman et al., 2002) may form. Nanotubes are of cylindrical symmetry and may be single or multi-walled. Besides inheriting the amazing mechanical properties from graphene, nanotubes also show remarkable electronic properties. Depending on its chirality the tube may either be metallic or semiconducting (Dai, 2002).

One convenient procedure of testing nanotubes (either in a pressure cell using Raman spectroscopy or in a computer experiment) is to apply hydrostatic pressure from the outside (Sun et al., 2013). The deformation of the nanotubes is first given by a reduction in radius without a change in shape for low pressure and an ovalization of the cross section of the tube that is accompanied by a subsequent softening of the tube for high pressure. This behavior, which corresponds to typical buckling of thin tubes under external pressure (Windenburg and Trilling, 1934), was predicted in computer simulations (Sun et al., 2004) using molecular dynamics and also found in experiments (Sun et al., 2014). Monte Carlo simulations of nanotubes under hydrostatic pressure show similar results as the molecular dynamics calculations (see Figure 2) (Sun et al., 2013). Details on the continuum mechanical

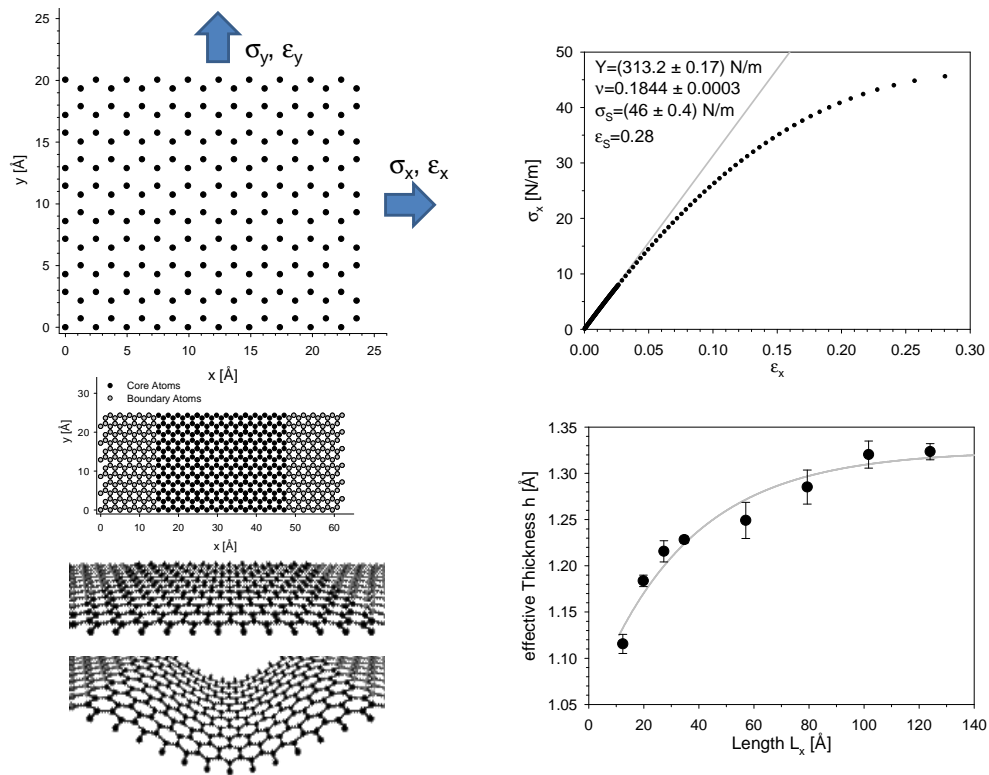


Figure 1. Determination of the effective elastic properties of graphene. Top row: The membrane stiffness Y , Poisson's ratio ν , the strength σ_S , and the ultimate strain ϵ_S of graphene is obtained by loading a sheet of graphene in uni-axial tension (left) and recording the corresponding strains in x and y -directions. Bottom row: Compression tests on graphene to obtain the effective thickness h . On the left the used geometry and two snapshots of the graphene layer before and after buckling are shown. On the right the effective thickness obtained for different lengths of the graphene patch is shown. For a length smaller than approximately 50 \AA the effective thickness of graphene decreases due to the breakdown of the continuum approximation, but attains a constant value of $\approx 1.32 \text{ \AA}$ for longer patches. (Figure reproduced with permission and adapted from (Hartmann et al., 2013)).

modeling of the behavior of nanotubes under external pressure can be found in Chapter 7.

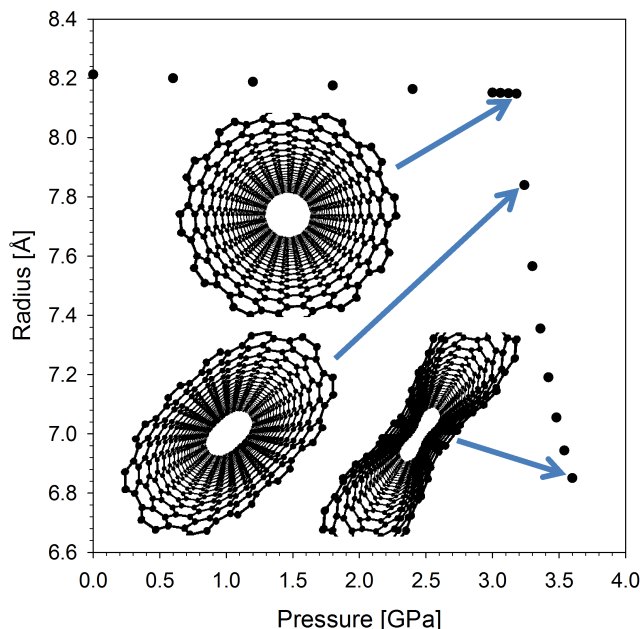


Figure 2. The behavior of nanotubes under radial compression (hydrostatic pressure). The figure shows the radius of the tube as a function of the applied load as obtained by Monte Carlo simulations. The radius is defined as the mean normal distance of all atoms with respect to the tube axis. For low loads the radius of the tubes shrinks homogeneously. After a certain critical pressure is exceeded the cross section of the tubes ovalizes and loses its circular shape. (Figure adapted from (Sun et al., 2013). Copyright Wiley-VCH Verlag GmbH & Co. KGaA. Reproduced with permission).

Using molecular dynamics methods in (Wang et al., 2005) the behavior of nanotubes under axial load was investigated. Here it was shown that depending on the length of the tube it fails either via local buckling or global bending. In (Hao et al., 2008) the influence of defects (vacancies) on the mechanical properties of nanotubes was modeled, while in (Walther et al., 2001) the interaction of water and nanotubes was modeled to investigate the radial-breathing-mode (RBM) vibration of nanotubes that shows a pronounced signal in Raman spectra. Also the buckling of double-walled nanotubes can be monitored in a simulation, where it was shown that the vdW interactions between the layers have a large influence on the buckling load (Zhang et al., 2007).

4.3 Fullerenes and Onions

In contrast to cylindrical nanotubes, spherical CNS can not be formed solely by hexagons. According to Euler's theorem at least 12 pentagons are necessary to close the structure. Fulfilling Euler's theorem is a necessary but not a sufficient condition for fullerenes to be thermodynamically stable. Additionally, the so called isolated pentagon rule (IPR) (Kroto, 1987) must be fulfilled and the fullerene must consist of an even number of atoms (Kroto, 1987). The IPR is an implication of the fact that the local stability – in terms of the position of the atoms – of a fullerene increases if the local curvature decreases (Klein et al., 1986). It states that only such fullerenes are thermodynamically stable for which the pentagons are not in direct contact with each other. These pentagons can be regarded as intrinsic intra-layer defects that result in a lower bond angle than the perfect hexagons. Due to the pentagons fullerenes have the shape of truncated icosahedrons, where the pentagons are located at the vertices of the icosahedrons. The thermodynamic stability of fullerenes up to C_{240} is investigated in (Klein et al., 1986) considering only fullerenes with their number of atoms being equal to $n = 20(m^2 + mk + k^2)$, $0 \leq k \leq m$, with m and k being integers. C_{60} , C_{180} , and C_{240} fullerenes are thermodynamically quite stable. The fullerenes C_{80} and C_{140} show a lower thermodynamic stability and therefore, are less likely to form than, e.g., a C_{60} fullerene. Thermodynamic stability considerations on larger fullerenes (Tang and Huang, 1995) show that all fullerenes with $k = m$ form a closed-cage structure, which is not necessarily the case for $k = 0$. Therefore, the number of atoms forming a fullerene - in terms of a closed-cage icosahedron – can be calculated as $n = 60k^2$.

As mentioned in Section 3.3 curved CNS possess an intrinsic curvature excess surface energy. In (Holec et al., 2010) the excess surface energy of fullerenes of different size is investigated in detail. First, classical potentials are obtained using *ab initio* calculations. In a second step the excess surface energy is calculated with *ab initio* for small fullerenes up to C_{240} and with Monte Carlo simulations for larger fullerenes up to C_{5120} . It is shown that Monte Carlo simulations over estimate the total amount of the surface energy by a constant factor of approximately 1.6. Nevertheless, the Monte Carlo method as well as the *ab initio* calculations lead to the same exponent $\beta = 1.4$ for the decay of the surface energy E_S as a function of radius $E_S \propto R^{-\beta}$. The results show that the excess surface energy is only of importance for small fullerenes, as it vanishes fast with increasing fullerene radius. For fullerenes the resulting surface stress σ_S (here in terms of a membrane force per unit area) corresponds to a plane hydrostatic stress state and can be related to the excess surface energy by the Shuttleworth

equation (Fischer et al., 2008) reading $\sigma_S = E_S + \frac{dE_S}{d\epsilon_S}$. The parameter ϵ_S denotes the strain in each circumferential direction of the sphere in a small strain setting (Fischer et al., 2008). For a first estimate, usually the second term of the right hand side of the Shuttleworth Equation is neglected.

Large fullerenes with $k = m$ tend to form multi-layer arrangements as they are more stable (Tang and Huang, 1995). Multi-layered particles were first observed by Iijima in 1980 (Iijima, 1980). These particles were called carbon onions (Kroto, 1992) and form from soot when subjected to intense electron irradiation (Ugarte, 1992). They show a rather polyhedral shape or are almost perfectly spherical. In a strict sense only the spherical particles should be denoted as carbon onions. Today, various methods are available to produce carbon onions, such as electron irradiation of graphite at elevated temperatures ($\geq 300^\circ\text{C}$) (Banhart and Ajayan, 1996; Banhart et al., 1997), high temperature annealing of nanodiamonds (Tomita et al., 2002), synthesis by decomposition of phenolic resin (Zhao et al., 2007), high pressure transformation of graphite, or thermo-mechanical processing of graphite powders (Güler and Evin, 2014). Onions produced by high-pressure transformation of single crystal graphite seem to grow from the inside to the outside (Blank et al., 2007; Du et al., 2007; Füller and Banhart, 1996). This corresponds to the presumption (Kroto, 1992) that carbon onions grow by the spiraling network mechanism (Kroto and McKay, 1988; Zhang et al., 1986). If high-temperature annealing of nanodiamonds is used to produce carbon onions, the particles grow from the outer boundaries of the nanodiamond towards the center (Tomita et al., 2002). Due to their multi-layer spherical structure carbon onions possess a high local electron density leading to a high ability for absorbing electromagnetic radiation. This makes them promising candidates as fillers in nanocomposites for electromagnetic shielding (Macutkevic et al., 2009). They have also potential application as additives in lubricants (Joly-Pottuz et al., 2008), as solid lubricants (Hirata et al., 2004), or as nanoscopic pressure cells for the production of nanodiamonds (Banhart and Ajayan, 1996).

In all of these applications the mechanical properties of carbon onions under external pressure and the size of these particles play a role. In (Peón-Escalante et al., 2014) the “bulk modulus” B – as applied pressure per relative change of the enclosed volume – of a C_{60} fullerene is predicted with *ab initio* and the space frame modeling approach discussed in Section 3.1. The obtained values of B are between 750 GPa and approximately 900 GPa and are in good agreement with references given in (Peón-Escalante et al., 2014). In (Peón-Escalante et al., 2014) the use of shell models for estimating B of fullerenes is considered as problematic with allusion to the definition of an appropriate shell thickness. This is in clear contradiction to

the results presented in (Todt et al., 2014b), where the applicability of shell models to describe the mechanical properties of fullerenes is investigated in detail. In (Todt et al., 2014b) icosahedral fullerenes up to a size of C_{1280} are modeled using continuum shells where different parameter sets of E , h , and ν are used. The fullerenes are subjected to an external pressure and a circumferential ring load allowing to obtain their hydrostatic and ringload stiffness, respectively. The results are compared to results obtained by MC simulations. Although larger fullerenes are not perfectly spherical the hydrostatic stiffness of the fullerenes could be well predicted by the continuum shell model and is almost the same for all parameter sets for E , h , and ν . This result is not surprising as hydrostatic pressure leads to a pure membrane stress state. As can be seen from Table 2 all parameter sets lead to comparable values of the membrane stiffness and therefore, to similar values of the hydrostatic stiffness. Further, it is shown that parameter sets for which h is chosen to be around 0.34 nm strongly overestimate the ring load stiffness of the fullerenes. Parameter sets with $h \approx 0.07$ nm and a thereof resulting E of around 5000 GPa gave the best prediction of the ring load stiffness. It is also shown that the loading conditions in the MC simulations and in the continuum model have to be similar to lead to comparable results.

For investigating the mechanical properties of spherical CNS consisting of a large number of atoms, such as carbon onions, atomistic methods become computationally expensive. In this case, continuum mechanical methods can be used to investigate their mechanical behavior. For example, in (Todt et al., 2014a) continuum mechanical shell models are applied to investigate a possible growth limit of carbon onions. There, the model used assumes that carbon onions grow from the inside to the outside and considers the excess surface energy as well as the vdW interactions between the layers. The arising boundary value problem is solved using the FEM method. The vdW interactions are described using the pressure-distance relations given in (Kelly, 1981) and (Todt et al., 2011) for graphite/graphene. These relations allow a straight forward implementation into the FEM model but neglect the curvature effect within the vdW interactions. The question regarding the growth limit of carbon onions is formulated as a buckling eigenvalue problem

$$\left(\underset{\approx}{\mathbf{K}}_N + \lambda_N \Delta \underset{\approx}{\mathbf{K}}_N \right) \underset{\approx}{\Phi}_N = \mathbf{0} \quad (40)$$

with $\underset{\approx}{\mathbf{K}}_N$ being the stiffness matrix of a N -layered onion in its equilibrium state. The matrix $\Delta \underset{\approx}{\mathbf{K}}_N$ represents the change in the stiffness of the onion due to an externally applied fictitious pressure. Hence, an eigenvalue $\lambda_N = 0$ means that no external pressure is required for the onion to loose its

structural stability, and therefore, indicates the growth limit of the onion. The vector Φ_N is the corresponding buckling mode to the eigenvalue λ_N . With this formulation it has been shown that the size of carbon onions is most likely limited by the occurrence of a structural instability. The loss of stability is caused by a self-equilibrating stress state emerging from the accommodation of misfitting carbon layers during the growing process. The self-equilibrating stresses in the layers are mainly introduced by the vdW interactions between the layers, whereas the excess surface energy is of importance for the innermost layers only, for details see (Todt et al., 2014a). Figure 3 a) shows the results of the eigenvalue problem, revealing that the use of different exponents in the pressure distance relations for the vdW interactions (see Section 3.3) are only of minor importance, whereas the choice of the Lennard-Jones parameters has a strong influence on the results. From the obtained buckling mode – depicted in Figure 3 (b) it can be concluded that the outermost layers start to buckle, and the innermost layers remain almost unaffected. This is because only the outermost layers of the onion are under compression, see Figure 3 (c), where the number of layers under compression increases during the growth of the onion. The largest onion obtained in the analysis has about 72 layers, which is close to experimental observations, e.g. in (Banhart, 1997; Banhart et al., 1997). In conclusion, it can be said that due to uncertainties in the parameters describing the layer properties and the high sensitivity on the vdW parameters, the results rather have a qualitative than a quantitative character. However, the model clearly indicates a growth limit of carbon onions and can act as basis for further research.

4.4 Carbon Fibers

Carbon fiber reinforced plastics (CFRP) are – due to their high stiffness and strength at low mass density – used in many lightweight applications. Although many different parameters, like the fiber content or the bonding between fibers and matrix influence the properties of CFRP, it is necessary to have detailed knowledge about the mechanical properties of the fibers. Hence, these properties are subject of intense research activities, see, e.g., (Gao et al., 2011; Hawthorne, 1993; Loidl et al., 2005; Naito et al., 2008; Sauder et al., 2004). Due to the small diameters of the fibers they show a tendency towards buckling when subjected to compressive loading, making it difficult to assess their compressive behavior experimentally. Methods to overcome these problems are, e.g., the loop test (Sinclair, 1950) or the tensile recoil method (Allen, 1987). For a more detailed review of experimental methods, see, e.g., (Oya and Johnson, 1999). Such experiments

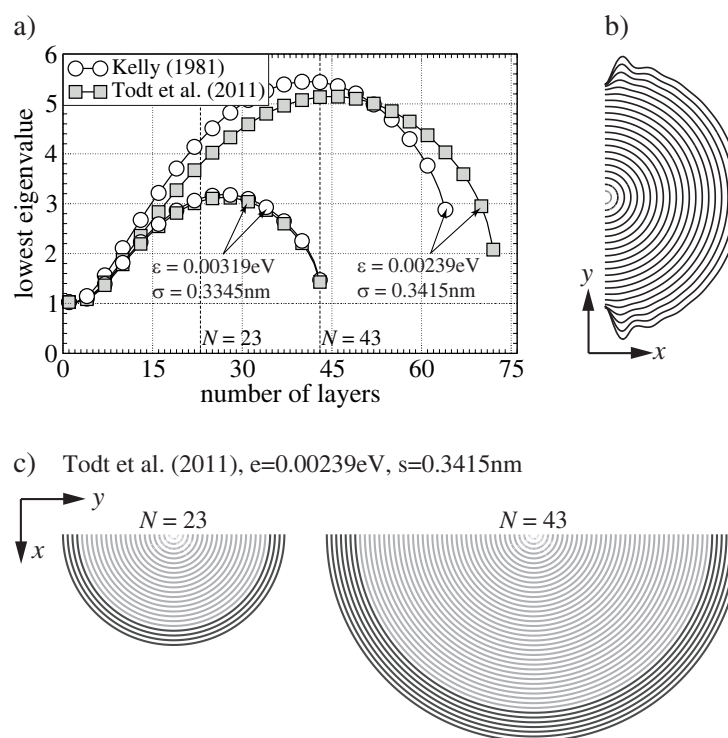


Figure 3. a) Results of the buckling eigenvalue analysis during the growth of carbon onions obtained with different vdW models and Lennard-Jones parameters. The loss of structural stability is indicated by the approach of the lowest eigenvalue to 0. b) Buckling mode of a carbon onion, where only every second layer is shown, see (Todt et al., 2014a) (Figure appearing with the permission of Elsevier). c) Layers under compression (black) and tension (gray) of onions grown to different sizes.

revealed that the nanostructure of the fibers has a strong influence on their compressive behavior (Dobb et al., 1995; Oya and Johnson, 2001; Nakatani et al., 1999; Loidl et al., 2005). For example, polyacrylonitrile (PAN) based carbon fibers show a skin-core structure (Paris and Peterlik, 2009), where the outer surface of the fibers is formed by a skin-like layer, and randomly distributed so called carbon crystallites form the inner region, see Figure 4. In fibers subjected to compressive loading, crystallite buckling was supposed to occur (Oya and Johnson, 2001; Nakatani et al., 1999) and was at first directly observed in (Loidl et al., 2005) using microbeam X-ray diffraction. Crystallite buckling is related to fiber failure (Dobb et al., 1995) and the non-Hookean behavior of fibers observed in loop tests (Hawthorne, 1993). Thus, it has a strong influence on the mechanical behavior of carbon fibers.

Besides experimental methods continuum mechanical modeling can help to gain further insight into the dependency of the fibers properties on their nanostructure, see, e.g., (Sauder and Lamon, 2005; Todt et al., 2010). In (Sauder and Lamon, 2005) the tensile properties of the fibers are determined using the theory of elasticity for anisotropic solids. It is shown that an artificially high interlayer shear stiffness is required to obtain a good representation of the Young's modulus of the fibers confirming observations made in (Loidl et al., 2003) for PAN based fibers. This model is also applicable to investigate the compressive and bending behavior of carbon fibers as long as crystallite buckling has not occurred. Crystallite buckling is inves-

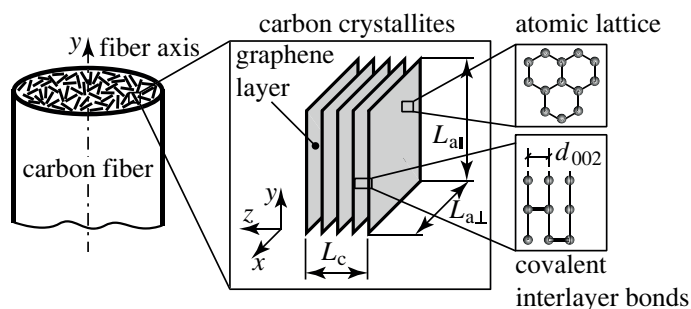


Figure 4. Nanostructure of PAN-based carbon fibers. (Figure taken from (Todt et al., 2010) and appearing with kind permission from Springer Science+Business Media.)

tigated in (Todt et al., 2010) using a detailed continuum mechanical model of a single crystallite. In (Todt et al., 2010) the layers of the crystallite depicted in Figure 4 are modeled using continuum shells. In the model the crystallite is assumed to consist of eight layers with in-plane dimensions of $L_{a||} \times L_{a\perp} = 4.32 \text{ nm} \times 3.87 \text{ nm}$, with the graphene planes being oriented parallel to the fiber axis. The vdW interactions between the individual layers are described using the pressure-distance relation given in Equation (36) and the interlayer defects are modeled using the defect model briefly discussed in Section 3.3. Defects randomly distributed within the whole crystallite lead to local dimples in the graphene layers, whereas defects located along the edges only cause an overall bending of the crystallite. This difference in the pre-deformation has a substantial influence on the mechanical behavior of carbon crystallites subjected to compressive loading along the fiber axis. In the pre-buckling state the apparent secant modulus of the crystallites is almost constant and independent of the amount of interlayer defects if the defects are distributed within the whole crystallite, see Figure 5 (left). After the occurrence of crystallite buckling the secant

modulus decreases significantly, where the axial load leading to the onset of buckling substantially increases with the amount of defects. If the defects are distributed along the edges only, the crystallite possesses a much lower initial secant modulus which strongly decreases already for small deformations and is almost independent of the amount of interlayer defects, Figure 5 (right). This behavior can be attributed to the pre-bending deformation introduced by the formation of the defects along the edges. Comparison with literature (Loidl et al., 2003) reveals that it is more likely that the defects are distributed within the whole crystallite, as in this case the obtained overall Young's modulus of the crystallites corresponds well with the experimentally obtained value (Loidl et al., 2003). The reduction of the secant modulus after the onset of buckling explains the observed shift in the neutral axis during loop-testing of fibers (Loidl et al., 2005). Although this continuum model contains some simplifications, especially regarding the structure of the defects and their properties, it provides some insight to mechanisms determining the compressive behavior of carbon fibers on a nanostructural level.

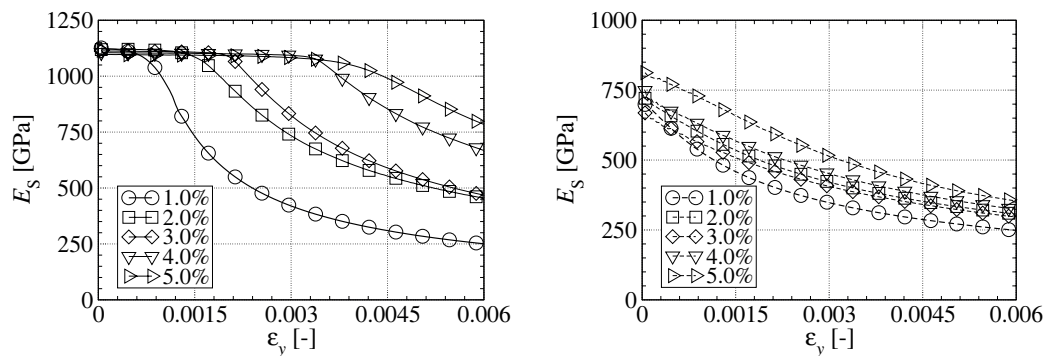


Figure 5. Deformation dependent apparent secant modulus of carbon crystallites with their interlayer defects being distributed within the whole crystallite (left) or along the edges only (right). The amount of interlayer defects is varied from 1% to 5% of the maximum number of possible interlayer defects.

5 Conclusion

Computational methods, such as molecular dynamics, Monte Carlo methods, and continuum mechanical approaches can be used to investigate the mechanical properties of carbon nanostructures. These methods should be

seen as complementary to experimental methods, allowing to investigate phenomena which are difficult to observe in experiments. The choice of the method depends on the length scale on which a specific phenomena occurs and the size of the carbon nanostructures to be investigated. Molecular dynamics and Monte Carlo methods allow to access the position of the individual atoms within a carbon nanostructure and phenomena like bond breaking and bond formation can directly be investigated. However, for carbon nanostructures consisting of a large number of atoms these methods can become computationally expensive. For such large nanostructures continuum mechanical methods can provide insight the overall mechanical behavior with relatively low computational costs. Overall it can be said, that an interplay between experimental, atomistic, and continuum mechanical methods is required to get a fundamental understanding of the mechanical behavior of carbon nanostructures.

Bibliography

- G.C. Abell. Empirical chemical pseudopotential theory of molecular and metallic bonding. *Physical Review B*, 31:6184, May 1985.
- S.R. Allen. Tensile recoil measurement of compressive strength for polymeric high performance fibres. *Journal of Materials Science*, 22:853–859, 1987.
- N.L. Allinger, Y.H. Yuh, and J.H. Lii. Molecular mechanics. The MM3 force field for hydrocarbons. *Journal of the American Chemical Society*, 111:8551–8566, 1989.
- R. Ansari and H. Rouhi. Analytical treatment of the free vibration of single-walled carbon nanotubes based on the nonlocal Flugge shell theory. *Journal of Engineering Materials and Technology*, 134:011008, 2012.
- R. Ansari, B. Motevalli, A. Montazeri, and S. Ajori. Fracture analysis of monolayer graphene sheets with double vacancy defects via MD simulation. *Solid State Communications*, 151:1141 – 1146, 2011.
- B. Arash and Q. Wang. A review on the application of nonlocal elastic models in modeling of carbon nanotubes and graphenes. *Computational Materials Science*, 51:303–313, 2012.
- P.T. Araujo, M. Terrones, and M.S. Dresselhaus. Defects and impurities in graphene-like materials. *Materials Today*, 15:98–109, 2012.
- S. Arghavan and A.V. Singh. Atomic lattice structure and continuum plate theories for the vibrational characteristics of graphenes. *Journal of Applied Physics*, 110:084308, 2011.
- A.A. Balandin. Thermal properties of graphene and nanostructured carbon materials. *Nat Mater*, 10:569–581, 2011.
- F. Banhart. The transformation of graphitic onions to diamond under electron irradiation. *Journal of Applied Physics*, 81:3440–3445, 1997.

- F. Banhart and P.M. Ajayan. Carbon onions as nanoscopic pressure cells for diamond formation. *Nature*, 382:433–435, 1996.
- F. Banhart, T. Füller, Ph. Redlich, and P.M. Ajayan. The formation, annealing and self-compression of carbon onions under electron irradiation. *Chemical Physics Letters*, 269:349–355, 1997.
- F. Banhart, J. Kotakoski, and A.V. Krasheninnikov. Structural defects in graphene. *ACS Nano*, 5:26–41, 2011.
- D. Baowan, N. Thamwattana, and J.M. Hill. Continuum modelling of spherical and spheroidal carbon onions. *European Physical Journal D*, 44: 117–123, 2007.
- R.H. Baughman, A.A Zakhidov, and W.A. de Heer. Carbon nanotubes – the route toward applications. *Science*, 297:787–792, 2002.
- V.D. Blank, V.N. Denisov, A.N. Kirichenko, B.A. Kulnitskiy, S. Yu Martushov, and B.N. Mavrin et al. High pressure transformation of single-crystal graphite to form molecular carbon onions. *Nanotechnology*, 18: 345601, 2007.
- D.W. Brenner. Empirical potential for hydrocarbons for use in simulating the chemical vapor deposition of diamond films. *Physical Review B*, 42: 9458, 1990.
- D.W. Brenner, O.A. Shenderova, J.A. Harrison, S.J. Stuart, B. Ni, and S.B. Sinnott. A second-generation reactive empirical bond order (REBO) potential energy expression for hydrocarbons. *Journal of Physics: Condensed Matter*, 14:783, 2002.
- B.R. Brooks, R.E. Bruccoleri, B.D. Olafson, D.J. States, S. Swaminathan, and M. Karplus. Charmm: A program for macromolecular energy, minimization, and dynamics calculations. *Journal of Computational Chemistry*, 4(2):187, 1983.
- E.M. Byrne, A. Letertre, M.A. McCarthy, W.A. Curtin, and Z. Xia. Optimizing load transfer in multiwall nanotubes through interwall coupling: Theory and simulation. *Acta Materialia*, 58:6324–6333, 2010.
- E. Cadelano, S. Giordano, and L. Colombo. Interplay between bending and stretching in carbon nanoribbons. *Physical Review B*, 81:144105, 2010.
- A.H. Castro Neto, F. Guinea, N.M. R. Peres, K.S. Novoselov, and A.K. Geim. The electronic properties of graphene. *Rev. Mod. Phys.*, 81:109–162, 2009.
- F. Cataldo. The impact of a fullerene-like concept in carbon black science. *Carbon*, 40:157–162, 2002.
- N. Chandra, S. Namilae, and C. Shet. Local elastic properties of carbon nanotubes in the presence of stone-wales defects. *Physical Review B*, 69: 094101, 2004.

- T. Chang. A molecular based anisotropic shell model for single-walled carbon nanotubes. *Journal of the Mechanics and Physics of Solids*, 58: 1422–1433, 2010.
- S. Chen and D.C. Chrzan. Continuum theory of dislocations and buckling in graphene. *Physical Review B*, 84:214103, 2011.
- W. Choi and J.W. Lee, editors. *Graphene Synthesis and Applications*. CRC Press, New York, 2012.
- A. Chuvilin, U. Kaiser, E. Bichoutskaia, N.A. Besley, and A.N. Khlobystov. Direct transformation of graphene to fullerene. *Nature Chemistry*, 2: 450–453, 2010.
- Wendy D. Cornell, Piotr Cieplak, Christopher I. Bayly, Ian R. Gould, Kenneth M. Merz, David M. Ferguson, David C. Spellmeyer, Thomas Fox, James W. Caldwell, and Peter A. Kollman. A second generation force field for the simulation of proteins, nucleic acids, and organic molecules. *Journal of the American Chemical Society*, 117(19):5179, 1995.
- H. Dai. Carbon nanotubes: opportunities and challenges. *Surface Science*, 500:218 – 241, 2002.
- M.A.N. Dewapriya, R.K.N.D. Rajapakse, and A.S. Phani. Atomistic and continuum modelling of temperature-dependent fracture of graphene. *International Journal of Fracture*, 187:199–212, 2014.
- M. Dion, H. Rydberg, E. Schröder, D.C. Langreth, and B.I. Lundqvist. Van der Waals density functional for general geometries. *Physical Review Letters*, 92:246401, 2004.
- M.G. Dobb, H. Guo, D.J. Johnson, and C.R. Park. Structure-compressional property relations in carbon fibres. *Carbon*, 33:1553–1559, 1995.
- G. Domínguez-Rodríguez, A. Tapia, and F. Avilés. An assesment of finite element analysis to predict the elastic modulus and poisson’s ratio of singlewall carbon nanotubes. *Computational Material Science*, 82:257–263, 2014.
- R.M. Dreizler and E.K.U. Gross. *Density Functional Theory: An Approach to the Quantum Many-Body Problem*. Springer-Verlag, 1990.
- A.B. Du, X.G. Liu, D.J. Fu, P.D. Han, and B.S. Xu. Onion-like fullerenes synthesis from coal. *Fuel*, 86:294–298, 2007.
- H. Dumlich and S. Reich. Nanotube bundles and tube-tube orientation: A van der Waals density functional study. *Physical Review B*, 84:064121, 2011.
- M. Eftekhari, S. Mohammadi, and A.R. Khoei. Effect of defects on the local shell buckling and post-buckling behavior of single and multi-walled carbon nanotubes. *Computational Materials Science*, 79:736 – 744, 2013.
- F.D. Fischer, T. Waitz, D. Vollath, and N.K. Simha. On the role of surface energy and surface stress in phase-transforming nanoparticles. *Progress in Materials Science*, 53:481–527, 2008.

- D. Frenkel and B. Smit. *Understanding Molecular Simulation*. Academic Press, 2002.
- T. Füller and F. Banhart. In situ observation of the formation and stability of single fullerene molecules under electron irradiation. *Chemical Physics Letters*, 254:372–378, 1996.
- A. Gao, C. Zhao, S. Luo, Y. Tong, and L. Xu. Correlation between graphite crystallite distribution morphology and the mechanical properties of carbon fiber during heat treatment. *Materials Letters*, 65:3444 – 3446, 2011.
- A.K. Geim. Graphene: Status and prospects. *Science*, 324:1530–1534, 2009.
- A.K. Geim and K.S. Novoselov. The rise of graphene. *Nature Materials*, 6: 183–191, 2007.
- S.K. Georgantzinis, D.E. Katsareas, and N.K. Anifantis. Limit load analysis of graphene with pinhole defects: A nonlinear structural mechanics approach. *International Journal of Mechanical Sciences*, 55:85–94, 2012.
- S. Grimme. Accurate description of van der Waals complexes by density functional theory including empirical conditions. *Computational Chemistry*, 25:1463–1473, 2004.
- Ö. Güler and E. Evin. Formation of carbon nano onions by thermo-mechanical processing of graphite powders. *Materials Testing*, 56:241–244, 2014.
- W. Guo, C.Z. Zhu, T.X. Yu, C.H. Woo, B. Zhang, and Y.T. Dai. Formation of sp^3 bonding in nanoindented carbon nanotubes and graphite. *Physical Review Letters*, 93:245502, 2004.
- Y. Guo, N. Karasawa, and W.A. Goddard III. Prediction of fullerene packing in C60 and C70 crystals. *Nature*, 351:464, 1991.
- H.C. Hamaker. The London–van der Waals attraction between spherical particles. *Physica IV*, 10:1058–1072, 1937.
- X. Hao, H. Qiang, and Y. Xiaohu. Buckling of defective single-walled and double-walled carbon nanotubes under axial compression by molecular dynamics simulation. *Composites Science and Technology*, 68:1809, 2008.
- M.A. Hartmann, M. Todt, F.G. Rammerstorfer, F.D. Fischer, and O. Paris. Elastic properties of graphene obtained by computational mechanical tests. *Europhysics Letters*, 103:68004, 2013.
- A. Hashimoto, K. Suenaga, A. Gloter, K. Urita, and S. Iijima. Direct evidence for atomic defects in graphene layers. *Nature*, 430:870–873, 2004.
- H.M. Hawthorne. On non-Hookean behavior of carbon fibers in bending. *Journal of Material Science*, 28:2531–2535, 1993.
- X.Q. He, S. Kitipornchai, and K.M. Liew. Buckling analysis of multi-walled carbon nanotubes: a continuum model accounting for van der Waals interaction. *Journal of the Mechanics and Physics of Solids*, 53:303–326, 2005.

- A. Hirata, M. Igarashi, and T. Kaito. Study on solid lubricant properties of carbon onions produced by heat treatment of diamond clusters or particles. *Tribology International*, 37:899–905, 2004.
- D. Holec, M.A. Hartmann, F.D. Fischer, F.G. Rammerstorfer, P.H. Mayrhofer, and O. Paris. Curvature-induced excess surface energy of fullerenes: Density functional theory and Monte Carlo simulations. *Physical Review B*, 81:235403, 2010.
- P.Y. Huang, C.S. Ruiz-Vargas, A.M. van der Zande, W.S. Whitney, M.P. Levendorf, J.W. Kevek, S. Garg, J.S. Alden, C.J. Hustedt, Y. Zhu, J. Park, P.L. McEuen, and D.A. Muller. Grains and grain boundaries in single-layer graphene atomic patchwork quilts. *Nature*, 469:389–392, 2011.
- X. Huang, H. Yuan, W. Liang, and S. Zhang. Mechanical properties and deformation morphologies of covalently bridged multi-walled carbon nanotubes: Multiscale modeling. *Journal of the Mechanics and Physics of Solids*, 58:1847–1862, 2010.
- Y. Huang, J. Wu, and K. C. Hwang. Thickness of graphene and single-wall carbon nanotubes. *Physical Review B*, 74:245413, 2006.
- S. Iglesias-Groth, J. Breton, and C. Girardet. An analytical approach for the interlayer interaction in spherical buckyonions. *Chemical Physics Letters*, 264:351–358, 1997.
- S. Iijima. Direct observation of the tetrahedral bonding in graphitized carbon black by high resolution electron microscopy. *Journal of Crystal Growth*, 50:675–683, 1980.
- S. Iijima. Helical microtubules of graphitic carbon. *Nature*, 354:56–58, 1991.
- L. Joly-Pottuz, N. Matsumoto, H. Kinoshita, B. Vacher, M. Belin, and G. Montagnac et al. Diamond-derived carbon onions as lubricant additives. *Tribology International*, 41:69–78, 2008.
- W.L. Jorgensen and D.L. Severance. Aromatic aromatic interactions—free-energy profiles for the benzene dimer in water, chloroform, and liquid benzene. *Journal of American Chemical Society*, 112:4768 – 4774, 1990.
- B. Kelly. *Physics of Graphite*, pages 79–80. Advanced Science Publishers, 1981.
- K. Kim, Z. Lee, W. Regan, C. Kisielowski, M.F. Crommie, and A. Zettl. Grain boundary mapping in polycrystalline graphene. *ACS Nano*, 5: 2142–2146, 2011.
- A. Kis, C. Csányi, J.P. Salvetat, T.N. Lee, E. Couteau, A.J. Kulik, W. Benoit, J. Brugger, and L. Forró. Reinforcement of single-walled carbon nanotube bundles by intertube bridging. *Nature Materials*, 3: 153–157, 2004.
- D.J. Klein, W.A. Seitz, and T.G. Schmalz. Icosahedral symmetry carbon cage molecules. *Nature*, 323:703–706, 1986.

- S.A. Hosseini Kordkheili and M. Moshrefzadeh-Sani. Mechanical properties of double-layered graphene sheets. *Computational Material Science*, 69: 335 – 343, 2013.
- H.W. Kroto. The stability of the fullerenes C_n , with $n = 24, 28, 32, 36, 50, 60$, and 70 . *Nature*, 329:529–531, 1987.
- H.W. Kroto. Carbon onions introduce new flavour to fullerene studies. *Nature*, 359:670–671, 1992.
- H.W. Kroto and K. McKay. The formation of quasi-icosahedral spiral shell carbon particles. *Nature*, 331:328–331, 1988.
- H.W. Kroto, J.R. Heath, S.C. O'Brien, R.F. Curl, and R.E. Smalley. C60: Buckminsterfullerene. *Nature*, 318:162–163, 1985.
- D.P. Landau and K. Binder. *A Guide to Monte-Carlo Simulations in Statistical Physics*. Cambridge University Press, 2009.
- C.N. Lau, W. Bao, and J. Velasco Jr. Properties of suspended graphene membranes. *Materials Today*, 15:238–245, 2012.
- C. Lee, X. Wei, J.W. Kysar, and J. Hone. Measurement of the elastic properties and intrinsic strength of monolayer graphene. *Science*, 321: 385–388, 2008.
- C. Li and T.W. Chou. A structural mechanics approach for the analysis of carbon nanotubes. *International Journal of Solids and Structures*, 40: 2487–2499, 2003a.
- C. Li and T.W. Chou. Elastic moduli of multi-walled carbon nanotubes and the effect of van der Waals forces. *Composite Science and Technology*, 63:1517–1524, 2003b.
- G. Van Lier, C. Van Alsenoy, V. Van Doren, and P. Geerlings. *Ab initio* study of the elastic properties of single-walled carbon nanotubes and graphene. *Chemical Physics Letters*, 326:181–185, 2000.
- K.M. Liew and Y.Z. Sun. Computational modelling and simulation of carbon nanotubes. In B.H.V Topping, J.M. Adam, F.J. Pallarés, R. Bru, and M.L. Romeo, editors, *Development and Applications in Engineering Computational Technology*, pages 201–217. Saxe-Coburg Publications, Stirlingshire, Scotland, 2010.
- W.K. Liu, E.G. Karpov, S. Zhang, and H.S. Park. An introduction to computational nanomechanics and materials. *Computer Methods in Applied Mechanics and Engineering*, 193:1529–1578, 2004.
- D. Loidl, H. Peterlik, M. Müller, Ch. Riekkel, and O. Paris. Elastic moduli of nanocrystallites in carbon fibers measured by in-situ X-ray microbeam diffraction. *Carbon*, 41:563–570, 2003.
- D. Loidl, O. Paris, M. Burghammer, C. Riekkel, and H. Peterlik. Direct observation of nanocrystallite buckling in carbon fibers under bending load. *Physical Review Letters*, 95:225501, 2005.

- Q. Lu and R. Huang. Nonlinear mechanics of single-atomic-layer graphene sheets. *International Journal of Applied Mechanics*, 1:443–467, 2009.
- Q. Lu, M. Arroyo, and R. Huang. Elastic bending modulus of monolayer graphene. *Journal of Physics D*, 42:102002, 2009a.
- W.B. Lu, B. Liu, J. Wu, J. Xiao, K.C. Hwang, and S.Y. Fu et al. Continuum modeling of van der Waals interactions between carbon nanotube walls. *Applied Physics Letters*, 94:101917, 2009b.
- J. Macutkevic, D. Seliuta, G. Valusis, J. Banys, P. Kuzhir, and S. Maksimenko et al. Dielectric properties of onion-like carbon based polymer films: Experiment and modeling. *Solid State Sciences*, 11:1828–1832, 2009.
- J.R. Maple, M.-J. Hwang, T.P. Stockfisch, U. Dinur, M. Waldman, C.S. Ewig, and A.T. Hagler. Derivation of Class II Force Fields. I. Methodology and Quantum Force Field for the Alkyl Functional Group and Alkane Molecules. *Journal of Computational Chemistry*, 15:162, 1994.
- S.L. Mayo, B.D. Olafson, and W.A. Goddard III. DREIDING: A Generic Force Field for Molecular Simulations. *Journal of Physics and Chemistry*, 94:8897, 1990.
- M. Meo and M. Rossi. Prediction of Young’s modulus of single wall carbon nanotubes by molecular-mechanics based finite element modelling. *Composites Science and Technology*, 66:1597–1605, 2006.
- N. Metropolis and S. Ulam. The Monte Carlo Method. *Journal of the American Statistical Association*, 44:335, 1949.
- N. Metropolis, A.W. Rosenbluth, M.N. Rosenbluth, A.H. Teller, and E. Teller. Equation of State Calculations by Fast Computing Machines. *Journal of Chemical Physics*, 21:1087–1092, 1953.
- J.C. Meyer, C. Kisielowski, R. Erni, M.D. Rossell, M.F. Crommie, and A. Zettl. Direct imaging of lattice atoms and topological defects in graphene membranes. *Nano Letters*, 8:3582–3586, 2008.
- K. Naito, Y. Tanaka, J.M. Yang, and Y. Kagawa. Tensile properties of ultrahigh strength PAN-based, ultrahigh modulus pitch-based and high ductility pitch-based carbon fibers. *Carbon*, 46:189–195, 2008.
- M. Nakatani, M. Shioya, and J. Yamashita. Axial compressive fracture of carbon fibers. *Carbon*, 37:601–608, 1999.
- I. Nikiforov, E. Dontsova, R.D. James, and T. Dumitrică. Tight-binding theory of graphene bending. *Physical Review B*, 89:155437, 2014.
- K.S. Novoselov, A.K. Geim, S.V. Morozov, D. Jiang, Y. Zhang, and S.V. Dubonos et al. Electric field effect in atomically thin carbon films. *Science*, 306:666–669, 2004.
- N. Oya and D.J. Johnson. Direct measurement of longitudinal compressive strength in carbon fibres. *Carbon*, 37:1539–1544, 1999.

- N. Oya and D.J. Johnson. Longitudinal compressive behaviour and microstructure of PAN-based carbon fibres. *Carbon*, 39:635–645, 2001.
- A. Pantano, D.M. Parks, and M.C. Boyce. Mechanics of deformation of single- and multi-wall carbon nanotubes. *Journal of the Mechanics and Physics of Solids*, 52:789–821, 2004.
- O. Paris and H. Peterlik. The structure of carbon fibres. In S. Eichhorn, J.W.S Hearle, M. Jaffe, and T. Kikutani, editors, *Handbook of textile fibre structure*, volume 2. Woodhead Publishing Limited, Cambridge, UK, 2009.
- B. Peng, Y. Li, S. Liu, Z. Guo, and L. Ding. The roles of crosslinks in the buckling behaviors and load transferring mechanisms of double-walled nanotubes under compression. *Computational Materials Science*, 55:95–99, 2012.
- R. Peón-Escalante, C. Villanueva, R. Quintal, F. Avilés, and A. Tapia. The bond force constant and bulk modulus of C60. *Computational Materials Science*, 83:120 – 126, 2014.
- N.M. Pugno and R.S. Ruoff. Quantized fracture mechanics. *Philosophical Magazine*, 84:2829–2845, 2004.
- H. Rafii-Tabar. *Computational physics of carbon nanotubes*. Cambridge University Press, Cambridge, 2008.
- C.Q. Ru. Effect of van der Waals forces on axial buckling of a double-walled carbon nanotube. *Journal of Applied Physics*, 87:7227–7231, 2000.
- A. Sakhaee-Pour. Elastic properties of single-layered graphene sheet. *Solid State Communications*, 149:91–95, 2009.
- C. Sauder and J. Lamon. Prediction of elastic properties of carbon fibers and CVI matrices. *Carbon*, 43:2044–2053, 2005.
- C. Sauder, J. Lamon, and R. Pailler. The tensile behavior of carbon fibers at high temperatures up to 2400°C. *Carbon*, 42:715–725, 2004.
- A. Sears and R.C. Batra. Macroscopic properties of carbon nanotubes from molecular-mechanics simulations. *Physical Review B*, 69:235406, 2004.
- S. Sharma, R. Chandra, P. Kumar, and N. Kumar. Effect of stone-wales and vacancy defects on elastic moduli of carbon nanotubes and their composites using molecular dynamics simulation. *Computational Materials Science*, 86:1 – 8, 2014.
- O.A. Shenderova, V.V. Zhirnov, and D.W. Brenner. Carbon Nanostructures. *Critical Reviews in Solid State and Materials Sciences*, 27:227, 2002.
- D. Sinclair. A bending method for measurement of the tensile strength and Young’s modulus of glass fiber. *Journal of Applied Physics*, 21:380–386, 1950.

- S. Stankovich, D.A. Dikin, G.H.B. Dommett, K.M. Kohlhaas, E.J. Zimney, and E.A. Stach et al. Graphene-based composite materials. *Nature*, 442: 282–286, 2006.
- S.J. Stuart, A.B. Tutein, and J.A. Harrison. A reactive potential for hydrocarbons with intermolecular interactions. *Journal of Chemical Physics*, 112:6472, 2000.
- D.Y. Sun, D.J. Shu, M. Ji, F. Liu, M. Wang, and X.G. Gong. Pressure-induced hard-to-soft transition of a single carbon nanotube. *Physical Review B*, 70:165417, 2004.
- Y.J. Sun, F. Ma, D.Y. Ma, K.W. Xu, and P.K. Chu. Stress-induced annihilation of Stone-Wales defects in graphene nanoribbons. *Journal of Physics D*, 45:305303, 2012.
- Y.W. Sun, D.J. Dunstan, M.A. Hartmann, and D. Holec. Nanomechanics of carbon nanotubes. *Proceedings in Applied Mathematics and Mechanics*, 7:13, 2013.
- Y.W. Sun, I. Hernández, A.J. Ghandour, C. Rice, I.F. Crowe, M.P. Halsall, A. Sapelkin, J. Gonzalez, F. Rodriguez, and D.J. Dunstan. Resonance Raman spectroscopy of carbon nanotubes: pressure effects on G-mode. *High Pressure Research*, 34(2):191–197, 2014.
- A.C. Tang and F.Q. Huang. Stability rules of icosahedral (Ih or I) fullerenes. *Chemical Physics Letters*, 247:494–501, 1995.
- A. Tapia, R. Peón-Escalante, C. Villanueva, and F. Avilés. Influence of vacancies on the elastic properties of a graphene sheet. *Computational Materials Science*, 55:255–262, 2012.
- R.H. Telling, C.P. Ewels, A.A. El-Barbary, and M.I. Heggie. Wigner defects bridge the graphite gap. *Nature Materials*, 2:333–337, 2003.
- H. Terrones and M. Terrones. The transformation of polyhedral particles into graphitic onions. *Journal of the Physics and Chemistry of Solids*, 58:1789–1796, 1997.
- H. Terrones, R. Lv, M. Terrones, and M.S. Dresselhaus. The role of defects and doping in 2d graphene sheets and 1d nanoribbons. *Reports on Progress in Physics*, 75:062501, 2012.
- J. Tersoff. Empirical Interatomic Potential for Carbon, with Applications to Amorphous Carbon. *Physical Review Letters*, 61:2879, 1988a.
- J. Tersoff. New Empirical approach for the structure and energy of covalent systems. *Physical Review B*, 37:6991, 1988b.
- M. Todt, F.G. Rammerstorfer, O. Paris, and F.D. Fischer. Nanomechanical studies of the compressive behavior of carbon fibers. *Journal of Material Science*, 45:6845–6848, 2010.
- M. Todt, F.G. Rammerstorfer, F.D. Fischer, P.H. Mayrhofer, D. Holec, and M.A. Hartmann. Continuum modeling of van der Waals interactions between carbon onion layers. *Carbon*, 49:1620–1627, 2011.

- M. Todt, R.D. Bitsche, M.A. Hartmann, F.D. Fischer, and F.G. Rammerstorfer. Growth limit of carbon onions - a continuum mechanical study. *International Journal of Solids Structures*, 51:706–715, 2014a.
- M. Todt, F.G. Rammerstorfer, and M.A. Hartmann. Continuum shell models for closed cage carbon nanoparticles. In W. Pietraszkiewicz and J. Górski, editors, *Shell Structures: Theory and Applications*, pages 149–152. Taylor & Francis Group, London, UK, 2014b.
- S. Tomita, A. Burian, J.C. Dore, D. LeBolloch, M. Fujii, and S. Hayashi. Diamond nanoparticles to carbon onions transformation: X-ray diffraction studies. *Carbon*, 40:1469–1474, 2002.
- K.I. Tserpes. Strength of graphenes containing randomly dispersed vacancies. *Acta Mechanica*, 223:669–678, 2012.
- K.I. Tserpes and P. Papanikos. Finite element modeling of single-walled carbon nanotubes. *Composites: Part B*, 36:468–477, 2005.
- D. Ugarte. Curling and closure of graphitic networks under electron-beam irradiation. *Nature*, 359:707–709, 1992.
- D. Ugarte. Onion-like graphitic particles. *Carbon*, 33:989–993, 1995.
- L. Verlet. Computer "Experiments" on Classical Fluids. I. Thermodynamical Properties of Lennard-Jones Molecules. *Physical Review*, 159:98, 1967.
- D. Vollath. *Nanomaterials*. Wiley-VCH, Weinheim, 2008.
- J.H. Walther, R. Jaffe, T. Halicioglu, and P. Koumoutsakos. Carbon Nanotubes in Water: Structural Characteristics and Energetics. *Journal of Physical Chemistry B*, 105:9980, 2001.
- C.Y. Wang, C.Q. Ru, and A. Mioduchowski. Axially compressed buckling of pressured multiwall carbon nanotubes. *International Journal of Solids and Structures*, 40:3893–3911, 2003.
- M.C. Wang, C. Yan, L. Ma, N. Hu, and M.W. Chen. Effect of defects on fracture strength of graphene sheets. *Computational Materials Science*, 54:236 – 239, 2012.
- Y. Wang, X. Wang, X. Ni, and H. Wu. Simulation of elastic response and the buckling modes of single-walled carbon nanotubes. *Computational Material Science*, 32:141, 2005.
- S.J. Weiner, P.A. Kollman, D.A. Case, U.C. Singh, C. Ghio, G. Alagona, S. Profeta, and P. Weiner. A new force field for molecular mechanical simulation of nucleic acids and proteins. *Journal of the American Chemical Society*, 106(3):765, 1984.
- D.F. Windenburg and C. Trilling. Collapse by instability of thin cylindrical shells under external pressure. *Transactions of the American Society of Mechanical Engineers*, 56(11):819, 1934.

- J. Wu, K.C. Hwang, and Y. Huang. An atomistic-based finite-deformation shell theory for single-wall carbon nanotubes. *Journal of the Mechanics and Physics of Solids*, 56:279–292, 2008a.
- J. Wu, J. Peng, K.C. Hwang, J. Song, and Y. Huang. The intrinsic stiffness of single-wall carbon nanotubes. *Mechanics Research Communications*, 35:2–9, 2008b.
- Z. Xin, Z. Jianjun, and Q.Y. Zhong-can. Strain energy and Young’s modulus of single-wall carbon nanotubes calculated from electronic energy-band theory. *Physical Review B*, 62:13692–13696, 2000.
- M. Xu, J.T. Paci, J. Oswald, and T. Belytschko. A constitutive equation for graphene based on density functional theory. *International Journal of Solids and Structures*, 49:2582–2589, 2012a.
- M. Xu, A. Tabarraei, J.T. Paci, J. Oswald, and T. Belytschko. A coupled quantum/continuum mechanics study of graphene fracture. *International Journal of Fracture*, 173:163–173, 2012b.
- R. Xu, Y. Wang, B. Liu, and D. Fang. Mechanics interpretation on the bending stiffness and wrinkled pattern of graphene. *Journal of Applied Mechanics*, 80:040910–1–5, 2013.
- B.I. Yakobson, C.J. Brabec, and J. Bernholc. Nanomechanics of carbon tubes: Instabilities beyond linear response. *Physical Review Letters*, 76:2511–2514, 1996.
- X. Yao, Q. Han, and H. Xin. Bending buckling behaviors of single- and multi-walled carbon nanotubes. *Computational Material Science*, 43:579–590, 2008.
- D.-B. Zhang, E. Akatyeva, and T. Dumitrica. Bending Ultrathin Graphene at the Margins of Continuum Mechanics. *Physical Review Letters*, 106:255503, 2011.
- H.W. Zhang, L. Wang, and J.B. Wang. Computer simulation of buckling behavior of double-walled carbon nanotubes with abnormal interlayer distances. *Computational Material Science*, 39:664, 2007.
- Q.L. Zhang, S.C. O’Brien, J.R. Heath, Y. Liu, R.F. Curl, and H.W. Kroto et al. Reactivity of large carbon clusters: Spheroidal carbon shells and their possible relevance to the formation and morphology of soot. *Journal of Physical Chemistry*, 90:525–528, 1986.
- T. Zhang, X. Li, and H. Gao. Defects controlled wrinkling and topological design in graphene. *Journal of the Mechanics and Physics of Solids*, 67:2 – 13, 2014.
- M. Zhao, H. Song, X. Chen, and W. Lian. Large-scale synthesis of onion-like carbon nanoparticles by carbonization of phenolic resin. *Acta Materialia*, 55:6144–6150, 2007.
- Y.X. Zhao and I.L. Spain. X-ray diffraction data for graphite to 20 GPa. *Physical Review B*, 40:993–997, 1989.

Computational Technology Reviews
Volume 10, 89-119, 2014.
doi:10.4203/ctr.10.4
©Saxe-Coburg Publications, 2014



Computational Simulation of Instability Phenomena in Nanoparticles and Nanofilms

M. Todt¹, F. Toth¹, M.A. Hartmann², D. Holec³, M.J. Cordill⁴, F.D. Fischer⁵
and F.G. Rammerstorfer¹

¹Institute of Lightweight Design and Structural Biomechanics
Vienna University of Technology, Austria

²Institute of Physics, Montanuniversität Leoben, Austria

³Department of Physical Metallurgy and Materials Testing
Montanuniversität Leoben, Austria

⁴Erich Schmid Institute of Materials Science
Austrian Academy of Sciences, Leoben, Austria

⁵Institute of Mechanics, Montanuniversität Leoben, Austria

Abstract

In structural mechanics, instabilities, such as buckling under loads, are typically considered as failure modes. In contrast to this, the present review deals with modelling and computational simulation of instability phenomena with the objective of explaining and interpreting experimental observations at the micro and nano level. Different modelling techniques and simulation methods at different length scales are presented and discussed in terms of multi-scale/multi-method approaches. The presentation of problem solutions and comparisons with experimental results accompany the theoretical considerations.

A typical example treated is finding a reason for the growth limit of carbon onions, which are nanoparticles consisting of many concentrically arranged spherical graphene layers. Another example discussed in this review is shedding light onto the question of why carbon fibres, built by nanocrystallites consisting of graphene layers, show different axial stiffness in tension and in compression. In both of these examples the appearance of instabilities are possible explanations for the observed phenomena.

Computational simulations in combination with experiments are frequently used for determining material parameters of nano-structured systems which cannot be measured directly. An example of this approach is modelling and simulation of the behaviour of just a few nanometres thick films, which buckle locally under global tensile loading and lift up from the substrate to which they are bonded. The combination of experimental observations and computational considerations of this process provides a possible way of determining parameters for assessing the strength of the interface between film and substrate in terms of solving an inverse problem.

Atomistic as well as continuum mechanics modelling techniques for the computational simulation of such stability problems are presented. At the meso-level, the nanostructures considered here can be modelled as thin plates or shells in the frame-

work of continuum mechanics. However, for using this approach, for instance for nanoparticles built by several stacked graphene layers, an effective thickness and effective elastic properties of graphene must be determined, and the van der Waals interaction must be modelled appropriately. Different approaches for solving these problems are presented, too.

Keywords: buckling, nanoparticles, nanofilms, finite element method, Monte Carlo simulations, *ab initio*.

1 Introduction

Nanostructures, such as nanoparticles and nanofilms are, as the notation says structures in the sense of mechanics. Thus, like structures in engineering constructions, under certain circumstances they can lose their stability of equilibrium, and bifurcation or snap-through buckling can be observed. In this review paper, instability is to be understood in the above mentioned sense. In contrast to most instability considerations in structural engineering, in which buckling is treated as failure of the construction, for certain purposes instability can be a desired phenomenon. Typical examples for this desired effect on the nano level are reviewed, and selected examples are briefly discussed in this paper.

Knowledge of the mechanical properties of nanoparticles and nanofilms is of substantial importance for taking advantage of their exceptional behaviour in high performance materials or for applications in electronic devices. However, because of their small size common experimental methods for determining these properties directly quite often cannot be used. It has been shown that information regarding mechanical properties can be gained by combining experiments and simulation in the sense of defining and solving something like an inverse problem. Especially the onset of instabilities, *i.e.* determination of buckling loads, and the consideration of the post-buckling behaviour can be used beneficially for such purposes. This combined experimental-numerical approach requires not only carefully prepared and performed experiments but also reliable computational models and suitable simulation methods allowing considerations at different length scales from the atomistic up to micro-structural levels. In accordance with these requirements atomistic as well as continuum mechanical methods and models are reviewed under the aspect of multi-scale, multi-method approaches in the following sections.

Some modelling methods of different accuracy and length-scale applicability are briefly discussed. Most accurate for atomistic modelling are *ab initio* methods that solve the Schrödinger equation more or less directly. Atomistic classical molecular dynamics and Monte Carlo methods rely on the use of force fields whose parameters can be determined by *ab initio* methods. Lastly, continuum mechanical methods neglect the atomistic nature of matter using macroscopic elastic parameters.

Although the methods are described in a quite general sense, one should bear in mind that the main focus of this paper lies on stability considerations and their use for gaining mechanical properties and explaining or interpreting experimental observations at the micro and nano level.

For instance, continuum mechanics approaches for studying the mechanical behaviour of nanostructures quite often use shell models. Thus, knowledge of properties like Young's modulus E , Poisson's ratio ν , and shell thickness h , is required. Surprisingly, as will be shown in the following sections, published values for these parameters differ by orders of magnitude! Some of them are quite useful for describing the membrane behaviour of nanolayers but not for bending. The problem lies in the fact that a layer of atoms, e.g., a graphene layer does not have a clearly defined physical thickness, h , in the sense of structural mechanics. However, it exhibits measurable membrane and bending stiffnesses, both being structural characteristics of plates or shells that depend on the three parameters mentioned as long as linear elasticity and isotropy can be assumed. Certainly, E , h , and ν must be seen as effective properties characterizing atomic layers in terms of continuum mechanical structures, such as plates or shells. Due to the fact that the buckling behaviour of plates and shells depends on the membrane stiffness as well as on the bending stiffness, stability considerations for well defined nanostructures are suitable approaches for clarifying the unclear situation regarding E , h , and ν .

It is well known that in carbon fibres built by carbon nanocrystallites the longitudinal Young's modulus in compression is smaller than in tension. Directly measuring the compression modulus is very difficult. Thus, bending experiments are performed in which a shift of the neutral axis towards the compressed portion of the fibre's cross section can be observed indicating a lower stiffness under compression than under tension. It has been argued that buckling of the nanocrystallites could be the reason for this stiffness reduction under compression. Computational simulations on the nano level confirm this argument and allow determination of the nonlinear elastic behaviour of such carbon fibres by evaluating the post-buckling deformation of the nanocrystallites.

Carbon onions are special carbon nanostructures with promising prospects of revolutionizing such diverse fields as electronic devices, photovoltaic applications, light weight materials, or lubricants. Although the number of layers in carbon onions can become very large it seems to be limited. Thus, the question arises regarding what might cause such a growth limit. As shown in the present paper, loss of stability could be the reason for this.

In applications of nanofilms consisting of a stiff metallic layer on a rather soft polymer substrate the knowledge of the interface strength is of importance. Direct measurement of this property can hardly be performed. Here again consideration of instability phenomena offers an indirect way for determining the interface parameters by combining experiment and simulation.

In the present review article instability of nanostructures is mainly treated under

the above mentioned aspects rather than in a fully general way. This is the reason why buckling of nanotubes, widely studied in literature [9, 94], is not considered here.

2 Computational Tools

In the quantum mechanical framework, addressing the solution of the Schroedinger equation for multi-body problem, the interatomic forces governing structural relaxations as well system dynamics, are obtained from electronic structure via the Hellman-Feynmann theorem. Using the Born-Oppenheimer approximation (also called the adiabatic approximation), the multi-body eigenvalue problem can be decoupled into a separate multi-body problem for electrons and ion. Since the ions are several orders of magnitude heavier and their motion is several orders of magnitude slower than electrons, their motion is well described by classical Newtonian equations of motion. The electronic part, however, has to be treated fully quantum mechanically. The most common approach in material science is the density functional theory (DFT) [45, 58] in which the search for a multi-body wavefunction is replaced with the search for charge density distribution. The biggest advantage of *ab initio* techniques is that the only input information needed is about the atoms making up the structure (*i.e.*, the type of elements) and approximate structure. Subsequently, scenarios are allowed to develop which were not considered before the simulations. However, solving the underlying equations is a computationally expensive task, and therefore only applicable for small structures which do not possess the crystal symmetry, and are not applicable to large multi-layer structures. However they can be used to obtain parameters needed in molecular dynamics and Monte Carlo simulations and also continuum mechanical methods.

MC simulation is a tool used in statistical physics to determine the static, *i.e.* time-independent, equilibrium properties of many particle systems [62]. The basic input of MC simulation is an expression for the potential (configurational) energy of the system, which is nothing more than the force field in MD. Given the potentials the MC algorithm used, like the Metropolis or Glauber algorithm drives the system into equilibrium [36, 75]. As long as the algorithm used obeys detailed balance, the different states of the system occur with their proper Boltzmann weight allowing thermodynamic averaging. In contrast to MD methods that directly integrate Newton's equation of motion, thus effectively performing a time average, MC methods perform an ensemble average [31]. Standard MC procedures are applied in the canonical ensemble, but the generalization to other ensembles is straightforward [31].

The covered length scales of MC (and MD) simulations lie in between *ab initio* and continuum mechanical methods. Still atomistic in nature MC methods can deal with system sizes ranging from several thousands to millions of atoms. Continuum mechanical methods neglect the atomistic nature of matter using macroscopic constitutive laws. Usually the boundary value problem arising is solved by the finite element (FE) method or other discretisation approaches.

For the sake of completeness multi-scale models also are mentioned but not discussed in detail. Multi-scale models take advantage of both atomistic and continuum mechanical approaches. Thus, they can be used to investigate the mechanical behaviour of large carbon nanostructures, where at specific positions the local atomic configurations are of importance. The main issue of multi-scale models lies on the smooth bridging between the atomistic and continuum length scale. An exhaustive review of these methods can be found in [65, 66].

3 Instabilities in Carbon Nanoparticles

The term carbon nanoparticles embraces carbon nanotubes [9, 51, 84, 127], graphene [15, 34, 35, 81, 129], fullerenes [60, 101], carbon crystallites [67, 68], and carbon onions [6, 59, 114, 117]. Graphene is the strongest and thinnest material ever discovered [34] and the main building block of all carbon nanoparticles. Thus, these particles should inherit the exceptional properties of graphene, making them promising candidates as fillers in nanocomposites especially for electronics applications [9, 72, 98]. However, for an expedient application of carbon nanostructures their properties should be well understood. Much experimental work has already been done to study the structure and properties of such nanoparticles, see [6, 50, 60] and computational techniques have also been shown to be powerful tools for investigating carbon nanoparticles [20, 70, 127].

In this section the focus is on the analytical and computational treatment of instabilities in carbon nanoparticles, especially carbon crystallites and carbon onions, see Sections 3.2 and 3.3. Carbon onions even buckle without external loading. Another example for buckling of carbon nanostructures in the absence of external loads is the buckling of patches of graphene sheets discussed in [92] and papers cited therein. Carbon nanotubes are excluded from the following considerations, as detailed reviews on their buckling behaviour and their applications can be found elsewhere, see [9, 94].

3.1 Modelling Aspects

The simulation of instabilities in carbon nanostructures involves different aspects, such as the correct representation of the carbon layers, the van der Waals (vdW) interactions and for curved carbon nanoparticles also the description of the excess surface energy. The input parameters required and the simplifications to be made depend strongly on the simulation technique used.

Ab initio simulations, due to their complexity and, hence high computational costs, are usually not used to investigate stability phenomena in single and multi-layer carbon nanostructures. Furthermore, in *ab initio* simulations the treatment of vdW interactions is a complicated task due to their non-local long-range nature. Nevertheless some concepts are proposed in [23, 37]. In the context of investigating instability phenomena in large nanostructures *ab initio* methods are mainly used for determining

input parameters required in MC, MD or FE simulations and also for gaining information about the excess surface energy being active in curved carbon nanoparticles.

In MC simulations the atoms forming the layers are explicitly modelled where the interactions between the individual atoms are described via potentials. Most famous is the Tersoff-Brenner potential [12, 13, 105]. Potentials are either found empirically or by *ab initio* calculations. Thus, most important for a reliable simulation is the knowledge of the underlying potential. A successful approach is to decompose the full potential into a sum of many body interactions

$$E = E_{stretch} + E_{bend} + E_{torsion} + \dots + E_{nonbond}. \quad (1)$$

with $E_{stretch}$ representing the two body stretching potential, E_{bend} being the three body bending potential, $E_{torsion}$ the four body torsion potential and $E_{nonbond}$ for all non-covalent interactions, *i.e.* vdW or Coulombic interactions. Additional coupling terms, like stretching-bending or stretching-torsion, may also be added [2, 73]. In literature many parameter sets can be found that have been shown reasonably well to describe the carbon-carbon interactions.

Using *ab initio* calculations another parameter set was obtained and tested using MC simulations in [46]. The parameters for the stretching and bending potential were obtained by calculating the energy of deformed, but still planar graphene, while the torsion contribution was found by analysing nanotubes of different sizes and chiralities. Whenever possible the results of the *ab initio* calculations and MC simulations were compared to investigate the influence of the classical approximation according to Equation (1) on the outcome of the simulations. It was shown further in [46] that the splitting of the energies into a sum of different contributions as given by Equation (1) is not exact.

In comparison with *ab initio* and MC simulations, continuum mechanic tools have rather low computational costs and have been shown to be appropriate for studying the mechanical properties of carbon nanostructures [84, 99, 127, 128]. Within the continuum approach the layers of carbon nanostructures can be modelled either as a space frame structure using beam and/or spring elements [64, 89] or as continuum shells [84, 127], where only continuum shell models are considered in this review.

Using continuum shells for modelling carbon layers was first proposed by Jakobson *et al.* [127]. It is assumed that the layers can be modelled as thin, linear elastic, isotropic shells possessing a membrane stiffness $C = Eh$ and a bending stiffness $D = \frac{Eh^3}{12(1-\nu^2)}$, where E is the Young's modulus, ν the Poisson's ratio, and h the layer thickness. E , ν , and h should be treated as effective properties; they must always be considered in combination, leading at the same time to proper values for the membrane and the bending stiffness. The elastic constants are obtained by MD simulations leading to $E = 5500$ GPa, $\nu = 0.19$, and $h = 0.066$ nm. The consistency of this approach is confirmed in [126] by investigating the strain energy of carbon nanotubes. Isotropic thin shell models are successfully applied *e.g.*, in [84] to study buckling of multi-walled carbon nanotubes. More advanced shell models are

proposed, e.g. in [3, 4, 18, 124] allowing the capture of some features like the chirality introduced anisotropy of the carbon layers but also increasing the complexity of the models. However, the effect of anisotropy vanishes fast with increasing size of the carbon nanoparticles, see [18] and need not be considered as long as strains are small [125].

The small strain assumption holds for the carbon nanoparticles being investigated in the following, so the shell model proposed in [127] is used. Nanoindentation experiments revealed that graphene behaviour is elastic [63] almost until breaking. Therefore, the layer properties can be described using three independent parameters: the elastic modulus E , Poisson's ratio ν , and the layer thickness h . Although, as discussed in the previous paragraph, using continuum shell models for carbon nanostructures is well established, the choice of the appropriate parameters is far from obvious. Since the first attempts to determine these parameters made in [127] much experimental and theoretical work has been carried out to estimate the elastic properties of a single carbon layer. Nevertheless, the values of the parameters given span an extremely wide range. The values reported for the membrane stiffness range from 159 to 480 N/m [15, 63, 124, 131] (and references therein). An even broader range of different values spanning more than one order of magnitude is reported for the effective thickness of graphene, ranging from $h = 0.617$ to 6.9 \AA [48]. This peculiar behaviour of the thickness was given the name Yakobson Paradox [93]. Among the different suggestions proposed to resolve this paradox is the observation that the thickness of nanotubes is not constant, but may depend on its size, chirality and loading situation [48] or that plate theory breaks down for a monolayer of graphene [129]. Using the potential obtained in [46] Hartmann *et al.* [41] determined the bending stiffness and Poisson's ratio by stretching graphene, while the thickness was found by determining the compressive buckling load of graphene sheets of different lengths. It was found that graphene sheets longer than 50 \AA could be described well with $C = 313 \text{ N/m}$, $\nu = 0.1844$ and $h = 1.32 \text{ \AA}$. For graphene patches smaller than 50 \AA the continuum approximation breaks down and the effective thickness decreases.

In multi-layer carbon nanoparticles the vdW interactions in terms of interaction forces between the individual layers must be considered in addition to the layer behaviour. VdW interactions are non-local induced dipole interactions between uncharged atoms or molecules and are relatively weak compared to covalent bonds between the atoms forming a layer. The non-local interactions between two atoms can be described using a pair potential of the interaction forces, where usually the Lennard-Jones (LJ) potential [54]

$$U_{12} = 4\epsilon \left[\left(\frac{\sigma}{r} \right)^{12} - \left(\frac{\sigma}{r} \right)^6 \right], \quad (2)$$

is used with r being the current atom-atom distance. The parameters σ and ϵ describe the atom-atom distance at $U_{12} = 0$ and the depth of the potential well, respectively, see Figure 1. These parameters are usually referred to as Lennard-Jones parameters, and values can be found in [71, 130]. The pair potential consists of an attractive part

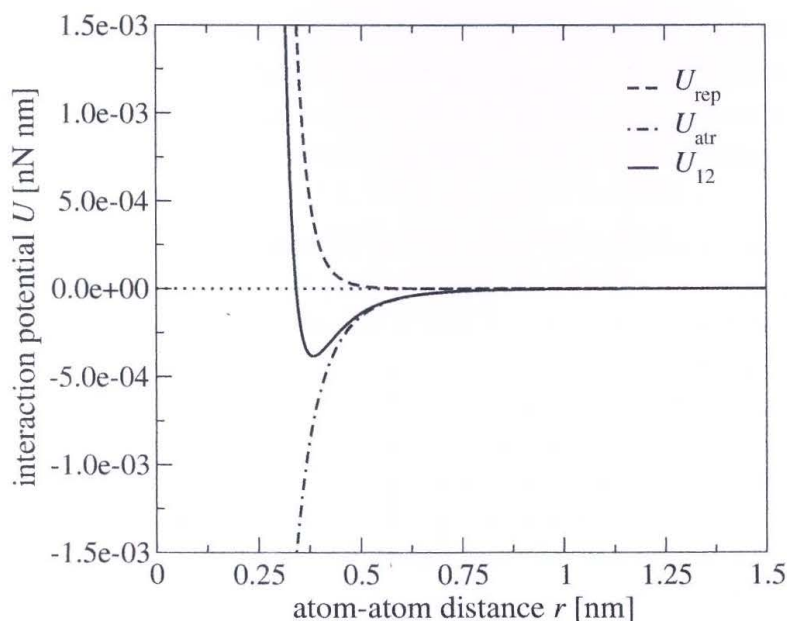


Figure 1: Van der Waals interaction potential U of two interacting carbon atoms for $\sigma = 0.3415 \text{ nm}$ $\epsilon = 0.00239 \text{ eV}$ (values taken from [71])

$U_{\text{atr}} = \left(\frac{\sigma}{r}\right)^6$ and a repulsive part $U_{\text{rep}} = \left(\frac{\sigma}{r}\right)^{12}$. The 6th power in the attractive part follows from the London equation [69], whereas the 12th power in the repulsive part is used only for practical reasons and has no specific physical meaning.

In atomistic description the vdW interactions between two layers result from vdW interactions between discrete atoms forming the layers. In MD or MC simulations the vdW interactions are included via the term E_{nonbond} , see Equation (1), where for E_{nonbond} the LJ-potential given in Equation (2) can be used. The atom-atom interactions, however, are not applicable in continuum mechanical shell models where pressure-distance relations are more suitable. In the case of planar nanoparticles (graphite or multi-layer graphene) it is justified to assume that opposite layers consist of the same number of atoms leading to equal vdW pressures on the opposing layers. Pressure distance relations for planar nanoparticles can be found in [54, 107]. For curved carbon nanoparticles like multi-walled carbon nanotubes or carbon onions the number of atoms in neighbouring layers is not the same. This different number of atoms has to be considered in the formulation of the vdW interactions to obtain appropriate pressure distance relations [71, 107]. Based on the work of Hamaker [39] for spherical nanoparticles in [107] a pressure distance relation for carbon onions is derived by integrating over the vdW interactions between different layers, where the number of atoms in the layers is accounted for by the atom area density. A similar approach is used in [71] to obtain a pressure-distance-relation for multi-walled carbon nanotubes. It is shown in [71, 107] that using a correct vdW model is especially crucial if the displacements and the subsequent stresses in the layers are of importance if the mechanical stability of a structure is considered. However, the analytical vdW mod-

els have the drawback that they hardly can be incorporated into standard commercial FE codes. Thus, for finite element simulations usually the pressure distance relations derived for planar carbon nanoparticles are used [84, 106, 128].

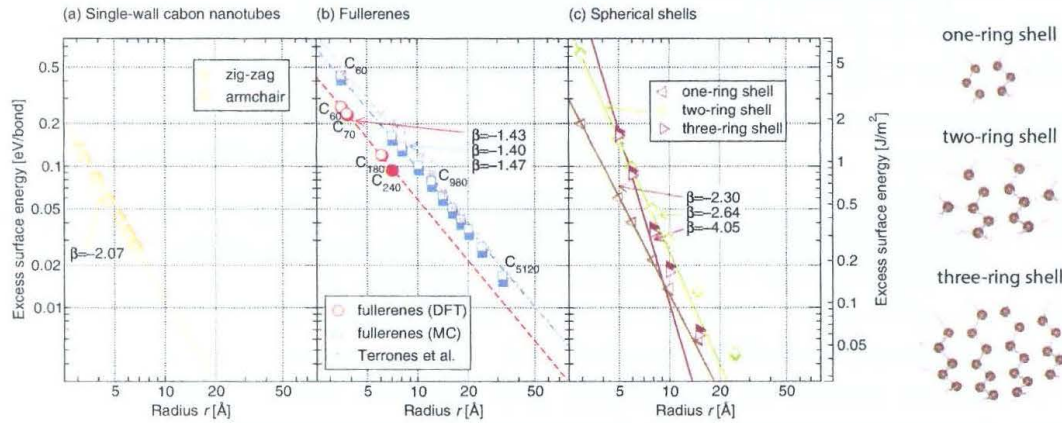


Figure 2: Double logarithmic plot of excess surface energy vs radius: (a) the zigzag (down triangle) and armchair (up triangle) SWNTs from the DFT calculations, (b) fullerenes as calculated by *ab initio* (circles) and the MC (squares) using the full structures, and (c) the ring-shell models fitted for data with $r > 10 \text{ \AA}$. The full (open) symbols correspond to the generalised gradient approximation (local density approximation) approximations. This figure from [46] appears with permission of APS publishing

For curved nanoparticles such as fullerenes, carbon onions, or carbon nanotubes the intrinsic curvature induced excess surface energy $E^{(S)}$ [46] has to be considered. In [46] both *ab initio* and MC simulations showed that the excess surface energy can be well fitted by a power law $E^{(S)} \sim r^\beta$, where r is the radius of the curved structure. The values obtained for the fitting parameter β range from -1.40 to -2.51 depending on the type of nanostructure considered, see Figure 2. Due to the high computational costs *ab initio* calculations could only be performed for fullerenes up to the C_{240} , while MC simulations could extend this range up to C_{5120} . The MC simulations also revealed that for curved structures like fullerenes the torsion contribution is by far the largest contribution to the total energy albeit its small force constant. Due to the presence of the excess surface energy a surface stress $\sigma^{(S)}$ develops as a "plane hydrostatic" stress state. For spherical particles the Shuttleworth equation [29] $\sigma^{(S)} = E^{(S)} + \frac{dE^{(S)}}{d\epsilon^{(S)}}$ holds, where $\epsilon^{(S)}$ is the strain in each circumferential direction. For a first estimate the second term of this relation can be neglected leading to $\sigma^{(S)} = E^{(S)}$. Note that $E^{(S)}$ and $\sigma^{(S)}$ are physically different quantities possessing the same unit (force per unit length). In a finite element model $\sigma^{(S)}$ can be taken into account by applying an external pressure $p^{(S)} = \frac{2\sigma^{(S)}}{r}$. As can be seen from Figure 2 the excess surface energy, and consequently the surface stress, decreases fast with increasing radius r . Therefore, it is only of relevance for small carbon nanoparticles.

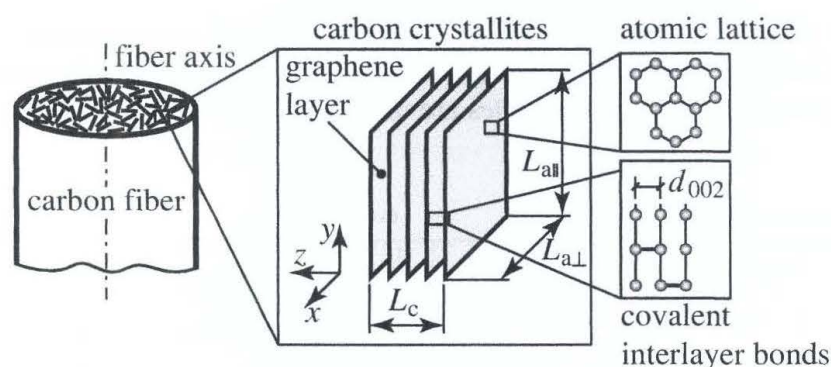


Figure 3: Nanostructure of PAN-based carbon fibres. This figure from [110] appears with kind permission from Springer Science+Business Media

3.2 Carbon Crystallites

Carbon fibre reinforced plastics are widely used for structural applications in aircraft, space, automotive, and sports industries. Hence, the mechanical properties of carbon fibres are of great interest and subject of intense research [42, 67, 78, 91]. The tensile properties of the fibres are well described [78, 91]. Estimating the compressive properties is more difficult due to the small diameters of the fibres and their consequential tendency towards buckling. Some testing methods like the loop test [95], the single fibre composite test [43], or the direct compression method [82] have been developed to overcome the problem of fibre buckling. An extensive overview about these methods can be found in [82].

Bending experiments of polyacrylonitril (PAN) based fibres revealed a non-Hookean fibre behaviour in compression, which is related to buckling phenomena occurring in the nanostructure of the fibre [42]. The cross section of such a PAN fibre is depicted in Figure 3. PAN fibres usually show a skin-core structure [85], where the outer surface is formed by a skin-like layer and randomly distributed carbon crystallites form the inner region. In [79, 83] it is assumed that these crystallites buckle if the fibre is subjected to compressive loading and in [24] fibre failure is related to crystallite buckling. Microbeam x-ray diffraction of bent carbon fibers revealed a shift of the neutral axis towards the stretched area of the cross section indicating crystallite buckling [67]. These experimental results show that the mechanical behaviour of carbon fibres under compression is dominated by instability phenomena on the nano scale, *i.e.* crystallite buckling.

To get further insight into the mechanisms determining the compressive behaviour of PAN fibres a continuum mechanical study of the stability of carbon crystallites under compressive loading was performed in [110]. For this purpose a continuum shell model of a single crystallite is used and the finite element method is employed for solving the arising boundary value problem. In the following the modelling assumptions used and the results obtained in [110] are briefly discussed.

In [110] the layers of the crystallite schematically shown in Figure 3 are assumed

to be oriented parallel to the fibre axis and modelled as thin elastic plates with $E = 5.5 \text{ TPa}$, $\nu = 0.19$, and 0.066 nm (values taken from [127]), interacting with each other by vdW interactions and covalent interlayer bonds. For the crystallite dimensions parallel and perpendicular to the fibre axis $L_{a\parallel} = 4.32 \text{ nm}$ and $L_{a\perp} = 3.87 \text{ nm}$, respectively, are used being in good agreement with experimental values [24, 83]. The vdW interactions between adjacent layers are considered using the pressure-distance-relation $p(\alpha) = \frac{C_{33}}{6} \left[\left(\frac{\sigma}{\alpha}\right)^{10} - \left(\frac{\sigma}{\alpha}\right)^4 \right]$ with $C_{33} = 36.5 \text{ GPa}$, see [54]. The equilibrium vdW distance $\alpha_{\text{eq}} = \sigma$ is chosen as $\sigma = 0.344 \text{ nm}$ giving a good approximation of experimental values ranging from 0.339 nm to 0.356 nm [68, 83]. The crystallite is assumed to consist of eight layers resulting in a total width of $L_c = 2.512 \text{ nm}$ which is in the range of experimentally determined values [24]. Furthermore, covalent interlayer bonds connecting two adjacent layers (see Figure 3) are taken into account. Possible sources of such bonds are vacancies or interstitial atoms [103] within the layers or dangling bonds at their edges [103]. In [14] it is shown that covalent interlayer bonds constrain sliding between nanotube walls and that the load transfer between the tubes is best if the bonds are uniformly distributed. Covalent interlayer bonds may also be an explanation of the "compared to graphite" increased shear modulus of carbon crystallites in PAN fibres observed in [68]. For the sake of simplicity, in [110] the interlayer bonds are modelled as trusses with their axial stiffness being far larger than the membrane stiffness of the layers. It is assumed that the bonds at the edges and in the interior of the crystallite are similar and that they locally reduce the interlayer distance to $d_c = 0.258 \text{ nm}$ [103]. Two different distributions of the interlayer bonds are investigated where (i) the bonds are distributed over the whole crystallite (including the edges) and (ii) the bonds are distributed only along the edges.

To get a reasonable representation of the self-equilibrated stress state in the layers due to interlayer bond formation the bonds are first introduced with an initial length of $d_c^{(0)} = 0.344 \text{ nm}$. Then the bonds are subjected to a virtual temperature change, ΔT , reducing their length from $d_c^{(0)}$ to $d_c = 0.258 \text{ nm}$, where the boundary conditions are chosen in a form to constrain the crystallite as little as possible. The deformations of the crystallite obtained by this initial step are illustrated in Figure 4 (left and middle). The vdW interactions between adjacent layers prevent a uniform distance reduction leading to the formation of dimples at the interlayer bond locations. If the bonds are randomly distributed within the whole crystallite the layers remain almost parallel to the fibre axis (y -axis) and only local dimples form, see Figure 4 (a). In contrast to this deformation pattern a pre-bending deformation in the form of an overall bulge can be observed if the interlayer bonds are located only at the edges, as shown in Figure 4 (b). This bulge leads to a misalignment of the whole crystallite with respect to the fibre axis, resulting in a larger geometrical imperfection in terms of structural stability analysis notations.

The different deformation states obtained after the initial step lead to different behaviours of the crystallites when subjected to compressive loading. The axial compression is applied via prescribed displacements u_y in the direction of the fiber axis, where all layers are assumed to be subjected to the same axial displacement at the up-

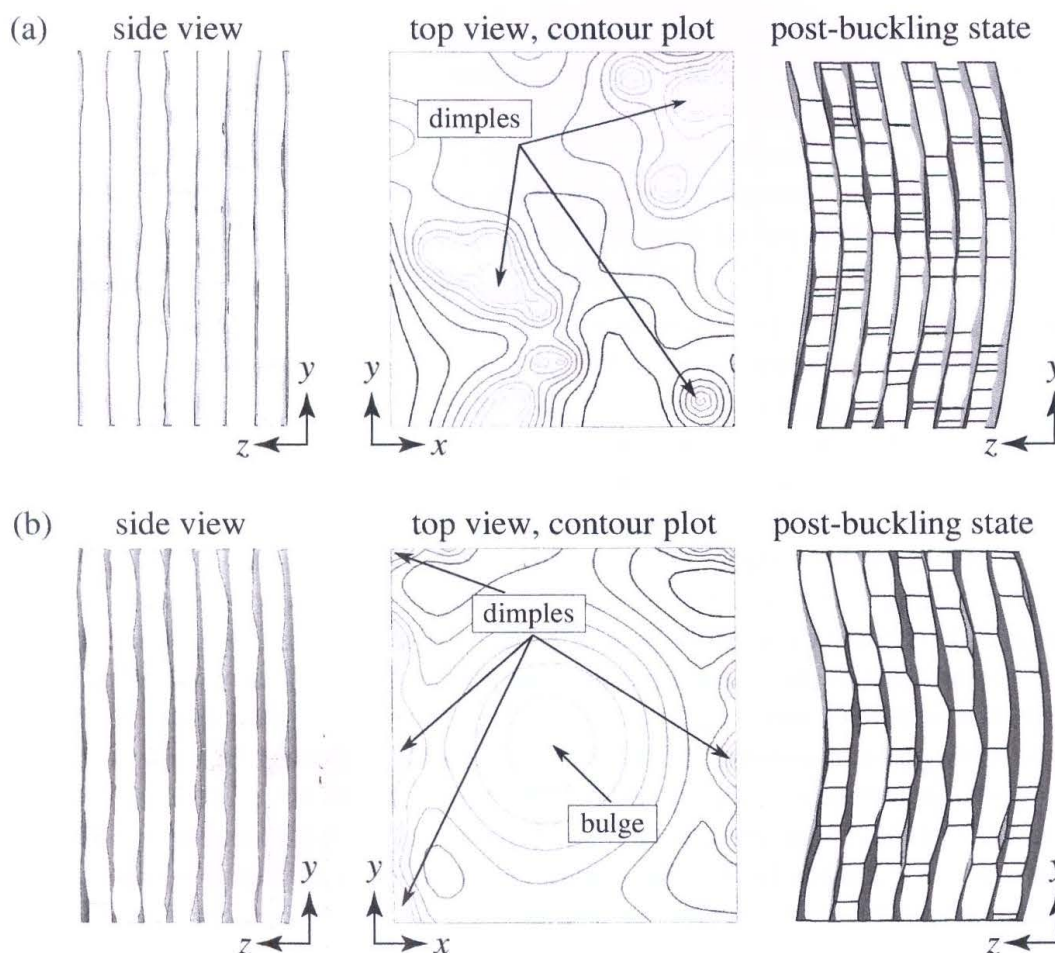


Figure 4: Deformation states of carbon crystallites with their interlayer bonds being randomly distributed over the whole crystallite (a) or being located only at the edges (b). The side view of the deformation state after the formation of the interlayer bonds and the corresponding contour lines of the z -displacements of the uppermost layer are depicted on the left side and in the middle, respectively [110]. The right figure shows the post-buckling state due to the applied axial displacement

per edge. The obtained post-buckling states of the compressed crystallites are depicted in Figure 4 (right). The distribution of the interlayer bonds has no significant influence on the character of the post-buckling shape. In both cases an overall bending deformation occurs and no layer separation can be observed. Although the post-buckling behaviour seems to be independent of the distribution of interlayer bonds, the load-displacement behaviour shows a strong dependency on the bond distribution and also on the amount of interlayer bonds. Figure 5 shows the obtained secant modulus E_S of the crystallites depending on the amount of interlayer bonds and the distribution of the bonds. If the interlayer bonds are distributed over the whole crystallite, secant moduli in the range of 1076 GPa to 1158 GPa are obtained for the pre-buckling state. E_S remains almost constant until buckling occurs, where the critical strain in-

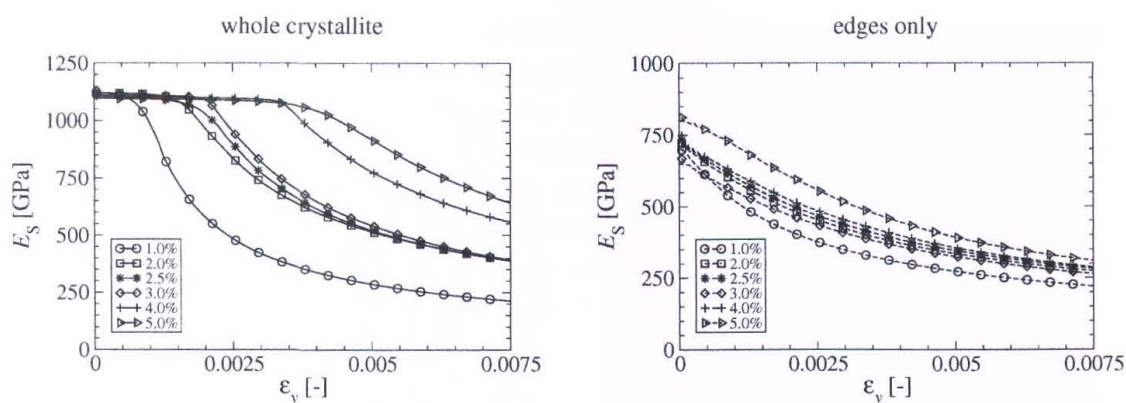


Figure 5: Secant modulus E_S in compression in dependence on the different proportions of covalent interlayer bonds, expressed in terms of % of bonded pairs of atoms; (left) for interlayer bonds distributed randomly in the whole crystallite and (right) for bonds distributed at the edges only

creases substantially with the amount of interlayer bonds. If the interlayer bonds are located only at the edges of the crystallite much lower secant moduli ranging from 670 GPa to 812 GPa are obtained and no constant regime of E_S is observed. E_S decreases with increasing compressive strain and is almost independent of the amount of interlayer bonds. It can be concluded that covalent bonds randomly distributed over the whole crystallite have a stabilizing effect, whereas interlayer bonds located only at the edges lead to a reduction of the axial stiffness of the crystallites already for small compressive loads. Comparison with experimental values of the secant modulus (1140 ± 40 GPa [68]) show that it is more likely that interlayer bonds form within the whole crystallite and not only at the edges. The reduction of the secant modulus after the onset of buckling observed for this distribution of interlayer bonds is a possible explanation for the shift of the neutral axis observed experimentally for bent PAN fibres. Generally it can be said that with the continuum shell model used the behaviour of carbon crystallites can be well predicted. Although the crystallite model includes some simplifications it can serve as the basis for further investigations regarding the compressive behaviour of carbon fibres.

3.3 Carbon Onions

Carbon onions are almost spherical carbon nanostructures consisting of a number of concentric carbon layers. Figure 6 shows a transmission electron micrograph and a sketch of the atomic structure of such carbon nanostructures, respectively.

Carbon onions were first discovered by Iijima in 1980 [50] and can be produced by intense electron irradiation of soot [114]. Since that time several production techniques have become available to produce carbon onions such as electron irradiation of graphite at elevated temperatures ($> 300^\circ\text{C}$) [6, 7], annealing of diamond nanoparticles [53, 111], high pressure transformation of single-crystal graphite [10], using a

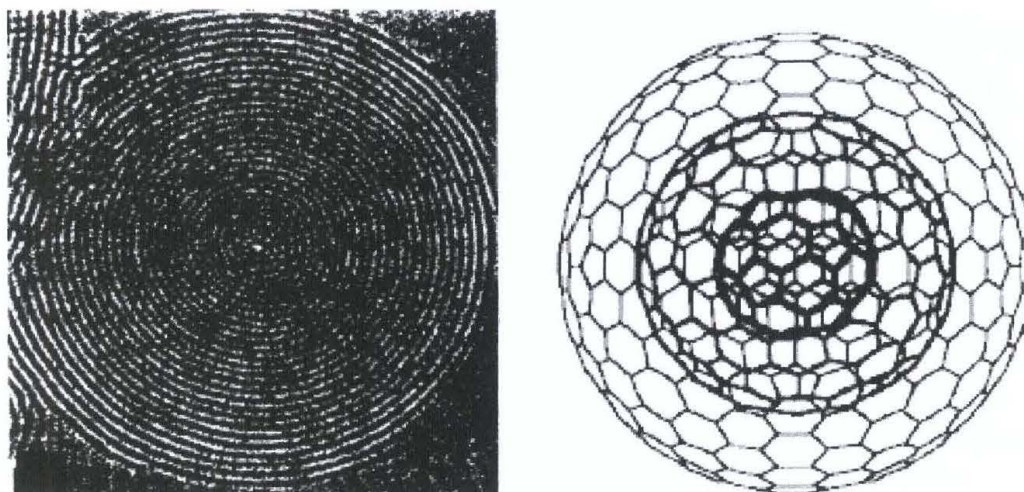


Figure 6: Transmission electron microscope (TEM) micrograph of a carbon onion (left) from Banhart *et al.* [7], appears with permission from Elsevier and (right) the atomic structure of carbon onions from Ugarte [117] appears with permission from Elsevier

radio frequency plasma process [26, 32], or synthesis by decomposition of phenolic resin [132].

The different productions techniques lead to different growth scenarios. Onions produced by high pressure transformation of graphite or by radio frequency plasma synthesis seem to grow from the inside to the outside [10, 26]. This type of growth scenario is directly observed in [33] and [20]. Atomistic simulations performed in [20] revealed that the formation of a single close-caged carbon layer is a multi-step process. First, the loss of carbon atoms at the edges of the graphene flake lead to the formation of pentagonal atomic rings resulting in a curvature of the graphene sheet [17]. Then the free edges of the curved graphene sheet zip open and form the closed cage structure. In contrast to onions produced by high-temperature annealing of nanodiamonds the onion starts its formation at the outer boundaries of the nanodiamond [61, 111]. This growth scenario is also proposed in [50, 115] for particles produced by electric arc discharge experiments. Atomistic simulations of this kind of onion formation show that at a temperature of 1500K the outer region of the nanodiamond transforms into graphitic layers [70]. Increasing the temperature to 3000K leads to a graphitization of the whole nanodiamond.

Some of the present production techniques lead to rather polyhedral particles [10, 32, 60, 132], leading to the assumption that the layers of these particles and also of carbon onions are icosahedral fullerenes [8, 59, 102]. The polyhedral particles can be transformed to spherical particles by intense irradiation [6, 7, 114]. Irradiation at room temperature leads to almost spherical particles containing many defects, whereas irradiation at elevated temperatures (≈ 700 K) leads to perfectly spherical particles [7].

At elevated temperatures a shrinkage of the layers is also observed which is attributed to a knocking out of atoms and a rearrangement of the atoms in the individual layers [7, 116]. In [104, 122] it is shown by atomistic simulations that the formation of additional pentagonal rings or Stone-Wales defects leads to a higher sphericity of the layers. However, the formation of the pentagonal rings and Stone-Wales defects is not necessarily caused by the loss of atoms in the layers. Irradiation at temperatures above ≈ 900 K leads to the shrinkage of the layers, but also to the formation of nanodiamonds in the centre of large onions [5, 6, 87].

From an application point of view, carbon onions should, due to their similar structure, inherit the exceptional mechanical and electrical properties of graphene. These properties make them promising candidates as fillers in nanocomposites, especially for electronics applications [9, 72, 98], as additives in lubricants [53], or as solid lubricants [44].

In all applications the size of the multi-layered particles is of substantial interest. But what is the maximum size to which these particles can be grown? In reality carbon onions can consist only of a few layers [53, 117], be of intermediate size [7, 10], or consists of many layers [123, 134] with diameters up to 50 nm. In [134] it is shown that the precursor material and the irradiation dose influence the size of the particles. Thus, the questions arise, can carbon onions be grown to far larger sizes, or is there a growth limit?

This question is extensively addressed in [106]. The main modelling assumptions and results discussed therein are briefly reviewed in the following. In contrast to investigations in [102] the deformations of the onion layers due to vdW interactions are considered and the assumption of the layers remaining spherical due to deformation is abandoned in [106].

In [106] all investigations regarding the growth limit of carbon onions are based on the assumption that the size of these particles is limited by the occurrence of a structural instability. This instability is stated to be evoked by the formation of an additional layer on an already existing onion. The carbon onions are assumed to consist of perfect spherical and concentric layers. To keep computational costs low an axi-symmetric shell model is used which is admissible for the pre- and also for the post-buckling state [25, 90]. The layers are modelled using thin shells with $E = 4840$ GPa, $\nu = 0.19$ and $h = 0.075$ nm. This set of shell parameters has shown to give reasonable results for the mechanical properties of single fullerene layers [108]. Due to the relatively high stiffness of the innermost layers of a carbon onion, buckling most likely occurs in the outer regions of the onions. As the curvature effect of the vdW interactions is only of importance for the innermost layers [84], neglecting this effect seems to be admissible. Therefore, the pressure-distance relations given in [54, 107] for planar carbon nanoparticles are used to describe the vdW interactions between the layers. To simulate the growth of carbon onions it is assumed that they grow layer-by-layer starting with the innermost layer. Each layer of the carbon onion is assumed to be an icosahedral fullerene [57, 101] consisting of $n = 60i^2$ atoms [101], with $i = 1, 2, \dots$ denoting

the layer number and $i = 1$ for the innermost layer. The radius $R^{(0)}$ of a fullerene is related to the number of its atoms n by $R^{(0)} = a^{(0)}\sqrt{0.103374 n - 0.424548}$ [120] where $a^{(0)}$ is the carbon-carbon bond length. Therefore, the radii of the onion layers are not arbitrary leading to a distance α between an already existing onion and a newly formed layer that is usually different from the equilibrium distance α_{eq} of the vdW interactions. As a consequence the vdW interactions between a new layer and the onion underneath become active introducing compressive or tensile stresses in the new layer and all layers underneath. The excess surface energy, resulting in membrane compressive stresses due an external pressure, gives significant contributions to the stress states in small, *i.e.* in the most inner fullerenes only (compare Figure 2 and [46]). Analysis with a simplified vdW model has shown that it has no influence on the growth limit of carbon onions [106, 109] thus, it is not considered further. The boundary value problem arising when a new layer is added to an existing onion is solved using the finite element method. The self-equilibrated stress state introduced by the vdW interactions may lead to the occurrence of a structural instability. Therefore, a buckling analysis is performed after each added layer in order to check whether or not the carbon onion has grown to its critical size. The corresponding eigenvalue problem is defined as

$$\left(\mathbf{K}_{\approx N} + \bar{\lambda}_N^j \Delta \bar{\mathbf{K}}_{\approx N} \right) \bar{\Phi}_N^j = \mathbf{0} \quad (3)$$

with $\mathbf{K}_{\approx N}$ being the stiffness matrix of the N -layered onion in its equilibrium state including the vdW interactions. The matrix $\Delta \bar{\mathbf{K}}_{\approx N}$ represents the change in the stiffness of the onion due to an external pressure $p_N^{(\text{ext})}$. The variables $\bar{\lambda}_N^j$ and $\bar{\Phi}_N^j$ are the eigenvalues and the corresponding eigenvectors, respectively. For this model the smallest eigenvalue $\bar{\lambda}_N^1$ is the factor by which the pressure $p_N^{(\text{ext})}$ on the outermost layer has to be multiplied to bring the N -layered onion to a critical state. The external pressure $p_N^{(\text{ext})}$ is required as perturbation load in the eigenvalue analysis and must not necessarily have a physical meaning. It is defined as the critical pressure of the newly added layer without the supporting layers underneath and, thus, reads [86]

$$p_N^{(\text{ext})} = \frac{2Eh^2}{\sqrt{3(1-\nu^2)}(R_N^{(0)})^2}, \quad (4)$$

where $R_N^{(0)}$ is the radius of the new undeformed layer. The choice of $p_N^{(\text{ext})}$ as critical pressure of the layer is not based on necessity but provides information about the effect of bedding due to the inner layers. An eigenvalue $\bar{\lambda}_N^1 \leq 1$ means that the external pressure leading to buckling of the onion is smaller than the critical pressure of the outermost layer. The growth limit of the onion is indicated by $\bar{\lambda}_N^1 = 0$ meaning that no external pressure is required to bring the onion to its critical state and that the self-equilibrated stress state introduced by the vdW interactions is sufficient to cause buckling. To investigate the influence of the vdW interactions on the growth limit of the onion different vdW models and parameter sets are used which are listed in Table 1.

Figure 7 (left) shows the results of the eigenvalue analysis for the different vdW models listed in Table 1. For a low number of layers $\bar{\lambda}_N^1$ first increases to values far

Model	Equation	σ in nm	ϵ in eV	$C_{33}/6$ in GPa	C_0 in GPa
M1S1	[54], values [71]	0.3415	0.00239	6.083	-
M2S1	[107], values [71]	0.3415	0.00239	-	4.79
M1S2	[54], values [130]	0.3345	0.00319	6.083	-
M2S2	[107], values [130]	0.3345	0.00319	-	6.26

Table 1: Nonlinear vdW models used in the stability analysis of carbon onions

larger than 1. This indicates that the critical pressure of the onion is larger than the critical pressure of the outermost layer, *i.e.* the outermost layer is sufficiently supported by the layers underneath to prevent buckling. After a certain number of layers is reached the inner layers still support the outermost layer but the supporting effect is reduced with every additional layer. An eigenvalue $\bar{\lambda}_N^1 = 0$ is not reached as the algebraic system describing the boundary value problem becomes ill-conditioned (the stiffness matrix \mathbf{K}_N approaches a singularity). The maximum number of layers reached depends slightly on the pressure-distance-relation used but rather strongly on the LJ-parameters used in the relations. The largest onion obtained in the analysis has about 72 layers, which is close to experimental observations [7]. In Figure 7 (right) an example of a buckling mode is depicted, revealing that the outermost layers start to buckle whereas the innermost layers remain almost unaffected. This is because only the outermost layers of the onion are under compression, see Figure 8, where the number of layers under compression increases during the growth of the onion.

The simulations show that the occurrence of a structural instability is a possible explanation for the limited size of carbon onions. The self-equilibrating stress state leading to this instability emerges due to accommodation of misfitting carbon layers during the growing process and is introduced by the vdW interactions between the layers. The critical sizes of the onions obtained are highly sensitive to the interlayer distances and compressive constants used in the vdW models and, thus have a qualitative rather than a quantitative character. Furthermore, some other effects, such as interlayer bonds or other combinations of fullerenes can lead to much larger layer numbers. Nevertheless, the models used clearly indicate a growth limit of carbon onions and can serve as a basis for further investigations concerning the growth of such particles.

3.4 Conclusions - Nanoparticles

In conclusion, it can be said that continuum shell models are appropriate to investigate instabilities occurring in carbon nanostructures. For the nanoparticles investigated in this review the mechanical behaviour is qualitatively well predicted. For the carbon crystallites the quantitative behaviour also could be well predicted and verified against experimental data. However further experiments and atomistic simulations are required to reduce the scattering for the input parameters for the layers as well as for the vdW interactions.

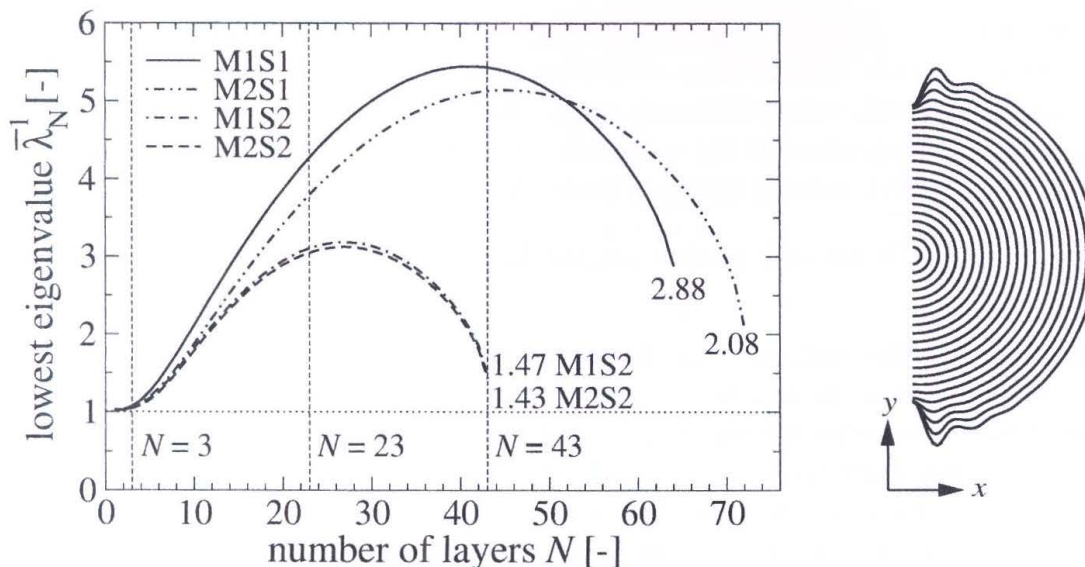


Figure 7: Lowest eigenvalue $\bar{\lambda}_N^{-1}$ versus the current number of layers N forming the carbon onion (left), where the different curves correspond to the different vdW interface models. The right figure shows an example of a buckling mode of a carbon onion where only every second layer is shown. Both figures are from [106] appearing with permission from Elsevier

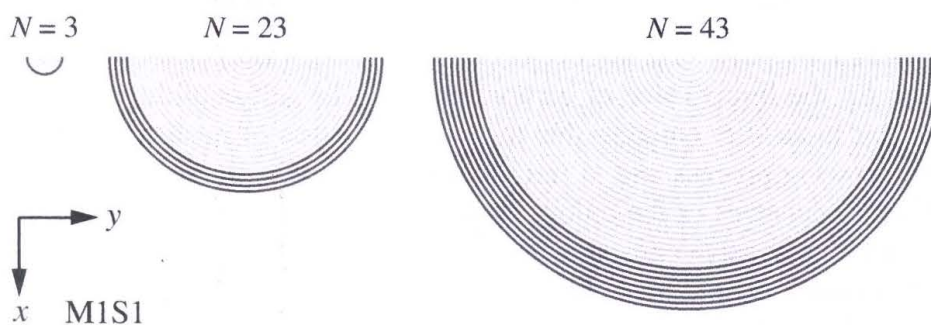


Figure 8: Number of layers under compression (black) and tension (grey) for onions of different sizes. Figure from [106] appears with permission from Elsevier

4 Instabilities in Nanofilms

In this section the stability of a class of nanostructure, namely nanofilms, is treated which, albeit in dimensions of nanometres, can be simulated directly by continuum mechanics methods.

A very recent review on film buckling and delamination can be found in [80]. While early works on buckling and delamination of thin films consider these phenomena as failure modes [49], advances in the understanding of the underlying instability phe-

nomena have resulted in useful applications. For example, in flexible electronics applications instability phenomena are exploited in order to create highly stretchable forms of semiconducting materials [55, 100] or metal interconnects [121], also summarized in a review by Rogers [88]. Wrinkling of stiff films on compliant substrates creates patterns in the micrometer regime [11]. Understanding of this wrinkling phenomenon enables the creation of defined patterns for applications such as optical gratings [40], or microfluidic sieves [27]. On the other hand, wrinkling patterns can be used to identify the properties of thin films [19, 47, 96, 97], nanowires [16] or nanotubes [56].

Depending on the combination of film and substrate either wrinkling or buckling and delamination can occur. In some cases concomitant wrinkling and buckling delamination is possible [74]. Buckling and delamination are preferred over wrinkling for films with higher bending stiffness, softer substrates and weaker interfaces. By a selective introduction of weaknesses in the interface microfluidic networks can be created between buckled film and substrate [76].

In systems where delamination buckling is observed, this phenomenon may be used to determine the interface parameters between film and substrate [21, 22, 112, 119]. Various ways exist to introduce buckling delamination. In some cases buckles form spontaneously due to compressive residual stresses in the film, which may result from the production process, thermal dilatation, swelling, etc. Spontaneous buckles may form in various shapes from blisters to worm-like telephone-cord buckles [21] and complex patterns [76]. The formation of telephone-cord buckles is energetically favourable for certain film-substrate combinations [77], and apart from analytical descriptions computational simulations have been used to describe the buckle formation [28, 38, 52].

In experiments where the interface strength should be deduced from the buckling delamination, it is necessary that buckles can be produced in a well controlled manner. This can be done for example by indentation [119, 133], especially for stiff substrates. For films on compliant substrates compressive stresses may be introduced by bending experiments [1, 118]. Another method is to use the uni-axial tension test [22, 112]. Here the brittle film first cracks perpendicular to the straining direction, forming thin film strips between so called channel cracks. Due to the Poisson's effect the substrate is compressed in the transverse in-plane direction. This leads to compressive stress in the film strips which finally cause buckling and delamination.

4.1 Modelling Buckling-Delamination in Uni-axial Tension Tests

The uni-axial tension test can be used to introduce buckling delamination of thin, brittle films on compliant substrate [22, 30, 112]. Common test samples consist of a thin (in the micrometer regime) polymer substrate to which an even thinner (in the nanometre regime) film is bonded. Small (several millimetre), rectangular compound specimens are strained in a tension test device. The strained specimens show a global curvature with the free edges curved downwards, as can be seen in Figure 9. The

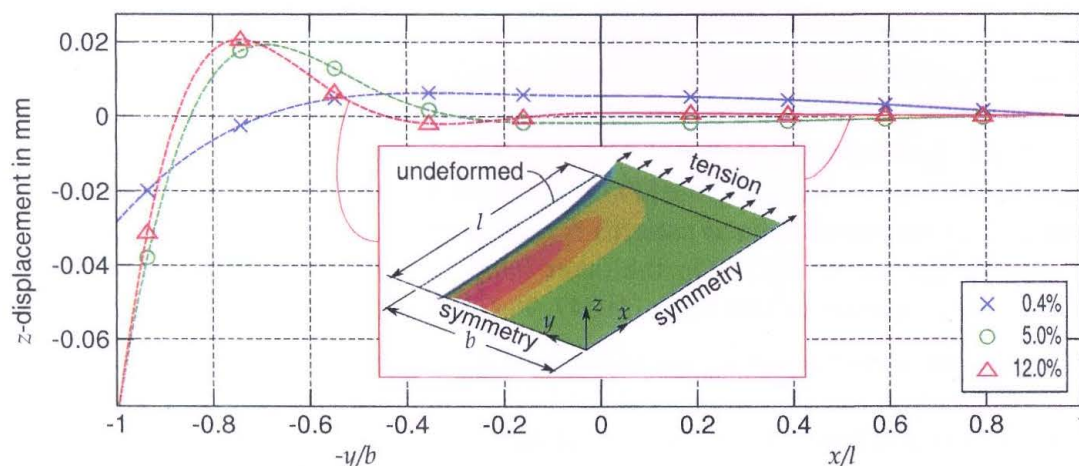


Figure 9: The z -displacements in the symmetry planes of a specimen with cracked film at different global strain levels

global curvature arises due to the non-symmetric laminate composed of a thick layer of compliant substrate joined with the thin stiff film on top.

At low strain ($<1\%$) the brittle film fractures perpendicular to the straining direction forming channel cracks. The number of channel cracks per specimen length in straining direction, *i.e.* the crack density, grows with increasing strain until no further cracks can form. At this point, the crack density with respect to the global strain reaches a constant. Due to the Poisson's effect the specimen shrinks in a transverse direction, which leads to compressive stresses in the transverse direction in the film strips (between the channel cracks). These compressive stresses are widely independent of the mismatch of the Poisson's ratio of film and substrate. Because of the presence of channel cracks the film is free of normal stresses along the straining direction. Finally, the growing compressive stresses lead to buckling of the film strips and delamination from the substrate. Figure 10(a) shows typically observed crack patterns with buckled film strips. Buckles, *i.e.* post-buckling deformations occur in two different characters classified by the shape of their footprint area, rectangular and triangular, see Figure 10(b).

Buckling starts at a critical global strain, which can be determined experimentally. As the global strain level at which buckling commences depends on the interface parameters, they can be deduced from experimental results in combination with results of computational simulations if this dependency can be appropriately quantified.

Analytical models have been developed for solving this type of inverse problem [22, 49]. However, these models suffer from their simplifying assumptions, particularly, the assumptions of two dimensional geometry and linear elasticity of the materials. To overcome these limitations a computational modelling procedure of the uni-axial tension test has been proposed in [112]. There, a two stage modelling procedure was employed.

In a macromodel the complete tension test specimen was modelled by composite

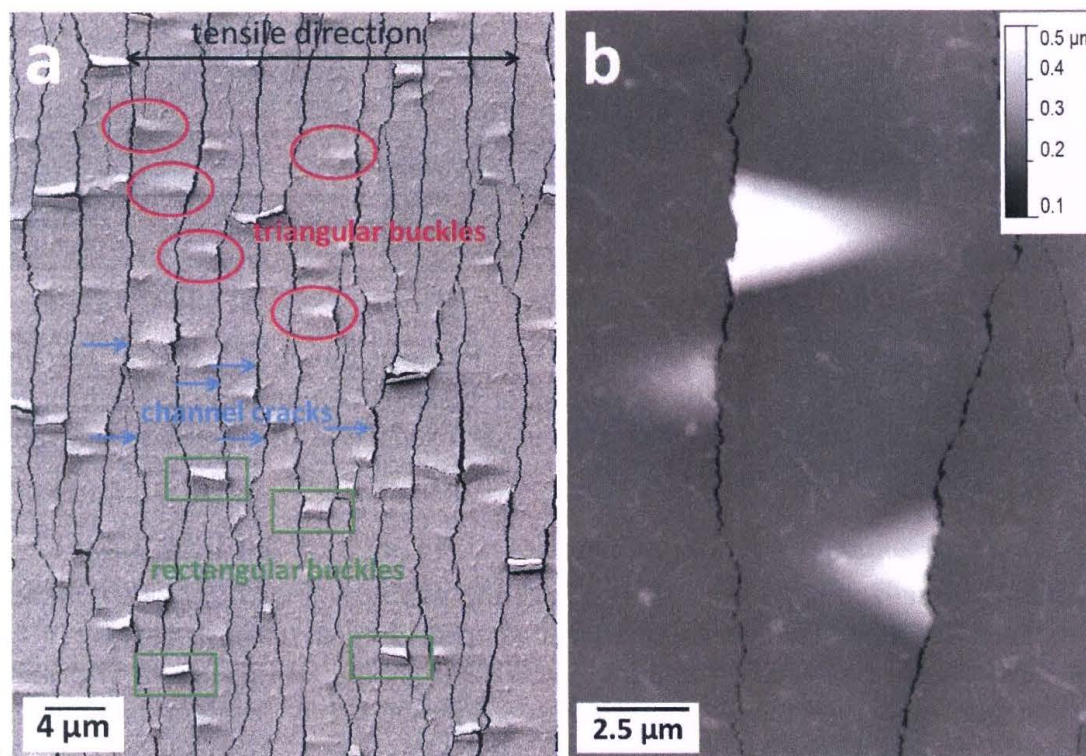


Figure 10: Typical channel crack pattern with buckled film strips (a), and, in detail, triangular buckles (b)

shell elements. The loss of longitudinal stiffness due to the appearance of multiple transverse film cracks (the channel cracks) can be appropriately taken into account by modelling the film with beam elements oriented transversely to the global straining direction. These beam elements represent the film strips between channel cracks. Nonlinear material behaviour as well as geometrical non-linearities are taken into account. The global deformation of the tension test specimen as well as the strain state at arbitrary points can be computed for every global strain of interest. In this way displacement boundary conditions for the micro model, comprising of a part of a single film strip, are obtained.

The micro model is a three dimensional model of a part of a film strip with underlying substrate. Film and substrate are connected by cohesive zone elements, which behave according to their traction separation relation [113]. A bilinear traction separation law was chosen, and the ultimate traction as well as the energy release rate, *i.e.* the work of separation per unit area, were varied in a parameter study to determine the relation between the global strain at which buckling occurs and the interface parameters.

In the finite element model a small initial imperfection introduced in order to trigger buckling and bifurcation from the trivial equilibrium path was used. The formation of the buckles with progressive delamination is widely independent of the initial imperfection, provided it is sufficiently small. A typical sequence in the post-buckling

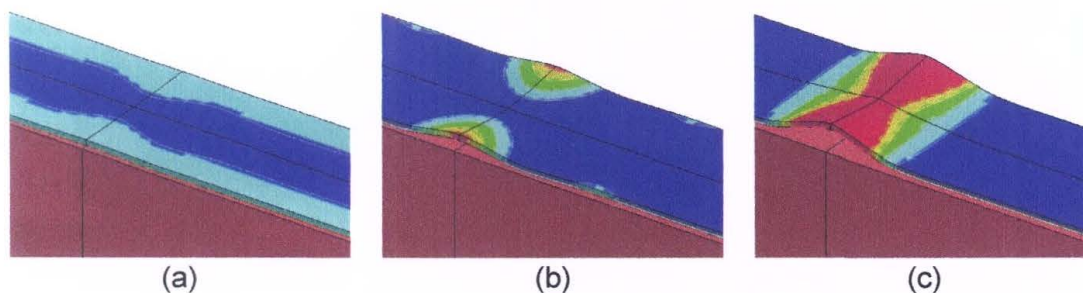


Figure 11: Sequence of buckle formation: (a) Mode II failure at edges of the film strip; (b) Localisation at the initial imperfection and formation of a triangular buckle; (c) Change to mode I failure in the interface and rapid delamination, from [112]

process is visualized in Figure 11. The buckling process starts with mode II failure of the interface along the channel cracks, accompanied by an upwards curving of the film strip edges. Eventually the failure localizes at the initial imperfection forming a triangular buckle. As the triangular buckle grows the failure mode in the interface gradually changes to mode I, and the delaminated area grows towards the center of the film strip. Once the center is reached the two (symmetric) triangular buckles join and the film rapidly delaminates.

Observing the load displacement diagram (Figure 12) relating the global strain to the gap width between film and substrate, *i.e.* the buckle height, one can clearly recognise the critical global strain at which the bifurcation instability takes place and the buckle starts to form.

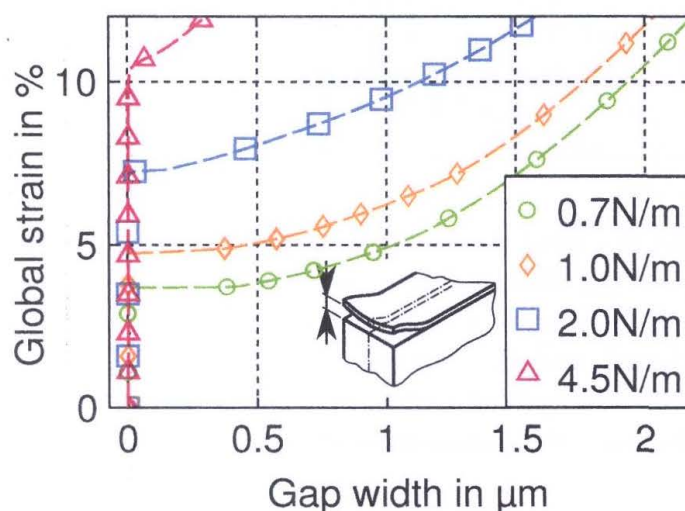


Figure 12: Dependence of the gap width between film and substrate on the global strain for different values of the interface energy release rate. Modified figure, after [112]

5 Conclusion

In this review paper an overview is provided on methods and models for simulating the stability behaviour of nano-sized structures, such as nanoparticles and nanofilms. It is shown that careful simulations of instability phenomena can help in explaining and interpreting experimental observations at the micro and nano level.

In particular the rather unclear situation regarding structural mechanical properties, such as Young's modulus, Poisson's ratio, and thickness, of graphene layers is clarified. Furthermore, it is shown how multi-scale and multi-method computational modelling and simulation can be used for determining mechanical properties on the nano scale and can shed light onto experimental observations which ask for interpretation.

In this sense the decrease of the longitudinal Young's modulus of carbon fibres under compression can be explained by buckling of the nanocrystallites forming the fibre. As a possible answer to the question of what limits the size of carbon onions, the appearance of instabilities is discussed, and it is shown how careful simulation of buckling and delamination of nanofilms on compliant substrates in combination with experiments allows the determination of interface strength parameters in an indirect way.

Acknowledgements

Partial funding of the research study has been provided by the Austrian Science Fund FWF (project no. P22648-N20)

References

- [1] A.A. Abdallah, D. Kozodaev, P.C.P. Bouten, J.M.J. den Toonder, U.S. Schubert, G. de With, "Buckle morphology of compressed inorganic thin layers on a polymer substrate", *Thin Solid Films*, 503: 167–176, 2006.
- [2] N.L. Allinger, Y.H. Yuh, J.H. Lii, "Molecular mechanics. The MM3 force field for hydrocarbons. 1", *J. Am. Chem. Soc.*, 111: 8551, 1989.
- [3] R. Ansari, H. Rouhi, "Analytical treatment of the free vibration of single-walled carbon nanotubes based on the nonlocal Flugge shell theory", *Journal of Engineering Materials and Technology*, 134: 011008, 2012.
- [4] B. Arash, Q. Wang, "A review on the application of nonlocal elastic models in modeling of carbon nanotubes and graphenes", *Computational Materials Science*, 51: 303–313, 2012.
- [5] F. Banhart, "The transformation of graphitic onions to diamond under electron irradiation", *Journal of Applied Physics*, 81: 3440–3445, 1997.

- [6] F. Banhart, P. Ajayan, “Carbon onions as nanoscopic pressure cells for diamond formation”, *Nature*, 382: 433–435, 1996.
- [7] F. Banhart, T. Füller, P. Redlich, P. Ajayan, “The formation, annealing and self-compression of carbon onions under electron irradiation”, *Chemical Physics Letters*, 269: 349–355, 1997.
- [8] D. Baowan, N. Thamwattana, J. Hill, “Continuum modelling of spherical and spheroidal carbon onions”, *European Physical Journal D*, 44: 117–123, 2007.
- [9] R. Baughman, A. Zakhidov, W. de Heer, “Carbon Nanotubes – the Route Toward Applications”, *Science*, 297: 787–792, 2002.
- [10] V. Blank, V. Denisov, A. Kirichenko, B. Kulnitskiy, S.Y. Martushov, B. Mavrin, I.A. Perezhogin, “High pressure transformation of single-crystal graphite to form molecular carbon onions”, *Nanotechnology*, 18: 345601, 2007.
- [11] N. Bowden, S. Brittain, A.G. Evans, J.W. Hutchinson, G.M. Whitesides, “Spontaneous formation of ordered structures in thin films of metals supported on an elastomeric polymer”, *Nature*, 393(6681): 146–149, May 1998.
- [12] D.W. Brenner, “Empirical potential for hydrocarbons for use in simulating the chemical vapor deposition of diamond films”, *Phys. Rev. B*, 42: 9458, 1990.
- [13] D.W. Brenner, O.A. Shenderova, J.A. Harrison, S.J. Stuart, B. Ni, S.B. Sinnott, “A second-generation reactive empirical bond order (REBO) potential energy expression for hydrocarbons”, *J. Phys.: Condens. Matter*, 14: 783, 2002.
- [14] E. Byrne, A. Letertre, M. McCarthy, W. Curtin, Z. Xia, “Optimizing load transfer in multiwall nanotubes through interwall coupling: Theory and simulation”, *Acta Materialia*, 58: 6324–6333, 2010.
- [15] E. Cadelano, P.L. Palla, S. Giordano, L. Colombo, “Nonlinear Elasticity of Monolayer Graphene”, *Phys. Rev. Lett.*, 102: 235502, 2009.
- [16] Y.P. Cao, X.P. Zheng, B. Li, X.Q. Feng, “Determination of the elastic modulus of micro- and nanowires/tubes using a buckling-based metrology”, *Scripta Materialia*, 61: 1044–1047, 2009.
- [17] F. Cataldo, “The impact of a fullerene-like concept in carbon black science”, *Carbon*, 40: 157–162, 2002.
- [18] T. Chang, “A molecular based anisotropic shell model for single-walled carbon nanotubes”, *Journal of the Mechanics and Physics of Solids*, 58: 1422–1433, 2010.
- [19] J.Y. Chung, A.J. Nolte, C.M. Stafford, “Surface Wrinkling: A Versatile Platform for Measuring Thin-Film Properties”, *Advanced Materials*, 23: 349–368, 2011.
- [20] A. Chuvilin, U. Kaiser, E. Bichoutskaia, N. Besley, A. Khlobystov, “Direct transformation of graphene to fullerene”, *Nature Chemistry*, 2: 450–453, 2010.
- [21] M. Cordill, D. Bahr, N. Moody, W. Gerberich, “Adhesion measurements using telephone cord buckles”, *Materials Science and Engineering: A*, 443: 150–155, 2007.
- [22] M.J. Cordill, F.D. Fischer, F.G. Rammerstorfer, G. Dehm, “Adhesion energies of Cr thin films on polyimide determined from buckling: Experiment and model”, *Acta Mater*, 58(16): 5520 – 5531, 2010.

- [23] M. Dion, H. Rydberg, E. Schröder, D. Langreth, B. Lundqvist, “Van der Waals Density Functional for General Geometries”, *Physical Review Letters*, 92: 246401, 2004.
- [24] M. Dobb, H. Guo, D. Johnson, C. Park, “Structure-compressional property relations in carbon fibres”, *Carbon*, 33: 1553–1559, 1995.
- [25] M. Drmota, R. Scheidl, H. Troger, E. Weinmüller, “On the imperfection sensitivity of complete spherical shells”, *Computational Mechanics*, 2: 63–74, 1987.
- [26] A.B. Du, X.G. Liu, D.J. Fu, P.D. Han, B.S. Xu, “Onion-like fullerenes synthesis from coal”, *Fuel*, 86: 294–298, 2007.
- [27] K. Efimenko, M. Rackaitis, E. Manias, A. Vaziri, L. Mahadevan, J. Genzer, “Nested self-similar wrinkling patterns in skins”, *Nat Mater*, 4(4): 293–297, Apr. 2005.
- [28] J.Y. Faou, G. Parry, S. Grachev, E. Barthel, “How Does Adhesion Induce the Formation of Telephone Cord Buckles?”, *Physical Review Letters*, 108(11), Mar 2012.
- [29] F. Fischer, T. Waitz, D. Vollath, N. Simha, “On the role of surface energy and surface stress in phase-transforming nanoparticles”, *Progress in Materials Science*, 53: 481–527, 2008.
- [30] S. Frank, U.A. Handge, S. Olliges, R. Spolenak, “The relationship between film fragmentation and buckle formation: Synchrotron-based in situ studies and two-dimensional stress analysis”, *Acta Mater*, 57: 1442–1453, 2009.
- [31] D. Frenkel, B. Smit, *Understanding Molecular Simulation*, Academic Press, 2002.
- [32] D. Fu, X. Liu, X. Lin, T. Li, H. Jia, B. Xu, “Synthesis of encapsulating and hollow onion-like fullerenes from coal”, *Journal of Material Science*, 42: 3805–3809, 2007.
- [33] T. Füller, F. Banhart, “In situ observation of the formation and stability of single fullerene molecules under electron irradiation”, *Chemical Physics Letters*, 254: 372–378, 1996.
- [34] A. Geim, “Graphene: Status and Prospects”, *Science*, 324: 1530–1534, 2009.
- [35] A. Geim, K. Novoselov, “The rise of graphene”, *Nature Materials*, 6: 183–191, 2007.
- [36] R.J. Glauber, “Time-dependent statistics of Ising Model”, *J. Math. Phys.*, 4: 294, 1963.
- [37] S. Grimme, “Accurate description of van der Waals complexes by density functional theory including empirical conditions”, *Computational Chemistry*, 25: 1463–1473, 2004.
- [38] F. Gruttmann, V.D. Pham, “A finite element model for the analysis of buckling driven delaminations of thin films on rigid substrates”, *Computational Mechanics*, 41(3): 361–370, 2008.
- [39] H. Hamaker, “The London–van der Waals attraction between spherical particles”, *Physica IV*, 10: 1058–1072, 1937.
- [40] C. Harrison, C.M. Stafford, W. Zhang, A. Karim, “Sinusoidal phase grating

- created by a tunably buckled surface”, *Applied Physics Letters*, 85(18): 4016–4018, 2004.
- [41] M.A. Hartmann, M. Todt, F.G. Rammerstorfer, F.D. Fischer, O. Paris, “Elastic properties of graphene obtained by computational mechanical tests”, *Europhys. Lett.*, 103: 68004, 2013.
- [42] H. Hawthorne, “On non-Hookean behavior of carbon fibers in bending”, *Journal of Material Science*, 28: 2531–2535, 1993.
- [43] H. Hawthorne, E. Teghtsoonian, “Axial compression fracture in carbon fibres”, *Journal of Material Science*, 10: 41–51, 1975.
- [44] A. Hirata, M. Igarashi, T. Kaito, “Study on solid lubricant properties of carbon onions produced by heat treatment of diamond clusters or particles”, *Tribology International*, 37: 899–905, 2004.
- [45] P. Hohenberg, W. Kohn, “Inhomogeneous Electron Gas”, *Phys. Rev.*, 136: B864–B871, Nov 1964.
- [46] D. Holec, M.A. Hartmann, F.D. Fischer, F.G. Rammerstorfer, P.H. Mayrhofer, O. Paris, “Curvature-induced excess surface energy of fullerenes: Density functional theory and Monte Carlo simulations”, *Phys. Rev. B*, 81: 235403, 2010.
- [47] J. Huang, M. Juszkiwicz, W.H. de Jeu, E. Cerda, T. Emrick, N. Menon, T.P. Russell, “Capillary Wrinkling of Floating Thin Polymer Films”, *Science*, 317(5838): 650–653, 2007.
- [48] Y. Huang, J. Wu, K.C. Hwang, “Thickness of graphene and single-wall carbon nanotubes”, *Phys. Rev. B*, 74: 245413, 2006.
- [49] J.W. Hutchinson, Z. Suo, “Mixed mode cracking in layered materials”, *Adv Appl Mech*, 29: 63–191, 1992.
- [50] S. Iijima, “Direct observation of the tetrahedral bonding in graphitized carbon black by high resolution electron microscopy”, *Journal of Crystal Growth*, 50: 675–683, 1980.
- [51] S. Iijima, “Helical microtubules of graphitic carbon.”, *Nature*, 354: 56–58, 1991.
- [52] E.A. Jagla, “Modeling the buckling and delamination of thin films”, *Phys. Rev. B*, 75: 085405, Feb 2007.
- [53] L. Joly-Pottuz, N. Matsumoto, H. Kinoshita, B. Vacher, M. Belin, G. Montagnac, J.M. Martin, N. Ohmae, “Diamond-derived carbon onions as lubricant additives”, *Tribology International*, 41: 69–78, 2008.
- [54] B. Kelly, *Physics of Graphite*, pages 79–80, Advanced Science Publishers, 1981.
- [55] D.Y. Khang, H. Jiang, Y. Huang, J.A. Rogers, “A Stretchable Form of Single-Crystal Silicon for High-Performance Electronics on Rubber Substrates”, *Science*, 311(5758): 208–212, 2006.
- [56] D.Y. Khang, J. Xiao, C. Kocabas, S. MacLaren, T. Banks, H. Jiang, Y.Y. Huang, J.A. Rogers, “Molecular Scale Buckling Mechanics in Individual Aligned Single-Wall Carbon Nanotubes on Elastomeric Substrates”, *Nano Letters*, 8 (1): 124–130, 2008.
- [57] D. Klein, W. Seitz, T. Schmalz, “Icosahedral symmetry carbon cage

- molecules”, *Nature*, 323: 703–706, 1986.
- [58] W. Kohn, L.J. Sham, “Self-Consistent Equations Including Exchange and Correlation Effects”, *Phys. Rev.*, 140: A1133–A1138, Nov 1965.
- [59] H. Kroto, “Carbon onions introduce new flavour to fullerene studies”, *Nature*, 359: 670–671, 1992.
- [60] H. Kroto, J. Heath, S. O’Brien, R. Curl, R. Smalley, “C60: Buckminsterfullerene”, *Nature*, 318: 162–163, 1985.
- [61] V. Kuznetsov, A. Chuvilin, Y. Butenko, I. Malkov, V. Titov, “Onion-like carbon from ultra-disperse diamond”, *Chem Phys Lett*, 222: 343–348, 1994.
- [62] D.P. Landau, K. Binder, *A Guide to Monte-Carlo Simulations in Statistical Physics*, Cambridge University Press, 2009.
- [63] C. Lee, X. Wei, J. Kysar, J. Hone, “Measurement of the elastic properties and intrinsic strength of monolayer graphene”, *Science*, 321: 385–388, 2008.
- [64] C. Li, T. Chou, “A structural mechanics approach for the analysis of carbon nanotubes”, *International Journal of Solids and Structures*, 40: 2487–2499, 2003.
- [65] K. Liew, Y. Sun, “Computational Modelling and Simulation of Carbon Nanotubes”, in B. Topping, J. Adam, F. Pallarés, R. Bru, M. Romeo (Editors), *Development and Applications in Engineering Computational Technology*, pages 201–217. Saxe-Coburg Publications, Stirlingshire, Scotland, 2010.
- [66] W. Liu, E. Karpov, S. Zhang, H. Park, “An introduction to computational nanomechanics and materials”, *Computer Methods in Applied Mechanics and Engineering*, 193: 1529–1578, 2004.
- [67] D. Loidl, O. Paris, M. Burghammer, C. Riekkel, H. Peterlik, “Direct Observation of nanocrystallite buckling in carbon fibers under bending load”, *Physical Review Letters*, 95: 225501, 2005.
- [68] D. Loidl, H. Peterlik, M. Müller, C. Riekkel, O. Paris, “Elastic moduli of nanocrystallites in carbon fibers measured by in-situ X-ray microbeam diffraction”, *Carbon*, 41: 563–570, 2003.
- [69] F. London, “Zur Theorie und Systematik der Molekularkräfte”, *Zeitschrift für Physik*, 63: 245–279, 1930.
- [70] J. Los, N. Pineau, G. Chevrot, G. Vignoles, J. Leyssale, “Formation of multi-wall fullerenes from nanodiamonds studied by atomistic simulations”, *Physical Review B*, 80: 155420, 2009.
- [71] W. Lu, B. Liu, J. Wu, J. Xiao, K. Hwang, S. Fu, Y. Huang, “Continuum modeling of van der Waals interactions between carbon nanotube walls”, *Applied Physics Letters*, 94: 101917, 2009.
- [72] J. Macutkevic, D. Seliuta, G. Valusis, J. Banys, P. Kuzhir, S. Maksimenko, V. Kuznetsov, S. Moseenkov, O. Shenderova, P. Lambin, “Dielectric properties of onion-like carbon based polymer films: Experiment and modeling”, *Solid State Sciences*, 11: 1828–1832, 2009.
- [73] J.R. Maple, M.J. Hwang, T.P. Stockfisch, U. Dinur, M. Waldman, C.S. Ewig, A.T. Hagler, “Derivation of Class II Force Fields. I. Methodology and Quantum Force Field for the Alkyl Functional Group and Alkane Molecules”, *J. Comput.*

- Chem.*, 15: 162, 1994.
- [74] H. Mei, C.M. Landis, R. Huang, “Concomitant wrinkling and buckle-delamination of elastic thin films on compliant substrates”, *Mech Mater*, 43 (11): 627–642, 2011.
- [75] N. Metropolis, A.W. Rosenbluth, M.N. Rosenbluth, A.H. Teller, E. Teller, “Equation of State Calculations by Fast Computing Machines”, *J. Chem. Phys.*, 21: 1087–1092, 1953.
- [76] M.W. Moon, S. Chung, K.R. Lee, K.H. Oh, H.A. Stone, J.W. Hutchinson, “Directed assembly of fluidic networks by buckle delamination of films on patterned substrates”, *International Journal of Materials Research*, 98: 1203–1208, 2007.
- [77] M.W. Moon, H.M. Jensen, J.W. Hutchinson, K.H. Oh, A.G. Evans, “The characterization of telephone cord buckling of compressed thin films on substrates”, *J Mech Phys Solids*, 50: 2355–2377, 2002.
- [78] K. Naito, Y. Tanaka, J. Yang, Y. Kagawa, “Tensile properties of ultrahigh strength PAN-based, ultrahigh modulus pitch-based and high ductility pitch-based carbon fibers”, *Carbon*, 46: 189–195, 2008.
- [79] M. Nakatani, M. Shioya, J. Yamashita, “Axial compressive fracture of carbon fibers”, *Carbon*, 37: 601–608, 1999.
- [80] Y. Ni, A.K. Soh, “On the growth of buckle-delamination pattern in compressed anisotropic thin films”, *Acta Materialia*, 69(0): 37–46, 2014.
- [81] K. Novoselov, A. Geim, S. Morozov, D. Jiang, Y. Zhang, S. Dubonos, I. Grigorieva, A. Firsov, “Electric field effect in atomically thin carbon films”, *Science*, 306: 666–669, 2004.
- [82] N. Oya, D. Johnson, “Direct measurement of longitudinal compressive strength in carbon fibres”, *Carbon*, 37: 1539–1544, 1999.
- [83] N. Oya, D. Johnson, “Longitudinal compressive behaviour and microstructure of PAN-based carbon fibres”, *Carbon*, 39: 635–645, 2001.
- [84] A. Pantano, D. Parks, M. Boyce, “Mechanics of deformation of single- and multi-wall carbon nanotubes”, *Journal of the Mechanics and Physics of Solids*, 52: 789–821, 2004.
- [85] O. Paris, H. Peterlik, “The structure of carbon fibres”, in S. Eichhorn, J. Hearle, M. Jaffe, T. Kikutani (Editors), *Handbook of textile fibre structure*, Volume 2. Woodhead Publishing Limited, Cambridge, UK, 2009.
- [86] A. Pflüger, *Stabilitätsprobleme der Elastostatik*, Springer-Verlag, Berlin, 1975.
- [87] P. Redlich, F. Banhart, Y. Lyutovich, P. Ajayan, “EELS study of the irradiation-induced compression of carbon onions and their transformation to diamond”, *Carbon*, 36: 561–563, 1998.
- [88] J.A. Rogers, T. Someya, Y. Huang, “Materials and mechanics for stretchable electronics”, *Science*, 327(5973): 1603–1607, 2010.
- [89] A. Sakhaee-Pour, “Elastic properties of single-layered graphene sheet”, *Solid State Communications*, 149: 91–95, 2009.
- [90] M. Sato, M. Wadee, K. Iiboshi, T. Sekizawa, H. Shima, “Buckling patterns of complete spherical shells filled with an elastic medium under external pres-

- sure”, *International Journal of Mechanical Sciences*, 59: 22–30, 2012.
- [91] C. Sauder, J. Lamon, R. Pailler, “The tensile behavior of carbon fibers at high temperatures up to 2400°C”, *Carbon*, 42: 715–725, 2004.
- [92] M. Schwarzbart, A. Steindl, “Buckling of a Supported Annular Plate with a Non-Euclidean Metric”, in H. Altenbach, N.F. Morozov (Editors), *Surface Effects in Solid Mechanics: Advanced Structured Materials 30*. Springer-Verlag, Berlin Heidelberg, 2013.
- [93] O.A. Shenderova, V.V. Zhirnov, D.W. Brenner, “Carbon Nanostructures”, *Crit. Rev. Solid State Mater. Sci.*, 27: 227, 2002.
- [94] H. Shima, “Buckling of carbon nanotubes: A state of the art review”, *Materials*, 5: 47–84, 2012.
- [95] D. Sinclair, “A bending method for measurement of the tensile strength and Young’s modulus of glass fiber”, *Journal of Applied Physics*, 21: 380–386, 1950.
- [96] C.M. Stafford, S. Guo, C. Harrison, M.Y.M. Chiang, “Combinatorial and high-throughput measurements of the modulus of thin polymer films”, *Review of Scientific Instruments*, 76(6): –, 2005.
- [97] C.M. Stafford, C. Harrison, K.L. Beers, A. Karim, E.J. Amis, M.R. VanLandingham, H.C. Kim, W. Volksen, R.D. Miller, E.E. Simonyi, “A buckling-based metrology for measuring the elastic moduli of polymeric thin films”, *Nat Mater*, 3(8): 545–550, Aug. 2004.
- [98] S. Stankovich, D. Dikin, G. Dommett, K. Kohlhaas, E. Zimney, E. Stach, R. Piner, S. Nguyen, R. Ruoff, “Graphene-based composite materials”, *Nature*, 442: 282–286, 2006.
- [99] C. Sun, K. Liu, “Combined torsional buckling of multi-walled carbon nanotubes coupling with axial loading and radial pressures”, *International Journal of Solids and Structures*, 45: 2128–2139, 2008.
- [100] Y. Sun, W.M. Choi, H. Jiang, Y.Y. Huang, J.A. Rogers, “Controlled buckling of semiconductor nanoribbons for stretchable electronics”, *Nat Nano*, 1(3): 201–207, Dec. 2006.
- [101] A. Tang, F. Huang, “Stability rules of icosahedral (Ih or I) fullerenes”, *Chemical Physics Letters*, 247: 494–501, 1995.
- [102] A. Tang, F. Huang, “Theoretical study of multishell fullerenes”, *Physical Review B*, 52: 17435–17438, 1995.
- [103] R. Telling, C. Ewels, A. El-Barbary, M. Heggie, “Wigner defects bridge the graphite gap”, *Nature Materials*, 2: 333–337, 2003.
- [104] H. Terrones, M. Terrones, “The transformation of polyhedral particles into graphitic onions”, *Journal of the Physics and Chemistry of Solids*, 58: 1789–1796, 1997.
- [105] J. Tersoff, “Empirical Interatomic Potential for Carbon, with Applications to Amorphous Carbon”, *Phys. Rev. Lett.*, 61: 2879, 1988.
- [106] M. Todt, R.D. Bitsche, M.A. Hartmann, F.D. Fischer, F.G. Rammerstorfer, “Growth limit of carbon onions A continuum mechanical study”, *International Journal of Solids and Structures*, 51: 706–715, 2014.

- [107] M. Todt, F.G. Rammerstorfer, F.D. Fischer, P.H. Mayrhofer, D. Holec, M.A. Hartmann, “Continuum modeling of van der Waals interactions between carbon onion layers”, *Carbon*, 49: 1620–1627, 2011.
- [108] M. Todt, F.G. Rammerstorfer, M.A. Hartmann, “Continuum shell models for closed cage carbon nanopraticles”, in W. Pietraszkiewicz, J. Górski (Editors), *Shell Structures: Theory and Applications*, pages 149–152. Taylor & Francis Group, London, UK, 2014.
- [109] M. Todt, F.G. Rammerstorfer, M.A. Hartmann, O. Paris, F.D. Fischer, “Shell-Models for multi-layer carbon nano-particles”, in H. Altenbach, V. Eremeyev (Editors), *Advanced Structured Materials: Shell-like Structures*, pages 585–602. Springer-Verlag, Berlin, 2011.
- [110] M. Todt, F.G. Rammerstorfer, O. Paris, F.D. Fischer, “Nanomechanical studies of the compressive behavior of carbon fibers”, *Journal of Material Science*, 45: 6845–6848, 2010.
- [111] S. Tomita, A. Burian, J. Dore, D. LeBolloch, M. Fujii, S. Hayashi, “Diamond nanoparticles to carbon onions transformation: X-ray diffraction studies”, *Carbon*, 40: 1469–1474, 2002.
- [112] F. Toth, F.G. Rammerstorfer, M.J. Cordill, F.D. Fischer, “Detailed modelling of delamination buckling of thin films under global tension”, *Acta Materialia*, 61(7): 2425 – 2433, 2013.
- [113] V. Tvergaard, J.W. Hutchinson, “The relation between crack growth resistance and fracture process parameters in elastic-plastic solids”, *J Mech Phys Solids*, 40: 1377–1397, 1992.
- [114] D. Ugarte, “Curling and closure of graphitic networks under electron-beam irradiation”, *Nature*, 359: 707–709, 1992.
- [115] D. Ugarte, “Morphology and structure of graphitic soot particles generated in arc-discharge C60 production”, *Chemical Physics Letters*, 198: 596–602, 1992.
- [116] D. Ugarte, “Formation mechanism of quasi-spherical carbon particles induced by electron bombardment”, *Chemical Physics Letters*, 207: 473–479, 1993.
- [117] D. Ugarte, “Onion-like graphitic particles”, *Carbon*, 33: 989–993, 1995.
- [118] O. van der Sluis, A.A. Abdallah, P.C.P. Bouten, P.H.M. Timmermans, J.M.J. den Toonder, G. de With, “Effect of a hard coat layer on buckle delamination of thin ITO layers on a compliant elasto-plastic substrate: An experimental-numerical approach”, *Eng Fract Mech*, 78(6): 877–889, 2011.
- [119] A.A. Volinsky, N.R. Moody, W.W. Gerberich, “Interfacial toughness measurements for thin films on substrates”, *Acta Mater*, 50: 441–466, 2002.
- [120] Y. Voytekhovskiy, “A formula to estimate the size of a fullerene”, *Acta Crystallographica A*, 59: 193–194, 2003.
- [121] S. Wagner, S.P. Lacour, J. Jones, P.h.I. Hsu, J.C. Sturm, T. Li, Z. Suo, “Electronic skin: architecture and components”, *Physica E: Low-dimensional Systems and Nanostructures*, 25(23): 326 – 334, 2004.
- [122] B. Wang, H. Wang, J. Chang, H. Tso, Y. Chou, “More spherical large fullerenes and multi-layer fullerene cages”, *Journal of Molecular Structure*, 540: 171–176, 2001.

- [123] P. Wesolowski, Y. Lyutovich, F. Banhart, H. Carstanjen, H. Kronmüller, “Formation of diamond in carbon onions under MeV ion irradiation”, *Applied Physics Letters*, 71: 1948–1950, 1997.
- [124] J. Wu, K. Hwang, Y. Huang, “An atomistic-based finite-deformation shell theory for single-wall carbon nanotubes”, *Journal of the Mechanics and Physics of Solids*, 56: 279–292, 2008.
- [125] J. Wu, J. Peng, K. Hwang, J. Song, Y. Huang, “The intrinsic stiffness of single-wall carbon nanotubes”, *Mechanics Research Communications*, 35: 2–9, 2008.
- [126] Z. Xin, Z. Jianjun, Q. Zhong-can, “Strain energy and Young’s modulus of single-wall carbon nanotubes calculated from electronic energy-band theory”, *Physical Review B*, 62: 13692–13696, 2000.
- [127] B. Yakobson, C. Brabec, J. Bernholc, “Nanomechanics of Carbon Tubes: Instabilities beyond Linear Response”, *Physical Review Letters*, 76: 2511–2514, 1996.
- [128] X. Yao, Q. Han, H. Xin, “Bending buckling behaviors of single- and multi-walled carbon nanotubes”, *Computational Material Science*, 43: 579–590, 2008.
- [129] D.B. Zhang, E. Akatyeva, T. Dumitrica, “Bending Ultrathin Graphene at the Margins of Continuum Mechanics”, *Phys. Rev. Lett.*, 106: 255503, 2011.
- [130] H. Zhang, L. Wang, J. Wang, “Computer simulation of buckling behavior of double-walled carbon nanotubes with abnormal interlayer distances”, *Computational Materials Science*, 39: 664–672, 2007.
- [131] P. Zhang, Y. Huang, P. Geubelle, P. Klein, K. Hwang, “The elastic modulus of single-wall carbon nanotubes: a continuum analysis incorporating interatomic potentials”, *International Journal of Solids and Structures*, 39: 3893–3906, 2002.
- [132] M. Zhao, H. Song, X. Chen, W. Lian, “Large-scale synthesis of onion-like carbon nanoparticles by carbonization of phenolic resin”, *Acta Materialia*, 55: 6144–6150, 2007.
- [133] M.H. Zhao, F. Yang, T.Y. Zhang, “Delamination buckling in the microwedge indentation of a thin film on an elastically deformable substrate”, *Mechanics of Materials*, 39(9): 881–892, Sept. 2007.
- [134] M. Zwanger, F. Banhart, A. Seeger, “Formation and decay of spherical concentric-shell carbon clusters”, *Journal of Crystal Growth*, 163: 445–454, 1996.

Chapter 3

Thin Films

3.1 Introduction

The term “thin films” comprises all systems where a layer of material with an overall thickness in the nm or μm range is bonded to a substrate with a thickness that is substantially larger than that of the layer. The general idea behind this concept is, that the specific properties of the thin film and the substrate can be combined such that a structure with enhanced mechanical, electrical, optical, or visual properties is obtained.

Thin film systems are of major importance for various industrial applications. Examples are protective coatings to increase abrasive wear and corrosion resistance, electrically active coatings such as metallization layers in power semiconductor devices, optical coatings such as anti-reflection coatings on lenses, as well as decorative coatings. In the following the considerations are limited to nanoscale multilayer coatings (nanolayered coatings) and power metallization layers within semiconductor devices.

3.1.1 Nanoscale Multilayer Coatings

Thin film coatings can be categorized into monolithic and multi-layer coatings. Typical examples for monolithic coatings are thin CrN- or TiN-layers which have been used as protective coatings for cutting tools for decades. Due to their monolithic structure the overall properties of the coated system can only be adjusted within certain limits. In contrast, multilayer coatings – which can be viewed as special class of architected materials [2] – allow for a more specific tailoring of their properties towards target applications by varying

the selection of materials as well as the thicknesses and sequence of layers. Following [28], multilayer coatings can be grouped into three categories:

1. Coatings with a low number of layers: The general idea is to combine different materials to design a coating with enhanced overall properties [8] as well as to interrupt columnar grain growth in the direction normal to the layers. These coatings are already established for industrial applications such as the protection of cutting tools, see, e.g., [62, 40]. Other examples are the coatings with ultra-high reflectivity (at certain wavelengths) designed in [63]. The typical thickness of the individual layers is in the range of a few hundred nm.
2. Multilayer coatings with a high number of non-isostructural single layers: These coatings can consist of up to several hundred layers, where the thickness of the individual layers and consequently the multilayer period are in the low nm range. Besides the combination of layer materials and the interruption of columnar grain growth, the influence of the high interface density on the overall coating properties becomes important [3, 28]. Examples are CrN/w-AlN and TiN/w-AlN multilayers with AlN in its wurtzite (w) structure [67, 38].
3. Superlattice coatings: The coating consists of a high number of isostructural single layers, i.e., layers with the same lattice structure as well as similar lattice distance, atomic ratio, and bonding type. The thickness of the individual layers is in the range of the atomic lattice dimensions, i.e., in the range of a few nm [1, 48, 51, 54]. Examples for a combination of isostructural materials are TiC/TiN and TiN/VN [25, 28]. Alternatively, isostructural conditions can be enforced by epitaxially stabilizing one constituent to match the lattice structure of the other material. Examples are CrN/B1-AlN and TiN/B1-AlN superlattice coatings with AlN stabilized in its metastable cubic rock-salt (B1) structure [67]. In this case the maximum layer thickness of B1-AlN is limited to approximately 1 – 3 nm [48, 67, 70] depending on the thickness of the adjacent layers and the lattice mismatch [38]. However, in [12] it is shown that the maximum layer thickness of B1-AlN can be increased up to approximately 10 – 15 nm by an appropriate

choice of the substrate in terms of mechanical properties, crystallographic orientation, and lattice parameters.

Nanoscale multilayer coatings (categories 2 and 3) have drawn a lot of attention within the past decades, especially since technologies for their large-scale manufacturing are available [18, 30, 31, 54]. Particularly, superlattice coatings show exceptional properties such as extreme mechanical hardness [4, 25, 55], increased fracture toughness [67], high wear and corrosion resistance [29, 31, 54], and a low coefficient of friction [29]. These properties cannot necessarily be predicted by standard homogenization techniques [1, 55, 69] as interfacial effects become predominant due to the high interface area density within nanoscale coatings [1]. A detailed discussion on interfacial effects can be found, e.g., in [1] and references therein.

For a technological application the relation between the structure and the properties has to be well understood. This requires a correct evaluation of the overall properties of the coating as well as of the properties of the individual constituents. The latter point takes on special importance when one of the constituents is epitaxially stabilized into a lattice structure which is not stable in bulk under ambient conditions. An example is B1-AlN that is only thermodynamically stable for pressures higher than approximately 13–23 GPa [16]. Consequently, the properties of such layers can only be evaluated from experiments conducted on the whole multilayer coating or on samples where the coating is attached to a substrate. For extracting the material properties aimed at, appropriate analytical or numerical continuum mechanical models are required. These models are discussed in more detail in Section 3.2 and in **TF-1** [5] a model for estimating the coefficient of thermal expansion of B1-AlN is presented.

3.1.2 Metallization Layers in Semiconductor Devices

Power semiconductor devices are used in many industrial applications including low-voltage motor controllers, battery charging units in mobile phones, AC/DC converters, automotive control applications, large-scale power converters for energy transmission, and in countless other appliances in the IT and electronics industry. Modern power semiconductor devices

are subjected to extreme operational conditions in the form of high switching frequencies and high electrical power densities. They have to withstand millions of switching events [58] for an envisaged lifetime of up to 30 years [47]. Consequently, the reliability of these devices is of major importance and addressed in many publications, e.g., [37, 57] and references therein.

Thin films play an important role within semiconductor devices and occur as dielectric layers which are only a few nm in thickness as well as metallization layers with thicknesses up to $20\ \mu\text{m}$ [57]. These layers are deposited in the form of a multilayer arrangement onto an insulating substrate, usually silicon [57]. For metal-oxide-semiconductor field-effect transistors degradation of the metallization layer has been shown to be the main reason for device failure [49].

The metallization layers serve as electric connections but also act as heat sinks for removing the thermal energy generated during the switching events. Each switching event leads to high temperatures and high temperature gradients within the multilayer stack [64]. Locally, the temperatures in the metallization layer can be as high as $350^\circ\ \text{C}$ [58]. Due to the different coefficients of thermal expansion of the individual constituents high stresses and strains [41, 87] are introduced. The stresses within the metallization layers can exceed the yield limit of the material. Continuous active cycling leads to evolving changes in the micro-structure of the metallization layer [41]. On the meso-scale these micro-structural changes are experienced as degradation of the material properties [37, 41], i.e., the evolution of fatigue damage. Eventually, fatigue cracks emerge and propagate within the metallization layers causing fatal device failure. The fatigue of copper metallization layers is addressed in detail, e.g., in [7] wherein also a brief literature review on thermo-mechanical fatigue of thin films is provided. Furthermore, the thermal fatigue of copper films with a few hundred nm in thickness is investigated experimentally in [53].

Additionally to experimental studies, physical damage models that allow for predicting fatigue damage within metallization layers are in great demand [37]. A suitable simulation framework was gradually developed in [42, 43, 74, 75, 76]. The associated constitutive model is based on continuum damage mechanics methods and allows for predicting onset

and evolution of fatigue damage on the material level. Implemented into a commercial finite element software it provides the capability for simulating the emergence and spatial evolution of fatigue cracks within metallization layers. Additionally, delamination between adjacent layers within the multilayer stack can be simulated. The required cohesive zone model is presented in [77]. In [27] the existing framework has been extended such that more realistic thermo-mechanical boundary conditions can be applied, see also publication **TF-2** in Section 3.3.

3.2 Continuum Mechanics Modeling

The application of continuum mechanics models in the context of thin films is manifold and includes the evaluation of residual stresses [32, 33, 36], the extraction of material properties from experiments [5, 22], the interpretation of experimental results [44, 89], studies on the influence of the multilayer structure on the effective coating properties [40, 93], and simulations of the (thermo-)mechanical fatigue of thin films [20, 27, 42, 43, 74, 75].

The literature on continuum mechanical models employed for studying thin film substrate systems is vast and the provided references can only be considered as an excerpt of the existing literature.

3.2.1 Analytical Models

In the context of thin films, analytical continuum mechanics models are mainly employed in conjunction with experimental methods for evaluating residual stresses arising during the manufacturing process as well as for determining the (effective) thermo-mechanical properties of the films.

Residual stresses observed in thin films can be in the GPa range [15, 30, 60] and consequently they can have a strong impact on the mechanical response and the structural integrity of coated systems [15, 60, 90, 94]. The origin of these stresses is discussed, e.g., in [11, 60]. For the following discussion only their classification into intrinsic and extrinsic residual stresses is important. Intrinsic stresses develop during the deposition process of the thin film whilst extrinsic stresses are introduced during the post-deposit cooling process

due to the mismatch of coefficients of thermal expansions of the individual constituents.

The origin of analytical residual stress models can be found at the beginning of the 20th century when Stoney published his famous equation on the relation between film stress and sample curvature [78]. The equation is based on Euler-Bernoulli beam theory under assumption of a uniaxial stress state and considers a monolithic thin film on a thick substrate. A discussion on the accuracy of Stoney's equation is presented in [39] as well as in [36]. Since then, various models that are based on Stoney's equation have been proposed, including an extension to biaxial stress states and anisotropic substrates [35, 36], the consideration of multiple layers within the film [82], an extension towards thick films [32, 39, 82], and the consideration of external bending moments [32, 91]. In [36] it is explicitly pointed out that the developed model only considers intrinsic stresses. Extrinsic stresses are explicitly modeled in [32, 33, 82, 91]. A clear distinction between intrinsic and extrinsic stresses is made in the models presented in [56, 83] where also the layer-by-layer formation of multi-layer coatings is considered. Stoney's equation and its derivatives are still widely employed in the experimental evaluation of residual stresses from wafer curvature experiments [34, 45, 46, 73], illustrating the importance of these relations.

Wafer curvature experiments belong to the group of mechanical stress measurement methods [90]. Another method to be mentioned in this context is the incremental layer removal method [50, 68] for which the respective analytical method is closely related to models accounting for a layer-by-layer formation of multi-layer thin films [56, 83]. An overview on further experimental methods for evaluating residual stresses and the employed (analytical) continuum mechanical models can be found in [90].

For making a statement about the impact of residual stresses on the integrity of coated systems, the residual stresses within the film have to be related to critical stresses associated with possible failure modes. Relations for film cracking, decohesion, or buckling are presented, e.g., in [17, 79]. A more detailed study on the delamination behavior of thin film systems is presented in [22]. Therein, analytical relations for the critical energy release rate for steady state delamination are derived where plastic yielding of the substrate as well as the effect of an elastic layer between thin film and substrate are included in the

model.

For the evaluation of the effective properties of monolithic and multilayer thin films the most direct way is by the means of nanoindentation [59]. This method provides information about the (effective) elastic modulus and the (effective) hardness of (multilayer) coatings. However, for thin films the substrate can have a substantial influence on the measured properties which is observed as a dependency of the effective elastic modulus and hardness on the indentation depth [65]. One possible way to account for this effect is the volume-law-of-mixtures model presented in [9, 10] for the case of a hard film on a soft substrate. This model is used, e.g., in [8] to estimate the overall hardness of multilayer thin films. For further information on nanoindentation of thin films the reader is referred to [9, 59, 65] and references therein. Other examples of "mechanical measurement methods" that use analytical continuum mechanics models for estimating the mechanical properties of thin films are the bulge test [72], the cantilever beam test [84], the method for tensile testing of thin films introduced in [71] which also allows for estimating the fracture strength, the membrane deflection technique proposed in [19], or the structures designed in [52] which exploit existing tensile residual stresses within the film.

Besides the estimation of residual stresses within thin films wafer curvature experiments can also be employed to determine the elastic properties of individual layers within multilayer thin films [5]. The model is closely related to the ones introduced in [32, 33, 82, 91] for predicting the extrinsic residual stresses. Instead of Euler-Bernoulli beam theory, lamination theory is employed for finding a relation between the thin film properties, the applied temperature change, and the curvature of the sample. The model is discussed in detail in the attached publication **TF-1** [5], see also Section 3.3.1 for a brief overview.

Many of the models presented above also allow investigating the influence of the various parameters of multilayer thin films on the effective film properties and residual stresses. The biggest advantage of these models are the low computational costs making them economic tools in the early design process of multilayer thin films. However, analytical models are limited to relatively simple geometries, boundary conditions, and loading scenarios. Furthermore, they are often based on certain assumptions on the resulting stress and strain

fields within the thin film or the individual layers occurring under specific loading conditions. Consequently, they may not capture all mechanisms that determine the mechanical response of multilayer thin films. These issues can be addressed with numerical continuum mechanics models as discussed next.

3.2.2 Numerical Models

Generally the finite element method is employed for studying the (thermo-)mechanical response of (multilayer) thin film substrate systems. This section provides an overview about the used modeling concepts and illustrates the capabilities of the finite element method for gaining further insight into the thermo-mechanical behavior of thin film systems. Other promising concepts such as the boundary element method [92] are not discussed here.

One of the biggest issues in modeling thin film substrate systems is the significant difference between the thickness of the film and the thickness of the substrate. A reasonable discretization of the thin film also leads to a fine mesh in the substrate, at least close to the film/substrate interface. Consequently, mainly two dimensional plane strain [20, 21, 22, 61], plane stress [95] or axi-symmetric [89, 92] models have been employed to keep the model size within reasonable bounds. If three dimensional (3D) models are used, usually only the region of interest is discretized, see, e.g., [26, 66, 86] where the influence of ductile interlayers on the indentation response of multilayer thin films was studied in detail. Other concepts in the context of 3D modeling are multi-scale models as employed in [80, 81] for studying the delamination buckling of thin films, or model-order reduction concepts used, e.g., in [6] for identifying the effective heat transfer coefficient of multilayer coatings.

The issue of model size becomes more severe if multi-layer systems are to be investigated. Usually the maximum number of layers considered within the finite element models is approximately 20-50 [89, 93] or even less [85, 44, 40, 61, 24]. For reducing the computational requirements the layers are often discretized using only one element over the thickness [23, 40, 85] or the multilayer thin film is represented by a monolithic one with appropriate effective properties, see, e.g., [6]. However, superlattice coatings can consist of several hundred layers [5] making pure continuum element models not applicable at present, even if only one element over the thickness of each layer is used. In [88] a shell based layer-level

modeling concept is proposed which allows to overcome this issue. Therein the individual layers are discretized using shell elements and the interfaces between the layers are modeled using cohesive zone elements. With this model the layer-by-layer growth of multilayer thin films and the resulting residual stresses can be simulated. Furthermore, the effect of free edges as well as delamination between the individual layers can be accounted for.

The scope of application of the finite element method in the area of (multilayer) thin films is manifold. Appropriate finite element models allow to gain further insight into experimental results that cannot be accessed with analytical models. Nonlinear and rate dependent material behavior of the layers and the substrate can be considered by using appropriate material models, see, e.g., [26, 44, 74, 86, 89]. This way the stresses and deformations within the layers can be evaluated in great detail, e.g., for the case of nanoindentation experiments [14, 26, 44, 86, 89]. This allows to gain valuable information on how the substrate [14, 44, 66] and the plastic deformations that occur during unloading [89] influence the measured hardness and elastic modulus. Furthermore, the influence of the layer structure on the stress distribution within the thin film [93] can be studied and even complex phenomena such as the emergence and propagation of cracks [86] can be investigated. Other applications in the context of the experimental characterization of multilayer thin films involve the verification of analytical models [22, 68] and the identification of material parameters [6]. In other theoretical studies, finite element models are used to investigate the influence of irregularly shaped interfaces/layer boundaries on the occurrence of stress concentrations within the layers [61] and they are employed in combination with *ab initio* simulations for estimating the critical thickness of metastable phases within superlattice coatings [12, 13]. Similar to the analytical models introduced in Section 3.2.1, finite element models can also be used for evaluating residual stresses [88, 95] within the individual layers of thin films. Furthermore, the finite element method can be utilized for studying the thermo-mechanical response of (multilayer) thin films under application-oriented loading conditions. Examples are the investigation of the thermo-mechanical behavior of multilayer coatings in dry machining [24, 23, 40], the simulation of thermo-mechanical fatigue in thin films occurring, e.g., in metallization layers of semiconductor devices due to cyclic thermal

overload pulses [74, 75] or at contact points of gear wheels due to sliding-rolling contact conditions [20]. The simulation framework developed in [74, 75] is employed in publication **TF-2** for studying the influence of lateral temperature gradients on the formation and propagation of fatigue cracks in a cluster of metal-oxide semiconductor cells.

3.3 Own Contribution to the Research Field

The own contribution to the research field consists of two publications, viz.

- **Publication TF-1:** M. Bartosik, M. Todt, D. Holec, J. Todt, Z. Zhang, L. Zhou, H. Riedl, H.J. Böhm, F.G. Rammerstorfer, P.H. Mayrhofer: *Thermal Expansion of Rock-Salt Cubic AlN*. Applied Physics Letters, 107 (2015), 071602.
- **Publication TF-2:** P. Hoffmann, M. Nelhiebel, B. Karunamurthy, H.E. Pettermann, M. Todt: *Simulation of Fatigue Damage in Clusters of DMOS-cells Subjected to Non-Uniform Transient Thermo-Mechanical Loading*; in 2020 21st International Conference on Thermal, Mechanical and Multi-Physics Simulation and Experiments in Microelectronics and Microsystems (EuroSimE); (2020), pp. 1-9; doi:10.1109/EuroSimE48426.2020.9152728.

The declaration of own contribution to these publications is provided in Subsection 3.3.3.

3.3.1 Material Properties of Superlattice Coatings

In the journal paper **TF-1** [5] a continuum mechanics method is developed that allows determining the coefficient of thermal expansion (CTE) of metastable material phases within superlattice coatings from wafer curvature experiments. The method is based on lamination theory and links the experimentally measured curvatures and the applied temperature changes to the stress resultants within the sample in the form of a constitutive relation. The CTE of the metastable phase is obtained by solving the inverse problem where a closed form solution is obtained under the assumption of isotropic linear-elastic material behavior.

Specifically, metastable cubic rock salt (B1) AlN is considered being stabilized by coherency strains in CrN/AlN multi-layer thin films. B1-AlN in bulk form is only thermodynamically stable for pressures above 13 – 23 GPa [16] and therefore its properties cannot be

measured directly from standard experiments. The results show that the calculated CTE depends on the number of CrN/AlN bi-layers within the thin film, where for a low number of bi-layers good agreement with *ab initio* calculations was found. These findings are attributed to the fact that thicker CrN layers are more effective in stabilizing the metastable phase and that atoms at the interfaces are bonded differently than within the individual layers.

In conclusion, the developed approach can be used to determine the CTE of metastable phases within multilayer thin films as long as linear elastic material behavior can be assumed. For reliable results a low interface density and thick stabilizing layers are desirable and the number of layers needs to be sufficiently large to provoke measurable sample curvature. The method can also be modified such that other material parameters can be obtained but in this case may not lead to a closed-form solution.

3.3.2 Fatigue Damage in Power Metallization Layers

In the proceedings paper **TF-2** [27] an existing framework [42, 43, 74, 75] for simulating fatigue damage in metallization layers in semiconductor devices is extended such that more realistic transient thermo-mechanical loading conditions can be considered. The extended framework is implemented in a way that the computations of the transient thermal and mechanical fields are conducted in a sequentially coupled manner. Besides the more realistic loading conditions also the effect of the evolving fatigue damage on the thermal fields can be accounted for.

The extended framework is used to study the effect of lateral temperature gradients on the formation and propagation of fatigue cracks in a cluster of double-diffused metal-oxide-semiconductor (DMOS) cells. The results show that fatigue cracks form predominantly in regions where the maximum temperatures are observed during active cycling. The temperature gradient has only a minor influence on the locations where fatigue cracks form. For all investigated configurations of DMOS cell clusters the formation of a dominant crack can be observed which subsequently suppresses the growth of neighboring cracks due to shielding effects.

3.3.3 Declaration of Own Contribution to the Enclosed Publications

- **Publication TF-1:** My own contribution involved the development of the analytical model and the implementation of the respective solution procedure for determining the coefficient of thermal expansion. The paper was mainly written by M. Bartosik and myself, with contributions from all other co-authors.
- **Publication TF-2:** I am the main scientific supervisor of the PhD-thesis of P. Hoffmann and responsible for the research direction of the associated project. All simulations were carried out by P. Hoffmann and the paper also was mainly written by P. Hoffmann. H.E. Pettermann acts as academic supervisor of the thesis.

3.4 Bibliography

- [1] G. Abadias, A. Michel, C. Tromas, C. Jaouen, and S. N. Dub. Stress, interfacial effects and mechanical properties of nanoscale multilayered coatings. *Surface and Coatings Technology*, 202:844–853, 2007.
- [2] M. Ashby. Designing architected materials. *Scripta Materialia*, 68:4–7, 2013.
- [3] S. A. Barnett, A. Madan, I. Kim, and K. Martin. Stability of nanometer-thick layers in hard coatings. *MRS Bulletin*, 28:169–172, 2003.
- [4] S. A. Barnett and M. Shinn. Plastic and elastic properties of compositionally modulated thin films. *Annual Review of Materials Science*, 24:481–511, 1994.
- [5] M. Bartosik, M. Todt, D. Holec, J. Todt, L. Zhou, H. Riedl, H. J. Böhm, F. G. Rammerstorfer, and P. H. Mayrhofer. Thermal expansion of rock-salt cubic AlN. *Applied Physics Letters*, 107:071602, 2015.
- [6] T. Bechtold, D. Hohlfeld, E. B. Rudnyi, and M. Günther. Efficient extraction of thin-film thermal parameters from numerical models via parametric model order reduction. *Journal of Micromechanics and Microengineering*, 20:045030, 2010.

- [7] S. Bigl. *Thermo-mechanical behaviour of thick copper metallizations for power electronics*. PhD thesis, Montanuniversität Leoben, 2017.
- [8] S. J. Bull and A. M. Jones. Multilayer coatings for improved performance. *Surface and Coatings Technology*, 78:173–184, 1996.
- [9] P. J. Burnett and D. S. Rickerby. The mechanical properties of wear-resistant coatings: I: Modelling of hardness behaviour. *Thin Solid Films*, 148:41 – 50, 1987.
- [10] P. J. Burnett and D. S. Rickerby. The mechanical properties of wear-resistant coatings: II: Experimental studies and interpretation of hardness. *Thin Solid Films*, 148:51 – 65, 1987.
- [11] E. Chason and A. M. Engwall. Relating residual stress to thin film growth processes via a kinetic model and real-time experiments. *Thin Solid Films*, 596:2 – 7, 2015.
- [12] V. Chawla, D. Holec, and P. H. Mayrhofer. Stabilization criteria for cubic AlN in TiN/AlN and CrN/AlN bi-layer systems. *Journal of Physics D: Applied Physics*, 46:045305, 2013.
- [13] V. Chawla, D. Holec, and P. H. Mayrhofer. The effect of interlayer composition and thickness on the stabilization of cubic AlN/Ti-Al-N superlattices. *Thin Solid Films*, 565:94–100, 2014.
- [14] X. Chen and J. J. Vlassak. Numerical study on the measurement of thin film mechanical properties by means of nanoindentation. *Journal of Materials Research*, 16:2974–2982, 2001.
- [15] G.-A. Cheng, D.-Y. Han, C.-L. Liang, X.-L. Wu, and R.-T. Zheng. Influence of residual stress on mechanical properties of TiAlN thin films. *Surface and Coatings Technology*, 228, Supplement 1:S328–S330, 2013.
- [16] N. E. Christensen and I. Gorczyca. Optical and structural properties of III-V nitrides under pressure. *Physical Review B*, 50:4397–4415, Aug 1994.

- [17] T. W. Clyne and S. C. Gill. Residual stresses in thermal spray coatings and their effect on interfacial adhesion: A review of recent work. *Journal of Thermal Spray Technology*, 5:401–418, 1996.
- [18] L. A. Donohue, W. D. Münz, D. B. Lewis, J. Cawley, T. Hurkmans, T. Trinh, I. Petrov, and I. E. Greene. Large-scale fabrication of hard superlattice thin films by combined steered arc evaporation and unbalanced magnetron sputtering. *Surface and Coatings Technology*, 93:69–87, 1997.
- [19] H. D. Espinosa, B. C. Prorok, and M. Fischer. A methodology for determining mechanical properties of freestanding thin films and MEMS materials. *Journal of the Mechanics and Physics of Solids*, 51:47–67, 2003.
- [20] J. Farley, L. C. Wrobel, and K. Mao. Low cycle fatigue simulation and fatigue life prediction of multilayer coated surfaces. *Wear*, 269:639–646, 2010.
- [21] J. Farley, L. C. Wrobel, and K. Mao. Performance evaluation of multilayer thin film coatings under mixed rolling-sliding dry contact conditions. *Wear*, 268:269–276, 2010.
- [22] P. J. J. Forschelen, A. S. J. Suiker, and O. van der Sluis. Effect of residual stress on the delamination response of film-substrate systems under bending. *International Journal of Solids and Structures*, 97-98:284–299, 2016.
- [23] W. Grzesik. Determination of temperature distribution in the cutting zone using hybrid analytical-FEM technique. *International Journal of Machine Tools and Manufacture*, 46:651 – 658, 2006.
- [24] W. Grzesik and P. Nieslony. A computational approach to evaluate temperature and heat partition in machining with multilayer coated tools. *International Journal of Machine Tools & Manufacture*, 43:1311–1317, 2003.
- [25] U. Helmersson, S. Todorova, S. A. Barnett, J. Sundgren, L. C. Markert, and J. E. Greene. Growth of single-crystal TiN/VN strained-layer superlattices with extremely high mechanical hardness. *Journal of Applied Physics*, 62:481–484, 1987.

- [26] P. Hoffmann. Elasto-plastic finite element simulations of nanoindentation problems utilizing Hill's potential. Master's thesis, TU Wien, 2018. Supervisors: H.E. Pettermann and M. Springer.
- [27] P. Hoffmann, M. Nelhiebel, B. Karunamurthy, H. E. Pettermann, and M. Todt. Simulation of fatigue damage in clusters of DMOS-cells subjected to non-uniform transient thermo-mechanical loading. In *2020 21st International Conference on Thermal, Mechanical and Multi-Physics Simulation and Experiments in Microelectronics and Microsystems (EuroSimE)*, pages 1–9, 2020.
- [28] H. Holleck and V. Schier. Multilayer PVD coatings for wear protection. *Surface and Coatings Technology*, 76-77:328–336, 1995.
- [29] P. E. Hovsepian, D. B. Lewis, Q. Luo, W.-D. Münz, P. H. Mayrhofer, C. Mitterer, Z. Zhou, and W. M. Rainforth. TiAlN based nanoscale multilayer coatings designed to adapt their tribological properties at elevated temperatures. *Thin Solid Films*, 485:160–168, 2005.
- [30] P. E. Hovsepian, D. B. Lewis, and W.-D. Münz. Recent progress in large scale manufacturing of multilayer/superlattice hard coatings. *Surface and Coatings Technology*, 133-134:166–175, 2000.
- [31] P. E. Hovsepian and W.-D. Münz. Recent progress in large-scale production of nanoscale multilayer/superlattice hard coatings. *Vacuum*, 69:27 – 36, 2002.
- [32] C.-H. Hsueh. Modeling of elastic deformation of multilayers due to residual stresses and external bending. *Journal of Applied Physics*, 91:9652–9656, 2002.
- [33] C.-H. Hsueh. Thermal stresses in elastic multilayer systems. *Thin Solid Films*, 418:182–188, 2002.
- [34] S. Inamdar, M. Ramudu, M. M. Raja, and S. V. Kamat. Effect of process temperature on structure, microstructure, residual stresses and soft magnetic properties of sputtered Fe₇₀Co₃₀ thin films. *Journal of Magnetism and Magnetic Materials*, 418:175 – 180, 2016.

- [35] G. C. A. M. Janssen. Stress and strain in polycrystalline thin films. *Thin Solid Films*, 515:6654–6664, 2007.
- [36] G. C. A. M. Janssen, M. M. Abdalla, F. van Keulen, B. R. Pujada, and B. van Venrooy. Celebrating the 100th anniversary of the Stoney equation for film stress: Developments from polycrystalline steel strips to single crystal silicon wafer. *Thin Solid Films*, 517:1858–1867, 2009.
- [37] W. Kanert. Active cycling reliability of power devices: Expectations and limitations. *Microelectronics Reliability*, 52:2336–2341, 2012.
- [38] I. W. Kim, Q. Li, L. D. Marks, and S. A. Barnett. Critical thickness for transformation of epitaxially stabilized cubic AlN in superlattices. *Applied Physics Letters*, 78:892–894, 2001.
- [39] C. A. Klein. How accurate are Stoney’s equation and recent modifications. *Journal of Applied Physics*, 88:5487–5489, 2000.
- [40] F. Kone, C. Czarnota, B. Haddag, and M. Nouari. Finite element modelling of the thermo-mechanical behavior of coatings under extreme contact loading in dry machining. *Surface and Coatings Technology*, 205:3559–3566, 2011.
- [41] O. Kraft, P. Wellner, M. Hommel, R. Schwaiger, and E. Arzt. Fatigue behavior of polycrystalline thin copper films. *Zeitschrift für Metallkunde*, 93:392–400, 2002.
- [42] G. Kravchenko, B. Karunamurthy, M. Nelhiebel, and H. E. Pettermann. Finite element analysis of fatigue cracks formation in power metallization of a semiconductor device subjected to active cycling. In *Proceedings of the 14th Conference on Thermal, Mechanical and Multi-Physics Simulation and Experiments in Microelectronics and Microsystems*, pages 1–6, 2013.
- [43] G. Kravchenko, B. Karunamurthy, and H. E. Pettermann. FEM study of fatigue crack growth in a power semiconductor chip subjected to transient thermal loading. In *Proceedings of the ECF20, Procedia Materials Science*, 3, pages 63–70, 2014.

- [44] J. Lackner, L. Major, and M. Kot. Microscale interpretation of tribological phenomena in Ti/TiN soft-hard multilayer coatings on soft austenite steel substrates. *Bulletin Of The Polish Academy Of Sciences Technical Sciences*, 59:343–355, 2011.
- [45] J.-W. Lee, S.-K. Tien, Y.-C. Kuo, and C.-M. Chen. The mechanical properties evaluation of the CrN coatings deposited by the pulsed DC reactive magnetron sputtering. *Surface and Coatings Technology*, 200:3330–3335, 2006.
- [46] H. Ljungcrantz, C. Engström, L. Hultman, M. Olsson, X. Chu, M. S. Wong, and W. D. Sproul. Nanoindentation hardness, abrasive wear, and microstructure of TiN/NbN polycrystalline nanostructured multilayer films grown by reactive magnetron sputtering. *Journal of Vacuum Science & Technology A*, 16:3104–3113, 1998.
- [47] J. Lutz, H. Schlangenotto, U. Scheuermann, and R. De Doncker. *Semiconductor Power Devices – Physics, Characteristics, Reliability*. Springer, Berlin, Heidelberg, 2011.
- [48] A. Madan, I. W. Kim, S. C. Cheng, P. Yashar, V. P. Dravid, and S. A. Barnett. Stabilization of cubic AlN in epitaxial AlN/TiN superlattices. *Physical Review Letters*, 78:1743–1746, 1997.
- [49] D. Martineau, C. Levade, M. Legros, P. Dupuy, and T. Mazeaud. Universal mechanisms of Al metallization ageing in power mosfet devices. *Microelectronics Reliability*, 54:2432 – 2439, 2014.
- [50] S. Massl, J. Keckes, and R. Pippan. A direct method of determining complex depth profiles of residual stresses in thin films on a nanoscale. *Acta Materialia*, 55:4835 – 4844, 2007.
- [51] P. H. Mayrhofer, C. Mitterer, L. Hultman, and H. Clemens. Microstructural design of hard coatings. *Progress in Materials Science*, 51:1032–1114, 2006.
- [52] M. Mehregany, R. T. Howe, and S. D. Senturia. Novel microstructures for the in-situ measurement of mechanical properties of thin films. *Journal of Applied Physics*, 62:3579–3584, 1987.

- [53] R. Mönig. *Thermal Fatigue of Cu Thin Films*. PhD thesis, Universität Stuttgart, 2005.
- [54] W.-D. Münz. Large-scale manufacturing of nanoscale multilayered hard coatings deposited by cathodic arc/unbalanced magnetron sputtering. *MRS Bulletin*, 28:173–179, 2003.
- [55] J. Musil. Hard and superhard nanocomposite coatings. *Surface and Coatings Technology*, 125:322–330, 2000.
- [56] M. Nagler. Analytical treatment of residual stresses in multilayer coatings. Master’s thesis, TU Wien, 2017. Supervisors: H.J. Böhm and M. Todt.
- [57] M. Nelhiebel, R. Illing, T. Detzel, S. Wöhlert, B. Auer, S. Lanzerstorfer, M. Rogalli, W. Robl, S. Decker, J. Fugger, and M. Ladurner. Effective and reliable heat management for power devices exposed to cyclic short overload pulses. *Microelectronics Reliability*, 53:1745 – 1749, 2013.
- [58] M. Nelhiebel, R. Illing, C. Schreiber, S. Wöhlert, S. Lanzerstorfer, M. Ladurner, C. Kadow, S. Decker, D. Dibra, H. Unterwalcher, M. Rogalli, W. Robl, T. Herzig, M. Poschgan, M. Inselsbacher, M. Glavanovics, and S. Fraissé. A reliable technology concept for active power cycling to extreme temperatures. *Microelectronics Reliability*, 51:1927–1932, 2011.
- [59] W. D. Nix. Mechanical properties of thin films. *Metallurgical Transactions A*, 20:2217–2245, 1989.
- [60] H. Oettel and R. Wiedemann. Residual stresses in {PVD} hard coatings. *Surface and Coatings Technology*, 76–77:265–273, 1995.
- [61] K. Perzyński, Ł. Major, Ł. Madej, and M. Pietrzyk. Analysis of the stress concentration in the nanomultilayer coatings based on digital representation of the structure. *Archives of Metallurgy and Materials*, 56:393–399, 2011.

- [62] R. Porat. Multilayer CVD coatings of TiC+TiN and their effect on cutting tool life. *Surface Engineering*, 8:292–294, 1992.
- [63] F. Richter, H. Kupfer, P. Schlott, T. Gessner, and C. Kaufmann. Optical properties and mechanical stress in SiO₂/Nb₂O₅ multilayers. *Thin Solid Films*, 389:278 – 283, 2001.
- [64] S. Russo, R. Letor, O. Viscuso, L. Torrisi, and G. Vitali. Fast thermal fatigue on top metal layer of power devices. *Microelectronics Reliability*, 42:1617–1622, 2002.
- [65] R. Saha and W. D. Nix. Effects of the substrate on the determination of thin film mechanical properties by nanoindentation. *Acta Materialia*, 50:23–38, 2002.
- [66] N. A. Sakharova, J. V. Fernandes, M. C. Oliveira, and J. M. Antunes. Influence of ductile interlayers on mechanical behavior of hard coatings under depth-sensing indentation: a numerical study. *Journal of Materials Science*, 45:3812–3823, 2010.
- [67] M. Schlögl, C. Kirchlechner, J. Paulitsch, J. Keckes, and P. H. Mayrhofer. Effects of structure and interface on fracture toughness of CrN/AlN multilayer coatings. *Scripta Materialia*, 68:917–920, 2013.
- [68] R. Schöngrundner, R. Treml, T. Antretter, D. Kozic, W. Ecker, D. Kiener, and R. Brunner. Critical assessment of the determination of residual stress profiles in thin films by means of the ion beam layer removal method. *Thin Solid Films*, 564:321 – 330, 2014.
- [69] I. K. Schuller, A. Fartash, and M. Grimsditch. Elastic anomalies in superlattices. *MRS Bulletin*, 15:33–37, 1990.
- [70] M. Setoyama, A. Nakayama, M. Tanaka, N. Kitagawa, and T. Nomura. Formation of cubic-AlN in TiN/AlN superlattice. *Surface and Coatings Technology*, 86-87:225 – 230, 1996.

- [71] W. N. Sharpe Jr., B. Yuan, and R. L. Edwards. A new technique for measuring the mechanical properties of thin films. *Journal of Microelectromechanical Systems*, 6:193–199, 1997.
- [72] M. K. Small and W. D. Nix. Analysis of the accuracy of the bulge test in determining the mechanical properties of thin films. *Journal of Materials Research*, 7:1553–1563, 1992.
- [73] F. Spaepen. Interfaces and stresses in thin films. *Acta Materialia*, 48:31–42, 2000.
- [74] M. Springer, M. Nelhiebel, and H. E. Pettermann. Combined simulation of fatigue crack nucleation and propagation based on a damage indicator. *Frattura ed Integrità Strutturale*, 38:155–161, 2016.
- [75] M. Springer and H. E. Pettermann. Fatigue life predictions of metal structures based on a low-cycle, multiaxial fatigue damage model. *International Journal of Fatigue*, 116:355–365, 2018.
- [76] M. Springer and H. E. Pettermann. A thermo-mechanical fatigue damage modeling methodology for power semiconductor robustness validation studies. In *Proceedings of the 19th Annual International Conference on Thermal, Mechanical and Multi-Physics Simulation and Experiments in Microelectronics and Microsystems*, pages 1–8, 2018.
- [77] M. Springer, A. Turon, and H. E. Pettermann. A thermo-mechanical cyclic cohesive zone model for variable amplitude loading and mixed-mode behavior. *International Journal of Solids and Structures*, 159:257–271, 2019.
- [78] G. G. Stoney. The tension of metallic films deposited by electrolysis. *Proceedings of the Royal Society A*, 82:172–175, 1909.
- [79] V. Teixeira. Residual stress and cracking in thin pvd coatings. *Vacuum*, 64:393–399, 2002.

- [80] M. Todt, F. Toth, M. A. Hartmann, D. Holec, M. J. Cordill, F. D. Fischer, and F. G. Rammerstorfer. Computational simulation of instability phenomena in nanoparticles and nanofilms. *Computational Technology Reviews*, 10:89–119, 2014.
- [81] F. Toth, F. G. Rammerstorfer, M. J. Cordill, and F. D. Fischer. Detailed modelling of delamination buckling of thin films under global tension. *Acta Materialia*, 61:2425–2433, 2013.
- [82] P. H. Townsend, D. M. Barnett, and T. A. Brunner. Elastic relationships in layered composite media with approximation for the case of thin films on a thick substrate. *Journal of Applied Physics*, 62:4438–4444, 1987.
- [83] Y. C. Tsui and T. W. Clyne. An analytical model for predicting residual stresses in progressively deposited coatings Part 1: Planar geometry. *Thin Solid Films*, 306:23, 1997.
- [84] Y. C. Tsui, C. Doyle, and T. W. Clyne. Plasma sprayed hydroxyapatite coatings on titanium substrates Part 1: Mechanical properties and residual stress levels. *Biomaterials*, 19:2015–2029, 1998.
- [85] I. Uzun and K. Aslantas. Numerical simulation of orthogonal machining process using multilayer and single-layer coated tools. *The International Journal of Advanced Manufacturing Technology*, 54:899–910, 2011.
- [86] V. Unger. Non-linear finite element simulations of nanoindentation in gallium nitride considering fracture mechanics and plasticity. Master’s thesis, TU Wien, 2018. Supervisors: H.E. Pettermann and J. Stampfl.
- [87] R. P. Vinci, E. M. Zielinski, and J. C. Bravman. Thermal strain and stress in copper thin films. *Thin Solid Films*, 262:142 – 153, 1995.
- [88] A. Wagner. Efficient finite element modelling of residual stresses in multilayer coatings. Master’s thesis, TU Wien, 2017. Supervisors: H.J. Böhm and M. Todt.

-
- [89] F. L. Wen and Y. L. Shen. Plastic deformation in multilayered thin films during indentation unloading: a modeling analysis incorporating viscoplastic response. *Mechanics of Time-Dependent Materials*, 15:277–291, 2011.
- [90] P. J. Withers and H. K. D. H. Bhadeshia. Residual stress. Part 1 – Measurement techniques. *Materials Science and Technology*, 17:355–365, 2001.
- [91] N.-H. Zhang and J.-J. Xing. An alternative model for elastic bending deformation of multilayered beams. *Journal of Applied Physics*, 100:103519, 2006.
- [92] Y.-M. Zhang, Y. Gu, and J.-T. Chen. Internal stress analysis for single and multilayered coating systems using the boundary element method. *Engineering Analysis with Boundary Elements*, 35:708–717, 2011.
- [93] X. Zhao, Z. Xie, and P. Munroe. Nanoindentation of hard multilayer coatings: Finite element modelling. *Materials Science and Engineering: A*, 528:1111–1116, 2011.
- [94] Z. B. Zhao, J. Hershberger, and J. C. Bilello. In-situ observations of stress-induced thin film failures. *Thin Solid Films*, 518:2037 – 2044, 2010.
- [95] J. Zhu, H. Xie, Z. Hu, P. Chen, and Q. Zhang. Residual stress in thermal spray coatings measured by curvature based on 3D digital image correlation technique. *Surface and Coatings Technology*, 206:1396 – 1402, 2011.

3.5 Publications

APPLIED PHYSICS LETTERS 107, 071602 (2015)



Thermal expansion of rock-salt cubic AlN

M. Bartosik,^{1,a)} M. Todt,² D. Holec,³ J. Todt,⁴ L. Zhou,¹ H. Riedl,¹ H. J. Böhm,²
F. G. Rammerstorfer,² and P. H. Mayrhofer¹¹Institute of Materials Science and Technology, TU Wien, A-1060 Vienna, Austria²Institute of Lightweight Design and Structural Biomechanics, TU Wien, A-1060 Vienna, Austria³Department of Physical Metallurgy and Materials Testing, Montanuniversität Leoben, A-8700 Leoben, Austria⁴Department of Materials Physics, Montanuniversität Leoben, A-8700 Leoben, Austria

(Received 16 March 2015; accepted 6 August 2015; published online 18 August 2015)

We combine continuum mechanics modeling and wafer curvature experiments to characterize the thermal expansion coefficient of AlN in its metastable cubic rock-salt (B1) structure. The latter was stabilized as nm thin layers by coherency strains in CrN/AlN epitaxial multilayers deposited on Si (100) substrates using reactive magnetron sputtering. The extraction of the B1-AlN thermal expansion coefficient, from experimentally recorded temperature dependent wafer curvature data, is formulated as an inverse problem using continuum mechanics modeling. The results are cross-validated by density functional theory calculations. © 2015 Author(s). All article content, except where otherwise noted, is licensed under a Creative Commons Attribution 3.0 Unported License.

[<http://dx.doi.org/10.1063/1.4928911>]

Aluminum nitride is used for a wide range of applications reaching from optoelectronics¹ to hard protective coatings.² Its stable wurtzite (B4) variant as well as the metastable cubic B3 (zinc-blend) phase can be obtained as bulk materials at ambient pressures. Cubic B1 (rock-salt)-AlN, however, is stable only at pressures above ~ 13 – 23 GPa,³ and thus known as high-pressure phase. The metastable B1-phase can also be stabilized under ambient pressures by coherency strains, to lattice matched materials, but only up to a thickness of a few nm.^{4–11} Consequently, there is no straightforward way to experimentally characterize the properties of B1-AlN.

First principles calculations suggest superior mechanical properties of AlN of the metastable B1 structure as compared with its wurtzitic counterpart (e.g., higher bulk modulus³) or other B1 structured nitride materials as used for hard coating applications, for example.¹² The high specific volume increase of $\sim 26\%$ (Refs. 13 and 14) calculated for the B1 to B4 transformation has the potential for a phase-transformation-induced toughening effect¹⁵ or to implement compressive stresses in thin films.¹⁶ Similarly, the formation of coherent B1-AlN domains during spinodal decomposition of metastable $\text{Ti}_{1-x}\text{Al}_x\text{N}$ upon annealing age hardens $\text{Ti}_{1-x}\text{Al}_x\text{N}$ coatings.¹⁷

Thermal expansion plays an important role for the functionality of thin film-substrate systems. The mismatch in the thermal expansion coefficients (TEC) of a film and a substrate results in thermal stress formation upon temperature changes, which can lead to undesirable bending, cracks, and/or film delamination from the substrate.¹⁸ While the TEC of B4-AlN (Refs. 19 and 20) is known both theoretically and experimentally, the TEC of B1-AlN has yet to be reported experimentally.

Here, we propose an approach using continuum mechanics modeling to determine the TEC of B1-AlN from

experimentally recorded temperature dependent wafer curvature data. Although this study focuses on the AlN/CrN system, the methodology described below is general and can be applied to any metastable material. B1-AlN is stabilized in CrN/AlN multilayers on Si (100) substrates (specimen dimensions: $0.38 \times 20 \times 7$ mm³). The layers were grown at 743 K using reactive magnetron sputtering, see Table I. In addition, 1.5 μm thick monolithic CrN was studied to verify both the material properties of CrN and the methodological approach. The deposition parameters are reported in Ref. 11. Film growth stresses and the formation of thermal stresses when cooling down from deposition to room temperature lead to an initial curvature of the samples in the as-deposited state.

The stabilization of AlN in the B1 structure by local epitaxy to lattice matched CrN is shown on the nano-scale by employing transmission electron microscopy (TEM) using a Tecnai F20 TEM microscope operated at 200 kV. The coherent growth of AlN and CrN on each other is indicated by the columnar morphology with grains extending over several CrN (dark) and AlN (light) layers, as demonstrated by the bright field micrograph, Figure 1(a). The coherent growth is supported by high-resolution TEM, Figure 1(b), showing continuous lattice fringes throughout the CrN and AlN layers. In addition, the Fast Fourier Transformation (FFT) of the high-resolution TEM given in Figure 1(b) shows spots corresponding to a cubic phase with a lattice parameter between B1-AlN and CrN, see Figure 1(c).

In the wafer-curvature experiment (under vacuum conditions better than 10^{-4} mbar), the samples (placed with the substrate side facing down on a heating plate) were heated to ~ 450 K and cooled back to room temperature with a constant heating and cooling rate of 5 K/min. The wafer curvature system used is equipped with an array of parallel laser beams with a spot size of ~ 200 μm and a position sensitive charge-coupled device detector. More details about the experimental method can be found in Ref. 21. The evolution of

^{a)} Author to whom correspondence should be addressed. Electronic mail: matthias.bartosik@tuwien.ac.at.



TABLE I. CrN/AlN multilayer samples. The parameter N denotes the number of bilayers, h_{AIN} and h_{CrN} are the layer thicknesses of AlN and CrN, h_{tot} is the total film thickness, $\frac{1}{r_{exp}}$ and $\frac{1}{r_{an}}$ are the experimental and the analytically calculated curvature values, and δ is the relative deviation between the experimental and simulated curvature. The uncertainty of the layer thicknesses obtained by TEM is around 10% but not larger than 0.5 nm.

Sample ID	N	h_{AIN} (nm)	h_{CrN} (nm)	h_{tot} (nm)	$\frac{1}{r_{exp}}$ (m^{-1})	$\frac{1}{r_{an}}$ (m^{-1})	δ (%)
CrN	1500	1500	0.0683	0.0636	7.37
N-600-1	600	1	1	1200	0.0477	0.0901	46.99
N-500-1	500	1	2	1500	0.0650	0.0955	31.90
N-275-2	275	2	3.5	1512.5	0.0740	0.0991	25.36
N-240-3	240	3	3.25	1500	0.0818	0.1101	25.77
N-233-2	233	2	4.5	1514.5	0.0966	0.0939	2.87
N-178-2	178	2	6.5	1513	0.0945	0.0868	8.82

the sample curvature (in addition to the initial curvature) with temperature, originating from the mismatch of TEC and elastic properties between film and substrate materials, is presented for the different multilayers in Figure 2. After such a thermocycle, to ~ 450 K, the samples exhibit the same curvature as in the initial state, suggesting purely elastic deformation. This is because the maximum temperature of ~ 450 K is clearly below the deposition temperature of 743 K. Hence, the thermal energy is still below the minimum to activate recovery processes (e.g., point defect rearrangement or annihilation).

To cross-validate the results, the TECs of B1-AlN and the Si substrate were calculated employing DFT,^{22,23} as implemented in the Vienna *Ab initio* Simulation Package (VASP).²⁴ The single crystal elastic properties were calculated using the stress-strain method.^{25,26} Young's modulus and Poisson's ratio of the polycrystals were evaluated as the Hill's averages of the Reuss's and Voigt's limits on isotropic polycrystalline aggregates.¹² The phonopy code²⁷ was used as a pre- and post-processor to calculate the real space pho-

non frequencies and, hence, to evaluate the Helmholtz free energy.²⁸ The quasi-harmonic treatment applied to 10 volumes around the equilibrium 0 K volume subsequently allowed to establish the Gibbs free energy as a function of temperature and volume and, hence, to determine the TEC of B1-AlN. The result is in good agreement with Ref. 29. The TEC of paramagnetic CrN (Ref. 30) is taken from our recent *ab initio* calculations.

Lamination theory³¹ is used to describe the relationship between stresses and deformations of a reference surface of the sample, see Figure 3. As the sample curvature is measured on the topmost layer of the coating, the upper surface of the sample is chosen as the reference surface for the analytical model. The curvature change (relative to the initial curvature) generated by the thermal loading is calculated with respect to the initial curvature. This approach is permissible as long as linear-elastic behavior can be assumed, and the initial curvature as well as the sample deformations are small. Due to the relatively small sample thickness, plane stress conditions are assumed. For the model, we used the condition of a perfect bonding between the individual layers of the multilayer coating itself and between the coating and the substrate. Room temperature with $\theta_0 = 20^\circ\text{C} = 293.15$ K is chosen as reference temperature, and the initial deformation of the sample was set to zero. For straightforward calculations, the stresses within the individual layers of the multilayer coating are treated as constant over their layer thicknesses and the stresses within the substrate are treated as depending linearly on the distance from the interface to the film. Hence, we used the classical plate bending theory for the substrate. The stress resultants in terms of membrane forces per unit width $\underline{n} = [n_{xx}, n_{yy}, n_{xy}]^T$ and bending and twisting moments per unit width $\underline{m} = [m_{xx}, m_{yy}, m_{xy}]^T$ are related to the deformations of the reference surface of the sample as well as to the applied temperature load by

$$\begin{bmatrix} \underline{n} \\ \underline{m} \end{bmatrix} = \begin{bmatrix} \underline{A}_s + \underline{A}_c & \underline{B}_s + \underline{B}_c \\ \underline{B}_s + \underline{B}_c & \underline{D}_s + \underline{D}_c \end{bmatrix} \cdot \begin{bmatrix} \underline{\bar{\epsilon}} \\ \underline{\bar{\kappa}} \end{bmatrix} - \left(\begin{bmatrix} \underline{A}_s \\ -\underline{B}_s \end{bmatrix} \cdot \underline{\alpha}_s + \begin{bmatrix} \underline{A}_{CrN} \\ -\underline{B}_{CrN} \end{bmatrix} \cdot \underline{\alpha}_{CrN} + \begin{bmatrix} \underline{A}_{AIN} \\ -\underline{B}_{AIN} \end{bmatrix} \cdot \underline{\alpha}_{AIN} \right) \Delta\theta, \quad (1)$$

with

$$\begin{aligned} \underline{A}_s &= \underline{E}_s h_s, \quad \underline{A}_c = \underline{A}_{CrN} + \underline{A}_{AIN} = \sum_{i=1}^{n_{CrN}} \underline{E}_{CrN} h_{CrN} + \sum_{j=1}^{n_{AIN}} \underline{E}_{AIN} h_{AIN}, \\ \underline{B}_s &= -\underline{E}_s \frac{h_s^2 + 2h_c h_s}{2}, \quad \underline{B}_c = \underline{B}_{CrN} + \underline{B}_{AIN} = -\sum_{i=1}^{n_{CrN}} \underline{E}_{CrN} h_{CrN} \hat{z}_i - \sum_{j=1}^{n_{AIN}} \underline{E}_{AIN} h_{AIN} \hat{z}_j, \\ \underline{D}_s &= \underline{E}_s \left(\frac{(h_c + h_s)^3}{3} - \frac{h_c^3}{3} \right), \quad \underline{D}_c = \sum_{i=1}^{n_{CrN}} \underline{E}_{CrN} \left(h_{CrN} \hat{z}_i^2 + \frac{h_{CrN}^3}{12} \right) + \sum_{j=1}^{n_{AIN}} \underline{E}_{AIN} \left(h_{AIN} \hat{z}_j^2 + \frac{h_{AIN}^3}{12} \right). \end{aligned} \quad (2)$$

The indices "s" and "c" denote substrate and coating, respectively. The quantities $\underline{\bar{\epsilon}} = [\bar{\epsilon}_{xx}, \bar{\epsilon}_{yy}, \bar{\epsilon}_{xy}]^T$ and $\underline{\bar{\kappa}} = [\bar{\kappa}_{xx}, \bar{\kappa}_{yy}, \bar{\kappa}_{xy}]^T$ are the strains within the reference surface and the change in sample curvature, respectively. The vector of TEC is denoted as $\underline{\alpha} = [\alpha, \alpha, 0]^T$, and $\Delta\theta$ is the applied

temperature change with respect to θ_0 . The actual temperature $\theta_0 + \Delta\theta$ is assumed to be constant within the sample, i.e., temperature gradients are not considered. In Equation (2), \underline{E} is the elasticity matrix under plane stress conditions

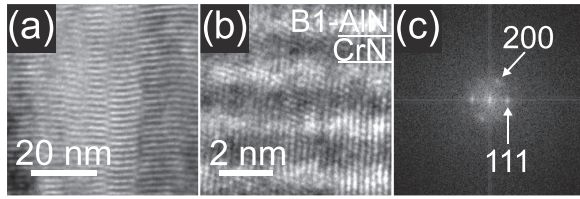


FIG. 1. Epitaxial stabilization of AlN in the B1 crystal structure by lattice matched B1-CrN template layers confirmed on the nano-scale using transmission electron microscopy: (a) bright field TEM image showing grains extending over several CrN (dark) and AlN (light) layers, (b) high-resolution TEM indicating continuous lattice fringes throughout the CrN and AlN layers, (c) FFT of (b) showing spots corresponding to a cubic phase with a lattice parameter between B1-AlN and CrN.

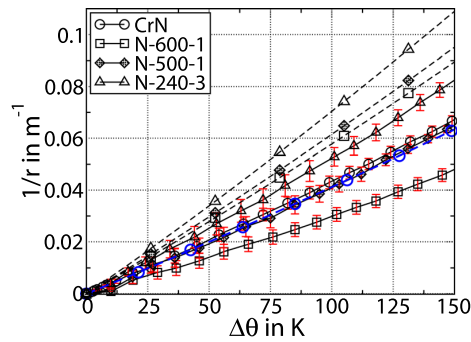


FIG. 2. Comparison between experimental (continuous lines) and simulated (dashed lines) curvature values as a function of temperature loading. For the sake of clarity, only every tenth experimental data point was plotted. The simulated curvature values for monolithic CrN are shown in blue color. The symbols denote the different multilayer samples. (The first number of the sample identifier denotes the number of bilayers and the second number the layer thicknesses of AlN in units of nanometer while keeping the total film thickness of $\sim 1.5 \mu\text{m}$ as constant.)

$$\underline{\underline{E}} = \begin{bmatrix} \frac{E}{1-\nu^2} & \frac{\nu E}{1-\nu^2} & 0 \\ \frac{\nu E}{1-\nu^2} & \frac{E}{1-\nu^2} & 0 \\ 0 & 0 & \frac{E}{2(1+\nu)} \end{bmatrix} \quad (3)$$

assuming isotropic material behavior. The quantities E and ν are the Young's modulus and the Poisson's ratio of the corresponding material, respectively. The respective layer thickness is denoted as h , and the mean distances of the CrN and

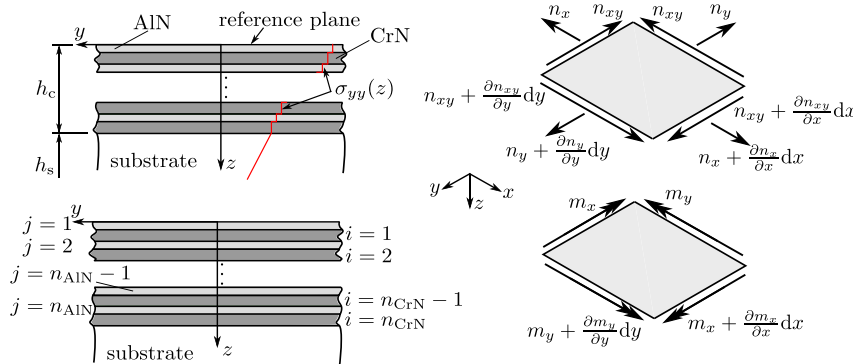


FIG. 3. Definition of the reference surface and the sample's coordinate system (left), membrane forces, and moments per unit width (right).

TABLE II. Single and polycrystalline elastic properties of B1-AlN, CrN, and Si determined using *ab initio* methods.

Material	C_{11} (GPa)	C_{12} (GPa)	C_{44} (GPa)	E (GPa)	ν (-)	B (GPa)
AlN (<i>cf.</i> Ref. 12)	418	169	308	505	0.166	252
CrN (<i>cf.</i> Ref. 30)	516	115	116	363	0.257	249
Si	154	57	75	153	0.213	89

AlN layers from the reference surface are denoted as \hat{z}_i and \hat{z}_j , respectively. In the following, E and ν of the individual materials are assumed to be independent of the sample temperature. Friction between the sample and the heating plate is neglected, and there are no external forces or moments acting on the sample, hence $\underline{n} = \underline{0}$, $\underline{m} = \underline{0}$. The sample curvature $\bar{\kappa}$ values depicted in Figure 2 were calculated according to Equation (1) using the *ab initio* calculated material properties listed in Table II. Note that the analytical model uses the integral TEC, α , being defined as

$$\alpha(\theta) = \frac{1}{\theta - \theta_0} \int_{\theta_0}^{\theta} \alpha'(\theta') d\theta', \quad (4)$$

where θ_0 is a reference temperature and $\alpha'(\theta) = (d\varepsilon_{\text{therm}}/d\theta)$. For the current simulations, θ_0 is chosen to be equal to the deformation free temperature of the sample.

A comparison between the experimental results and the analytical model reveals that, for the sample being coated with a single CrN layer, the curvature is well captured by our analytical model, see Figure 2. Hence, the elastic constants, E and ν , and the TEC of the Si substrate and the CrN layers, listed in Table II, give a good representation of the thermo-mechanical behavior of these materials. For the other samples, the differences between the experimental values and the analytical results are significant and increase with increasing volume fraction of interfaces (number of bilayers at constant film thickness), see Table I. Inaccurate values, used either for the elastic constants or TEC of B1-AlN, do not fully explain the dependence of the differences on the number of layers. Possible reasons for the discrepancies between simulation and experimental results are discussed at the end of the manuscript.

Equation (1) allows extracting $\underline{\alpha}_{\text{AlN}} = [\alpha_{\text{AlN}}, \alpha_{\text{AlN}}, 0]^T$ from the experimentally obtained curvatures. Neglecting the free edge effects, the deformed sample corresponds to the

071602-4 Bartosik *et al.*Appl. Phys. Lett. **107**, 071602 (2015)

part of the volume of a sphere, as there are no external forces or moments acting on the sample. The temperature is constant within the sample and all constituents possess isotropic material behavior. This leads to $\bar{\kappa}_{yy} = \bar{\kappa}_{xx} = \bar{\kappa}$, $\bar{\epsilon}_{yy} = \bar{\epsilon}_{xx} = \bar{\epsilon}$, $\bar{\kappa}_{xy} = 0$, and $\bar{\epsilon}_{xy} = 0$.

Therefore, Equation (1) reduces to two scalar equations

$$\begin{aligned} n_{xx} = 0 = & (A_{s11} + A_{s12} + A_{c11} + A_{c12})\bar{\epsilon} \\ & + (B_{s11} + B_{s12} + B_{c11} + B_{c12})\bar{\kappa} \\ & - ((A_{s11} + A_{s12})\alpha_s + (A_{CrN11} + A_{CrN12})\alpha_{CrN} \\ & + (A_{AlN11} + A_{AlN12})\alpha_{AlN})\Delta\theta, \end{aligned} \quad (5)$$

$$\begin{aligned} m_{xx} = 0 = & (B_{s11} + B_{s12} + B_{c11} + B_{c12})\bar{\epsilon} \\ & + (D_{s11} + D_{s12} + D_{c11} + D_{c12})\bar{\kappa} \\ & + ((B_{s11} + B_{s12})\alpha_s + (B_{CrN11} + B_{CrN12})\alpha_{CrN} \\ & + (B_{AlN11} + B_{AlN12})\alpha_{AlN})\Delta\theta. \end{aligned} \quad (6)$$

Inserting the strain $\bar{\epsilon}$, obtained from Equation (5), into Equation (6) gives the analytical closed form solution for α_{AlN}

$$\alpha_{AlN} = - \left(I_s \alpha_s + I_{CrN} \alpha_{CrN} + J_{sc} \frac{\bar{\kappa}}{\Delta\theta} \right) I_{AlN}^{-1}, \quad (7)$$

with

$$\begin{aligned} I_{AlN} &= I_{sc}(A_{AlN11} + A_{AlN12}) + (B_{AlN11} + B_{AlN12}), \\ I_s &= I_{sc}(A_{s11} + A_{s12}) + (B_{s11} + B_{s12}), \\ I_{CrN} &= I_{sc}(A_{CrN11} + A_{CrN12}) + (B_{CrN11} + B_{CrN12}), \\ J_{sc} &= (D_{s11} + D_{s12} + D_{c11} + D_{c12}) \\ &\quad - I_{sc}(B_{s11} + B_{s12} + B_{c11} + B_{c12}), \\ I_{sc} &= \frac{B_{s11} + B_{s12} + B_{c11} + B_{c12}}{A_{s11} + A_{s12} + A_{c11} + A_{c12}}. \end{aligned} \quad (8)$$

There, $i, j = 1, 2$ denote the entries in the i th row and j th column of the corresponding matrices defined in Equation (2).

As shown in Figure 2, the absolute value of the measurement uncertainties remains almost constant for the temperature range under consideration. Hence, the relative error is higher for small sample curvatures. Furthermore, for small

temperature changes a nonlinear regime of the curvature can be observed. To avoid obstruction of the results due to measurement errors and the observed nonlinearities only curvature values for $\Delta\theta > 25$ K will be used for calculating α_{AlN} by solving the inverse problem.

The results for the temperature dependent values of α_{AlN} , calculated from the experimentally obtained curvatures, are given in Figure 4(a) for selected samples listed in Table I. The values obtained for α_{AlN} differ from the *ab initio* predictions, but the slopes of the individual curves correspond quite well. The relative deviation $\frac{|\alpha_{ab} - \alpha_{exp}|}{\alpha_{ab}}$ between *ab initio* and experimental values, Figure 4(b), decreases with decreasing volume fraction of interfaces. This trend can be observed for arbitrary temperature changes $\Delta\theta$. The relative deviation decreases with increasing temperature changes which can be explained by decreasing uncertainties of the α_{AlN} values for increasing $\Delta\theta$, see Figure 4(a). We envision that the decreasing relative deviation with decreasing volume fraction of interfaces is mainly based on two effects. (1) The binding-character at the interfaces is different than within the bulk materials due to different local chemical environment, e.g., elements directly at the interface are bonded differently than within the AlN and CrN layers. Here, we need to mention that the influence of the changed AlN-to-CrN volume ratio when changing the volume fraction of interfaces—if the ratio between the AlN and CrN layer-thicknesses changes as well—is already considered within the continuum mechanics model. This suggests that the relative deviation between *ab initio* results and the experimental values, Figure 4(b), is an interface-driven effect rather than a chemical-driven effect. (2) Furthermore, for our coatings a decreasing volume fraction of interfaces is also based on increased CrN-layer thicknesses (see Table I). These thicker CrN layers are more efficient in stabilizing the AlN layers in their metastable face centered cubic structure (B1-AlN) leading to a better agreement of *ab initio* results and experiments (where the AlN layers are probably not fully stabilized within their metastable B1 structure for very thin CrN layers).

Thus, our results show that when the impact of interfaces is minimized and sufficiently thick CrN template layers are provided, our method yields the desired results, which are in good agreement with *ab initio* predictions for single phase c-AlN.

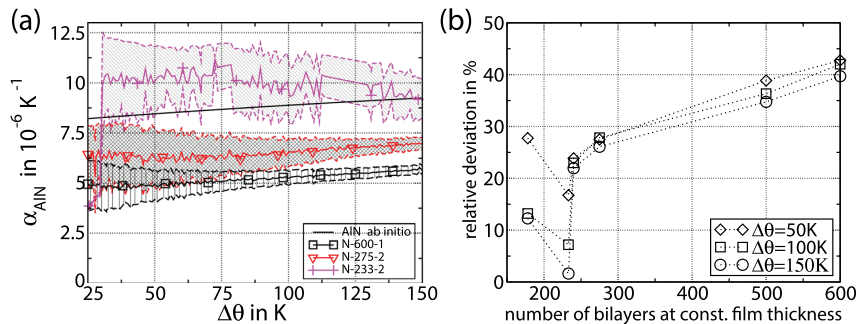


FIG. 4. (a) Results for α_{AlN} obtained with the analytical model for selected samples. The shaded areas denote uncertainties of TEC resulting from uncertainties in the curvature measurement. The first number of the sample identifier denotes the number of bilayers and the second number the layer thicknesses of AlN in units of nanometer. (b) Relative deviations between the *ab initio* and the experimental results calculated at different values of $\Delta\theta$. The number of bilayers at constant film thickness is directly proportional to the volume fraction of interfaces.

Based on our results, we confirm that AlN can be stabilized in its metastable cubic B1 crystal structure by preparing CrN/AlN multilayers. The coherency strains to lattice matched CrN templates allow for B1-AlN layers up to 3 nm. Using our approach, combining continuum mechanics modeling and experimental curvature measurements, the temperature dependent TEC of B1-AlN has been extracted from these cubic structured B1-CrN/AlN multilayers. Cross-validation with *ab initio* calculations gave the best agreement for multilayers with relatively thick CrN layers and a minimum interface volume fraction. Thereby, the interfering interface effects are minimized. However, the number of individual layers needs to be sufficiently high for an accurate wafer curvature measurement. Provided that linear elastic behavior is relevant, our approach can be applied to any similar system. It allows to extract TEC values of metastable phases, which are otherwise not accessible. In fact, almost all non-isostructural nitrides grow in a metastable structure in multilayers with small layer thicknesses (≤ 2 nm) due to the extremely high amount of interfacial energy in this type of structure, e.g., TiN/AlN, TiN/TaN, TiN/MoN, and TiN/Cr₂N.³²

The financial support by the START Program (Y371) of the Austrian Science Fund (FWF) is highly acknowledged. The computational results presented have been achieved using the Vienna Scientific Cluster (VSC).

- ¹S. C. Jain, M. Willander, J. Narayan, and R. V. Overstraeten, *J. Appl. Phys.* **87**, 965 (2000).
²P. H. Mayrhofer, C. Mitterer, L. Hultman, and H. Clemens, *Prog. Mater. Sci.* **51**, 1032 (2006).
³N. E. Christensen, *Phys. Rev. B* **50**, 4397 (1994).
⁴A. Madan, I. W. Kim, S. C. Cheng, P. Yashar, V. P. Dravid, and S. A. Barnett, *Phys. Rev. Lett.* **78**, 1743 (1997).
⁵I. W. Kim, Q. Li, L. D. Marks, and S. A. Barnett, *Appl. Phys. Lett.* **78**, 892 (2001).

- ⁶V. Pankov, M. Evstigneev, and R. H. Prince, *J. Appl. Phys.* **92**, 4255 (2002).
⁷G. Li, J. Lao, J. Tian, Z. Han, and M. Gu, *J. Appl. Phys.* **95**, 92 (2004).
⁸D. Chen, X. L. Ma, and Y. M. Wang, *Acta Mater.* **53**, 5223 (2005).
⁹J. Lin, J. J. Moore, B. Mishra, M. Pinkas, and W. D. Sproul, *Surf. Coat. Technol.* **204**, 936 (2009).
¹⁰V. Chawla, D. Holec, and P. H. Mayrhofer, *J. Phys. D: Appl. Phys.* **46**, 045305 (2013).
¹¹M. Schlögl, B. Mayer, J. Paulitsch, and P. H. Mayrhofer, *Thin Solid Films* **545**, 375 (2013).
¹²D. Holec, M. Friák, J. Neugebauer, and P. H. Mayrhofer, *Phys. Rev. B* **85**, 064101 (2012).
¹³P. H. Mayrhofer, D. Music, and J. M. Schneider, *J. Appl. Phys.* **100**, 094906 (2006).
¹⁴P. H. Mayrhofer, H. Willmann, and A. E. Reiter, *Surf. Coat. Technol.* **202**, 4935 (2008).
¹⁵M. Schlögl, C. Kirchlechner, J. Paulitsch, J. Keckes, and P. H. Mayrhofer, *Scr. Mater.* **68**, 917 (2013).
¹⁶M. Bartosik, R. Daniel, Z. Zhang, M. Deluca, W. Ecker, M. Stefanelli, M. Klaus, C. Genzel, C. Mitterer, and J. Keckes, *Surf. Coat. Technol.* **206**, 4502 (2012).
¹⁷P. H. Mayrhofer, A. Hörling, L. Karlsson, J. Sjöln, T. Larsson, C. Mitterer, and L. Hultman, *Appl. Phys. Lett.* **83**, 2049 (2003).
¹⁸L. B. Freund and S. Suresh, *Thin Film Materials: Stress, Defect Formation, and Surface Evolution* (Cambridge University Press, Cambridge, UK, 2003).
¹⁹G. A. Slack and S. F. Bartram, *J. Appl. Phys.* **46**, 89 (1975).
²⁰S. Figge, H. Kröncke, D. Hommel, and B. M. Epelbaum, *Appl. Phys. Lett.* **94**, 101915 (2009).
²¹E. Chason and B. W. Sheldon, *Surf. Eng.* **19**, 387 (2003).
²²P. Hohenberg and W. Kohn, *Phys. Rev.* **136**, B864 (1964).
²³W. Kohn and L. J. Sham, *Phys. Rev.* **140**, A1133 (1965).
²⁴G. Kresse and J. Furthmüller, *Comput. Mater. Sci.* **6**, 15 (1996).
²⁵R. Yu, J. Zhu, and H. Q. Ye, *Comput. Phys. Commun.* **181**, 671 (2010).
²⁶L. Zhou, D. Holec, and P. H. Mayrhofer, *J. Appl. Phys.* **113**, 043511 (2013).
²⁷A. Togo, F. Oba, and I. Tanaka, *Phys. Rev. B* **78**, 134106 (2008).
²⁸B. Grabowski, T. Hickel, and J. Neugebauer, *Phys. Rev. B* **76**, 024309 (2007).
²⁹S. Schmerler and J. Kortus, *Phys. Rev. B* **89**, 064109 (2014).
³⁰L. Zhou, F. Körmann, D. Holec, M. Bartosik, B. Grabowski, J. Neugebauer, and P. H. Mayrhofer, *Phys. Rev. B* **90**, 184102 (2014).
³¹R. M. Jones, *Mechanics of Composite Materials*, 2nd ed. (Taylor & Francis, Philadelphia, 1999), pp. 187–276.
³²P. C. Yashar and W. D. Sproul, *Vacuum* **55**, 179 (1999).

Simulation of Fatigue Damage in Clusters of DMOS Cells Subjected to Non-Uniform Transient Thermo-Mechanical Loading

Paul Hoffmann¹, Michael Nelhiebel^{2,3}, Balamurugan Karunamurthy^{2,3}, Heinz E. Pettermann¹, Melanie Todt¹

¹ TU Wien, Institute of Lightweight Design and Structural Biomechanics, Vienna, Austria

² KAI - Kompetenzzentrum Automobil- u. Industrieelektronik GmbH, Villach, Austria

³ Infineon Technologies Austria AG, Villach, Austria

Email: hoffmann@ilsb.tuwien.ac.at, Phone: +43 1 58801 31713

Abstract

Numerical predictions of thermo-mechanical fatigue in power semiconductors are carried out under consideration of transient thermo-mechanical loading conditions. An existing approach to model bulk fatigue damage is extended towards the usage of more general transient thermal loading conditions. To fully capture the effects of the forming fatigue cracks, a transient simulation of the thermal fields is sequentially coupled with the calculation of mechanical fields. This enables the application of the fatigue framework in larger structures featuring complex thermal boundary conditions and allows to capture the effect of fatigue cracks on thermal fields. For demonstration purposes, the developed bulk fatigue approach is applied to a generic copper-on-silicon geometry which is exposed to temperature pulses similar to cyclic overload switching in DMOS cells. Results of such generic copper-on-silicon geometries under various transient thermo-mechanical loading conditions are presented. The results highlight the novel capabilities of the extended framework and provide some qualitative statements regarding the influence of non-trivial temperature fields in power semiconductors on the thermo-mechanical fatigue behavior.

1. Introduction

The reliability of power semiconductor devices is a topic of key importance [1]. Due to decreasing device size, high cost pressure, and increasing requirements, new approaches are needed to better understand the mechanisms leading to reliability issues. In terms of thermo-mechanical fatigue, two distinct damage mechanisms can be addressed in the power metallization layer, i. e. delamination and material degradation, whereby this work will concentrate on the latter. The driving forces behind these failure modes are short electric overload pulses, which lead to high temperatures in the power metallization layer and the underlying substrate. A schematic cross-section of an exemplary semiconductor device is depicted in Figure 1. In addition, a scanning electron microscope (SEM) image of a typical fatigue crack caused by the thermo-mechanical fatigue is shown.

To model thermo-mechanical bulk fatigue in the metallization layer a continuum damage mechanics (CDM)

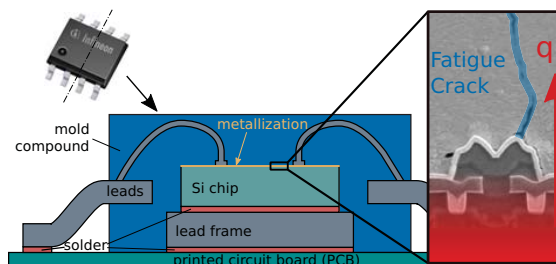


Figure 1: Cross-section of a exemplary semiconductor device and SEM image of a fatigue crack formed during active cycling. (Modified from [2])

based framework has been formulated and implemented into the Finite Element Method (FEM) [2], [3], [4], [5]. At the material point it uses a multiaxial fatigue criterion for the prediction of damage onset due to microvoid nucleation and an inelastic strain energy-based criterion to model the damage evolution caused by the growth and coalescence of microvoids. The spatial advance of fatigue damage is captured by means of the FEM. In [3] this approach has been applied to a generic submodel of a double diffused metal oxide semiconductor field-effect transistor (DMOSFET) cell subjected to simplified temperature loading conditions. In reality, however, non-uniform thermal loads occur in semiconductors [6].

In the present work the existing framework is therefore extended towards transient thermal loading conditions. As a result, the transient thermal and mechanical fields are treated in a sequentially coupled analysis and the effect of evolving fatigue damage on the thermal fields can be captured. This enables the investigation of clusters of multiple DMOS cell-like features. Shielding effects and the influence of non trivial thermal boundary conditions on the formation and propagation of fatigue cracks can be investigated in such arrangements.

2. Methodology

The CDM fatigue simulation framework has been proposed by Springer [3], [4], [5]. It has been implemented into the FEM framework ANSYS Mechanical APDL 19.2 (ANSYS Inc., Canonsburg, PA,USA) utilizing simplified

thermal boundary conditions. In the following, a brief overview of the framework is given (for details see [2], [3]) and the extension towards transient thermal analyses is presented.

A. Fatigue Damage Modeling in the Bulk Material

In the framework proposed in [3], [4], the fatigue life at the material level is divided into damage onset due to microvoid nucleation and into damage evolution caused by the growth and coalescence of microvoids. The lifetime before damage onset is modeled by an indicator approach, i.e. the material properties are not changed in that phase of the fatigue simulation. Once the indicator predicts damage onset, a damage evolution model sets in which can predict local material degradation based on CDM. The implementation of the above as constitutive material law into nonlinear FEM, eventually, allows the simulation of the spacial advance of fatigue cracks on the structural level.

A Fatemi-Socie (FS) multiaxial fatigue criterion [7] has been chosen for this indicator approach. It is primarily governed by the maximum cyclic shear strain amplitude, which has been reported to be the main cause for microvoid nucleation in copper [8]. The FS criterion along with the maximum damage method [9] is given as,

$$\left\{ \frac{\Delta\gamma}{2} \left(1 + \kappa \frac{\hat{\sigma}_n}{\sigma_Y} \right) \right\}_{\max} = \underbrace{\frac{\tau_f'}{G} (2N_O)^{b_\gamma}}_{\text{HCF}} + \underbrace{\gamma_f' (2N_O)^{c_\gamma}}_{\text{LCF}}, \quad (1)$$

where on the left hand side, $\Delta\gamma$ is the shear strain range on the considered plane, $\hat{\sigma}_n$ is the maximum normal stress on the considered plane, σ_Y is the yield stress, and κ is a material parameter. The left hand side is commonly called Fatigue Indicator Parameter (FIP). The subscript $\{-\}_{\max}$ indicates the plane in which the FIP reaches its maximum. The right hand side of Equation (1) is a superposition of the Basquin (High Cycle Fatigue, HCF) and the Coffin-Manson (Low Cycle Fatigue, LCF) relations, with G being the shear modulus, τ_f' the shear fatigue strength coefficient, b_γ the shear fatigue strength exponent, γ_f' the shear fatigue ductility coefficient, c_γ the shear fatigue ductility exponent, and N_O the number of cycles for damage onset, i.e. microvoid nucleation. For the present problems, it can be expected that the fatigue progress is dominated by the LCF term, the HCF part is disregarded. To account for variable amplitude loading a Palmgren-Miner linear damage accumulation rule is employed to predict damage onset.

Damage evolution is described by an inelastic strain energy-based approach. This approach is based on an energy parameter given as,

$$\Delta w_{\text{mod}} = \Delta w + \alpha \sigma_H^{\max}, \quad (2)$$

where Δw is the inelastic strain energy density of one stabilized cycle (for details see [3], [4]), σ_H^{\max} the maxi-

mum hydrostatic pressure occurring during that stabilized cycle, and α is an influence parameter. Using Δw_{mod} together with a damage evolution law similar to the one proposed in [10] provides an expression for the increase of the damage variable D per cycle, reading,

$$\frac{dD}{dN} = \frac{\varkappa_1}{l} (\Delta w_{\text{mod}})^{\varkappa_2}. \quad (3)$$

In this equation, \varkappa_1 and \varkappa_2 are material parameters which need to be obtained through calibration with experimental data and l is the characteristic element length in the context of the FEM. The increasing local loss of material integrity is modeled by CDM [3], [4] and determined by the damage variable D . Values of $D = 0$ corresponds to pristine material, while $D = 1$ stands for completely damaged material. Damage evolution is controlled by Equation 3. The number of cycles to accumulate the damage variable D from 0 to 1 is N_D . Combined with Equation (1) one can express the total number of cycles for local fatigue crack emergence as

$$N_N = N_O + N_D. \quad (4)$$

This methodology is implemented into a nonlinear FEM package as a constitutive material law in combination with a cycle jump technique (details see [3], [4]), which enables the prediction of the spatial advance of fatigue cracks as a function of cyclic loading.

B. Transient Thermo-Mechanical Loading

The CDM framework as implemented in [3], [4] allows to model fatigue damage under cyclic thermo-mechanical loading whereby the thermal loads have to be specified by a set of predefined temperature fields. In order to be able to model the complex thermal loading conditions occurring in semiconductors, the framework is extended towards transient thermal analyses. With this extension, it is possible to apply thermal boundary conditions that represent the thermal loading of a power semiconductor device. Heat can be introduced into the system with a time-dependent power density equal to the thermal energy dissipation in the chip during active power cycling. It is emphasized, that this also allows to capture the influence of propagating fatigue cracks on the temperature fields in a more realistic manner.

The most convenient way of modeling the given problem is a weak coupling between the thermal fields and the mechanical fields. Hereby, based on material properties, geometry, and boundary conditions, only the thermal analysis is conducted by a transient time-dependent approach.

As a result, the spatial temperature fields are obtained for any time point in the load history. These temperature fields are subsequently used as temperature boundary conditions in the mechanical analysis, which is performed quasi-statically for each given time step of the transient analysis and has to be repeated until a stabilized cycle is found. Subsequently, the fatigue damage is calculated.

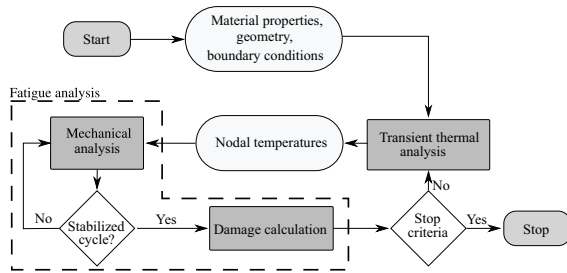


Figure 2: Simplified representation of the simulation procedure featuring the transient thermal loading conditions.

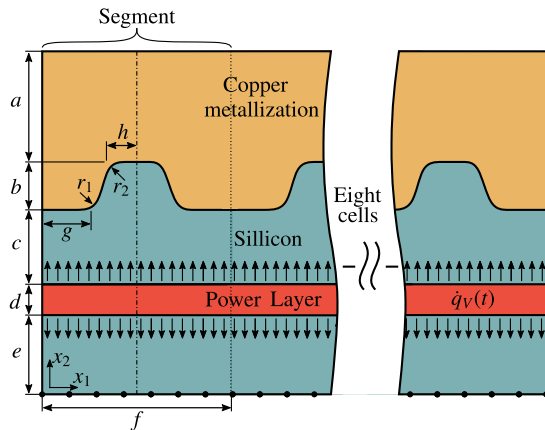


Figure 3: Schematic representation of the DMOS cell-like features.

(For a detailed explanation of the fatigue analysis refer to [3], [4].) Since the temperature fields also change with the introduction of fatigue damage, the previously calculated temperature fields are outdated and the transient thermal analysis has to be redone accounting for the fatigue damage. With the updated temperature fields a new mechanical analysis is conducted and the search for a stabilized cycle starts again. This iterative analysis cycle is illustrated in Figure 2.

3. FEM-Model

As representative examples, arrangements of DMOS cell-like features (see Figure 1 right) are used to show the capabilities of the framework. The complicated geometry of the DMOS cells is simplified since the goal is not to predict the behavior of actual devices.

A two-dimensional generic geometry is chosen for the FEM simulation, see Figure 3. Eight DMOS cell-like features consisting of a copper metallization layer and a silicon substrate, subsequently called segments, are modeled. A part of the silicon substrate acts as an active power layer that introduces thermal energy into the system. The dimensions are given in Table 1. A mesh consisting of isoparametric, linear interpolated, fully

Table 1: Dimensions of the model given in μm

a	b	c	d	e	f	g	h	r_1	r_2
21.7	3.2	5.1	5	30	12.8	3.8	1.9	1	1

Table 2: Elastic engineering moduli of silicon

$E_1 = E_2 = E_3$	$\nu_{12} = \nu_{23} = \nu_{31}$	$G_{12} = G_{23} = G_{31}$
130 GPa	0.28	79.6 GPa

integrated, four noded, plane strain elements is used for discretization. The element size (edge length) is around $0.9\mu\text{m}$ in the metallization layer and generally coarser in the silicon substrate. It has to be mentioned that the mesh in the copper is not regular, which means that there are small differences between the meshes of the individual segments. Material data for silicon and copper are taken from [3] and [2]. The material data of silicon is given in Tables 2 and 3 and represents the material properties of a standard (100) silicon wafer which has the principle axes aligned with the crystal direction [100], [010], and [001]. For the given model it is assumed that these axes are in turn aligned with the model axes $x_1 - x_2 - x_3$, see Figure 3. The secant coefficient of thermal expansion (CTE), the thermal conductivity, k , and the specific heat, c , are given in dependency of the temperature. The mass density, ρ , is independent of the temperature. The properties are summarized in Table 3. For the copper metallization layer the temperature independent elastic and thermal properties are defined in Table 5. The plastic behavior is described using a temperature dependent Chaboche model. The corresponding plastic parameters are listed in Table 4. The whole model is assumed to be stress free at room temperature, i.e. $T = 293\text{K}$, which is also the respective reference temperature for the CTEs. The required input parameters for the CDM fatigue framework have been determined in [5], based on micro cantilever experiments (see [11]). The properties are summarized in Table 6.

To highlight the capabilities of the modeling approach different loading configurations are presented. These configurations, illustrated in Figure 4, do not represent the actual geometry and loading conditions of a semiconductor. All configurations have the same mechanical symmetry boundary conditions, which restrict the displacement in

Table 3: Thermal properties of Silicon

Temperature K	CTE 10^{-6}K^{-1}	k $\frac{\text{W}}{\text{mm K}}$	c $\frac{\text{mJ}}{\text{g K}}$	ρ $\frac{\text{g}}{\text{mm}^3}$
325	2.76	0.071	730.80	0.00236
400	3.21	0.061	782.52	0.00236
475	3.52	0.053	816.32	0.00236
550	3.72	0.047	837.38	0.00236
625	3.88	0.042	854.16	0.00236

Table 4: Temperature depended plastic parameters

Temperature K	σ_Y MPa	C_1 MPa	γ_1 -
163	157	2000	9.0
293	142	1800	8.5
398	130	1600	8.0
473	107	1400	7.5
673	79	1200	7.0

Table 5: Elastic and thermal properties of polycrystalline copper

E GPa	ν -	CTE 10^{-6} K^{-1}	k $\frac{\text{W}}{\text{mm K}}$	c $\frac{\text{mJ}}{\text{g K}}$	ρ $\frac{\text{g}}{\text{mm}^3}$
100	0.35	16.7	0.385	385	0.00896

Table 6: Estimated fatigue properties for copper

κ	γ_f	c_γ	α	κ_1	κ_2
1	0.75	-0.45	0.0006	$1.9 \frac{10^{-6} \text{mm}}{\text{cycle} (\text{MPa})^{\kappa_2}}$	0.45

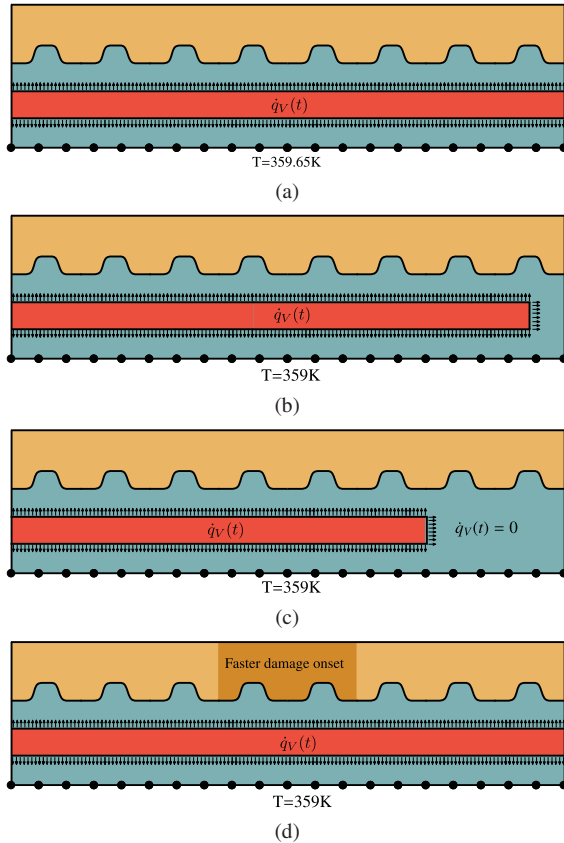


Figure 4: FEM models of DMOS cell-like features to study the influence lateral temperature differences (a-c) and locally accelerated fatigue damage onset (d) on the growth of fatigue cracks.

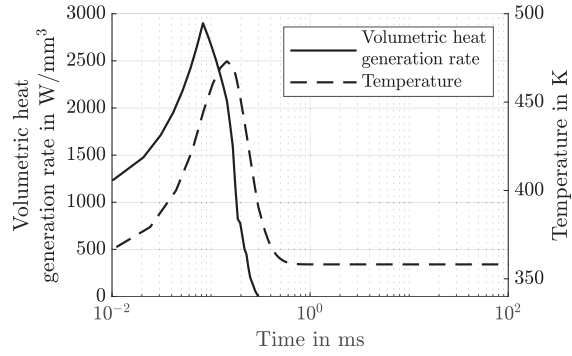


Figure 5: The volumetric heat generation rate $\dot{q}_V(t)$ in the power layer during one active cycle and the nodal temperature at the interface of the undamaged model (standard configuration Figure 4a).

the x_1 -direction at the left and the right side, respectively (see Figure 3). At the bottom nodes the displacement in the x_2 -direction is restricted. The thermal boundary conditions consist of a fixed temperature of $T = 359.65 \text{ K}$ at the bottom nodes, no heat transfer through the top, left, and right model boundary nodes and a volumetric heat generation rate, $\dot{q}_V(t)$, that introduces thermal energy into the power layer.

The model depicted in Figure 4a represents the standard configuration, with heat generation in all eight segments. The volumetric heat generation rate, $\dot{q}_V(t)$, and the corresponding temperature result at the interface in the middle of a representative segment (Figure 4a) are shown in Figure 5. In Figure 4b a small lateral temperature difference between the segments is introduced by deactivating the heating beneath the rightmost half cell (i.e. beneath a full DMOS cell due to symmetry boundary conditions). A much stronger lateral temperature difference is introduced, in Figure 4c by deactivating the power layer beneath two cells. The last configuration, Figure 4d, focuses on a different aspect. While the thermal and mechanical boundary conditions are the same as the ones of Figure 4a the fatigue behavior of the two center segments is modified. For these segments fatigue damage onset is accelerated by 20%, i.e. in these segments a lower number of cycles N_O is necessary to reach damage evolution.

4. Simulation Results

The results of the different loading configurations are presented and compared regarding the forming fatigue cracks. Fatigue cracks are defined as connected regions of elements in which the damage evolution has led to a complete loss of material integrity and the local fatigue failure cycle number $N_N = N_O + N_D$ has been reached. It should be noted that the used fatigue parameters have been obtained from mechanical loading. Hence, the presented cycle numbers are rather qualitative in their character.

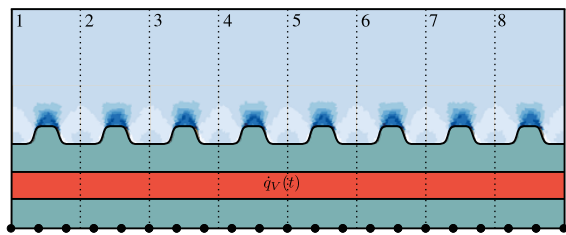


Figure 6: Distribution of FIP prior to the occurrence of fatigue cracks. Dark blue values indicate a high FIP, light blue values a low one.

Nevertheless, these cycle numbers allow a direct comparison between the individual configurations.

A. Standard Configuration

In the standard configuration, the load on each segment is the same. The only difference between the cells is the unstructured FEM mesh. At first, this leads to almost the same spatial FIP distribution for each of the eight segments, as can be seen in Figure 6. In this figure, and in all subsequent figures, dark blue indicates a high local FIP and light blue a low one. Since the FIP is directly related to damage onset, it can be expected that fatigue cracks emerge at locations with high FIP, in this case at the radii of the silicon humps.

It depends on the unstructured mesh at which of the eight humps the first fatigue crack forms. After 80555 cycles the first element has reached the local fatigue crack initiation cycle number N_N in segment 4. The position is indicated in Figure 7a. After 84651 cycles small fatigue cracks have formed in all 8 segments. Until around cycle number 106160, all 8 individual fatigue cracks propagate at roughly the same speed, mostly growing upwards but also slightly downwards along the copper-silicon interface. Figure 7a illustrates the fatigue crack pattern at this early stage. In this and in all following plots, the white areas are regions in which the elements are completely damaged ($D = 1$) and therefore a fatigue crack has formed. The coloring in the remaining part of the metallization layer again represents the FIP. One can see that the FIP fields are already unevenly distributed between the eight segments. In segments 2, 3, 5, 7, and 8 one can see regions of low FIP directly above the tip of fatigue crack. In contrast, the highest FIP values are reached in segment 4. Figure 7b shows the simulation at cycle 136620. At this stage, one dominant fatigue crack has formed in segment 4. As already predictable from Figure 7a, the fatigue cracks in segments 2, 3, and 5 have not grown much further since these are shielded by the dominant crack. This behavior can also be seen in Figure 7c which shows plots of the number of failed elements per segment over the cycle number. With the emergence of the dominant macro crack in segment 4, the fatigue crack growth in all

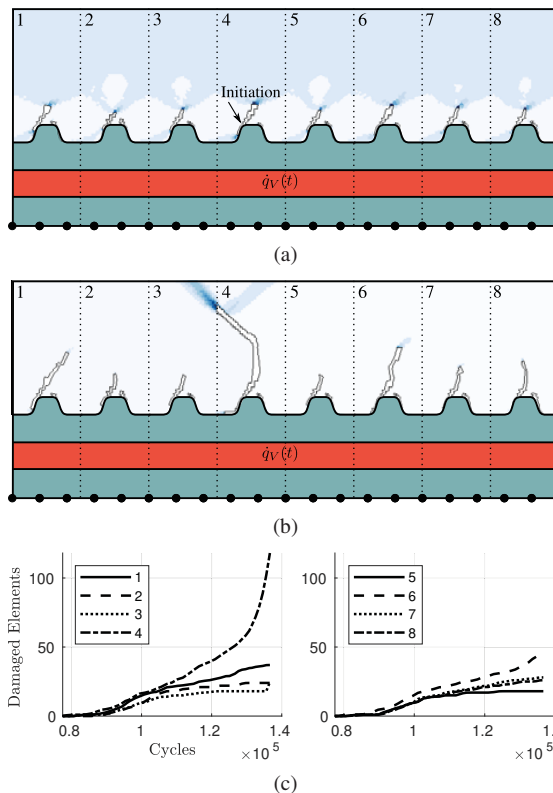


Figure 7: Fatigue damage characteristics of eight generic DMOS cell segments with lateral homogeneous thermal loading. Figure (a) shows the fatigue macro cracks and FIP values at cycle number 106160. Dark blue values indicate a high FIP light blue values a low one. Figure (b) shows fatigue macro cracks and FIP values at cycle number 136620. In Figure (c) one can see the evolution of the fatigue cracks in the different segments.

other segments slows down and stops almost completely in segments 3 and 5.

B. Configuration with a Small Lateral Temperature Gradient

In the following the results of configuration 4b are presented. Hereby, a relatively small lateral temperature gradient is introduced by deactivating the heating beneath only one-half segment. Overall, this reduces the total thermal energy introduced by 6.25%. The distribution of the FIP prior to the occurrence of fatigue cracks is depicted in Figure 8. The influence of the modified temperature field is visible, in particular when comparing it with Figure 6. How this lateral thermal gradient affects the emerging fatigue cracks is presented in Figure 9. The first fatigue crack emerges at 105220 cycles at the hump in segment 4, similar to the standard configuration. Figure 9a shows how the fatigue cracks have developed

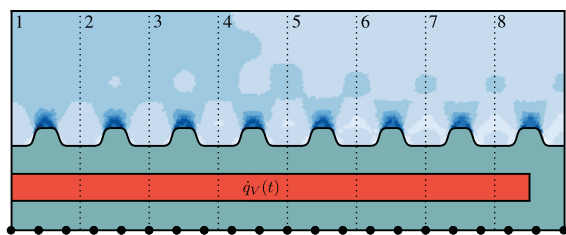
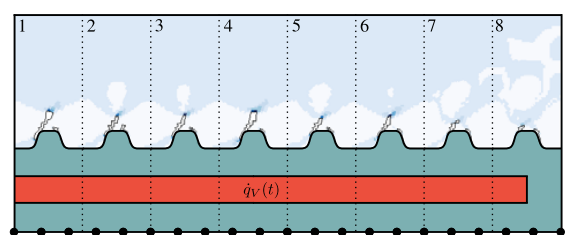
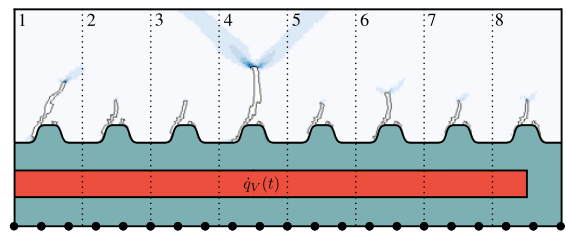


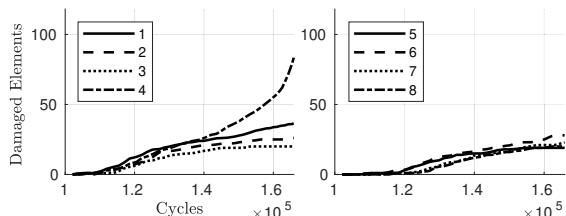
Figure 8: Distribution of FIP prior to the occurrence of fatigue cracks. Dark blue values indicate a high FIP, light blue values a low one.



(a)



(b)



(c)

Figure 9: Fatigue damage characteristics of eight generic DMOS cell segments with a small lateral temperature gradient induced by deactivating the power layer beneath one-half cell. Figure (a) shows the fatigue macro cracks and FIP values at cycle number 132 350. Dark blue values indicate a high FIP light blue values a low one. Figure (b) shows fatigue macro cracks and FIP values at cycle number 165 890. In Figure (c) one can see the evolution of the fatigue cracks in the different segments.

after 132 350 cycles. The cracks in the segments 1-6 have all reached a relatively similar size, whereas the fatigue cracks in segments 7 and 8 are much smaller. This can also be seen in Figure 9c, which illustrates that the fatigue cracks in segments 7 and 8 initiate at higher cycle numbers than the fatigue cracks in the other segments.

Figure 9b depicts the model at a later stage in the simulation, namely after 165 890 cycles. Again, a dominant fatigue crack has formed in segment 4, shielding the neighboring segments. Interestingly, the fatigue cracks of segments 7 and 8 have reached a length similar to that of the other non-dominant cracks.

It can be summarized, that deactivating the heating beneath one-half segment (i.e. one DEMOS cell) influences the fatigue crack formation not enough to drastically change the forming crack patterns. Nevertheless, the thereby caused reduction of the total thermal energy by 6.25% increases the number of cycles needed to reach a similar crack pattern by roughly 25%, compare Figures 7c and 9c.

C. Configuration with a Strong Lateral Temperature Gradient

To get a better understanding of the effects of a stronger lateral temperature gradient, the number of segments without heating is increased from a half segment to two segments, see Figure 4c. This reduces the total amount of thermal energy introduced by 25%. While in the previously presented simulations the position of the first fully damaged element depends on the unstructured mesh, in this simulation the thermal differences between the segments are stronger than the influence of the unstructured mesh. This leads to the first fatigue crack initiating in segment 1 at cycle number 199 280.

This number is significantly higher as the two previously observed cycle numbers for fatigue crack initiation, and it also takes much longer until the first large fatigue cracks have formed. In Figure 10a the damage state at cycle number 265 820 is presented. While this cycle number is more than double as high as the one of Figure 9a very little fatigue crack progression can be observed. The first two segments show small fatigue cracks and also the first elements are completely damaged in segments 3-6. No fatigue crack has formed yet in segment 7 and 8. Even at cycle number 353 120, as depicted in Figure 10b, no significant fatigue cracks can be seen in these two segments. A dominant crack has emerged in segment 2. This is interesting regarding two aspects. First, it shows that the lateral temperature gradient is now strong enough to force the dominant crack away from the mesh favored position in previously presented simulations. Secondly, it does not form in segment 1 which shows the first fatigue crack and also has the highest temperature. This can be explained by the boundary conditions. The mechanical symmetry boundary conditions at the left border of the first segment imply that also in the imaginative neighboring segment a

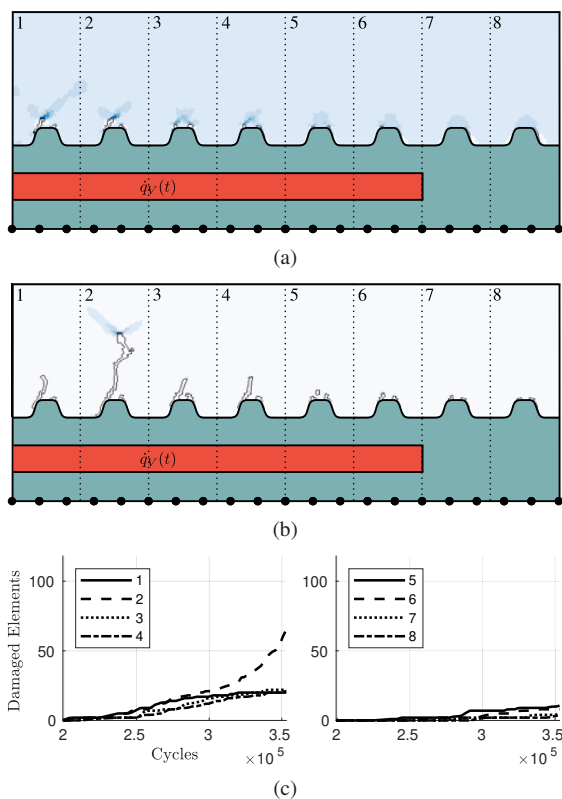


Figure 10: Fatigue damage characteristics of eight generic DMOS cell segments with a strong lateral temperature gradient induced by deactivating the power layer beneath two cells. Figure (a) shows the fatigue macro cracks and FIP values at cycle number 265820. Dark blue values indicate a high FIP light blue values a low one. Figure (b) shows fatigue macro cracks and FIP values at cycle number 353120. In Figure (c) one can see the evolution of the fatigue cracks in the different segments.

symmetric crack occurs. Therefore, the crack growth is slowed down because it is shielded by itself through the symmetry assumption.

The plots in Figure 10c illustrate all of the explained effects in more detail. The fatigue crack initiation in segment 1 can be seen as well as the formation of the dominant crack in segment 2 and the minimal crack growth in segments 5-8.

In Figure 11 the temperature field, at the time of the maximum temperature in the respective cycle, is shown for the undamaged model (Figure 11a) and the model after 353120 cycles (Figure 11b). It is clearly visible that the fatigue cracks have a strong influence on the temperature fields. Locally the crack in segment 2 restricts the thermal flow from the left to the right side, see in Figure 11b. Globally, the evolving fatigue damage seems to have two effects on the overall behavior. The highest temperature

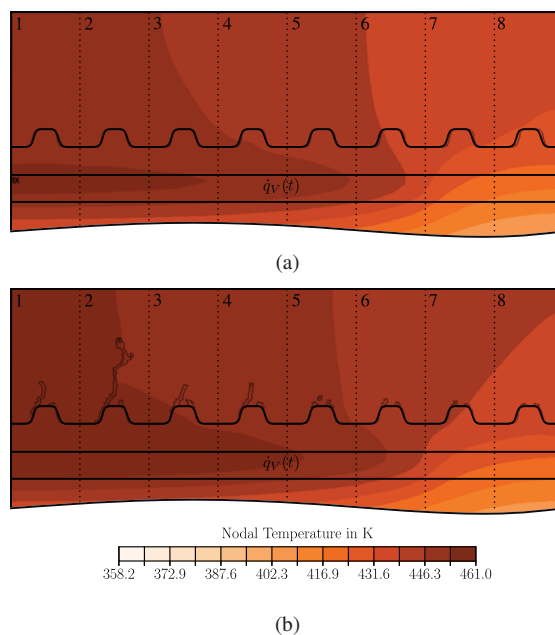


Figure 11: Temperatures plots of the arrangement with a strong lateral temperature gradient. The temperature field of the undamaged model at the time of the maximum temperature ($t = 0.136$ ms), is depicted in (a). Figure (b) shows the temperature field of the model after 353120 cycles at the time of the maximum temperature ($t = 0.144$ ms)

occur later in the cycle and higher overall temperatures are reached.

D. Configuration with Regions of Faster Damage Onset

The last results presented in this work illustrate a different aspect of propagating fatigue cracks. The main question which is addressed here is how faster growing cracks affect their surrounding. Therefore, the fatigue damage onset in the two center segments is sped up by 20%. Otherwise the model is equivalent to the standard configuration in Figure 4a. As a result, the first fatigue cracks appear simultaneously at cycle number 70654 in segments 4 and 5. In Figure 12a one can see that at cycle 97278 the fatigue cracks in the two center segments have grown substantially whereas in the remaining segments little (to no) fatigue cracks have formed. The faster crack growth in the two center segments continues, with both growing at a similar pace without interfering too much with each other. The crack pattern after 108540 cycles is depicted in Figure 12b. One can see that at this cycle number the fatigue crack in segment 4 has grown towards the crack in segment 5. The lower FIP values for this crack indicate that it is about to stop. Plot 12c highlights how much such dominant cracks influence their surrounding. The black and the grey solid lines give the total number of

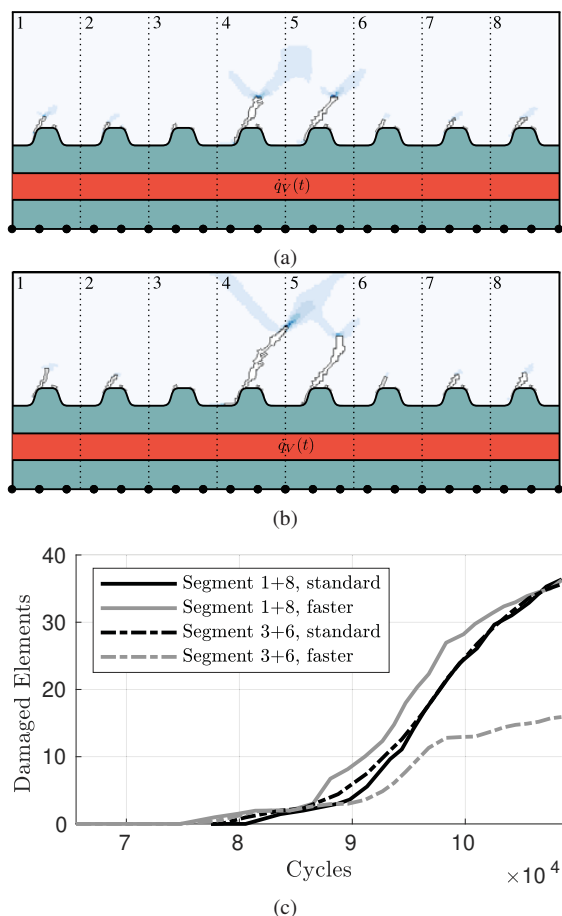


Figure 12: Fatigue damage characteristics of eight generic DMOS cell segments with accelerated fatigue damage onset in segments 4 and 5. Figure (a) shows the fatigue macro cracks and FIP values at cycle number 97278. Dark blue values indicate a high FIP light blue values a low one. Figure (b) shows fatigue macro cracks and FIP values at cycle number 108540. In Figure (c) one can see the evolution of the fatigue cracks in the different segments.

failed elements over cycle number of segment 1 and 8 of the standard configuration (Section 4-A) and the current simulation, respectively. One can see that the fatigue cracks evolve relatively similarly for both configurations. Contrary to this result, the dashed lines, which depict the overall number of failed elements in segments 3 and 6, for both simulations, differ quite strongly. Looking back at Figure 7a, one can see that at the given maximum cycle number of Plot 12c, no dominant fatigue crack has formed and therefore no distinct shielding has taken place. As a result, the two black lines are almost identical. However, the forced fatigue cracks in segment 4 and 5 (Figure 12b), have a strong shielding effect on the neighboring segments and reduces the fatigue crack growth significantly in these

segments.

5. Conclusions

The bulk fatigue framework proposed in [3], [4] is extended towards the usage of sequentially coupled transient thermo-mechanical loading conditions.

Different configurations of eight DMOS cell-like structures are simulated utilizing a bulk fatigue framework under transient thermo-mechanical loading conditions. In such arrangements, the influence of non-uniform temperature fields on the fatigue damage initiation and on the fatigue crack propagation is studied.

A configuration that has no thermal difference between the individual cells is used as the reference solution. In this case, numerical perturbations by the unstructured mesh set the position at which a dominant crack forms. Small lateral temperature differences do not influence the fatigue behavior enough to change the position of the dominant crack, however, it significantly decreases the crack growth rate. It is shown that a substantially stronger lateral temperature gradient changes the position of the dominant crack. Furthermore, it is demonstrated that dominant fatigue cracks lead to shielding effects, i.e. significantly slow down the fatigue crack growth in their vicinity.

This modeling approach, together with appropriate experimental analyses, can enhance physical lifetime modeling and simulation of power semiconductors.

Acknowledgements

This work was funded by the Austrian Research Promotion Agency (FFG, Project No. 874907).

References

- [1] W. Kanert, R. Pufall, O. Wittler, R. Dudek, and M. Bouazza. Modelling of metal degradation in power devices under active cycling conditions. In *2011 12th Int. Conf. on Thermal, Mechanical and Multi-Physics Simulation and Experiments in Microelectronics and Microsystems, EuroSimE 2011*, pages 1–6. IEEE, 2011.
- [2] G. Kravchenko. *Numerical simulations of fatigue crack problems in semiconductor devices subjected to thermomechanical loading*. PhD thesis, Vienna University of Technology, 2014.
- [3] M. Springer and H.E. Pettermann. A thermo-mechanical fatigue damage modeling methodology for power semiconductor robustness validation studies. In *2018 19th International Conference on Thermal, Mechanical and Multi-Physics Simulation and Experiments in Microelectronics and Microsystems, EuroSimE 2018*, pages 1–8. IEEE, 2018.
- [4] M. Springer. *Modeling and Simulation of Fatigue Damage in Power Semiconductors*. PhD thesis, TU Wien, 2017.
- [5] M. Springer and H.E. Pettermann. Fatigue life predictions of metal structures based on a low-cycle, multiaxial fatigue damage model. *International Journal of Fatigue*, 116:355–365, 2018.
- [6] T. Smorodin, J. Wilde, P. Nelle, E. Lilleodden, and M. Stecher. Modeling of DMOS subjected to fast temperature cycle stress and improvement by a novel metallization concept. In *International Reliability Physics Symposium Proceedings*, pages 689–690. IEEE, 2008.
- [7] A. Fatemi and D.F. Socie. A critical plane approach to multiaxial fatigue damage including out of phase loading. *Fatigue and Fracture of Engineering Materials and Structures*, 11:149–165, 1988.

- [8] M. Goto, S.Z. Han, K. Euh, N. Teshima, T. Yakushiji, and N. Kawagoishi. Fatigue damage formation and microstructure of ultrafine grained copper under two-step loading. *WIT Transactions on Modelling and Simulation*, 55:317–326, 2013.
- [9] J.A. Bannantine and D.F. Socie. A variable amplitude multiaxial fatigue life prediction method. In *Third International Conference on Biaxial/Multiaxial Fatigue*, pages 12.1 – 12.20, 1989.
- [10] J.H. Lau, S.H Pan, and C. Chang. A New Thermal-Fatigue Life Prediction Model for Wafer Level Chip Scale Package (WLCSP) Solder Joints. *Journal of Electronic Packaging*, 124:212–220, 2002.
- [11] A. Wimmer, A. Leitner, T. Detzel, W. Robl, W. Heinz, R. Pippan, and G. Dehm. Damage evolution during cyclic tension-tension loading of micron-sized Cu lines. *Acta Materialia*, 67:297–307, 2014.

Chapter 4

Lattice Materials

4.1 Introduction

Lattice materials represent a special class of open-cell architected materials [21]. They possess a remarkable potential for industrial applications due to their multi-functionality [21, 89] and may be used, e.g., in heat exchangers [38, 80], as damping media in acoustic applications [92], or as materials for energy absorption [1, 67, 76]. In contrast to open-cell foams, their internal structure is strictly periodic and mainly determines their overall material properties. Hence, by appropriately designing the internal architecture of lattice materials their effective properties can be tailored towards the requirements of specific applications [4, 21]. This aspect has become of more relevance due to the rapid progress made in additive manufacturing techniques within the past years. Nowadays lattice materials with highly complex and even hybrid multi-material internal structures can be manufactured [30, 49, 53, 55, 62, 90] where modern additive technologies can provide accuracy in the micrometer range [52] or even in the nanometer range [36, 59].

Especially in lattice materials with low relative densities and consequently slender lattice members the occurrence of micro-scale buckling, i.e., the loss of structural stability of the lattice members is an important phenomenon to be considered in the design process. In this context, buckling phenomena can be viewed from two perspectives. From a common engineering standpoint the occurrence of buckling can be seen as cause of catastrophic failure which needs to be avoided. This is of relevance when lattice materials are used in standard engineering structures, for example, as core materials in sandwich structures

[44, 60]. In this case the compressive strength of the lattice material is governed by the buckling load and a high buckling resistance is desirable. Alternatively, buckling can also be viewed as novel opportunity for functionality in the design of lattice materials [41] or smart applications [39] requiring a deep understanding of the buckling and post-buckling mechanisms [11]. Examples are a negative Poisson's ratio induced by structural instabilities [6, 46, 69] or instability driven pattern formations [69, 72, 73]. Regardless of whether buckling is seen as source of catastrophic failure or as opportunity in the design of lattice materials, reliable predictive tools are required for studying the overall mechanical behavior of lattice materials as well as the critical buckling load and the associated post-buckling behavior. For this purpose both analytical and numerical modeling techniques can be employed which will be discussed in more detail in the following.

4.2 Continuum Mechanics Modeling

The mechanical behavior of lattice materials under various loading conditions can be studied using experimental methods as well as analytical or numerical modeling techniques. Experimental methods allow for material property characterization and also for the investigation of the failure behavior of lattice materials [12, 34, 49, 53, 76], but are not economic for designing new lattice materials. The implementation of design changes requires the manufacturing of new samples and their subsequent testing which is time consuming and costly. Analytical and numerical modeling techniques allow for a virtualization of the design process and the experimental testing. Design changes can easily be accounted for and their influence on the mechanical behavior can be studied in a more cost efficient way. Furthermore, models can provide additional information on the governing deformation mechanisms and the underlying physics. This information can be utilized to guide the design process of lattice materials towards a desired physical behavior [46, 50, 58] or maybe used within optimization algorithms [79], the latter being effectively impossible with experimental methods.

The various modeling strategies will be briefly introduced where the focus lies on numerical modeling by means of the finite element method. Special interest is put onto the

evaluation of the buckling load and post-buckling behavior of lattice materials. The discussion in Sections 4.2.1 and 4.2.2 is based on the review paper [87] to which the author of this thesis contributed the section on numerical modeling.

4.2.1 Analytical Modeling

Analytical models comprise all models where the problem can be stated analytically, no matter if a closed form solution of the governing equations can be found or numerical tools have to be employed for solving the equations. In the following only a brief overview about relevant analytical methods is provided. Further information can be found in the cited references.

Analytical models of lattice materials are in general based on beam theory, see, e.g., [4, 15, 28, 58, 83]. These models have successfully been applied to determine the effective properties of various lattice materials depending on the relative density $\bar{\rho}$ [4, 33, 61] or to derive relations for the peak compressive stress, i.e., the buckling strength [4, 27, 35, 83], the yield strength [4, 27, 61, 83, 92] as well as the fracture strength [4, 27, 71]. In general the derived equations follow a power law reading, e.g., $E_L \propto E_C \bar{\rho}^m$ and $\sigma_L^* \propto \sigma_C \bar{\rho}^n$ for the elastic modulus and the yield strength, respectively. The indices L and C denote the effective properties of the lattice and the properties of the constituents, respectively. The exponents m and n depend on the configuration of the lattice [4], i.e., if the deformations are bending or stretching dominated [14]. These equations provide basic information on the mechanical behavior of lattice materials, but do not allow to explore the behavior in the nonlinear regime, i.e., after the onset of plastic yielding or buckling.

An analytical procedure allowing to access the post buckling behavior is the method of minimizing the potential energy [37, 78]. In Thompson and Hunt [78] the potential energy is described as a function of a few generalized coordinates. The relation between applied load and deformations, i.e., the generalized coordinates, is then derived by formulating the total derivative of the potential energy with respect to the generalized coordinates. The resulting system of equations is then solved numerically. This method provides a large deflection formulation and can also account for imperfections within the lattice. It has been successfully applied to large scale stayed columns used in civil engineering [88, 94]

and recently to model co-linear fiber-stayed lattice structures [95].

Another method to access the nonlinear behavior of lattice materials is presented in [77]. Therein, relations for the elastic, post-yielding, post-buckling, and lock-up responses are derived by dividing the response into three regimes viz. (i) elastic regime, (ii) plastic collapse, and (iii) post-lock-up regime. For each of these regimes the individual equations are formulated separately. The obtained relations describe the relation between the macroscopic stress and the macroscopic strain, i.e., the response of the lattices in a homogenized sense. The analytical results show very good agreement with numerical simulations, although the transition between the different regimes may not always be captured correctly.

Furthermore, analytical beam models are used in combination with homogenization schemes to derive the effective behavior of lattice materials in terms of constitutive relations [16, 17, 18, 19, 47, 86]. These constitutive models can subsequently be employed in finite element simulations where the lattice is treated as homogeneous material instead of modeling it in its entire complexity.

Analytical models are commonly formulated on the basis of the smallest geometric unit cf. [4, 27], the so called base cell, and therefore assume an infinite periodic lattice. At most an arrangement of a few base cells is considered, e.g., when buckling is investigated [35]. Phenomena such as size effects in finite sized lattices, the development of crush bands or the propagation of cracks can therefore not be treated with analytical models. These require the application of numerical modeling techniques as discussed in Section 4.2.2. Furthermore, analytical models are commonly developed for lattices with low relative densities neglecting transverse shear deformations within the lattice members and the material aggregation around the vertices. An approach that is capable to account for large relative densities is presented in [58].

The biggest advantage of analytical models is that once the equations are stated, a systematic variation of the lattice parameters can be performed at low computational costs. This makes analytical methods useful tools for optimizing a pre-defined lattice architecture towards a desired application.

4.2.2 Numerical Modeling

When employed in conjunction with experimental and analytical methods numerical models are useful tools for gaining further insight into the physics of lattice materials. They are capable of providing detailed information on the macro-scale deformation state as well as on the local stress and strain state within the individual members cf. [25, 51, 75, 76]. Large deformations as well as material nonlinearities can be considered within the models. Thereby, the effects of buckling, plastic yielding, and damage within the lattice members can be studied in great detail [15, 22, 71, 75, 77, 91]. This involves the crushing of lattices subjected to compressive stress states [51, 56, 57, 65, 64, 75] as well as their fracture behavior under various loading conditions [68, 70, 71].

The focus within this thesis lies on numerical approaches utilizing the finite element method. These approaches can be grouped into discrete and continuum modeling approaches. Both will be briefly discussed in the following.

Discrete Modeling Approaches

Within discrete modeling approaches each lattice member is explicitly resolved. This means that the internal lattice structure is modeled in its entire complexity. Discrete modeling approaches can be classified into unit cell (UC) models and models of the whole finite-sized lattice.

UC models are closely related to the models used for the analytical approaches especially when beam elements are used for discretization. In general, they assume a lattice of infinite size. Periodic boundary conditions [9] are employed to allow for the application of meso-scale stress and strain states. A UC can consist of a single base cell or may be formed by an arrangement of several base cells. In the following, the base cell is the smallest geometric micro-structure with which the finite-sized or infinitely large lattice can be reconstructed by a periodic shift along the axes of the base cell [82]. It should be noted, that in the literature the term UC is not well-defined and often used to describe the base cell of a lattice. The size of the UC (defined by the number of base cells forming the UC) that is used within a simulation depends on the mechanism to be studied. A single base cell model is sufficient

for determining the effective linear or nonlinear elastic properties of the lattice by means of computational homogenization, see, e.g., [15, 55, 56]. To some extent also structural irregularities may be included in such models [53, 56, 70]. If more complex phenomena such as buckling are investigated, the UC has to be large enough to capture all relevant micro-scale deformation mechanisms [64]. Studies employing UC models for studying buckling in lattice materials can be found, e.g., in [6, 8, 13, 53, 64, 69, 75, 82]. In combination with the Bloch Wave method, even buckling modes with wave lengths (far) larger than the dimensions of the UC can be accounted for in the simulations [31, 32, 81, 82] even if the UC consists only of a single base cell. This can be exploited, e.g., in the optimization of lattice materials towards a high buckling resistance [79]. Furthermore, UC models can be used to determine the yield strength [15, 51] and can also provide valuable information on the crushing behavior of lattice materials [64, 75].

Models of the entire finite sized-lattice are required if the formation of crush bands [1, 6, 12, 51, 53, 56, 57, 64], the formation of shear bands, e.g., [68], or the fracture behavior [68, 70, 71] are to be studied as these effects cannot be treated with UC models. Furthermore, finite-sized models allow to apply boundary conditions similar to those used in experiments and also include effects resulting from free edges. Consequently, the results of these models can be directly compared with experimental measurements [6, 10, 12, 25, 51]. Additionally, structural irregularities such as the misalignment of lattice members [1, 53, 56, 57, 64, 71, 74], variations in the radii of the lattice members [10, 53], missing lattice members [1, 57, 74] or the porosity of the parent material [10] can be considered in a statistical manner.

For the discretization with finite elements either structural elements such as beams [10, 13, 15, 31, 35, 53, 56, 57, 65, 82, 91] or shells [1, 51] or continuum elements [6, 8, 51, 53, 69, 76, 79] have been used.

Finite element models of lattice materials employing structural elements show a much higher computational efficiency than comparable continuum element models. Commonly, beam element models are used and therefore will be discussed in more detail. Numerical beam element models exhibit the same issues as their analytical counterparts when it

comes to the modeling of the vertices, especially for lattices with high relative densities. In this case the material aggregation at the vertices leads to a locally increased stiffness and also has an influence on the estimated relative density of the lattice material. Methods to overcome these issues are presented in [55, 75]. Beam models have been shown to provide reliable predictions of the mechanical behavior of lattice materials involving the overall (non-)linear elastic properties [13, 55, 56], the onset of buckling [31, 32, 35, 64, 82], the collapse and crushing behavior [15, 56, 57, 75] as well as the fracture behavior of lattice structures [68, 70, 71]. These models are also suitable for studying the influence of misaligned or missing lattice members [56, 57] and to some extent also the local variation of the thickness of the individual members can be approximated [10, 53].

Continuum element models allow an improved representation of the geometry compared to beam models. The material aggregation at the vertices [55] and the variation of the radii of the individual lattice members [76] can be resolved in greater detail. Even manufacturing defects as obtained by computed tomography scans can be directly included into the model [53]. Continuum models also provide highly resolved information about the stress and strain fields within the lattice members and close to the vertices [55, 75, 76] as well as changes in the thickness of the lattice members under large deformations are naturally included in the model [8]. Continuum element models are computationally demanding and consequently mainly used for simulations at the UC level [6, 8, 51, 55, 69, 75, 79]. However, due to increasing computational power they are getting more frequently employed for studying the mechanical behavior of finite-sized lattices [6, 69, 76].

Alternatively, a combination of continuum elements and structural elements can be used to model finite-sized lattices [25]. In this case, a limited number of base cells are discretized with continuum elements allowing for a detailed representation of the stress and strain states within these cells. The rest of the lattice is discretized using structural elements.

Continuum Modeling

Continuum models are employed if it is computationally too expensive to resolve the lattice in its entire complexity, e.g., if the lattice consists of a large number of base cells. In this

case it is more efficient to represent the lattice by a homogeneous material possessing the same effective mechanical behavior.

The effective behavior can be describe by a classical Cauchy continuum if the principle of separation of scales is satisfied, i.e., the size of the base cell is far smaller than the characteristic length of the macroscopic problem. Common first-order homogenization schemes [9] such as asymptotic homogenization [3, 53] or the periodic microfield approach [55, 56] can then be used to derive the corresponding effective linear properties. In [3] a comparison of different homogenization schemes for predicting the effective elastic properties of lattice materials can be found.

However, in many engineering applications of lattice materials the principle of separation of scales is violated. Either the size of the base cell is of the same order of magnitude as the macroscopic problem leading to noticeable size effects [2, 40, 48, 93] or highly heterogeneous deformations occur, e.g., during the formation of crush bands [12, 51, 53, 64] or around sharp corners and crack tips [68]. These phenomena can be related to the absolute size of the microstructure and therefore, are not captured by Cauchy continuum theory. In contrast, generalized continuum theories allow to account for the size of the microstructure as they introduce a material length scale into the constitutive relations. In this context, micropolar [16, 17, 18, 19, 29], strain-gradient [5, 29, 54], or micromorphic [7] continua have been employed to describe the effective behavior of lattice materials. Reviews and classifications of the various generalized continuum theories can be found in [20, 23, 63]. For lattice materials with a simple internal architecture the constitutive behavior can be derived using models based on beam theory [16, 17, 18, 19, 29, 47] which in some cases may lead to a closed form solution for the tangent stiffness tensor [29, 47]. For complex micro-structures and especially if material nonlinearities are involved computational homogenization schemes have to be used, see, e.g., [7, 45]. These schemes do not lead to a closed form solution for the constitutive relation but rather are applied concurrently within structural simulations.

Other concepts that have been employed in the context of continuum modeling of lattice materials are the quasi-continuum theory [66], the nonlinear constitutive models

presented in [85, 86], and numerical multi-scale approaches [26, 66, 84]. The latter have been especially employed for modeling localization phenomena occurring around sharp corners and crack tips or due to local base cell buckling.

The various continuum models have been successfully employed for simulating complex phenomena such as the propagation of cracks [66] or the localization of deformation observed, e.g., in plates with circular holes under various loading conditions [85], during indentation experiments [22, 47, 66], or other (macroscopically) inhomogeneous deformation states [29].

4.3 Own Contribution to the Research Field

The own contribution to the research field consists of three publications viz.

- **Publication LM-1:** G. Ganzosch, M. Todt, A. Köllner, C. Völlmecke: *Experimental Investigations on pre-stressed stayed columns on smaller length scales*; in: Proceedings of the 8th International Conference on Thin Walled Structures; D. Camotim, N. Silvestre (ed.); (2018), ISBN: 978-989-20-8665-1; Paper ID 135, 15 pages.
- **Publication LM-2:** A. Köllner, M. Todt, G. Ganzosch, C. Völlmecke: *Experimental and numerical investigation on pre-stressed lattice structures*; Thin-Walled Structures, 145 (2019), 106396; 1 - 9.
- **Publication LM-3:** B. Werner, M. Todt, H.E. Pettermann: *Nonlinear Finite Element Study of Beams with Elasto-Plastic Damage Behavior in the Post-Buckling Regime*; PAMM, 19 (2019), 1; 2 pages.

The declaration of own contribution to these publications is provided in Subsection 4.3.3.

4.3.1 Lattice Materials with Tunable Buckling Behavior

Buckling phenomena play an important role in the design of lattice materials, as discussed in Section 4.1. In common light weight design applications lattice materials with low relative densities are desirable. Nevertheless, these materials should still possess a high buckling strength preferentially with a stable post-buckling behavior.

For designing such a material, the main idea has been to transfer the concept of pre-stressed stayed columns [88, 94] used in civil engineering for increasing the buckling loads of scaffolds and facades to the microscale. In other words, a lattice material is developed that is pre-stressed by suitably inserted fibers, see publications **LM-1** and **LM-2** [24, 43]. The main differences between pre-stressed stayed columns and a pre-stressed lattice material lie in the altered geometrical conditions and the altered elastic contrast between the individual constituents. Within common lattice materials all lattice members are approximately of the same size and slenderness whereas in civil engineering applications the stays are much shorter and more slender than the column. Furthermore, in pre-stressed stayed columns, the column, the stays, and the cables are made of the same material (usually steel), whereas for the considered lattice material a high elastic contrast between the lattice members (epoxy, PLA) and the fibers (carbon fibers) occurs. These aspects can have a huge impact when downsizing the concept of pre-stressed stayed columns.

With a combination of experiments and finite element simulations a proof-of-concept of the proposed pre-stressed lattice material is demonstrated in publications **LM-1** and **LM-2** [24, 43]. In [42] the mechanical behavior of these materials is studied in more detail. Manufacturing strategies as well as the influence of pre-stress on the buckling load, ultimate load, and mode interactions in the post-buckling regime are presented. All investigations are carried out using a base cell of the lattice material subjected to structural boundary conditions. It is shown that the buckling load can be adjusted by varying the pre-stress in the fibers and that the fibers lead to a stabilization of the first buckling mode. The ultimate load is reached when higher buckling modes or mode interactions occur. The results clearly indicate that the proposed configuration has the potential to lead to a new class of meta-materials with tunable buckling behavior.

4.3.2 Efficient Modeling Beyond the Elastic Response

For a detailed investigation of phenomena such as the formation of localization bands [1, 6, 12, 51, 53, 56, 68] accompanying the fracture behavior [68, 70, 71], the lattice material has to be resolved in its entire complexity at least in the proximity of the area of interest. Plastic yielding and damage within the lattice members have to be considered

appropriately to obtain reliable results. Using continuum element models for discretizing the lattice members can become computationally too expensive even when multiscale modeling approaches are used. Consequently, beam element based models need to be employed, especially when a systematic variation of the lattice parameters is to be carried out.

This modeling concept is addressed in publication **LM-3** [91], where the long term goal is on studying the formation of localization bands in the post-buckling regime of lattice materials under consideration of the elasto-plastic material behavior of the parent material including damage. The aim is to find a suitable discretization in terms of elements per lattice member and number of section points over the cross section that allows to capture the essential mechanisms but still provides high computational efficiency. It is shown that a relatively coarse discretization in combination with a high number of section points leads to a sufficiently accurate prediction of the reaction force. The coarse discretization is also beneficial for the numerical stability of the simulation. These results form the basis for further investigations of lattice materials with ductile damage behavior of the parent material.

4.3.3 Declaration of Own Contribution to the Enclosed Publications

- **Publication LM-1:** All numerical simulations, their evaluation, and their discussion within the paper were carried out by myself. Furthermore, I was involved in the early design of the 3D printed samples and the respective experiments.
- **Publication LM-2:** My contribution is equal to that of the first author. All numerical simulations, their evaluation, and their discussion within the paper were carried out by myself. Furthermore, I was involved in the early design of the 3D printed samples and the respective experiments.
- **Publication LM-3:** The main research work was carried out by B. Werner. H.E. Pettermann and myself acted as scientific supervisors. H.E. Pettermann mainly contributes to the modeling of damage and failure. My contribution focuses on the simulation of structural instabilities and the post-buckling behavior of the structures.

4.4 Bibliography

- [1] A. Ajdari, H. Nayeb-Hashemi, and A. Vaziri. Dynamic crushing and energy absorption of regular, irregular and functionally graded cellular structures. *International Journal of Solids and Structures*, 48:506–516, 2011.
- [2] E. W. Andrews, G. Gioux, P. Onck, and L. J. Gibson. Size effects in ductile cellular solids. Part II : experimental results. *International Journal of Mechanical Sciences*, 43:701–713, 2001.
- [3] S. Arabnejad and D. Pasini. Mechanical properties of lattice materials via asymptotic homogenization and comparison with alternative homogenization methods. *International Journal of Mechanical Sciences*, 77:249–262, 2013.
- [4] M. F. Ashby. The properties of foams and lattices. *Philosophical Transactions of the Royal Society A*, pages 15–30, 2006.
- [5] N. Auffray, J. Dirrenberger, and G. Rosi. A complete description of bi-dimensional anisotropic strain-gradient elasticity. *International Journal of Solids and Structures*, 69-70:195–206, 2015.
- [6] K. Bertoldi, P. M. Reis, S. Willshaw, and T. Mullin. Negative Poisson’s ratio behavior induced by an elastic instability. *Advanced Materials*, 22:361–366, 2010.
- [7] R. Biswas, L. H. Poh, and A. S. Shedbale. A micromorphic computational homogenization framework for auxetic tetra-chiral structures. *Journal of the Mechanics and Physics of Solids*, 135:103801, 2020.
- [8] G. L. Bluhm, O. Sigmund, F. Wang, and K. Poullos. Nonlinear compressive stability of hyperelastic 2D lattices at finite volume fractions. *Journal of the Mechanics and Physics of Solids*, 137:103851, 2020.
- [9] H. J. Böhm. *Mechanics of Microstructured Materials*. Springer Verlag, Wien, 2004.

-
- [10] G. Campoli, M. S. Borleffs, S. Amin Yavari, R. Wauthle, H. Weinans, and A. A. Zadpoor. Mechanical properties of open-cell metallic biomaterials manufactured using additive manufacturing. *Materials and Design*, 49:957–965, 2013.
- [11] A. J. Crosby. Why should we care about buckling? *Soft Matter*, 6(22):5660–5660, 2010.
- [12] V. Crupi, E. Kara, G. Epasto, E. Guglielmino, and H. Aykul. Static behavior of lattice structures produced via direct metal laser sintering technology. *Materials & Design*, 135:246–256, 2017.
- [13] S. Demiray, W. Becker, and J. Hohe. Strain-energy based homogenisation of two- and three-dimensional hyperelastic solid foams. *Journal of Materials Science*, 40:5839–5844, 2005.
- [14] V. S. Deshpande, M. F. Ashby, and N. A. Fleck. Foam topology bending versus stretching dominated architectures. *Acta Materialia*, 49:1035–1040, 2001.
- [15] V. S. Deshpande, N. A. Fleck, and M. F. Ashby. Effective properties of the octet-truss lattice material. *Journal of the Mechanics and Physics of Solids*, 49:1747–1769, 2001.
- [16] F. Dos Reis and J. F. Ganghoffer. Construction of micropolar continua from the asymptotic homogenization of beam lattices. *Computers and Structures*, 112-113:354–363, 2012.
- [17] F. Dos Reis and J. F. Ganghoffer. Equivalent mechanical properties of auxetic lattices from discrete homogenization. *Computational Materials Science*, 51:314–321, 2012.
- [18] K. El Nady, F. Dos Reis, and J. F. Ganghoffer. Computation of the homogenized nonlinear elastic response of 2D and 3D auxetic structures based on micropolar continuum models. *Composite Structures*, 170:271–290, 2017.
- [19] K. El Nady, I. Goda, and J. F. Ganghoffer. Computation of the effective nonlinear mechanical response of lattice materials considering geometrical nonlinearities. *Computational Mechanics*, 58:957–979, 2016.

- [20] J. Fatemi, F. Van Keulen, and P. R. Onck. Generalized continuum theories: Application to stress analysis in bone. *Meccanica*, 37:385–396, 2002.
- [21] N. A. Fleck, V. S. Deshpande, and M. F. Ashby. Micro-architected materials: past, present and future. *Proceedings of the Royal Society of London A: Mathematical, Physical and Engineering Sciences*, 466:2495–2516, 2010.
- [22] S. Forest, J. S. Blazy, Y. Chastel, and F. Moussy. Continuum modeling of strain localization phenomena in metallic foams. *Journal of Materials Science*, 40:5903–5910, 2005.
- [23] S. Forest and R. Sievert. Nonlinear microstrain theories. *International Journal of Solids and Structures*, 43:7224–7245, 2006.
- [24] G. Ganzosch, M. Todt, A. Köllner, and C. Völlmecke. Experimental investigations on pre-stressed stayed columns on smaller length scales. In *Proceedings of the Eighth International Conference on Thin-Walled Structures*, pages 1–15, 2018.
- [25] X. Geng, L. Ma, C. Liu, C. Zhao, and Z. F. Yue. A FEM study on mechanical behavior of cellular lattice materials based on combined elements. *Materials Science and Engineering A*, 712:188–198, 2018.
- [26] S. Ghosh, K. Lee, and P. Raghavan. A multi-level computational model for multi-scale damage analysis in composite and porous materials. *International Journal of Solids and Structures*, 38:2335–2385, 2001.
- [27] L. J. Gibson. Modelling the mechanical behavior of cellular materials. *Materials Science and Engineering: A*, 110(Supplement C):1 – 36, 1989.
- [28] L. J. Gibson and M. F. Ashby. *Cellular solids: structure and properties*. Cambridge university press, 1999.
- [29] R. N. Glaesener, C. Lestringant, B. Telgen, and D. M. Kochmann. Continuum models for stretching- and bending-dominated periodic trusses undergoing finite deformations. *International Journal of Solids and Structures*, 171:117–134, 2019.

- [30] G. D. Goh, Y. L. Yap, S. Agarwala, and W. Y. Yeong. Recent Progress in Additive Manufacturing of Fiber Reinforced Polymer Composite. *Advanced Materials Technologies*, 4:1800271, 2019.
- [31] L. Gong and S. Kyriakides. Compressive response of open cell foams. Part II: Initiation and evolution of crushing. *International Journal of Solids and Structures*, 42:1381–1399, 2005.
- [32] L. Gong, S. Kyriakides, and N. Triantafyllidis. On the stability of Kelvin cell foams under compressive loads. *Journal of the Mechanics and Physics of Solids*, 53:771–794, 2005.
- [33] J. L. Grenestedt. Effective elastic behavior of some models for perfect cellular solids. *International Journal of Solids and Structures*, 36(10):1471 – 1501, 1999.
- [34] R. Gümürük, R. A. W. Mines, and S. Karadeniz. Static mechanical behaviours of stainless steel micro-lattice structures under different loading conditions. *Materials Science & Engineering A*, 586:392–406, 2013.
- [35] B. Haghpanah, J. Papadopoulos, D. Mousanezhad, H. Nayeb-Hashemi, and A. Vaziri. Buckling of regular, chiral and hierarchical honeycombs under a general macroscopic stress state. *Proceedings of the Royal Society A: Mathematical, Physical and Engineering Sciences*, 470:20130856, 2014.
- [36] W. Haske, V. W. Chen, J. M. Hales, W. Dong, S. Barlow, S. R. Marder, and J. W. Perry. 65 nm feature sizes using visible wavelength 3-D multiphoton lithography. *Optics Express*, 15:3426–3436, 2007.
- [37] R. Hill. Elastic properties of reinforced solids: Some theoretical principles. *Journal of the Mechanics and Physics of Solids*, 11:357–372, 1963.
- [38] J. Y. Ho, K. C. Leong, and T. N. Wong. Additively-manufactured metallic porous lattice heat exchangers for air-side heat transfer enhancement. *International Journal of Heat and Mass Transfer*, 150:119262, 2020.

- [39] N. Hu and R. Burgueño. Buckling-induced smart applications: recent advances and trends. *Smart Materials and Structures*, 24:063001, 2015.
- [40] S. Khakalo and J. Niiranen. Lattice structures as thermoelastic strain gradient metamaterials: Evidence from full-field simulations and applications to functionally step-wise-graded beams. *Composites Part B: Engineering*, 177:107224, 2019.
- [41] D. M. Kochmann and K. Bertoldi. Exploiting Microstructural Instabilities in Solids and Structures: From Metamaterials to Structural Transitions. *Applied Mechanics Reviews*, 69, 2017.
- [42] C. Kölbl. Untersuchung der strukturellen Stabilität und des Nachbeulverhaltens einer seilverspannten Gitterstruktur. Master’s thesis, TU Wien, 2019. Supervisors: M. Todt and H.E. Pettermann.
- [43] A. Köllner, M. Todt, G. Ganzosch, and C. Völlmecke. Experimental and numerical investigation on pre-stressed lattice structures. *Thin-Walled Structures*, 145:106396, 2019.
- [44] J. A. Kolodziejska, C. S. Roper, S. S. Yang, W. B. Carter, and A. J. Jacobsen. Research update: Enabling ultra-thin lightweight structures: Microsandwich structures with microlattice cores. *APL Materials*, 3:050701, 2015.
- [45] V. G. Kouznetsova, M. G. D. Geers, and W. A. M. Brekelmans. Multi-scale second-order computational homogenization of multi-phase materials: A nested finite element solution strategy. *Computer Methods in Applied Mechanics and Engineering*, 193:5525–5550, 2004.
- [46] S. Krödel, T. Delpero, A. Bergamini, P. Ermanni, and D. M. Kochmann. 3D Auxetic Microlattices with Independently Controllable Acoustic Band Gaps and Quasi-Static Elastic Moduli. *Advanced Engineering Materials*, 16:357–363, 2014.
- [47] R. S. Kumar and D. L. McDowell. Generalized continuum modeling of 2-D periodic cellular solids. *International Journal of Solids and Structures*, 41:7399–7422, 2004.

- [48] R. S. Lakes. Experimental microelasticity of two porous solids. *International Journal of Solids and Structures*, 22:55–63, 1986.
- [49] C. Li, H. Lei, P. Wang, and D. Fang. Architecture design of periodic truss-lattice cells for additive manufacturing. *Additive Manufacturing*, 34:101172, 2020.
- [50] T. Li, Y. Chen, X. Hu, Y. Li, and L. Wang. Exploiting negative Poisson’s ratio to design 3D-printed composites with enhanced mechanical properties. *Materials and Design*, 142:247–258, 2018.
- [51] X. Li, Z. Lu, Z. Yang, and C. Yang. Anisotropic in-plane mechanical behavior of square honeycombs under off-axis loading. *Materials and Design*, 158:88–97, 2018.
- [52] S. C. Ligon, R. Liska, J. Stampfl, M. Gurr, and R. Mülhaupt. Polymers for 3D Printing and Customized Additive Manufacturing. *Chemical Reviews*, 117:10212–10290, 2017.
- [53] L. Liu, P. Kamm, F. García-Moreno, J. Banhart, and D. Pasini. Elastic and failure response of imperfect three-dimensional metallic lattices: the role of geometric defects induced by Selective Laser Melting. *Journal of the Mechanics and Physics of Solids*, 107:160–184, 2017.
- [54] M. Lombardo and H. Askes. Higher-order gradient continuum modelling of periodic lattice materials. *Computational Materials Science*, 52:204–208, 2012.
- [55] M. H. Luxner, J. Stampfl, and H. E. Pettermann. Finite element modeling concepts and linear analyses of 3D regular open cell structures. *Journal of Materials Science*, 40(22):5859–5866, 2005.
- [56] M. H. Luxner, J. Stampfl, and H. E. Pettermann. Numerical simulations of 3D open cell structures – influence of structural irregularities on elasto-plasticity and deformation localization. *International Journal of Solids and Structures*, 44:2990–3003, 2007.

- [57] M. H. Luxner, J. Stampfl, and H. E. Pettermann. Nonlinear simulations on the interaction of disorder and defects in open cell structures. *Computational Materials Science*, 47:418–428, 2009.
- [58] L. R. Meza, S. Das, and J. R. Greer. Strong, lightweight, and recoverable three-dimensional ceramic nanolattices. *Science*, 345(6202):1322–1327, 2014.
- [59] G. Mitterramskogler, R. Gmeiner, R. Felzmann, S. Gruber, C. Hofstetter, J. Stampfl, J. Ebert, W. Wachter, and J. Laubersheimer. Light curing strategies for lithography-based additive manufacturing of customized ceramics. *Additive Manufacturing*, 1-4:110–118, 2014.
- [60] P. Moongkhamklang, V. S. Deshpande, and H. N. G. Wadley. The compressive and shear response of titanium matrix composite lattice structures. *Acta Materialia*, 58(8):2822 – 2835, 2010.
- [61] P. Moongkhamklang, D. M. Elzey, and H. N. G. Wadley. Titanium matrix composite lattice structures. *Composites Part A: Applied Science and Manufacturing*, 39(2):176 – 187, 2008.
- [62] F. Ning, W. Cong, J. Qiu, J. Wei, and S. Wang. Additive manufacturing of carbon fiber reinforced thermoplastic composites using fused deposition modeling. *Composites Part B: Engineering*, 80:369–378, 2015.
- [63] A. K. Noor. Continuum modeling for repetitive lattice structures. *Applied Mechanics Reviews*, 41:285–296, 1988.
- [64] S. D. Papka and S. Kyriakides. In-plane compressive response and crushing of honeycomb. *Journal of the Mechanics and Physics of Solids*, 42:1499–1532, 1994.
- [65] S. D. Papka and S. Kyriakides. Experiments and full-scale numerical simulations of in-plane crushing of a honeycomb. *Acta Materialia*, 46(8):2765 – 2776, 1998.

- [66] G. P. Phlipot and D. M. Kochmann. A quasicontinuum theory for the nonlinear mechanical response of general periodic truss lattices. *Journal of the Mechanics and Physics of Solids*, 124:758–780, 2019.
- [67] D. T. Queheillalt and H. N. G. Wadley. Cellular metal lattices with hollow trusses. *Acta Materialia*, 53:303 – 313, 2005.
- [68] I. Quintana Alonso and N. A. Fleck. Compressive response of a sandwich plate containing a cracked diamond-celled lattice. *Journal of the Mechanics and Physics of Solids*, 57:1545–1567, 2009.
- [69] X. Ren, J. Shen, P. Tran, T. D. Ngo, and Y. M. Xie. Design and characterisation of a tuneable 3D buckling-induced auxetic metamaterial. *Materials and Design*, 139:336–342, 2018.
- [70] N. E. R. Romijn and N. A. Fleck. The fracture toughness of planar lattices : Imperfection sensitivity. *Journal of the Mechanics and Physics of Solids*, 55:2538–2564, 2007.
- [71] I. Schmidt and N. A. Fleck. Ductile fracture of two-dimensional cellular structures. *International Journal of Fracture*, 111:327–342, 2001.
- [72] S. Shan, S. H. Kang, P. Wang, C. Qu, S. Shian, E. R. Chen, and K. Bertoldi. Harnessing multiple folding mechanisms in soft periodic structures for tunable control of elastic waves. *Advanced Functional Materials*, 24:4935–4942, 2014.
- [73] J. Shim, S. Shan, A. Košmrlj, S. H. Kang, E. R. Chen, J. C. Weaver, and K. Bertoldi. Harnessing instabilities for design of soft reconfigurable auxetic/chiral materials. *Soft Matter*, 9:8198–8202, 2013.
- [74] M. J. Silva. The effects of non-periodic microstructure and defects on the compressive strength of two-dimensional cellular solids. *International Journal of Mechanical Sciences*, 39:549–563, 1997.

- [75] M. Smith, Z. Guan, and W. J. Cantwell. Finite element modelling of the compressive response of lattice structures manufactured using the selective laser melting technique. *International Journal of Mechanical Sciences*, 67:28–41, 2013.
- [76] T. Tancogne-Dejean, A. B. Spierings, and D. Mohr. Additively-manufactured metallic micro-lattice materials for high specific energy absorption under static and dynamic loading. *Acta Materialia*, 116(Supplement C):14 – 28, 2016.
- [77] H. C. Tankasala, V. S. Deshpande, and N. A. Fleck. Tensile response of elastoplastic lattices at finite strain. *Journal of the Mechanics and Physics of Solids*, 109:307–330, 2017.
- [78] J. M. T. Thompson and G. W. Hunt. *Elastic instability phenomena*. Wiley, 1984.
- [79] C. R. Thomsen, F. Wang, and O. Sigmund. Buckling strength topology optimization of 2D periodic materials based on linearized bifurcation analysis. *Computer Methods in Applied Mechanics and Engineering*, 339:115–136, 2018.
- [80] J. Tian, T. Kim, T. J. Lu, H. P. Hodson, D. T. Queheillalt, D. J. Sypeck, and H. N. G. Wadley. The effects of topology upon fluid-flow and heat-transfer within cellular copper structures. *International Journal of Heat and Mass Transfer*, 47(14–16):3171 – 3186, 2004.
- [81] N. Triantafyllidis and W. C. Schnaidt. Comparison of microscopic and macroscopic instabilities in a class of two-dimensional periodic composites. *Journal of the Mechanics and Physics of Solids*, 41:1533–1565, 1993.
- [82] N. Triantafyllidis and M. W. Schraad. Onset of failure in aluminum honeycombs under general in-plane loading. *Journal of the Mechanics and Physics of Solids*, 46:1089–1124, 1998.
- [83] L. Valdevit, S. W. Godfrey, T. A. Schaedler, A. J. Jacobsen, and W. B. Carter. Compressive strength of hollow microlattices: Experimental characterization, modeling, and optimal design. *Journal of Materials Research*, 28:2461–2473, 2013.

- [84] F. J. Vernerey and M. Kabiri. An adaptive concurrent multiscale method for microstructured elastic solids. *Computer Methods in Applied Mechanics and Engineering*, 241-244:52–64, 2012.
- [85] A. Vigliotti, V. S. Deshpande, and D. Pasini. Non linear constitutive models for lattice materials. *Journal of the Mechanics and Physics of Solids*, 64:44–60, 2014.
- [86] A. Vigliotti and D. Pasini. Linear multiscale analysis and finite element validation of stretching and bending dominated lattice materials. *Mechanics of Materials*, 46:57–68, 2012.
- [87] C. Völlmecke, M. Todt, and S. Yiatros. Buckling and postbuckling of architected materials: a review of methods for lattice structures and metal foams. *Advanced Composite Letters*, submitted, 2020.
- [88] M. A. Wadee, L. Gardner, and T. A. Hunt. Buckling mode interaction in prestressed stayed columns. *Proceedings of the Institution of Civil Engineers - Structures and Buildings*, 166:403–412, 2013.
- [89] H. N. G. Wadley. Multifunctional periodic cellular metals. *Philosophical Transactions of the Royal Society of London A*, 364:31–68, 2006.
- [90] K. Wang, C. Wu, Z. Qian, C. Zhang, B. Wang, and M. A. Vannan. Dual-material 3D printed metamaterials with tunable mechanical properties for patient-specific tissue-mimicking phantoms. *Additive Manufacturing*, 12:31–37, 2016.
- [91] B. Werner, M. Todt, and H. E. Pettermann. Nonlinear finite element study of beams with elasto-plastic damage behavior in the post-buckling regime. *PAMM*, 19:e201900248, 2019.
- [92] J. Yang, J. Xiong, L. Ma, B. Wang, G. Zhang, and L. Wu. Study on vibration damping of composite sandwich cylindrical shell with pyramidal truss-like cores. *Composite Structures*, 117:362 – 372, 2014.

- [93] M. Yoder, L. Thompson, and J. Summers. Size effects in lattice structures and a comparison to micropolar elasticity. *International Journal of Solids and Structures*, 143:245–261, 2018.
- [94] J. Yu and M. A. Wadee. Mode interaction in triple-bay prestressed stayed columns. *International Journal of Non-Linear Mechanics*, 88:47–66, 2017.
- [95] C. Zschoernack, M. A. Wadee, and C. Völlmecke. Nonlinear buckling of fibre-reinforced unit cells of lattice materials. *Composite Structures*, 136:217–228, 2016.

4.5 Publications

Eighth International Conference on
THIN-WALLED STRUCTURES – ICTWS 2018
Lisbon, Portugal, July 24-27, 2018

EXPERIMENTAL INVESTIGATIONS ON PRE-STRESSED STAYED COLUMNS ON SMALLER LENGTH SCALES

Gregor Ganzosch*, Melanie Todt, Anton Köllner* and Christina Völlmecke***

* Technische Universität Berlin, Institute of Mechanics, Stability and Failure of Functionally Optimized Structures Group, Einsteinufer 5, 10587 Berlin, Germany
e-mails: ganzosch@tu-berlin.de, anton.koellner@tu-berlin.de, christina.voellmecke@tu-berlin.de

** Technische Universität Wien, Institute of Lightweight Design and Structural Biomechanics, Getreidemarkt 9, A-1060 Vienna, Austria
e-mail: mt@ilsb.tuwien.ac.at

Keywords: Structural Stability; Stayed Columns, Post-buckling, Experiments.

Abstract. *Various studies have shown that steel columns, which are additionally reinforced by pre-stressed cable stays, generally possess an increased buckling resistance under axial compression as buckling displacements are suppressed. So far, this concept has only been applied on a large length scale. To investigate whether or not this concept can be transferred to smaller length scales, experimental investigations on the buckling and post-buckling behavior of simply supported, pre-stressed stayed columns under pure axial compression are conducted on different length scales. For all investigated samples, an increase in the buckling load compared to the unsupported column is observed. The mode shape at the onset of buckling depends on the geometry of the pre-stressed stayed columns and the pre-stress in the fibers. At all length scales it was observed that the post-buckling behavior gradually changes to an interactive asymmetric mode resulting in a reduction of the load bearing capacity. The results compare well with previous experiments (large length scale) as well as finite element simulations (medium length scale).*

1 INTRODUCTION

Lattice materials are cellular materials with an open and periodic internal structure. Compared with standard engineering materials, they are lighter and more compact in their design, which allows to save weight and space. Several industrial branches, e.g. the mobility industry, the medical sector or civil engineering, focus on these multifunctional materials. Lattice materials can be used, e.g. as damping materials in acoustic applications [1], as materials for energy absorption [2, 3, 4], or as heat exchangers in thermal applications [5].

The periodicity of lattice materials ensures that the global material properties mainly depend on the internal architecture [6]. Hence, the mechanical properties of lattice materials such as the Poisson's ratio [7], the energy absorption [2], and the mechanical behavior when used in structural parts [8, 9] might be tailored towards the requirements of specific applications by designing the lattice structure accordingly [9]. This aspect becomes more relevant since advanced manufacturing technologies such as additive manufacturing enable the production of highly complex lattice structures in series production [10]. The materials used for additively manufactured lattice structures involve metals [2, 11], polymers [10], and even ceramic-polymer composites [12].

In lightweight constructions, lattice materials are used due to their extremely high strength-to-density ratio [6, 13]. The rising demand for energy saving and, consequently, lighter construction has led to the manufacture of very slender lattice structures. Slender structures are highly prone to the loss of structural stability when subjected to compressive loading [6, 14,

15]. Hence, the compressive strength is governed by the buckling load of the lattice structure. Buckling as the dominant failure mechanism for lattice materials is observed, e.g. in [12, 15, 16] where the “pure” lattice material has been tested in compressive and three-point bending tests of sandwich panels with lattice cores. Besides the onset of buckling also the post-buckling behavior is of major importance, which should be stable for ensuring the exploitation of the load bearing capacity of the lattice material [17].

This work presents an interdisciplinary approach to manufacture unit cells of prospective hybrid lightweight lattice materials with the potential to be manufactured in customized mass production using 3D printing technology. Therefore, the existing conflict between slender internal structure and structural instabilities in lattice materials has to be solved. Inspired by the concept of large length scale pre-stressed stayed structures [18, 19, 20, 21] the buckling resistance of slender lattice materials shall be increased using interwoven fibers without substantially increasing the weight. This concept dates back into the 1960s [22, 23] and was developed for increasing the buckling load of towers, facades and scaffolding in civil engineering. The aim of this study is to investigate whether or not the principle of pre-stressed stayed columns can be transferred to smaller length scales, i.e. to lattice materials as proposed in [24]. Therefore, experimental investigations on the buckling and post-buckling behavior of simply supported, pre-stressed stayed columns under pure axial compression are conducted on different length scales.

In the current work, the terminology large length scale, medium length scale, and small length scale refers to the meter range, the centimeter range, and the millimeter range, respectively.

2 INVESTIGATIONS ON THE MEDIUM LENGTH SCALE

2.1 Experimental Setup

First, tests were conducted on a medium length scale. For this purpose an aluminum column of 230 mm length with a cross-section of 10 x 1 mm was supported by a cross-arm of 110 mm overall length and a cross section of 5 x 5 mm. The cross-arm was mounted to the column such that column buckling with respect to the axis with the lowest moment of inertia is suppressed. For the cable stays, aramid fibers were used which were fixed at the ends of the column and the cross-arm, respectively. The dimensions of the samples are shown in Figure 1 (left). The fibers were pre-stressed before they were connected to the aluminum structure, however, with the used manufacturing setup it was not possible to determine the actual pre-stress in the fibers.

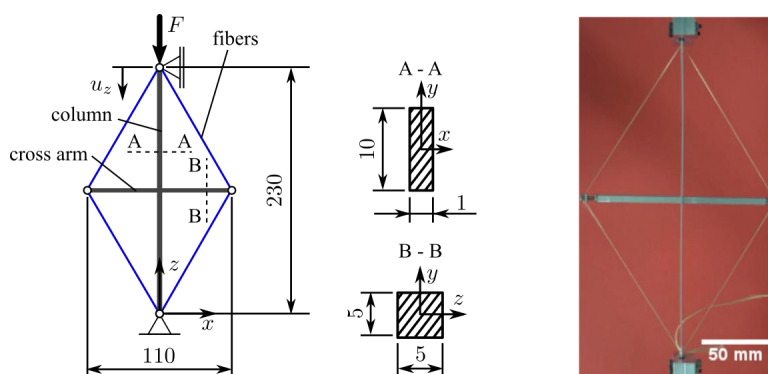


Figure 1: Schematic of pre-stressed stayed column used for experiments on the medium length scale (left); Prototype mounted in test device (right); all dimensions are in mm.

Overall, fifteen samples were tested using the micro-force testing device MTS Tytron 250 (MTS Systems Corporation, Eden Prairie, USA). The samples were simply supported at the ends of the column and subjected to axial displacements in z -direction (see Figure 1 (left) and (right)) where the reaction force was measured using the device-own loading-cell with an accuracy of 0.25 N (0.1 % of the maximum force of 250 N).

2.2 Finite Element Modeling

For modeling the pre-stressed stayed columns, structural elements, i.e. beams and trusses, were used to save computational time compared to continuum elements. The column and the cross arm were discretized using two-noded cubically interpolated Hermite beam elements with a characteristic length of 1 mm. The cross sections of the vertical strut and the cross arm were defined as given in Figure 1. The material behavior of aluminum was assumed to be linear elastic where a Young's modulus of $E_S = 70000$ MPa and a Poisson's ratio of $\nu = 0.33$ were used.

The aramid fibers were modeled using two-noded linearly interpolated truss elements for which the compressive stiffness was set to zero within the material definition. The fibers were assumed to have a diameter of 0.1 mm, a Young's modulus of $E_F = 60000$ MPa and a Poisson's ratio of $\nu_F = 0.3$. For connecting the fibers with the vertical strut and the cross arm direct node-to-node coupling was employed.

The pre-stressed column was simply supported at the ends of the vertical column, see Figure 1, where additionally the rotational degrees of freedom around the z -axis were constrained to avoid rigid body rotations. Geometrical imperfections were not considered and the perfect geometry was discretized. The pre-stress σ_1 in the aramid fibers was introduced as stress-type initial condition. Before the structure was subjected to any external loading or displacement, the equilibrium state of the structure with respect to σ_1 was sought in an initial step. The obtained equilibrium state was defined to be the un-deformed configuration of the structure and corresponds to an external loading $F = 0$ N and axial displacement $u_z = 0$ mm. This configuration was the base state for all conducted analyses.

2.2.1 Buckling analysis

Linear buckling analysis was employed to estimate the critical load of the pre-stressed stayed columns for different values of the pre-stress σ_1 in the aramid fibers. As reference for the buckling analysis, either the un-deformed or a pre-deformed configuration of the structure was used. The pre-deformed configuration was obtained by applying an axial compressive force F in a pre-loading step where geometrically nonlinear behavior was considered. The compressive force was set to $F = 10$ N for $\sigma_1 = 0$ N/mm² and $F = 17$ N for all other values of σ_1 .

2.2.2 Load-displacement analysis and post-buckling behavior

In analogy to the experiments, a displacement-controlled analysis was used to obtain the load-displacement behavior. The vertical displacement u_z at the upper end of the column was prescribed (see Figure 1) and the thereof resulting reaction force was evaluated using the standard Newton-Raphson method as solution procedure. To trigger the post-buckling behavior, i.e. to follow the non-trivial equilibrium path, a small imperfection was applied. The imperfection was introduced as torque M around the y -axis at the upper end of the column in an additional pre-loading step.

2.3 Results and Discussion

All forces F measured in the experiments and obtained in the finite element (FE) analysis were normalized with respect to the theoretical buckling load $F_C^* = 10.883$ N of the

unsupported vertical column. Within the FE simulations, the initial pre-stress σ_1 in the fibers was varied between 0 N/mm² and 200 N/mm² to get information about its influence on the overall mechanical behavior of the structure.

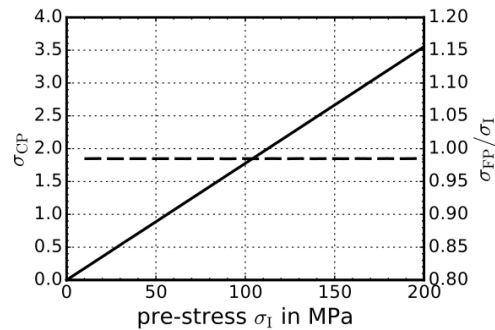


Figure 2: Compressive stress in the vertical column σ_{CP} (solid line) and the normalized stress in the fibers σ_{FP}/σ_1 (dashed line) resulting from an initial pre-stress σ_1 in the fibers.

Figure 2 shows the compressive stress in the vertical column σ_{CP} and the normalized stress in the fibers σ_{FP}/σ_1 as obtained by the FE simulations after equilibrium of the structure was established. The pre-stress in the column σ_{CP} increased linearly with σ_1 and was far below the yield stress of aluminum (assumed $\sigma_Y = 250$ N/mm²). For $\sigma_1 > 60$ N/mm² the stress in the column was larger than the critical stress $\sigma_C = 1.0833$ N/mm² of the unsupported column. However, buckling of the structure was not observed due to the support of the cross-arms in conjunction with the aramid fibers. Within the fibers, the resulting equilibrium pre-stress σ_{FP} was about 98.5 % of the initially applied pre-stress σ_1 , showing that σ_1 was mainly sustained in the fibers.

The results of the linear eigenvalue analysis are depicted in Figure 3. The buckling load of the pre-stressed stayed column was up to a factor 8 higher than the buckling load of the unsupported column. The supporting effect decreased with increasing initial pre-stress σ_1 in the fibers where for $\sigma_1 > 0$ the pre-load F had no influence on the results. In this case the first and second eigenvalue λ_1 and λ_2 , respectively, and the thereof resulting critical loads were almost equal. Hence, the corresponding buckling modes, shown in Figure 3 (middle), have the same probability to occur in the post-buckling regime. Both buckling modes possess a node at the position where the cross-arm is mounted to the column, revealing that the first eigenform of the unsupported column is suppressed.

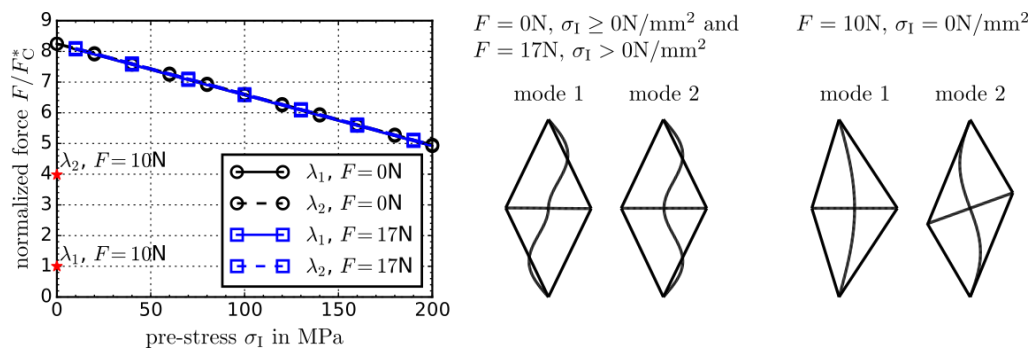


Figure 3: Results of the eigenvalue buckling analysis with and without a pre-buckling deformation due to an applied pre-load F .

For $\sigma_1 = 0 \text{ N/mm}^2$, the eigenvalue analysis conducted with an initial pre-load lead to a critical load being equal to the critical load of the unsupported column. The corresponding eigenform (mode 1, Figure 3 (right)) is similar to the buckling mode of the unsupported column. For the case of $\sigma_1 = 0 \text{ N/mm}^2$, an axial compressive force F lead to a slackening of the fibers and therefore, the supporting effect of the cross-arm was cancelled out. It can be concluded that for triggering the supporting effect, the pre-stress σ_1 in the fibers (see Figure 2) has to be large enough such that the stress in the fibers σ_{FP} is still larger than zero when the critical load of the unsupported column is reached. However, σ_1 should be as small as possible to minimize its negative impact on the supporting effect, see Figure 3 (left).

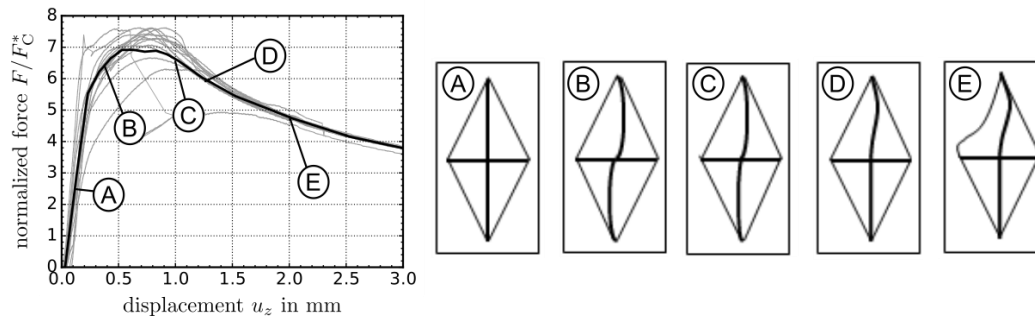


Figure 4: Experimental results for the load-displacement behavior of a pre-stressed stayed aluminum column subjected to compressive loading. Grey lines: results of the individual samples. Black line: mean value estimated every 0.1 mm.

For the experimentally tested samples the vertical column remained straight up to loads larger than the critical load of the unsupported column ($N = F/F^* > 1$), see Figure 4 (A). In the post-buckling regime, first an antisymmetric S-shape (B) deformation was observed which then gradually transformed into a localized bulge in the upper part of the column ((C) and (D)). All samples showed qualitatively the same behavior but differed slightly quantitatively regarding their maximum load. The observed S-shape (B) mode corresponds well to the buckling mode predicted with the FE analysis, see Figure 3 (middle). The maximum load observed in the experiments was about seven times higher than the critical load of the unsupported column. Once the maximum load was reached, a transition from the S-shape to the localized mode occurred during the subsequent post-buckling response. The maximum load also constitutes a limit point indicating an unstable post-buckling behavior. The experimental results correspond also well with results for pre-stressed columns on large length scales [18–21].

The load-displacement behavior of the structure, predicted by the FE simulations, is similar to the experimental results, see Figure 5. The smallest imperfection moment $M = 0.1 \text{ Nmm}$ does not cause any visible initial deformations of the column, allowing to consider the column as initially straight. For $\sigma_1 > 0$, the column remains straight up to loads F being much higher than F_C^* (e.g. $F/F_C^* = 5$ for $\sigma_1 = 200 \text{ N/mm}^2$) and then instantaneously switches into the S-shape mode (B) predicted by the buckling eigenvalue analysis (Figure 3 (middle)) and observed in the experiments, see Figure 4. At the maximum load, being between 7 to 8 times higher than the critical load of the unsupported column, the post-buckling mode transforms to an unstable localized mode (C) and (D) which was also observed in the experiments.

Larger imperfection moments ($M = 10 \text{ Nmm}$ and $M = 50 \text{ Nmm}$) caused already visible pre-buckling deformations (A) which were similar to the unstable localized mode. These pre-buckling deformations yield a smaller compressive stiffness in comparison with a straight column. The transition to the S-shape mode (B) was only observed when the pre-stress was

large enough. This can be seen for the case of $\sigma_I = 100 \text{ N/mm}^2$ and $\sigma_I = 200 \text{ N/mm}^2$ for $M = 10 \text{ Nmm}$, and $\sigma_I = 200 \text{ N/mm}^2$ for $M = 50 \text{ Nmm}$, see Figure 5. When a transition to the S-shape mode occurred, it was much smoother than for the small imperfection moment $M = 0.1 \text{ Nmm}$.

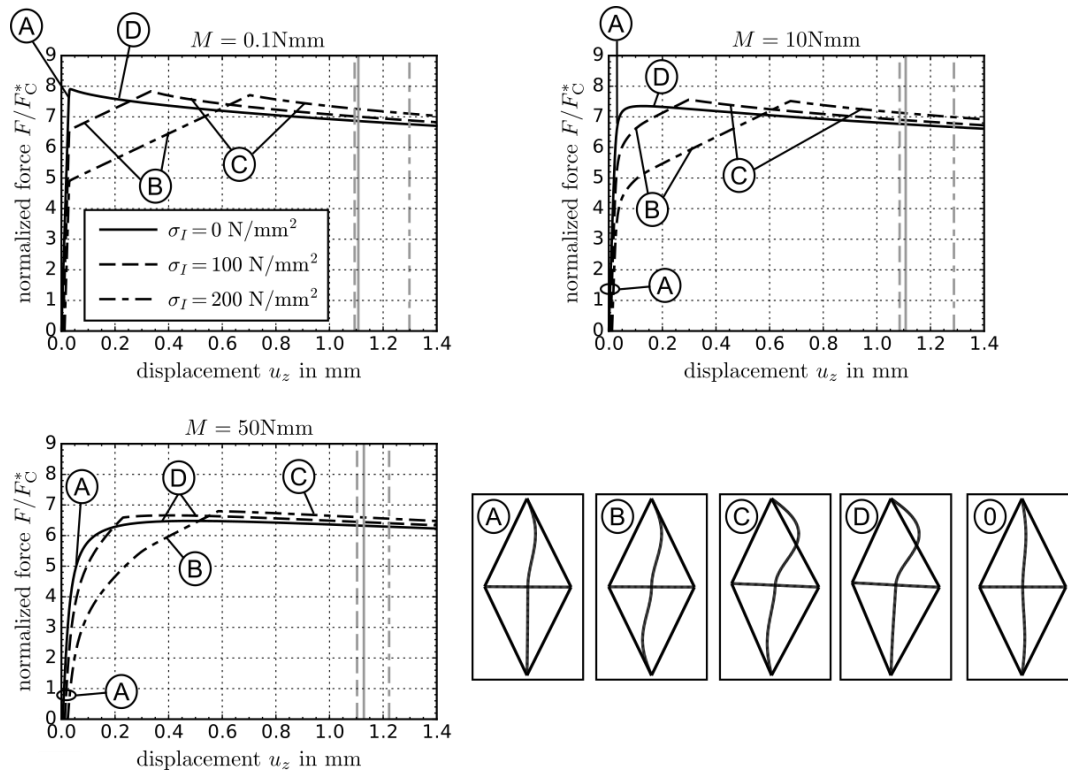


Figure 5: Results of the load-displacement behavior of pre-stressed stayed aluminum columns as predicted by finite element simulations. The simulations have been carried out for different imperfection moments M impinged at the upper end of the column.

As can be seen in Figure 5, the maximum load of the load-displacement paths decreases with increased imperfection moments. Furthermore, the maximum load describes a limit point from where - for the cases of pre-stressed columns - the stable S-shape (B) transform to the unstable localized mode (C). Whenever the pre-stress in the fibers is too small, the S-shape mode is not triggered. However, the load displacement behavior is still stable until the maximum load was reached. In this case, an instantaneous transition from the pre-buckling deformation (A) to the localized mode (D) occurs.

The maximum loads and the post-buckling deformations obtained by the FE analysis agree well with the experimental results. However, the axial displacements for which the maximum axial load was obtained are smaller than the corresponding displacements observed in the experiments. This difference can be attributed to the pre-stress σ_I in the fibers. Larger values of σ_I lead to larger displacements at which the maximum load occurred. It should be noted that the actual pre-stress in the fibers of the tested samples was not determined. Furthermore, the significant decrease in the load carrying capacity after the occurrence of the localized mode was not obtained with the FE simulations. In the FE simulations, linear-elastic material behavior was assumed. However, the von Mises equivalent stress reached the yield limit (assumed $\sigma_F = 250 \text{ N/mm}^2$) at the localized bulge for axial displacements larger than indicated by the grey

vertical lines in Figure 5. The actual yield stress of the aluminum used for manufacturing the samples was not determined experimentally and might be significantly lower than the assumed value. As the samples used in the experiments show plastic deformations, the significant drop in the load carrying capacity may indicate that the plastic limit load is reached directly after the unstable localized mode occurs. For a further improvement of the predictive capabilities of the FE simulations yielding should be taken into account, requiring the characterization of the yield limit and the elastic-plastic material behavior of the strut and column material.

3 INVESTIGATIONS ON THE SMALL LENGTH SCALE

To investigate whether or not the concept of stayed columns for increasing the buckling load is also feasible on a smaller length scale, structures with a size in the mm-range were manufactured in-house and subjected to compressive loading (see Figure 6 (left)). These small structures can be considered as smallest periodic unit, i.e. the Unit Cell (UC) of a periodic lattice material (see Figure 6 (right)). For such small structures, manufacturing strategies developed for larger length scales such as welding or screwing are not applicable. However, for obtaining interpretable and comparable experimental results, a consistent and reproducible manufacture of UC samples is required. Hence, in a first step, a suitable manufacturing process was elaborated, for which two different manufacturing processes were considered. The produced samples were then tested and the influence of the manufacturing strategy on the reproducibility of the experimental results was evaluated. Furthermore, the scalability of the stayed column concept was investigated.

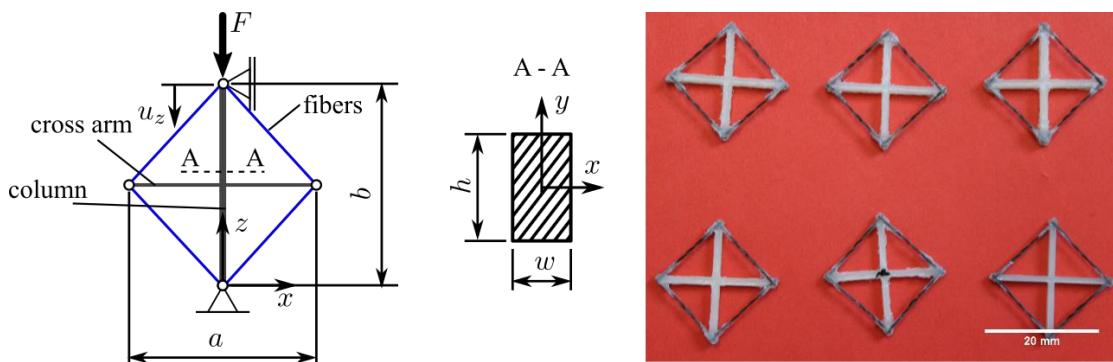


Figure 6: schematic of a UC (left); six in-house casted UCs made out of epoxy (right).

3.1 Manufacture of specimen

With the development and progress in 3D-printing technology, the manufacturing of complex geometries became possible in the recent past. For the in-house production of the specimen, the 3D-Printer Ultimaker 3 Extended (Ultimaker B.V., Cambridge, USA) based on the Fused Deposition Modeling (FDM) technique was used. 3D-FDM-Prototyping allows the design and the production of molding-systems and forming tools to manufacture small length scaled UCs as well as to directly print pre-stressed stayed columns. To obtain reasonable and comparable results from the experiments, easily to use and well-known materials from the lightweight 3D-printing industry were chosen to ensure consistent manufacture of the specimen. Similar to [10], in-house manufacturing processes were developed which are described in detail henceforth.

3.1.1 Epoxy cast using PVA-based water-soluble molding-system (manufacturing strategy A)

With the help of the commercial CAD software Siemens NX 11.0 (Siemens PLM Software, Plano, USA) a 3D-model of the mold was designed (Figure 7 (left)) and exported to surface-based STL-data.

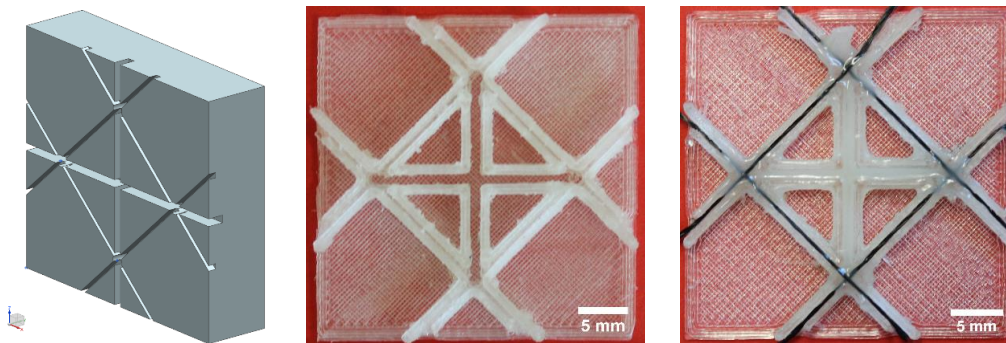


Figure 7: CAD-model of a UC-model (left); 3D-printed UC-mold made out of PVA (middle); epoxy casted UC-mold incl. pre-stressed carbon fibers (right).

Using the free software Cura 3.1.4 (Ultimaker B.V., Cambridge, USA) STL-data was transformed to GCODE-format, which was used as an input for the Ultimaker 3 Extended FDM 3D-printer. Molds with the dimensions of 32 x 32 x 8 mm, made out of water-soluble PVA were printed at 210 °C with an accuracy of ± 0.05 mm (Figure 7 (middle)). PAN-based carbon fibers with a diameter of 500 μm (Sigrafil, SGL Carbon SE, Wiesbaden, Germany) were mounted into the tool. Epoxy resin (Loctite 9466, Henkel, Garching, Germany) was carefully cast into the printed mold-system (Figure 7 (right)) using a needle with a diameter of 0.8 mm with the aim to avoid inhomogeneities such as bubbles. After a curing time of 24 hours, the specimen was put for another 4 hours in regular tap water, so that the water-soluble PVA based forming tool vanished non-invasively leaving the UC made out of epoxy (dimensions: 20 x 20 mm with a cross-section of 2 x 1 mm; see Figure 8 (left)).

Additionally, a forming tool with the dimensions of 32 x 32 x 8 mm, made out of aluminum, was manufactured at Ellinger GmbH, Berlin, Germany (Figure 4 (middle)), with the aim to increase the surface quality of the form tool and to compare it with the PVA-mold. After sealing (Semipermanente Versiegelung, Göbl & Pfaff GmbH, Karlskron/Brautlach, Germany), cleaning (Trennmittel, Göbl & Pfaff GmbH, Karlskron/Brautlach, Germany), casting, and curing, one prototype specimen (dimensions: 20 x 20 mm with a cross-section of 2 x 1 mm) with increased quality was manufactured (Figure 8 (right)).

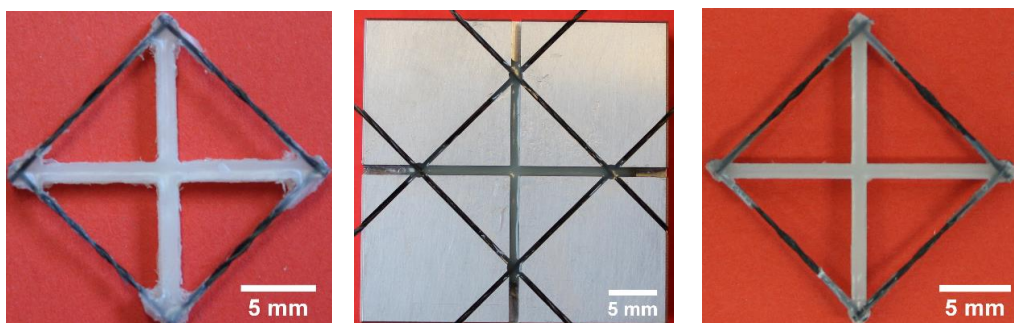


Figure 8: UC-prototype made of epoxy casted in a PVA-mold (left); epoxy casted UC incl. pre-stressed fibers in an aluminium-mold (middle); UC made out of epoxy, which was cast in an aluminium-mold (right).

Furthermore, forming tools for UCs with smaller dimensions (20 x 20 mm with a cross-section of 2 x 0.5 mm; see Figure 9 (left)) were printed successfully. Additionally, form tools made of different materials such as thermo-plastic Polyurethane (TPU, black mold) or Acrylonitrile-Butadiene-Sterol-Copolymers (ABS, white molds), as shown in Figure 9 (right), were printed using rapid prototyping without improving the manufacturing of the specimen.

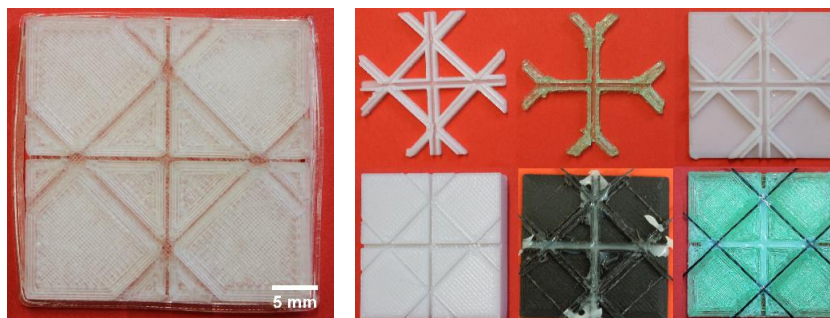


Figure 9: PVA-mold of smaller UC with outer dimensions of 20 x 20 mm with a cross-section of 2 x 0.5 mm (left); several UC-molds made out of different materials like ABS/PLA/TPU (right).

3.1.2 Directly printed specimen using PLA based filaments (manufacturing strategy B)

A printing-process was developed in which the carbon-fibers were directly embedded into the raw printing material (see Figure 10 (left)). This manufacturing strategy has the advantage that no mold is required and hence the manufacturing times and costs are lower in comparison with manufacturing strategy A. Using the same software tools as in Section 3.1.1 a 3D-CAD-model of the prototype (Figure 10 (right)) was generated. For introducing the fiber reinforcements into the structure, the input-file for the 3D-printer was manipulated in the following way: The virtual model was sliced into twenty planes in y -direction according to Figure 6. After the print of ten planes, the printing-process was paused so that the PAN-based carbon fibers could be mounted into the printing-device. The weakly pre-stressed fibers were fixed onto the top of the tenth layer. Then the printing-process was resumed and the remaining layers were added. However, the 10th layer hardened during the mounting process because of cooling. As a result, the bonding between the fiber and the 10th layer is to some extent insufficient. In contrast, the bonding between the 11th layer and the fiber is sufficient since this layer is printed „around“ the fiber. Furthermore, printing of the 11th layer leads to a re-heating of the 10th layer improving the connection of the 10th layer and the fiber.

Specimens with smaller dimensions (10 x 10 mm with a cross-section of 1 x 0.5 mm) were also printed successfully (see smaller sample in Figure 10 (left)). By adjusting the printing- and design parameters as well as reducing the diameter of the carbon fiber down to about 250 μm (reduction of 50 %), for the first time sufficient sample-quality even for the smallest prototypes could be ensured. None of the smaller samples was tested within this work.

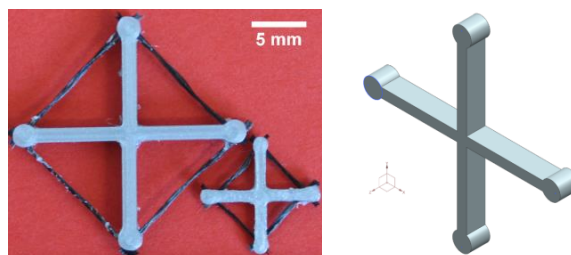


Figure 10: UC-prototypes made out of PLA, in which carbon-fibers are directly embedded into the raw material (left); CAD-model of an UC (right).

3.2 Experimental Setup

The buckling and post-buckling behavior of seven in-house manufactured specimens under pure axial compression was investigated. An overview of all investigated specimen is given in Table 1.

Table 1: Listing of specimen-series with material and geometry parameters (which refer to the left schematic in Figure 6(left)); a describes the length of the horizontal strut, b is the length of the cross-arm, $A = h \times w$ describes the cross-section of the beam with h as the height of the beam and w as the width of the beam; d is the diameter of the carbon-based fiber (500 μm equivalent to 100 %).

Specimen Number	Specimen Name	Series	Manufacture Strategy	Material of Column	Dimensions $a \times b \times h \times w$; d [mm; %]
1	Epoxy-Aluminum	I	A	Epoxy resin	20 x 20 x 2 x 1; 100
2	Epoxy-PVA1	I	A	Epoxy resin	20 x 20 x 2 x 1; 100
3	Epoxy-PVA2	I	A	Epoxy resin	20 x 20 x 2 x 1; 100
4	Epoxy-PVA3	I	A	Epoxy resin	20 x 20 x 2 x 1; 100
5	PLA1	II	B	PLA	20 x 20 x 2 x 1; 100
6	PLA2	II	B	PLA	20 x 20 x 2 x 1; 100
7	PLA3	II	B	PLA	20 x 20 x 2 x 1; 100

All specimen were horizontally tilt-mounted into a micro-force testing device (MTS Tytron 250, MTS Systems Corporation, Eden Prairie, USA) with the help of special adapters (Figure 11 (left)) and axially loaded with a velocity of 0.05 mm/s (displacement-controlled). An overview of the experimental setup is shown in Figure 11 (right). The hydraulic mounting system of the testing device ensures to measure the reaction-force with an accuracy of 0.1 % (0.25 Newton) on the device-own loading-cell.

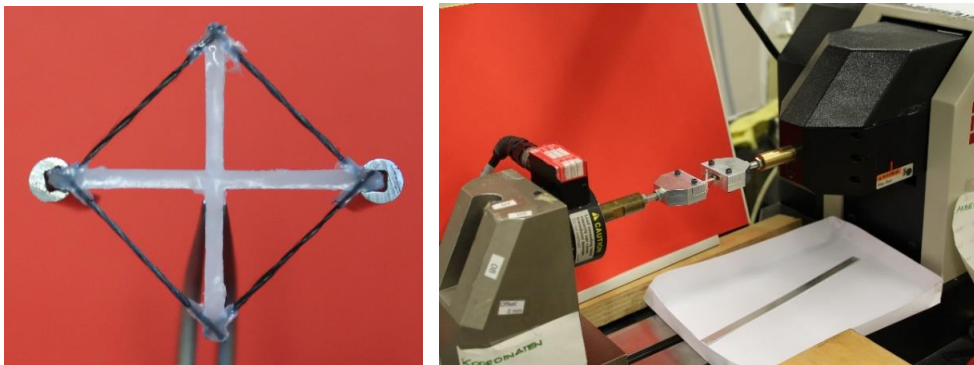


Figure 11: Mounting adapters fixed onto one of to be tested specimens (left); compression device MTS Tytron 250 with device-own load-cell on the left hand side and mounted specimen in the middle (right).

3.3 Results and Discussion

For all measurement series, the load-displacement behavior was recorded and the measured loads F were normalized with respect to the buckling load F_C^* of the unsupported column ($N = F / F_C^*$).

3.3.1 Results of experimental studies on epoxy-based specimen (manufacture strategy A)

The results for the epoxy-based specimens are shown in Figure 12. The critical load of an unsupported column was experimentally determined as $F_C^* = 9.63$ N. Initially, all pre-stressed

samples as well as the unsupported column show the same load-displacement behavior. Significant higher maximum loads ($N \approx 3.6-4.7$) can be reached by the pre-stressed samples. For reaction forces up to F_C^* no visible deflections of the column and the cross-arm occur. For prescribed displacements leading to larger reaction forces than F_C^* , the vertical column shows an S-shape deflection (B) which, however, does not have a negative influence on the stiffness of the structure. The load-displacement behavior in this region is almost linear. At prescribed displacements corresponding to the maximum loads, the buckling displacements localize in the upper bulge of the S-shape (C and D). This leads to a significant decrease in the load carrying capacity. At this point, the yield limit of the epoxy resin might be reached. The maximum loads that could be reached for the pre-stressed stayed columns are at minimum 3.6 times larger than F_C^* . The S-shape deformations for $F > F_C^*$ show that the supporting effect due to fibers is large enough to provoke a higher order buckling mode by causing a bearing effect at the position where the cross-arm is mounted. The results of the sample manufactured with the aluminum mold are in good agreement with the results of the samples manufactured with the PVA molds.

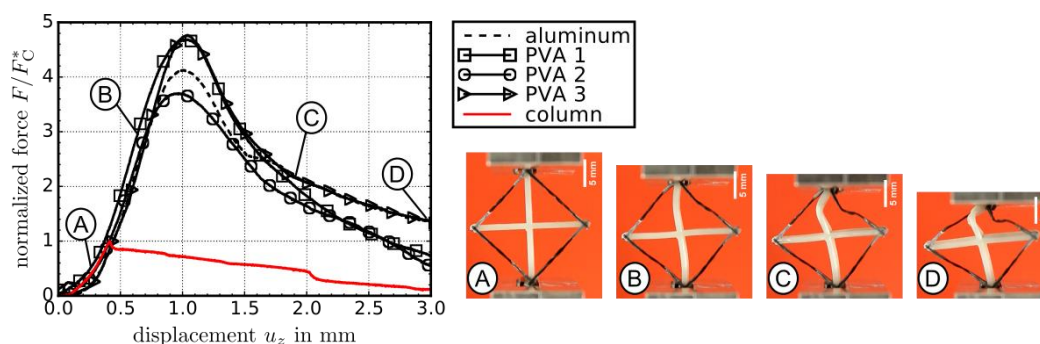


Figure 12: Experimental results for the epoxy-based pre-stressed stayed columns as well as the un-supported column (left) and the deformation sequence as obtained for the sample manufactured with the aluminum mold (right).

However, after hardening the detachment of the prototype from the aluminum-mold system, was very difficult, even with a sealed mold. Therefore, a redesign of the mold geometries is recommended. A possibility is to define the wall depths at an angle of $>1^\circ$. This will help to remove the prototype in a much easier way. In addition, undercuts based on manufacturing process will not appear anymore. Furthermore, it was observed that the fibers are not ideally centered in the $x-y$ -plane of the casted specimen. The diameter of the fiber has to be also reconsidered in the process of redesigning. Therefore, the depth of the gap of the diagonal fiber-guide should be increased at least by the half of the diameter of a fiber. Additionally, a preloading-device for the fibers should be designed not only to guarantee a defined pre-stress in the fibers, but also to provide better bonding of the fibers to the epoxy resin.

3.3.2 Results of experimental studies on PLA-based specimen (manufacture strategy B)

Results for the specimen made out of PLA are shown in Figure 13. The critical load $F_C^* = 20.30$ N of an unsupported PLA column was used for normalizing the reaction forces obtained for the pre-stressed stayed columns. The results of the samples comprising series II are scattered. For all tested samples, a larger maximum load as for the unsupported column is obtained. In contrast to the unsupported sample, the tested supported specimens show different load-displacement behavior, even for reaction forces far smaller than F_C^* . One reason might be that the incooperated fibers have locally a negative impact on the material properties of the PLA. Another reason might be that the printed material is not perfectly attached to the fibers

leading to local voids and pores and hence, reducing the stiffness of the structure. With increasing prescribed displacements, the differences between the individual samples become even larger and the maximum loads are also strongly scattered.

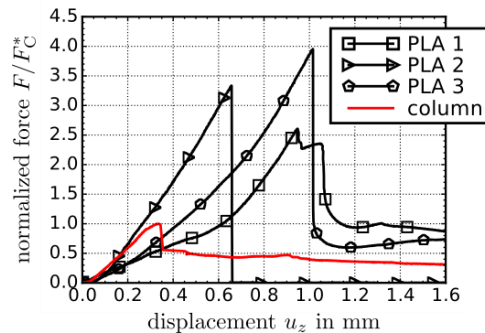


Figure 13: Experimental results for PLA-based un-supported columns (left) and pre-stressed stayed columns (right) manufactured by the 3D printing process.

All samples show initially a C-shape deflection being equal to the buckling mode of the unsupported column. Samples PLA 1 and PLA 3 fail by de-bonding of the fibers leading to the significant drop in the load bearing capacity as shown in Figure 13. Only for sample PLA 2 an out-of-plane buckling mode occurs, causing the specimen to slip out of the mounting system and leading to a reaction force $F = 0$ N. The fact that fiber debonding leads to sample failure in most cases, strengthens the statement that the raw material is not perfectly attached to the fibers. This is also emphasized by the fact that the sample PLA 2 for which no fiber debonding occurs shows the same initial stiffness up to $F = F_C^*$ as the unsupported column, see Figure 13. Furthermore, the supported columns first deform in the C-shape mode of the unsupported column showing that the supporting effect is not strong enough to provoke any higher-order buckling mode. This might be due to the lack of pre-stress in the fibers or due to the non-perfect attachment of the fibers to the raw material.

In summary, the quantitative results obtained from investigations of series I (see Figure 12) and series II (see Figure 13) are in the same range resulting in an average critical load about four times higher than that of the measured bare column without fibers. In contrast, by comparing results of series I and series II with each other qualitatively, a different deformation/material behavior is observed. Nevertheless, after failure of the structure, the loading behavior approximates in both series to $N = 1$, the regular loading capacity of the bare column. After an antisymmetric S-shape deflection, the buckling behavior of the specimens in series I change to a superimposed asymmetric mode resulting in a controlled decrease of loading, whereas the linear and symmetric C-shape deflection of specimen in series II stay until a sudden decrease of loading occurs. The reason for this behavior in series II lies not in a sudden rupture of a fiber as assumed at first, but in the debonding of fiber and raw-material. The fiber detaches from the raw material because of lack of surface contact due the manufacturing process B as described in Section 3.1.2. Therefore, a parameter optimization for the 3D-printing-system is strongly recommended to improve the quality of the specimens, especially the interface between fiber and raw-material. This will help to prevent debonding of the fibers and the raw-material.

4 CONCLUSION & OUTLOOK

The concept of reinforcing slender columns with pre-stressed cable stays to increase their buckling load is widely applied in civil engineering, i.e. on a large length scale. In this study, experiments and finite element simulations on pre-stressed stayed structures have been conducted revealing that this concept is also applicable to structures with dimensions in the centimeter range (medium length scale) and millimeter range (small length scale). The load bearing capacity of the investigated structures was significantly increased compared to corresponding unsupported columns where the post-buckling deformations show a strong dependency on the actual structural conditions. Results obtained from experiments and finite element simulations on the medium length scale show about eight times higher load bearing capacity compared to the bare column ($N \approx 8$).

For the small scaled specimens (series I and series II), the quantitative results are in good agreement with each other and show an increase of the load bearing capacity by a factor four ($N \approx 4$). Differences can be linked to the different material properties and the different manufacturing processes. Because of the de-bonding of fiber and raw-material for samples in series II, the qualitative loading as well as buckling and post-buckling behavior are different with respect to series I. In a next step, finite element simulations on the small-scale samples will be performed to gain further insight in their mechanical behavior.

Furthermore, manufacturing the pre-stressed stayed structures with dimensions in the millimeter range required the development of corresponding manufacturing strategies. A mold based and a 3D-printing type strategy have been successfully implemented. The results show that the biggest challenge lies within the attachment of the involved fibers to the raw material. A strong bonding between fiber and raw material is essential for fully exploiting the supporting effect of the pre-stressed fiber stays. Further improvements of the developed modeling strategies are envisaged.

The developed strategies allow not only to manufacture single pre-stressed stayed structures but also a periodic arrangement of such structures, i.e. to manufacture a pre-stressed stayed lattice material. Examples of CAD-models of mold-systems for 2D-lattice-structures are shown in Figure 14 (left and middle). An ABS-based mold system has already been manufactured in-house successfully (see Fig. 14 (right)). Investigations and experiments on 2D-lattice-structures should be conducted in the near future.

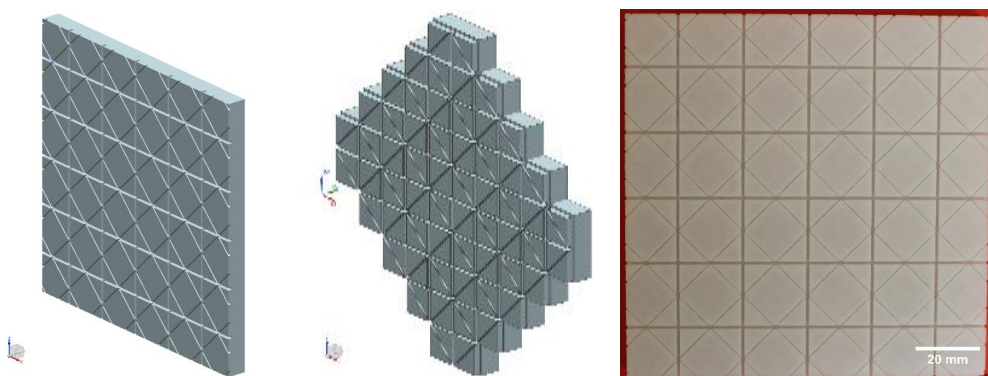


Figure 14: CAD-model of a cubic 2D-lattice-structure (left); CAD-model of a hexagonal 2D-lattice-structure (middle); in-house manufactured cubic 2D-lattice-mold based on ABS (right).

The negligible increase in weight due to the fibers in relation to the potential significant increase in load bearing capacity of such lattice materials is an outstanding advantage in contrast

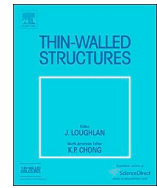
to conventional lattice materials. This would make pre-stressed stayed lattice materials perfect materials for lightweight applications in the aircraft and automotive industries.

REFERENCES

- [1] Yang J., Xiong J., Ma L., Wang B., Zhang G. and Wu L., „Study on vibration damping of composite sandwich cylindrical shell with pyramidal truss-like cores”, *Composite Structures*, **117**, 2014.
- [2] Tancogne-Dejean T., Spierings A.B. and Mohr D., “Additively-manufactured metallic micro-lattice materials for high specific energy absorption under static and dynamic loading”, *Acta Materialia*, **116**, 14-28, 2016.
- [3] Queheillalt D.T. and Wadley H.N.G., “Cellular metal lattices with hollow trusses”, *Acta Materialia*, **53**(2), 303-313, 2005.
- [4] Zhu F., Lu G., Ruan D. and Wang Z., “Plastic Deformation, Failure and Energy Absorption of Sandwich Structures with Metallic Cellular Cores”, *International Journal of Protective Structures*, **1**(4), 507-541, 2010.
- [5] Tian J., Kim T., Lu T.J., Hodson H.P., Queheillalt D.T., Sypeck D.J. and Wadley H.N.G., “The effects of topology upon fluid-flow and heat-transfer within cellular copper structures”, *International Journal of Heat and Mass Transfer*, **47**(14-16), 3171 – 3186, 2004.
- [6] Gibson I.J and Ashby M.F., “Cellular solids: structure and properties”, Cambridge Solid State Science Series, Cambridge University Press, 1999.
- [7] Chen Y., Li T., Scarpa F. and Wang L., „Lattice Metamaterials with Mechanically Tunable Poisson’s Ratio for Vibration Control”, *Physical Review Applied*, **7**, 024012, 2017.
- [8] Rathbun H.J., Zok F.W., Waltner S.A., Mercer C., Evans A.G., Queheillalt D.T. and Wadley H.N.G., “Structural performance of metallic sandwich beams with hollow truss cores”, *Acta Materialia*, **54**(20), 5509 – 5518, 2006.
- [9] Valdevit L., Jacobsen A.J., Greer J.R., and Carter W.B. “Protocols for the optimal design of multi-functional cellular structures: From hypersonics to micro-architected materials”. *Journal of the American Ceramic Society*, **94**(S1), 15–34, 2011.
- [10] Nezami F. and Fuhr J.-P., “Digitale Entwicklung und automatisierte CFK-Verstärkung additiv gefertigter Teile”, *Lightweight Design*, **10**(6), 38-41, 2017.
- [11] Gümrük R. and Mines R.A.W., “Compressive behavior of stainless steel micro-lattice structures”, *International Journal of Mechanical Sciences*, **68**, 125-139, 2013.
- [12] J. Bauer J., Hengsbach S., Tesari I., Schwaiger R. and Kraft O., „High-strength cellular ceramic composites with 3D microarchitecture”, *Proceedings of the National Academy of Sciences of the United States of America*, **111**, 2453 – 2458, 2014.
- [13] Fleck N.A., Deshpande V.S. and Ashby M.F., “Micro-architected materials: past, present and future”, *Proceedings of the Royal Society of London A*, **466**, 2495-2516, 2010.
- [14] Bendsoe M.P. and Triantafyllidis N., “Scale effects in the optimal design of a microstructured medium against buckling”, *International Journal of Solids and Structures*, **26**(7), 725 - 741, 1990.
- [15] Moongkhamklang P., Deshpande V.S. and Wadley H.N.G., “The compressive and shear response of titanium matrix composite lattice structures”, *Acta Materialia*, **58**(8), 2822-2835, 2010.
- [16] Kolodziejska J.A., Roper C.S., Yang, S.S., Carter W.B. and Jacobsen A.J., “Research Update: Enabling ultra-thin lightweight structures: Microsandwich structures with microlattice cores”, *APL Materials*, **3**(5), 050701, 2015.
- [17] Hunt G.W., “Bifurcations of Structural Components”, *Proceedings of the Institution of Civil Engineers Part 2*, **87**, 443-467, 1989.
- [18] Osofero A.I., Wadee M.A. and Gardner L., “Experimental study of critical and post-buckling behaviour of prestressed stayed columns”, *Journal of Constructional Steel Research*, **79**, 226-241, 2012.

Gregor Ganzosch *et al.*

- [19] Saito D. and Wadee M.A., “Post-buckling behaviour of prestressed steel stayed columns”, *Engineering Structures*, **30**(5), 1224-1239, 2008.
- [20] Wadee M.A., Gardner L. and Osofero A.I., “Design of prestresses stayed columns”, *Journal of Constructional Steel Research*, **80**, 287-298, 2013.
- [21] Wadee M.A., Gardner L. and T.A. Hunt, “Buckling mode interaction in prestressed stayed columns”, *Proceedings of the Institution of Civil Engineers - Structures and Buildings*, **166**(8), 403-412, 2013.
- [22] Chu K.H. and Berge S.S., “Analysis and design of struts with tension ties”, *Journal of Structural Division*, **89**(1), 127-164, 1963.
- [23] Mauch H.R. and Felton L.P., “Optimum design of columns supported by tension ties”, *Journal of Structural Division*, **93**(3), 201-220, 1967.
- [24] Zschoernack C., Wadee M.A. and Völlmecke C., „Nonlinear buckling of fibre-reinforced unit cells of lattice materials”, *Composite Structures*, **136**, 217-228, 2016.



Full length article

Experimental and numerical investigation on pre-stressed lattice structures

Anton Köllner^{a,*}, Melanie Todt^b, Gregor Ganzosch^c, Christina Völlmecke^a^a Institute of Mechanics, Stability and Failure of Functionally Optimized Structures Group, Technische Universität Berlin, Einsteinufer 5, 10587, Berlin, Germany^b Institute of Lightweight Design and Structural Biomechanics, Technische Universität Wien, Getreidemarkt 9, 1060, Vienna, Austria^c Institute of Mechanics, Continuum Mechanics and Material Theory Group, Technische Universität Berlin, Einsteinufer 5, 10587, Berlin, Germany

ARTICLE INFO

Keywords:
Pre-stress
Lattice structures
Buckling
Experiment
Finite element method

ABSTRACT

The effect of pre-stress on the buckling behaviour of geometric unit cells of collinear square lattices is investigated experimentally and numerically. The geometric unit cells are manufactured using fused deposition modelling. Manufacturing strategies are presented which incorporate fibres subjected to pre-stress within the unit cell. The effect of pre-stressed fibres is analysed by comparing the compressive behaviour of unit cells with and without fibre reinforcement. The buckling behaviour of the unit cells is also investigated numerically by employing a parametric study within Abaqus varying the pre-stress in the fibres. The experimental test series shows that the addition of pre-stressed fibres to the system results in an increase in buckling and maximum load of 260%–480% and 220%–350% respectively. The increase strongly relates to the manufacturing quality, *i.e.* the bonding between the lattice material and the fibres, where a sufficient bonding yields significantly larger loads. The experimental findings on the qualitative and quantitative buckling behaviour correspond well with results obtain from the numerical study.

1. Introduction

With their open and periodic internal structure, lattice structures possess an extremely high strength-to-weight ratio and have remarkable potential regarding multi-functionality [6]. Owing to the periodicity of lattice materials their global material properties mainly depend on the internal architecture. Hence, by designing the lattice structure the overall properties of a lattice might be tailored according to the requirements of specific applications [4,22,24]. Recent developments in advanced manufacturing technologies such as additive manufacturing (AM) allow to produce highly complex and even hybrid lattice structures in customized massproduction [15]. Materials used in AM are polymers [15], metals [9,19] or even ceramics [2].

For applications in lightweight construction, lattices are created with very slender dimensions. This makes them highly prone to instabilities due to buckling under compressive loading conditions [3,8,14,23]. Since buckling is thus the dominant failure mode, the critical load determines the compressive strength of the lattice. Yet furthermore the post-critical behaviour is of major importance when determining the ultimate load bearing capacity of lattice materials. In order to prevent early buckling in large-scale columns in civil engineering applications, the concept of pre-stressed cable stays was first introduced in the 1960s [5,13] and is still topic of current research [1,16–18,21,25].

The aim of the present study is to investigate whether the concept of pre-stressed cables can be adapted to smaller dimensions, which will be regarded as geometric unit cells (UCs) of lattice structures. Previous analytical and numerical results of the post-buckling of UCs of lattices were highly encouraging [25] and recent experimental investigations also showed an increase in buckling load for UCs [7], where the concept of using fibres to introduce pre-stress was presented first. In the experiments, it was observed that the actual pre-stress in the fibres is of major importance for the buckling response. This had already been investigated on a larger scale in 1979 by Hafez et al. [10], where the findings are visualized in Fig. 1 and subsequently briefly summarized.

In Ref. [10], the effect of initial pre-stress in stays on the buckling of single-crossarm stayed columns is investigated. Fig. 1 illustrates the relationship between buckling load and initial¹ pre-stress in the cables of a single-crossarm stayed column. The relationship can be divided into three zones:

- Zone 1: initial pre-stress is smaller than a minimum effective pre-stress T_{\min} ; the system behaves as an unstayed column and buckles at the EULER load;
- Zone 2: initial pre-stress is between a minimum effective pre-stress T_{\min} and an optimum pre-stress T_{opt} ; linear relationship between pre-stress and buckling load up to T_{opt} ;

* Corresponding author.

E-mail address: anton.koellner@tu-berlin.de (A. Köllner).¹ "Initial" is here understood as before compressive loading is applied.

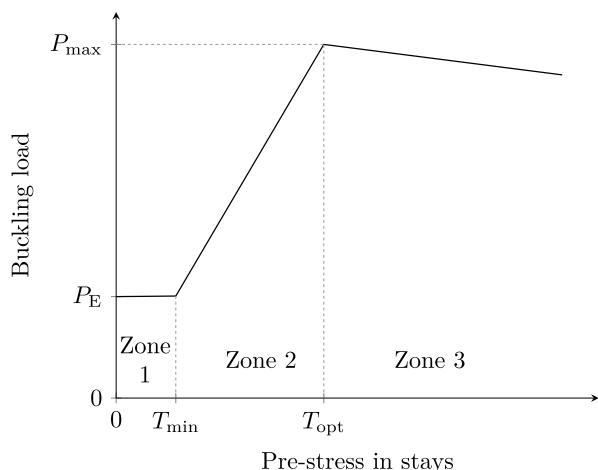


Fig. 1. Buckling load against pre-stress in stays; refers to single-crossarm stayed columns; adapted from Ref. [10].

- Zone 3: initial pre-stress is larger than an optimum pre-stress T_{opt} : decreasing buckling loads with increasing pre-stress and the system buckles with remaining stresses in the cables.

As shown in Fig. 1, the maximum buckling load, which is significantly larger than the respective EULER load, is present at the transition from zone 2 to zone 3 associated with an optimum pre-stress T_{opt} .

In the current work, it will be analysed whether the relationships illustrated in Fig. 1 hold for structures being part of small-sized lattice materials (e.g. as can be found in sandwich core constructions). In contrast to pre-stressed columns used in civil engineering, such structures, i.e. pre-stressed geometric UCs considered in this work, are much smaller as well as exhibit different geometric proportions and stiffness relations. In civil engineering structures, slender columns are supported by comparably short cross-arms (cf. [1,16]). The UCs investigated in this study have equal dimensions in height and width as it is representative for UCs of lattice materials (e.g. collinear lattices). Furthermore, the fibres replacing the cables in the investigated UCs have a significantly larger elastic modulus than the column and cross-arm, whereas for pre-stressed civil engineering columns all constituents are often made of the same material (e.g. steel).

As a consequence, the current work will provide insight into the effect of downsizing the concept of pre-stressed columns, altered geometric conditions and the high elastic contrast between the individual constituents present in geometric UCs and thus provide the basis for introducing the concept of pre-stressed columns into small-sized lattice construction. Moreover, the effect of pre-stress on the buckling mode, possible mode interactions and initial post-buckling behaviour will be discussed in relation to the structure studied.

The methodology of the work, describing the experimental test series and the finite element model, is subsequently provided in Section 2. In Section 3, the experimental and numerical results are presented. The paper concludes with a discussion of the results, the numerical analysis and the manufacturing in Section 4 followed by conclusions in Section 5.

2. Methodology

The effect of pre-stressed fibres on the compressive behaviour of a geometric unit cell (UC) of collinear lattice structures has been investigated by experimental and numerical studies. A geometric UC is to be understood as the smallest periodic unit of the lattice structure without implementing periodic boundary conditions. Fig. 2 shows a schematic of a UC. The specimens for the experiments were

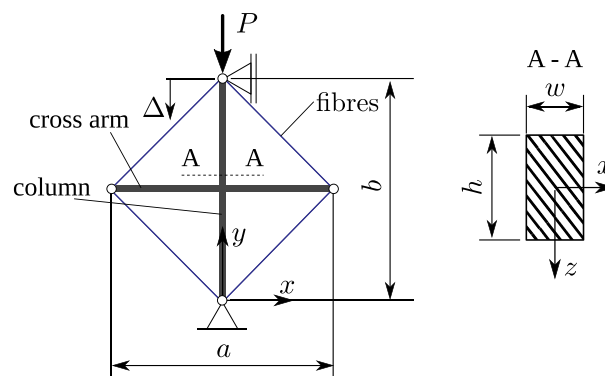


Fig. 2. Schematic of a UC; a – length of the horizontal strut, b – length of the cross-arm, cross-section ($w \times h$), h – height of beam, w – width of the beam.

manufactured with the aid of the 3D-printer Ultimaker 3 Extended (Ultimaker B.V., Cambridge, USA), based on Fused Deposition Modelling (FDM). The 3D-FDM-prototyping technique was used, owing to its capabilities to design and manufacture moulding-systems and forming tools of unit cells (UCs) in the mm-range. The manufacturing process and the test procedure is described in Sections 2.1.1 and Section 2.1.2 respectively.

The numerical study employing the finite element method (FEM) was performed to provide a simulation tool which captures the effects observed during experiments and also generates insight into the influence of variations in pre-stress and imperfections on the compressive behaviour. The FE model is described in Section 2.2.

2.1. Experiment

2.1.1. Manufacturing

The 3D-FDM-prototyping technique was used to enable a consistent and reproducible manufacture of the UC samples. Two manufacturing processes were considered, which are subsequently described. Respective prototypes of the UCs are shown in Fig. 3.

Epoxy cast using Polyvinyl Acetate (PVA) based water-soluble moulding-system. Moulds with the dimensions of $32 \times 32 \times 8$ mm, made of water-soluble PVA were printed at 210°C with an accuracy of ± 0.1 mm. Polyacryl-based (PAN) carbon fibres with a diameter of $500\ \mu\text{m}$ (Sigrafil, SGL Carbon SE, Wiesbaden, Germany) were mounted into the tool and manually fixed with an unspecified pre-stress. In the next step, epoxy resin (Loctite 9466, Henkel, Garching, Germany) was carefully cast into the printed mould-system using a needle with a diameter of 0.8 mm aiming to avoid inhomogeneities such as bubbles. After a curing time of 24 h, the specimens were put for another 24 h in regular tap water, so that the water-soluble PVA based forming tool vanishes non-invasively leaving the UC made of epoxy (dimensions: 20×20 mm with a cross-section of 2×1 mm, cf. Fig. 2).

Directly printed specimen using Polylactic Acid (PLA) based filaments. A printing-process was developed in which carbon fibres are directly embedded in the raw printing material (PLA). This manufacturing strategy has the advantage that no mould is required and hence the manufacturing times and costs are lower in comparison with the aforementioned manufacturing process. For introducing the fibre reinforcements into the structure, the input-file for the 3D-printer was manipulated as follows: the virtual model is sliced into twenty planes in the z -direction (cf. Fig. 2). After the printing of ten planes, the printing-process is paused so that the PAN-based carbon fibres can be mounted into the printing-device. The fibres are fixed manually with an unspecified pre-stress onto the top of the tenth layer. Then, the printing-process continues and the remaining layers are added.

However, it was observed that during the placement of the fibres the lower part of the print had begun to harden because of cooling. As a

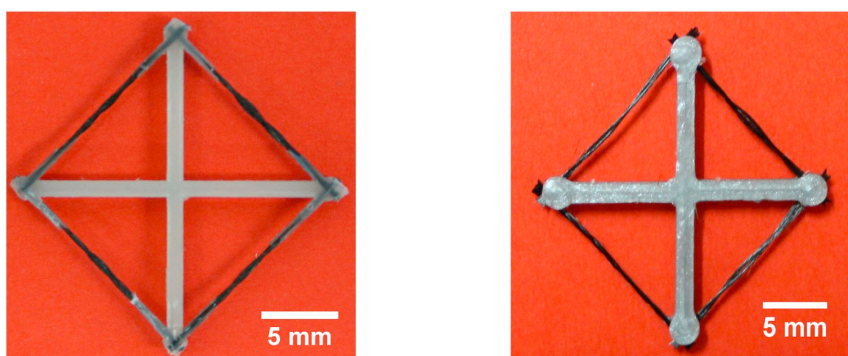


Fig. 3. UC made of epoxy (left) and PLA (right).

result, the bonding between the fibres and the 10th layer is to some extent insufficient. In contrast, the bonding between the 11th layer and the fibre is sufficient since this layer is printed "around" the fibre. Furthermore, printing of the 11th layer leads to a re-heating of the 10th layer improving the connection of the 10th layer and the fibre.

2.1.2. Test setup

The buckling and post-buckling behaviour of 80 in-house manufactured specimens (40 made of epoxy, 40 made of PLA) under pure axial compression were investigated. In order to investigate the effect of fibres on the compressive behaviour, UCs with and without fibres were produced for each manufacturing process. Ten specimens of each type were manufactured without fibres and 30 specimens with fibres.

All specimens were tilt-mounted horizontally into a micro-force testing device (MTS Tytron 250, MTS Systems Corporation, Eden Prairie, USA) with the help of special adapters that enable simply supported boundary conditions (cf. cubes in Fig. 4). The specimens were loaded axially with a velocity of 0.01 mm/s (displacement-controlled) simulating a quasi-static deformation process, where the maximum end-shortening was set to 3 mm. An overview of the experimental setup is shown in Fig. 4. The hydraulic mounting system of the testing device ensures the measurement of the reaction force with an accuracy of 0.1% (0.25 N) on the device-own loading-cell.

Force and displacement (end-shortening of the UC) were measured by the testing device with a sampling rate of 25 Hz and post-processing was performed with the software Python. The (post-)buckling behaviour is analysed in terms of force against displacement curves, which are presented and described in Section 3. Besides the acquisition of force and displacement, the tests were analysed qualitatively using footage of the

(post-)buckling deformation taken every 2 s during each test run with a Canon EOS 100D camera (4272 × 2848 pixels resolution).

2.2. Finite element model

In the finite element simulations only the idealized structure of the unit cell shown in Fig. 2 was modelled. The overall cell dimensions were taken to be $a \times b = 20 \times 20$ mm with a cross section for the column and cross arm of $h \times b = 2 \times 1$ mm. Deviations from these measures resulting from the different manufacturing processes were not considered. Furthermore, the fibres were assumed to be perfectly bonded to the column and the cross-arm. From a modelling point of view, the epoxy cast and the PLA printed cells only differ in the elastic modulus of the base materials. The elastic moduli of epoxy with $E = 1720$ MPa and PLA with $E = 2346.5$ MPa are in the same order of magnitude, and thus more than factor 100 smaller than the elastic modulus of the fibres ($E_F = 279000$ MPa). Owing to the similar elastic contrast of epoxy and PLA with respect to the fibres, no difference in the qualitative behaviour of UCs made of these two materials was expected. This is underlined by the results of the eigenvalue analysis for PLA which can be found in Appendix A. Hence, only the epoxy cast cell was considered in the simulations. All finite element simulations were conducted with Abaqus/Standard v2019 [20] using an implicit quasi-static solution procedure.

The column and the cross-arm of the cell were modelled using linearly interpolated two-noded Timoshenko beam elements employing numerical integration of the cross section. The material behaviour was assumed to be linear-elastic with $E = 1720$ MPa and a POISSON'S ratio of 0.3. The characteristic length of the elements was chosen to be 0.1 mm. The carbon fibres were represented using linearly interpolated two-noded truss elements with zero compressive stiffness. The fibres were assumed to have a diameter of 0.5 mm, an Elastic modulus of $E_F = 279000$ MPa, and a POISSON'S ratio of 0.3.

Simply-supported boundary conditions as shown in Fig. 2 were used, where additionally the rotational degrees of freedom around the z-axis were constrained to avoid rigid body rotations.

The initial pre-stress σ_1 in the fibres was introduced as a stress-type initial condition. The equilibrium state of the structure with respect to σ_1 was determined in an initial step before the structure was subjected to any external loading. This equilibrium state was defined to be the undeformed configuration of the structure and the resulting stress in the fibres σ_F is considered to be their actual pre-stress.

Initially, linear buckling analyses were conducted for the following configurations:

- C1: structure without fibres, no pre-loading ($P_{pre} = 0$ N)
- C2: structure with fibres, $\sigma_F = 0$ MPa, no pre-loading ($P_{pre} = 0$ N)
- C3: structure with fibres, $\sigma_F \geq 0$, pre-load P_{pre} being slightly smaller than the critical load $P^* = 7.073$ N of the unsupported column,

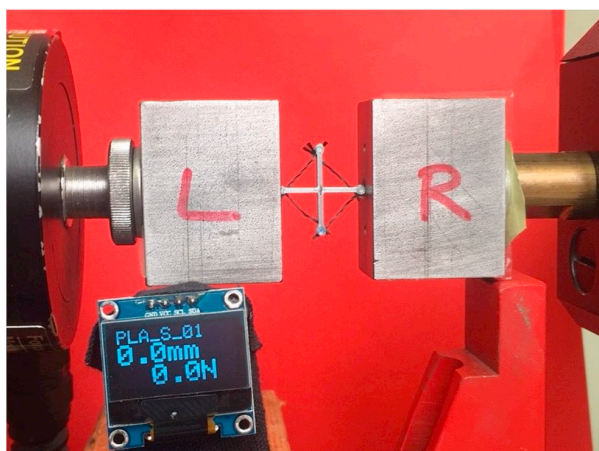


Fig. 4. Tension/compression testing device MTS Tytron 250 with device-own load-cell; specimens mounted in between two aluminium adapters (L & R).

Providing information about the critical loading state of the structure, the corresponding buckling eigenforms and the influence of the pre-stress σ_F in the fibres.

For type C3, a pre-load P_{pre} is applied in a pre-loading step in which geometrically non-linear behaviour of the structure is considered. It should be noted that the remaining stress in the fibres following the application of the pre-load plays a key role in the buckling analysis. In the subsequent analysis, this stress will be denoted by σ_p .

For all configurations, the critical load is estimated as $P^C = P_{pre} + \lambda_i P_B$ where P_B is the load applied in the buckling analysis and λ_i is the eigenvalue corresponding to the i -th buckling mode. Besides the lowest eigenvalue ($i = 1$) also eigenvalues corresponding to the second and third buckling mode are considered in the computation of the critical loads.

Owing to the fibres exhibiting zero compressive stiffness, their behaviour is strongly nonlinear. As a consequence, a strongly nonlinear behaviour of the structure subjected to compressive loading can also be expected as soon as the external loading leads to vanishing stress in at least one of the fibres. This nonlinear structural behaviour cannot be properly considered in a linear buckling analysis. Therefore, it was aimed to additionally determine the onset of buckling from the load-displacement behaviour of a slightly imperfect UC. For this purpose, the initially modelled perfect geometry of the UC was disturbed by small imperfections, trying to mimicking the situation in the experiments. However, the actual deviations (shape and magnitude) of the tested UCs from the idealized geometry as well as imperfections resulting from the boundary conditions were not accessible. Hence, geometric imperfections based on a linear combination of the eigenforms obtained in the buckling analysis for configurations C1 to C3 were used. The magnitudes for the imperfections were chosen such that the influence of the imperfections on the initial stiffness of the structure was negligible but the post-buckling regime could be accessed without any numerical issues. In contrast to the experiments, the load-displacement behaviour was obtained using a load controlled analysis, where a maximum axial force of $P = 50$ N was prescribed (cf. Fig. 2) and the geometrically nonlinear behaviour of the UC was considered.

3. Results

In the experimental and numerical study, three characteristic buckling modes of the column were identified which are visualized by means of UCs without fibres in Fig. 5. The modes observed are subsequently referred to as C-shape (left), S-shape (middle) and the U-shape (right). It should be noted that the C- and S-shape exhibit in-plane deformations, whereas the U-shape describes an out-of-plane deformation.

Subsequently, results from the experimental study are presented first. The load-displacement behaviour of UCs with and without fibre reinforcement for UCs made of epoxy and PLA is described. The second part of the section presents a numerical buckling analysis studying in detail the effect of pre-stress in the fibres on the buckling behaviour of a UC.

3.1. Load vs. end-shortening – experimental results

For the experimental test series, 30 UCs with fibres and 10 without fibres were made out of epoxy and PLA respectively. Manufacturing

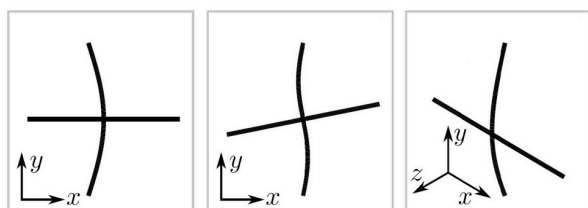


Fig. 5. Buckling modes obtained in the numerical studies for different configurations of the UC; C-shape (left), S-shape (middle), U-shape (right).

Table 1

Overview of specimens manufactured (epoxy and PLA); upper three rows list manufacturing defects (specimens excluded from analysis); lower three rows show buckling modes obtained.

	Epoxy	PLA
disbond fibre/UC	0	14
fibre failure	3	0
fibre misplacement	0	4
C-Mode	0	12
S-Mode	14	0
U-Mode	13	0

defects observed (e.g. disbond of fibres and UC, cracks in UC) are listed in Table 1 (only UCs with fibres are considered). These specimens have been excluded from the subsequent analysis. All remaining specimens were categorized according to the buckling response of the column (C-shape, S-shape or U-shape buckling mode).

Table 1 provides an overview about the number of specimens showing the characteristic buckling modes. As can be seen in Table 1, most of the epoxy specimens tested exhibit a S-shape or a U-shape buckling mode, whereas all PLA specimens buckle in a C-shape. In the subsequent analysis, focus is placed on specimens exhibiting in-plane deformations, thus S-mode buckling responses for epoxy and C-mode responses for PLA (cf. Table 1).

The compressive behaviour of UCs made of epoxy with and without fibre reinforcement is described in Fig. 6 in terms of load (P) against end-shortening (Δ) (Fig. 6a) as well as by showing corresponding buckling shapes (Fig. 6b UCs without fibres; Fig. 6c UCs with fibres). In Fig. 6a, mean valued results for UCs without carbon fibres (non-reinforced UCs) and with fibres (reinforced UCs) are visualized by a grey line and a black line respectively; corresponding standard deviations are shown by light red and dark red bars, respectively.

At first, both UCs show similar behaviour until the buckling load of the non-reinforced UCs (grey bullet point “●” in Fig. 6a) is reached. At the buckling load of the UCs without fibres, the system loses its linear behaviour exhibiting decreasing compressive stiffness until a limit point (cf. Fig. 6a “◊”), i.e. maximum load bearable by the non-reinforced UCs, is reached, from where the load gradually decreases to approximately 40% of the maximum load.

As can be seen in Fig. 6a, UCs with fibres can withstand loads significantly beyond the buckling load of the non-reinforced UCs. The compressive behaviour is characterized by an approximately constant compressive stiffness in between an end-shortening (Δ) of 0.25 mm and 1.00 mm. The loss of linearity is also associated with the occurrence of buckling at the black symbol “●”. As observed for the non-reinforced system, UCs with fibres also exhibit an initially stable post-buckling response until reaching a limit point (cf. black symbol “◊” in Fig. 6a). In the post-peak response, a significant drop in load occurs, where the load decreases to approximately 30% of the maximum load.

Analysing the mean-valued buckling and maximum loads of the systems investigated, UCs with fibres exhibit loads which are approximately 4.8 times and 3.5 times higher than the buckling and maximum loads of UCs without fibres respectively. The buckling load was determined with the aid of experimental footage, i.e. when in-plane deformation (cf. (x, y) -plane in Fig. 2) was observed first, which is in good agreement with the systems losing their linear compressive behaviour (cf. Fig. 6a). The corresponding experimental footage of characteristic buckling shapes in Fig. 6b and c and shows that the increase in load is associated with a change in the buckling mode. UCs without fibres exhibit a C-shape response (shapes ① to ③ in Fig. 6b), whereas UCs with fibres buckle in a S-mode (shapes ④ to ⑥ in Fig. 6c). Irrespective of the observed buckling shapes, once the buckling deformation reaches a certain magnitude (in between deformation states ② and ③ as well as ⑤ and ⑥ in Fig. 6a with corresponding buckling shapes in Fig. 6b and c

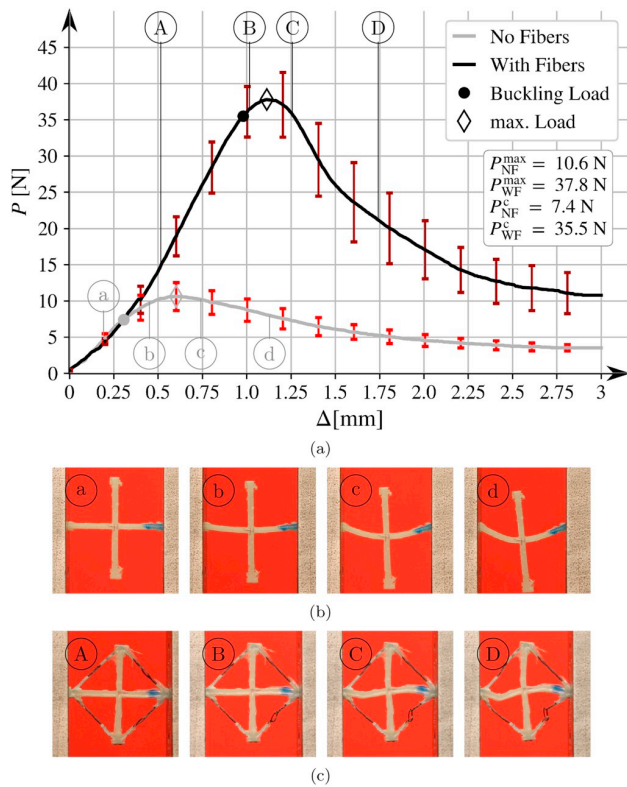


Fig. 6. (a) Load (P) against end-shortening (Δ) from experimental study of UCs made of epoxy; (b) experimental footage of UC without fibres and (c) with fibres at certain deformation states.

and) both systems lose their stability, where post-peak deformation is visually associated with accumulating material damage (cf. shapes @ and © in Fig. 6b and c and , respectively). Note that similar quantitative changes could be observed for reinforced specimens buckling in a U-shape, which is discussed in Section 4. The increase in buckling load and the corresponding buckling shapes could indicate that at the moment of buckling “pre-stress” is still acting in the fibres forcing the system in the S-mode response. This behaviour would correspond to zone 3 in Fig. 1. However, as will be discussed in Section 4, initial C-shape responses might be barely visible which are subsequently superimposed by the more pronounced S-shape as illustrated in Fig. 6c. Such a behaviour would relate to zone 2 and vanishing pre-stress in the fibres in the moment of buckling. Moreover, it can be seen in Fig. 6c (cf. © and ©) that buckling of the cross-arm (vertical part in Fig. 6c) also occurs, though being less pronounced than buckling of the column (horizontal part).

In Fig. 7a, the compressive behaviour of UCs made of PLA is shown in terms of load (P) against end-shortening (Δ), where characteristic deformation states are indicated by circled small and capital letters for UCs without and with fibre reinforcement respectively. The corresponding deformation shapes are provided in Fig. 7b and c. As in Fig. 6, the grey and black line refer to the mean-valued response of UCs without and with fibres respectively.

Initially, both types of UCs show almost identical responses with approximately the same compressive stiffness. Owing to the higher stiffness of PLA compared with epoxy, larger buckling loads were observed for UCs without fibres made of PLA than the respective UCs made of epoxy. The buckling load of the non-reinforced UCs is indicated in Fig. 7a by the grey symbol “●”. The qualitative behaviour of the post-buckling response is similar to the UCs without fibres made of epoxy, thus a short range of stable post-buckling is followed by a limit point and decreasing loads in the post-peak response until reaching a

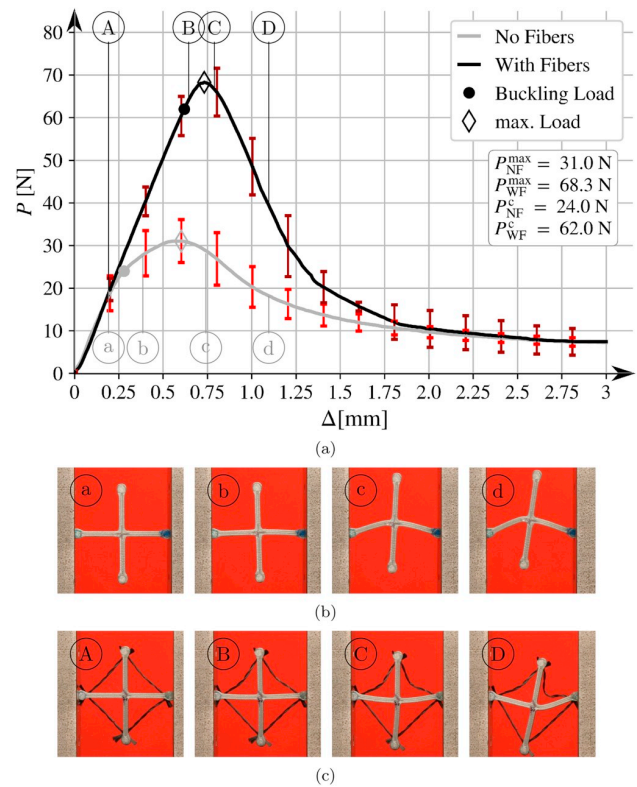


Fig. 7. (a) Load (P) against end-shortening (Δ) from experimental study of UCs made of PLA; (b) experimental footage of UC without fibres and (c) with fibres at certain deformation states.

plateau of approximately 28% of the maximum load. As for epoxy, the non-reinforced UCs all exhibit a C-shape buckling response (cf. shapes © to © in Fig. 7b).

In contrast to epoxy UCs with fibres, reinforced UCs made of PLA do not exhibit a S- or U-shape buckling response. In all tests, the system remains in a C-shape buckling response (cf. shapes © to © in Fig. 7c). However, an increase in load between UCs without and with fibres was also observed for UCs made of PLA. The buckling and maximum load of the UCs with fibres (black symbols “●” and “◊” in Fig. 7a) is approximately 2.6 and 2.2 times higher than for UCs without fibres, which is significantly smaller than for the UCs made of epoxy. This behaviour is associated with fibres slipping out of the print due to insufficient bonding in between fibres and PLA, which has been addressed in Section 2.1.1. As a consequence, in the moment of buckling, no pre-stress in the fibres can be upheld, so that the systems remain in the C-shape buckling response (cf. shapes © to © in Fig. 7c). This behaviour corresponds to Zone 2 in Fig. 1 where buckling occurs in the moment when all initial pre-stress in the fibres is vanished. The slipping of the fibres also causes the significant drop in load to approximately 12% of the maximum load in the post-peak response (cf. Fig. 7a), so that the effect of the fibres vanishes completely at a displacement of 2.0 mm reaching the plateau in response of the UCs without fibres.

3.2. Buckling analysis

The numerical buckling analysis of UCs made of epoxy was performed in two ways:

- linear eigenvalue analysis considering pre-buckling deformation due to the application of a pre-load (P_{pre}) and
- load-displacement analysis of imperfect systems which determines critical loads and buckling shapes by tracing the initial post-

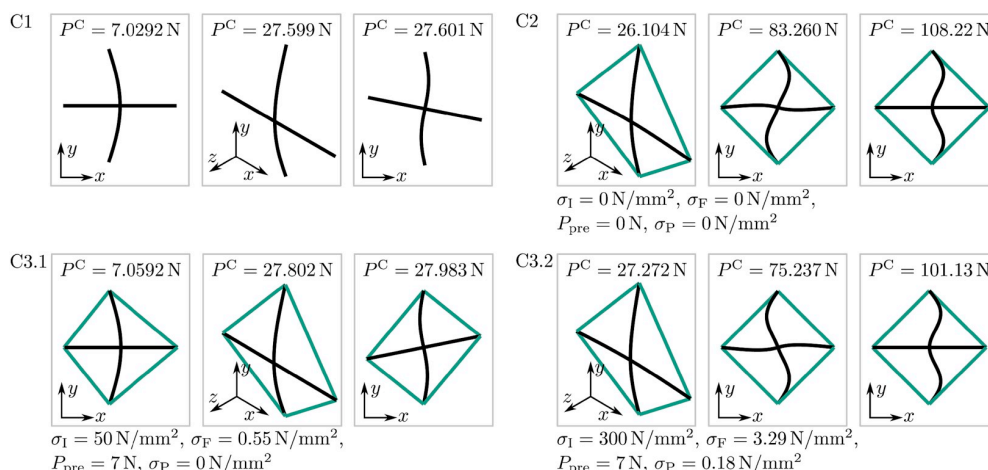


Fig. 8. Buckling modes obtained in the eigenvalue analysis for different configurations (C1, C2, C3.1, C3.2) of the unit cell.

buckling response.

Employing both methods will provide the possibility for verification as well as highlighting shortcomings of the linear eigenvalue analysis and the importance of considering imperfections. First, the results of the eigenvalue analysis are presented in Fig. 8, where

- C1 refers to UCs without fibre reinforcement,
- C2 to UCs with fibre reinforcement but no applied pre-load,
- C3.1 to UCs with fibre reinforcement and applied pre-load but vanishing stresses after application of the pre-load ($\sigma_P = 0$), and
- C3.2 to UCs with fibre reinforcement and applied pre-load, where stresses remain in the fibres after application of pre-load ($\sigma_P > 0$).

The results shown in Fig. 8 provide insight into the influence of pre-stress in the fibres on the buckling mode. As mentioned in Section 2.2, the remaining pre-stress σ_P in the deformed configuration of the UC due to a pre-load P_{pre} strongly affects the buckling response. The deformed configuration after applying the pre-load is the base state of the buckling eigenvalue analysis. Thus, if σ_P vanishes at P_{pre} , then the first three eigenforms correspond to the eigenforms observed for the unsupported column, cf. types C1 and C3.1 in Fig. 8, and also occur at almost the same critical load, which applies for the C-, U-shape and S-shape. As shown in Table 1, similar results were obtained by the experimental test series of epoxy, where S- and U-shape buckling responses occurred with roughly the same probability. However, as observed in the experiments (cf. Fig. 6c), for the S-shape response buckling of the cross-arms also occurred, which will be referred to as Double-S-shape. Such behaviour is predicted by the numerical (eigenvalue) analysis for much higher loads than the U-shape.

If $\sigma_P > 0$ at P_{pre} , instead of the C-shape response the U-shape is obtained as the critical buckling mode, cf. C3.2 in Fig. 8 and the S-shape mode occurs for much higher values of the critical load. However, as aforementioned, since the cross-arm also buckles, the mode is referred to as Double-S-shape, which is in contrast to C3.1 where the respective mode shows a S-shape with a straight but rotated cross-arm. Similar results, while indicating higher critical loads, were also observed for the initial eigenvalue analysis (C2) where neither a pre-stress in the fibres nor a pre-loading of the structure was considered.

It should be noted that the critical load obtained for the unsupported column ($\approx 7.03 \text{ N}$) corresponds well to the experimentally obtained value of 7.40 N . The slightly smaller value obtained in the simulations can be assigned to the idealized boundary conditions used.

Next, imperfections in the form of a linear combination of the buckling modes (C- and S-shape) observed in the experiments are considered in the load-displacement analysis studying the initial post-

buckling response to determine buckling loads and shapes (cf. Section 2.2). It is assumed that each of these two modes is triggered depending only on the given imperfection within the structure. The out-of-plane deformations of the UC were constrained and the first (C-shape) and third (S-shape with straight cross-arm) buckling modes according to configuration C3.1 were assigned as initial imperfections. The maximum displacement of the C and S-shape was scaled with factors 0.0002 and 0.0001, respectively. Tensile modes and higher order compressive modes were not considered. The critical load of the next compressive mode is about 2.5 times larger than those of the S-shape and hence, far larger than the buckling load observed in the experiments.

To determine the load at which the transition to the post-buckling regime occurs, in the following referred to as critical load, it is not sufficient to monitor the displacement of the load application point. Additionally, the centre node of the cell was monitored. The C-mode shape was identified via the x-displacement of this node (cf. coordinate system provided in Fig. 8), and the S-shape via the rotation around the z-axis. Owing to the imperfections, the transition to the individual modes is rather smooth than characterized by a single event leading to minimum and maximum values for the corresponding critical forces. The respective mean values of the critical loads are provided in Fig. 9, which shows the results for the load-displacement analysis (red symbols \square and \triangle) and eigenvalue analysis (blue symbols \circ).

In Fig. 9, results for UCs with constrained out-of-plane deformations are shown. As found in Ref. [10], the behaviour of the UC can be assigned to three zones. In zone 1, the structure buckles first in the C-shape and no increase of the critical load compared with the unsupported column can be observed. In Zone 2, the supporting effect of the fibres becomes visible and the load at which buckling occurs increases linearly with the pre-stress σ_F in the fibres. As indicated in Fig. 9, zone 2 can be subdivided into zones 2.1 and 2.2. In zone 2.1, the structure shows a C-shape type buckling behaviour, where the buckling load increases roughly linearly with increasing pre-stress. At a pre-stress of $\sigma_F \approx 14.76 \text{ MPa}$, indicating the transition to zone 2.2, the C-shape response is superimposed by an Double-S-shape, leading to an C+Double-S-shape higher order buckling mode. The C+Double-S-shape mode is also present in zones 1 and 2.1, when corresponding imperfections are applied. However, this mode is unaffected by the pre-stress, which results in the interaction of both modes at the transition from zone 2.1 to 2.2.

In zone 2.2, the buckling load also increases linearly with σ_F , however, with increasing values of σ_F the C-shape deformation in the C+Double-S-shape becomes less dominant and vanishes completely at $\sigma_F \approx 17 \text{ MPa}$. This marks the pre-stress at which the maximum buckling load can be observed and also the transition point to zone 3. In zone 3, the UC buckles in the Double-S-shape, where the buckling load

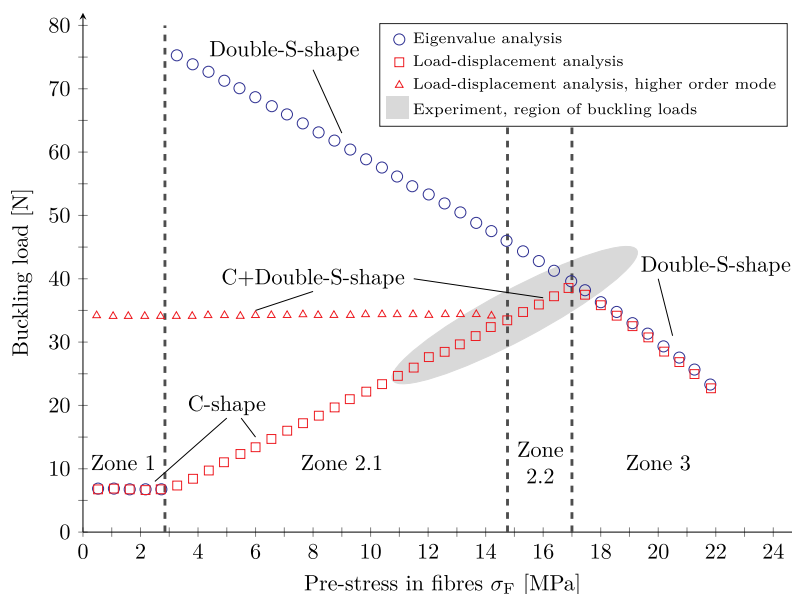


Fig. 9. Buckling load against pre-stress in fibres; results from eigenvalue and load-displacement analysis; out-of-plane deformation suppressed.

decreases considerably with increasing pre-stress in the fibres. The different buckling mode shapes observed during the analysis are illustrated in Fig. 10.

To better understand the influence of pre-stress on the critical load the results of the eigenvalue buckling prediction for the C- and Double-S-shape mode are also added to Fig. 9. As expected in Zone 1, the UC buckles in a C-shape and no increase in the buckling load can be observed. The eigenvalue analysis however cannot resolve zone 2 and hence, a jump in the buckling load is observed at the end of Zone 1. For the Double-S-shape, the buckling load obtained with the eigenvalue analysis decreases roughly linearly with σ_F and for $\sigma_F > 17$ MPa the results correspond well with those of the load-displacement analysis.

Even though the applied pre-stress could not be quantified in the experiments, with the aid of comparing buckling loads and shapes observed in the experiments (cf. Fig. 6) and numerical study (cf. Figs. 9 and 10), a region in Fig. 9 can be identified, where the experimental buckling loads would be present. This region adequately associates the phenomena observed in the experiments with findings obtained from the numerical analysis.

4. Discussion

The experimental and numerical analysis of the buckling behaviour of UCs reinforced by pre-stressed fibres provides insight into the effect of

- pre-stress,
- imperfections and

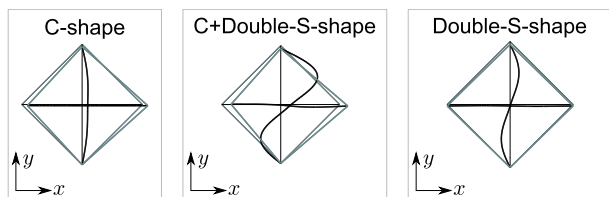


Fig. 10. Different buckling mode shapes occurring in the post-buckling analysis of the epoxy geometric UC. The displacements in x- and y-direction are scaled by factors 20 and 2 respectively.

- deformation constraints

on the buckling response. Beyond that, the implementation of both (numerical) modelling approaches (eigenvalue and load-displacement analysis) contributes to a correct numerical analysis of the buckling behaviour and highlights that in the eigenvalue analysis the parameter σ_p , i.e. the stress remaining in the fibres after applying the pre-load, is insufficient to fully trace the buckling response against pre-stress in the fibres. This is illustrated in Fig. 9 in zones 2.1 and 2.2, where $\sigma_F > 0$ causes buckling loads associated with a Double-S-shape in the eigenvalue analysis and thus significantly overestimates the buckling load of the system. The eigenvalue analysis fails to consider that stresses are further decreased during loading beyond the pre-load when buckling has not occurred. Thus, in zone 2.1, buckling occurs in the moment when all pre-stress vanishes in the fibres due to the applied compressive load. As a consequence, the system buckles still in the C-shape rather than in the Double-S-shape as predicted by the eigenvalue analysis. This behaviour can be considered in the load-displacement analysis of imperfect systems leading to results which compare well qualitatively with findings documented in Ref. [10] (cf. Fig. 1).

From the results presented in Section 3, the effect of pre-stress on the compressive strength of the UCs is demonstrated. In the experimental study, the buckling load and maximum load have been increased by factor 4.8 and 3.5 respectively when a S-shape buckling response could be observed (epoxy, cf. Fig. 6) and factors 2.6 and 2.2 when the system remained in a C-shape (PLA, cf. Fig. 6). Comparing these findings to the numerical analysis (cf. Fig. 9) associates the behaviour of UCs made of PLA with the lower region of zone 2.1 ($\sigma_F \approx 5$ MPa) and UCs made of epoxy with the higher region of zone 2.1 or zone 2.2 ($\sigma_F \approx 13-15$ MPa). However, in the load-displacement analysis, it has also been observed that with increasing σ_F the initial C-shape deformation becomes less pronounced and a mode switch to the C+Double-S-shape (as present in zone 2.2 and being the higher order mode for $\sigma_F < 14.76$ MPa) occurs.

Furthermore, it should be noted that for the C-shape the maximum x-displacement at the centre of the UC is relatively small. It is about 0.1 mm at the beginning of zone 1, 0.08 mm at the end of zone 1, and 0.04 mm in the middle of zone 2. As a consequence, such small amplitudes might have been overseen in the experimental study, such that buckling occurred at smaller loads and subsequently the systems shifts

into a C+Double-S-mode. In order to trace such behaviour in upcoming experimental studies, the C-shape amplitude as well as the pre-stress in the fibres have to be measured. This indicates that the C-shape response is associated with stable initial post-buckling and the system loses its stability, i.e. reaches a limit point (cf. maximum load in Fig. 6a), when the mode change to C+Double-S-shape and Double-S-shape occurs, which is a well-known phenomena associated with mode interaction in lightweight structures (e.g. Refs. [11,21]).

In comparison with [10], zone 3 exhibits a more pronounced decrease in buckling load with increasing pre-stress. The buckling load falls rapidly below magnitudes associated with C-shape buckling responses in zone 2.1. This behaviour is verified by the eigenvalue analysis, since in zone 3 the stresses in the fibres do not vanish in the moment of buckling. Thus, it seems that the decrease in buckling load with increasing σ_F is inherent to the structure.

It should also be noted that imperfections rather than purely in-plane modes (C- and S-shape, as considered in Fig. 9), such as the U-shape response observed in the experiments, may alter the buckling response and introduce further mode interactions (cf. [25]). Considering geometric UCs of collinear lattices, such additional out-of-plane modes are also inherent to the structure, where their occurrence strongly depends on the geometry of the lattice. Adding the buckling loads associated with these modes to Fig. 9 would provide a complete buckling analysis of such pre-stressed geometric UCs and the basis of extending the analysis to multiple cross-arms (e.g. Ref. [12]).

5. Conclusions

The work has demonstrated that the concept of pre-stressed columns can be employed to enhance the compressive strength of geometric unit cells (UCs) of collinear lattice structures. Therefore, UCs have been manufactured using additive manufacturing and carbon fibres. Experimental and numerical studies have been performed yielding the following insight:

- Incorporating pre-stressed fibres significantly increases the buckling and ultimate load, thus the compressive strength of the system, in comparison to UCs without fibre reinforcement. The experimental

and numerical study showed an increase in buckling load by factor 4.8 and 5.5 respectively.

- A continuous numerical analysis considering imperfections is required to adequately model the buckling response of pre-stressed UCs. Eigenvalue analysis employing the concept of pre-loads may be used for certain configurations only.
- Load and end-shortening information from experimental tests might not be sufficient to describe the buckling response in full detail, since C-shape responses may be barely visible leading to different buckling loads and buckling shapes.
- Mode interactions and thus mode changes are introduced by pre-stressed fibres. The initial buckling response may alter with increasing pre-stress (cf. transition from zone 2.1 to zone 2.2 in Fig. 9) as well as mode changes during the initial post-buckling response can occur. Even though not studied in detail, it has been observed (and partly shown by the experimental tests) that the C-shape response is associated with stable post-buckling, whereas instability is caused by mode interactions.
- The results obtained compare well qualitatively with findings on large-scale civil engineering applications (e.g. Refs. [10,17]). Deviations, such as the more pronounced decrease in buckling load in zone 3, are assumed to be related with the chosen geometry of the structure as well as the material used for the columns and fibres, i.e. the ratio of Young's moduli. As a consequence, general remarks can be made about the effect of pre-stress but parametric studies regarding material properties and geometry will be required to obtain general insight.
- Additive manufacturing seems to be a promising manufacturing strategy in order to incorporate fibres in small lattice structures. However, sufficient bonding between fibres and printed material has to be given to accomplish reliable strengthening effects (cf. compare Fig. 6, material: epoxy, with Fig. 7, material: PLA).

In summary, the study constitutes an initial effort to transfer the concept of pre-stressed load bearing structural members to lattice core structures. The strengthening effect of pre-stressed fibres on the buckling and ultimate load of geometric UCs has been demonstrated and its resulting complex buckling behaviour described.

Appendix A. Results of the buckling analysis for UCs made of PLA

The results of the buckling analysis for UCs made of PLA are provided in Fig. A.1. For all configurations C1 to C3.2, the same buckling mode shapes as for UCs made of epoxy (cf. Fig. 8) were obtained.

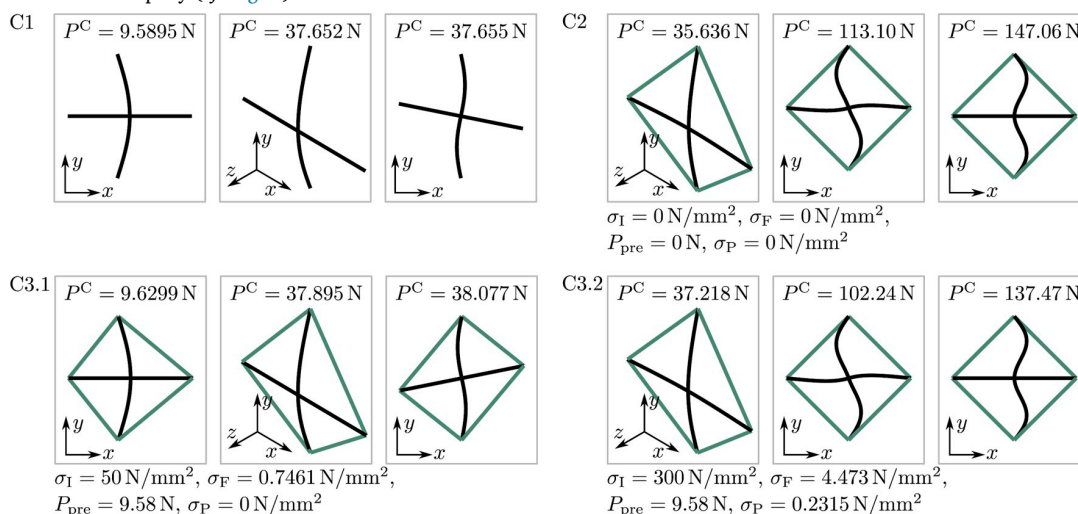


Fig. A.1. Buckling modes obtained in the eigenvalue analysis for PLA and different configurations (C1, C2, C3.1, C3.2) of the unit cell.

The corresponding critical loads of the PLA cell are by a factor $\delta = E_{\text{PLA}}/E_{\text{Epoxy}} = 2346.5/1720 \approx 1.36$ larger than those obtained for UCs made of epoxy. The critical loads and the comparison to UCs made of epoxy is summarized in Table A.1. The findings provided in Fig. A.1 and Table A.1 underline the statement made in Section 2.2 that no difference in the qualitative behaviour of cells made of epoxy and PLA can be expected. As a consequence, it is sufficient to perform the numerical studies only for epoxy UCs.

Table A.1

Comparison of the critical loads obtained for epoxy and PLA UCs (scaling with $\delta = E_{\text{PLA}}/E_{\text{Epoxy}}$ employed).

Mode	P_{Epoxy}^C in N	$P_{\text{Epoxy}}^C \cdot \delta$ in N	P_{PLA}^C in N	$\left \frac{P_{\text{Epoxy}}^C \cdot \delta - P_{\text{PLA}}^C}{P_{\text{PLA}}^C} \right $
C1 mode 1	7.0292	9.5895	9.5895	0.0
C1 mode 2	27.599	37.652	37.652	0.0
C1 mode 3	27.601	37.655	37.655	0.0
C2 mode 1	26.104	35.612	35.636	0.0007
C2 mode 2	83.260	113.59	113.10	0.0043
C2 mode 3	108.22	147.64	147.06	0.0039
C3.1 mode 1	7.0592	9.6300	9.6299	0.00002
C3.1 mode 2	27.802	37.929	37.895	0.0009
C3.1 mode 3	27.983	38.176	38.077	0.0026
C3.2 mode 1	27.272	37.206	37.218	0.0003
C3.2 mode 2	75.237	102.64	102.24	0.0039
C3.2 mode 3	101.13	137.97	137.47	0.0036

References

- [1] R.R. de Araujo, S.A.L. de Andrade, P.C.G. da S Vellasco, J.G.S. da Silva, L.R.O. de Lima, Experimental and numerical assessment of stayed steel columns, *J. Constr. Steel Res.* 64 (2008) 1020–1029.
- [2] J. Bauer, S. Hengsbach, I. Tesari, R. Schwaiger, O. Kraft, High-strength cellular ceramic composites with 3d microarchitecture, *Proc. Natl. Acad. Sci. U. S. A* 111 (2014) 2453–2458.
- [3] M. Bendsoe, N. Triantafyllidis, Scale effects in the optimal design of a micro-structured medium against buckling, *Int. J. Solids Struct.* 26 (1990) 725–741.
- [4] Y. Chen, T. Li, F. Scarpa, L. Wang, Lattice metamaterials with mechanically tunable Poisson's ratio for vibration control, *Phys Rev Appl* 7 (2017) 1–11.
- [5] K.H. Chu, S. Berge, Analysis and design of struts with tension ties, *J Struct Div-ASCE* 89 (1963) 127–164.
- [6] N. Fleck, V. Deshpande, M. Ashby, Micro-architected materials: past, present and future, *Proc R Soc A* 466 (2010) 2495–2516.
- [7] G. Ganzosch, M. Todt, A. Köllner, C. Völlmecke, Experimental investigations on prestressed stayed columns on smaller length scales, *Proceedings of the Eighth International Conference on Thin-Walled Structures*, 2018 978-989-20-8665-1, pp. 1–15.
- [8] L.J. Gibson, M.F. Ashby, *Cellular Solids: Structure and Properties*, Cambridge university press, 1999.
- [9] R. Gümriük, R. Mines, Compressive behavior of stainless steel micro-lattice structures, *Int. J. Mech. Sci.* 68 (2013) 125–139.
- [10] H.H. Hafez, M.C. Temple, J.S. Ellis, Pretensioning of single-crossarm stayed columns, *J Struct Div ASCE* 105 (1979) 359–375.
- [11] G.W. Hunt, M.A. Wadee, Localization and mode interaction in sandwich structures, *Proc R Soc A* 454 (1998) 1197–1216.
- [12] P. Li, M. Wadee, J. Yu, N. Christie, M. Wu, Stability of prestressed stayed steel columns with a three branch crossarm system, *J. Constr. Steel Res.* 122 (2016) 274–291.
- [13] H. Mauch, L. Felton, Optimum design of columns supported by tension ties, *J Struct Div-ASCE* 93 (1967) 201–220.
- [14] P. Moongkhamklang, D. Elzey, H. Wadley, Titanium matrix composite lattice structures, *Composites Part A* 39 (2008) 176–187.
- [15] F. Nezami, J.P. Fuhr, Digitale entwicklung und automatisierte cfk-verstärkung additiv gefertigter teile, *Lightweight Design* 10 (2017) 38–41.
- [16] A.I. Osofero, M.A. Wadee, L. Gardner, Experimental study of critical and post-buckling behaviour of prestressed stayed columns, *J. Constr. Steel Res.* 79 (2012) 226–241.
- [17] D. Saito, M. Wadee, Post-buckling behaviour of prestressed steel stayed columns, *Eng. Struct.* 30 (2008) 1224–1239.
- [18] D. Saito, M. Wadee, Buckling behaviour of prestressed steel stayed columns with imperfections and stress limitation, *Eng. Struct.* 31 (2009) 1–15.
- [19] T. Tancogne-Dejean, A.B. Spierings, D. Mohr, Additively-manufactured metallic micro-lattice materials for high specific energy absorption under static and dynamic loading, *Acta Mater.* 116 (2016) 14–28.
- [20] Abaqus, Abaqus/Standard V2019, Dassault Systèmes, Providence RI, USA, 2019.
- [21] M. Wadee, L. Gardner, T. Hunt, Buckling mode interaction in prestressed stayed columns, *P I Civil Eng-Str B* 166 (2013) 403–412.
- [22] H.N.G. Wadley, N.A. Fleck, A.G. Evans, Fabrication and structural performance of periodic cellular metal sandwich structures, *Compos. Sci. Technol.* 63 (2003) 2331–2343.
- [23] G. Zhang, B. Wang, L. Ma, J. Xiong, L. Wu, Response of sandwich structures with pyramidal truss cores under the compression and impact loading, *Compos. Struct.* 100 (2013) 451–463.
- [24] F.W. Zok, R.M. Latturre, M.R. Begley, Periodic truss structures, *J. Mech. Phys. Solids* 96 (2016) 184–203.
- [25] C. Zschernack, M.A. Wadee, C. Völlmecke, Nonlinear buckling of fibre-reinforced unit cells of lattice materials, *Compos. Struct.* 136 (2016) 217–228.



Received: 16 May 2019

Accepted: 1 July 2019

DOI: 10.1002/pamm.201900248

Nonlinear Finite Element Study of Beams with Elasto-Plastic Damage Behavior in the Post-Buckling Regime

Benjamin Werner^{1,*}, Melanie Todt¹, and Heinz E. Pettermann¹

¹ Institute of Lightweight Design and Structural Biomechanics, TU Wien, Getreidemarkt 9, A-1060 Vienna, Austria

Lattice structures with low density tend to localize under compressive loading. The localizations start in a single cell band due to buckling of the beams and lead to compaction of the cells. To identify an appropriate discretization and to determine the influence of damage in an elasto-plastic material behavior two simple load cases are analyzed with the finite element (FE) method. Simulations of an axial loaded beam in the post-buckling regime with and without damage are carried out. In addition, a triangular cell under compression with different discretizations is analyzed.

© 2019 The Authors *Proceedings in Applied Mathematics & Mechanics* published by Wiley-VCH Verlag GmbH & Co. KGaA Weinheim

1 Introduction

Lattice materials can be described as arrangements of rigid-jointed beams. Loads on the macroscopic level of the lattice can cause a loss of structural stability on the microscopic level. Gümrük et al. [1] have investigated the effect experimentally with samples of lattice structures with different densities. All investigated types of lattices showed localization bands under compression. The localization started with the buckling of beams in one band of cells and progressed up to full compaction of the cell band. The adjacent cell layers experienced the same deformation behavior with increasing load. Similar deformation patterns were shown by Luxner et al. [2] in a numerical study. Also Crupi et al. [3] reported localization bands due to buckling of struts in experimentally investigated lattice samples. Smith et al. [4] determined the buckling of struts in lattices under compression in experiments as well.

Simulating buckling and localization bands in lattices using nonlinear finite element analyses would allow for a systematic investigation of dominating parameters encouraging this failure mode. Of particular interest are lattice structures with an elasto-plastic base material including damage. The aim of the present study is to find a suitable discretization of a single lattice member with this kind of material behavior. A beam under axial loading (Fig. 1a) in the post buckling regime and a triangular cell under compression (Fig. 2a) are numerically investigated. The outcome is supposed to form a basis for future numerical investigations of lattice structures with elasto-plastic behavior with damage. It is assumed that the outcome of the 2D simulations can be easily adopted for 3D lattice structures.

2 Materials and Methods

Both structures have linear elastic perfectly plastic material behavior with and without damage. The Young's modulus is $E = 2000$ MPa and the Poisson ratio $\nu = 0.2$. The yield stress of the material is 18.4 MPa. A slight hardening of $H = 1$ MPa is applied to prevent numerical instability in the finite element simulations. Damage of the material is defined by the specific fracture energy $G_f = 1$ N/mm and linear softening. The critical strain $\varepsilon_{cr}^{pl} = 10^{-5}$ defines the onset of damage. A 2D 3-node Timoshenko beam element with a quadratic interpolation function is used for all numerical simulations. It is characterized by two integration points along the beam axis per element. In through thickness direction five or 25 integration points are used, which are indicated as section points. All numerical simulations are performed with the finite element software Abaqus/Standard 2018 (Dassault Systèmes Simulia Corp., Providence, RI, USA).

In the first loading scenario, a small horizontal force in the center of the beam is applied as perturbation in addition to the axial displacement (Fig. 1 a). The perturbation is only active in the first quarter of the simulation time and ramped down to zero after. The axial displacement is applied up to a maximum of 0.5 mm. The beam has a length of 1 mm and a width of 0.1 mm and is discretized by 25 elements with quadratic interpolation function. The two integration points per element have 25 section points. The beam is analyzed with linear elastic as well as with elasto-plastic behavior once with damage and once without damage.

Moreover, the collapse of a triangular cell under displacement controlled loading is studied (Fig. 2 a). A small moment is applied as perturbation at the top corner of the cell in the same way as in the single beam study. The members of the triangular cell have a length of 1 mm and are 0.1 mm in width. To study the influence of the element and section point number three different discretizations are compared. The first one has five elements per side and five section points, the second has five elements and 25 section points, and the third has 25 elements and 25 section points. All three simulations include damage.

* Corresponding author: e-mail benjamin.werner@tuwien.ac.at, phone +43 664 60588 31729



This is an open access article under the terms of the Creative Commons Attribution License 4.0, which permits use, distribution and reproduction in any medium, provided the original work is properly cited.

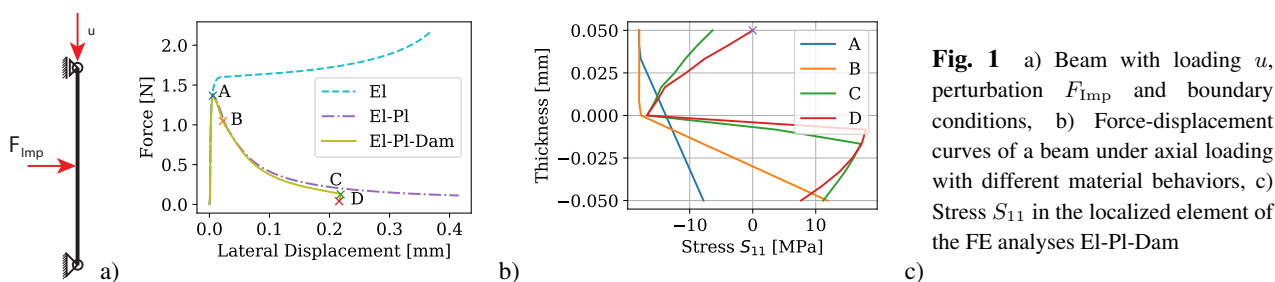


Fig. 1 a) Beam with loading u , perturbation F_{Imp} and boundary conditions, b) Force-displacement curves of a beam under axial loading with different material behaviors, c) Stress S_{11} in the localized element of the FE analyses EL-Pl-Dam

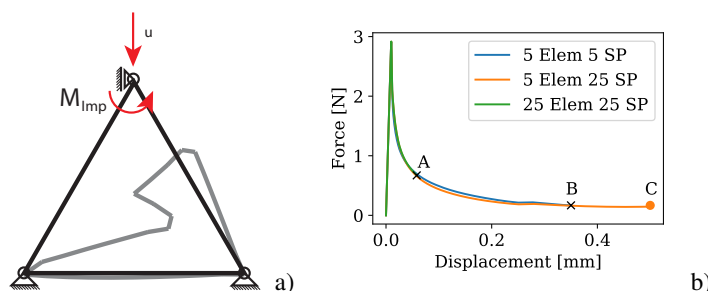


Fig. 2 a) Triangular cell with loading u , perturbation M_{Imp} and boundary conditions together with the deformed configuration (gray) b) Force-displacement curve of the triangular cell with three different discretizations

3 Results

Figure 1 b shows the reaction force over the lateral displacement of three FE analyses of a single beam under axial loading. The analysis indicated by EL is a simulation with linear elastic material. The one labelled by EL-Pl has elasto-plastic material without damage behavior, while EL-Pl-Dam is characterized by an elasto-plastic material including damage. After reaching point A the reaction forces of the simulation EL is increasing slightly further to 1.6 N where the curve reaches a plateau. The reaction forces of EL-Pl and EL-Pl-Dam decrease substantially after point A and both curves are nearly identical up to 0.08 mm displacement. Past 0.08 mm the force-displacement curve EL-Pl is characterized by slightly higher values of reaction force compared to the curve EL-Pl-Dam. Moreover, the reaction force of the curve EL-Pl-Dam drops at point C to almost zero and the analysis stops premature at point D while the simulation EL-Pl continues to the applied final displacement. In an early stage of both simulations the deformation begins to localize in an inelastic hinge in a single element. Figure 1 c shows the stresses in axial direction in the localized element for different stages of the simulation EL-Pl-Dam. The premature ending in D of the simulation EL-Pl-Dam coincides with a fully damaged section point with $S_{11} = 0$ MPa indicated by an \times in Fig. 1 c.

The three discretizations of the triangular cell lead to very similar force-displacement curves (Fig. 2 b). The analyses with 25 elements and 25 section points ends due to numerical instabilities at point A at 0.05 mm displacement. The simulation with five elements and five section points stops at point B at 0.35 mm displacement. Only the FE analyses with five elements and 25 section points reaches the applied displacement of 0.5 mm at point C (gray in Fig. 2 a).

4 Discussion and Conclusion

The aim of the study was to find an appropriate discretization to investigate lattice structures under compressive loading with elasto-plastic material including damage. Therefore, a single beam in the post buckling regime as well as a single triangular cell under compression was investigated. The two simulations of the single beam under axial loading with elasto-plastic material and with and without damage lead to similar force-displacement curves. The significant difference is the sudden drop in reaction force and a premature ending in the simulation including damage. The end of the simulation due to numerical instabilities is assumed to be related with the stresses in the inelastic hinge with one fully damaged section point. The number of elements and section points per side is rather insignificant to predict the reaction force of the triangular cell. This suggests that the mesh adjusted softening works well with the 3-node Timoshenko beam element in Abaqus. However, the numerical stability of the FE analyses seems to benefit from a combination of fewer elements and many section points. The results of the present study give a first indication on how to discretize lattice structures under compressive loading with elasto-plastic material behavior including damage and form a basis for future investigations.

References

- [1] R. Gümürük, R. A. W. Mines and S. Karadeniz, *Mater. Sci. Eng. A* **586**, 392–406 (2013).
- [2] M. H. Luxner, J. Stampfl, and H. E. Pettermann, *Int. J. Solids Struct.* **44**, 2990–3003 (2007).
- [3] V. Crupi, E. Kara, G. Epasto, E. Guglielmino and H. Aykul, *Mater. Des.* **135**, 246–256 (2017).
- [4] M. Smith, Z. Guan and W. J. Cantwell, *Int. J. Mech. Sci.* **67**, 28–41 (2013).